



Universitat Autònoma de Barcelona

ADVERTIMENT. L'accés als continguts d'aquesta tesi queda condicionat a l'acceptació de les condicions d'ús establertes per la següent llicència Creative Commons:  http://cat.creativecommons.org/?page_id=184

ADVERTENCIA. El acceso a los contenidos de esta tesis queda condicionado a la aceptación de las condiciones de uso establecidas por la siguiente licencia Creative Commons:  <http://es.creativecommons.org/blog/licencias/>

WARNING. The access to the contents of this doctoral thesis it is limited to the acceptance of the use conditions set by the following Creative Commons license:  <https://creativecommons.org/licenses/?lang=en>



PhD Thesis

**Epitaxial growth of complex functional oxide thin films
by green and sustainable chemical solution methods**

Hailin Wang

Supervised by:

Dr. Narcís Mestres

Prof. Benjamín Martínez

Tutor: Prof. Ramón Yáñez

PhD Programme in Materials Science
Chemistry Department-Science Faculty
Universitat Autònoma de Barcelona

2020



Memòria presentada per aspirar al Grau de Doctor per

Hailin Wang

Vist i plau

Prof. Ramón Yáñez
Departament de Química
(Tutor)

Dr. Narcís Mestres
(Director)

Prof. Benjamín Martínez
(Director)

Bellaterra, 6 de Novembre de 2020



MINISTERIO
DE CIENCIA, INNOVACIÓN
Y UNIVERSIDADES

ICMAB
INSTITUT DE CIÈNCIA DE MATERIALS DE BARCELONA

EXCELENCIA
SEVERO
OCHOA



El **Dr. Narcís Mestres Andreu**, Investigador Científic del Institut de Ciència de Materials de Barcelona (ICMAB), Consejo Superior de Investigaciones Científicas, CSIC,

El **Dr. Benjamín Martínez Perea**, Professor de Investigació del Institut de Ciència de Materials de Barcelona (ICMAB), Consejo Superior de Investigaciones Científicas, CSIC,

CERTIFIQUEN:

Que **Hailin Wang** ha realitzat sota la seva direcció el treball d'investigació que s'exposa a la memòria titulada "Epitaxial growth of complex functional oxide thin films by green and sustainable chemical solution methods" per optar al grau de **DOCTOR per la Universitat Autònoma de Barcelona**.

Que el dissenys dels experiments, síntesi de mostres, llur caracterització, l'anàlisi dels resultats, la redacció dels articles i d'aquesta memòria són fruit del treball d'investigació realitzat per **Hailin Wang**.

I perquè així consti, signen el present certificat,

Dr. Narcís Mestres

Prof. Benjamín Martínez

Bellaterra 3 de Novembre de 2020

Acknowledgments

I would first like to thank my supervisors, Dr. Narcís Mestres and Prof. Benjamín Martínez for inviting me to come to ICMAB and giving me the opportunity to perform my PhD Thesis work. I would also like to extend my deepest gratitude to Prof. Teresa Puig and Prof. Benjamín Martínez for gladly accepting me in the Superconducting Materials and Large Scale Nanostructures (SUMAN), and in the Advanced Characterization and Nanostructured Materials (ACNM) groups. I was the first student to face the challenges of the polymer assisted deposition method to prepare oxide films in ICMAB, Dr. Narcís Mestres helped me a lot to start the work properly in a short time. We discussed a lot about the work and almost met every workday, he always showed me the right direction to proceed, I have learned a lot from him. I work with magnetic materials, Prof. Benjamín Martínez expert in the field, helped me a lot on the understanding of the materials properties. Except for the work, he is patient with me and always encourages me.

I would like to thank Dr. Bernat Bozzo and Dr. Ferran Vallès for their technical support during magnetic measurements.

I would like to acknowledge Dr. Carles Frontera, Anna Crespi, Francesc Xavier Campos and Joan Esquiús for discussions and assistance on the X-ray diffraction, the 3D reciprocal space tomography and reciprocal space maps measurements and analysis.

I am extremely grateful to Víctor Fuentes for the training and the maintenance of the AFM. He taught me how to use the AFM, and helped me solve a lot of problems.

I'm deeply indebted to Dr. Alberto Pomar, Dr. Lluís Balcells and Mr. Sergi Martín for initiating me in the concepts of FMR experiments.

I would like to thank Dr. Jaume Gázquez and Dr. Matthew F. Chisholm for assistance with the STEM–EELS measurements and analysis.

I would like to acknowledge Prof. Pere Roura from Universitat de Girona for the thermal analysis of the precursor solutions.

I would like to thank Dr. Javier Herrero-Martín from ALBA Synchrotron Light Source and Dr. Carlos Frontera for assistance with the X-ray absorption spectroscopy study.

I would like to acknowledge Mrs. Mariona de Palau and Mr. Joshua Bailo for the technical support and maintenance of all the equipments in SUMAN group.

I am also thankful to Dr. Ignaci Villaroya of Servei d'Anàlisi Química de la UAB, for the professional ICP characterization of the PAD solutions.

I would like to thank Dr. Mar Tristany for her help in solving bureaucratic questions.

I'm very grateful to all the previous and present members of the 2 groups: Prof. Teresa Puig, Prof. Xavier Obradors, Dr. Xavier Granados, Dr. Anna Palau, Dr. Susagna Ricart, Dr. Mariona Coll, Dr. Joffre Gutiérrez, Dr. Cornelia Pop, Dr. Albert Queraltó, Dr. Kapil Gupta, Dr. Ziliang Li, Dr. Alexander Stangl, Dr. Júlia Jareño, Mr. Juri Banchewski, Mr. Alejandro Fernández, Mr. Artur Romanov, Mrs. Pengmei Yu, Mr. Pedro Barusco, Mr. Adrià Pacheco, Mrs. Pamela Machado, Mr. Jordi Alcalà, Mrs. Diana García, Mrs. Lavinia Saltarelli, Mr. Guilherme Telles, Mrs. Natalia Chamorro, and Mrs. Mónica Bernal for the help and friendship during the last four years.

I would like to thank all the Chinese friends in ICMAB and UAB, Zheng Ma, Songbai Zhang, Weiqiang Wang, Tingting Xiao, Hao Li, Junjie Zhu, Xiaodong Zhang, and others no explicitly mentioned for the help on the work and life here.

I very much appreciate the financial support from the China Scholarship Council.

This research was founded by the Spanish Ministry of Science, Innovation and Universities through Severo Ochoa (SEV-2015-04969) and Severo Ochoa FUNFUTURE (CEX2019-000917-S), SUMATE (RTI2018-095853-B-C21), HETEROCS (MAT2015-71664-R) and SPIN-CURIOX (RTI2018-099960-B-100) projects co-financed by the European Regional Development Fund, MCIU/AEI/FEDER, UE. Support from the Catalan Government through 2017-SGR-1519 project is also acknowledged.

Finally, I would like to thank my family for their love, encourage and support.

List of abbreviations

AFM: Antiferromagnetic

AFM: Atomic force microscopy

APB: Antiphase boundary

AS: anti-site

BHF: Buffered hydrofluoric acid

CMR: Colossal magnetoresistance

CPEI: Carboxylated polyethyleneimine

CPW: Coplanar waveguide

CSD: Chemical solution deposition

CVD: Chemical vapor deposition

DE: Double exchange

DI: De-ionized

DTA: Differential thermal analysis

EDTA: Ethylenediaminetetraacetic acid

FC: Field-cooled

FM: Ferromagnetic

FMI: Ferromagnetic insulator

FMM: Ferromagnetic and metallic

FMR: Ferromagnetic resonance

FWHM: Full width at half maximum

HS: High-spin

HTSC: High temperature superconductivity

ICP-AES: Inductively coupled plasma-atomic emission spectroscopy

IP: In plane

J-T: Jahn–Teller

KTO: KTaO_3

LAO: LaAlO_3

LCMO: $\text{La}_2\text{CoMnO}_6$

LCO: LaCoO_3

LLG: Landau-Lifshitz-Gilbert

LMO: $\text{La}_{0.92}\text{MnO}_3$

LNMO: $\text{La}_2\text{NiMnO}_6$

LSAT: $\text{La}_{0.18}\text{Sr}_{0.82}\text{Al}_{0.59}\text{Ta}_{0.41}\text{O}_3$
LSMO: $\text{La}_{0.7}\text{Sr}_{0.3}\text{MnO}_3$
MBE: Molecular beam epitaxy
ME: Magnetoelectric
MIT: Metal-insulator transitions
MOCVD: Metalorganic chemical vapor deposition
MOD: Metal-organic decomposition/deposition
MPMS: Magnetic Property Measurement System
MR: Magnetoresistance
OP: Out of plane
PAD: Polymer assisted deposition
PEI: Polyethyleneimine
PPEI: phosphorylated-polyethylenimine
PPMS: Physical Property Measurement System
PLD: Pulsed laser deposition
PVD: Physical vapor deposition
RHEED: Reflection high-energy electron diffraction
RSM: Reciprocal space map
RMS: Root mean square
RTA: Rapid thermal anneal
SEM: Scanning electron microscopy
SLD: super luminescent diode
SNR: Signal-to-noise ratio
SOFC: Solid oxide fuel cell
SPEI: Sulfonated polyethyleneimine
SQUID: Superconducting Quantum Interference Device
STO: SrTiO_3
TEM: Transmission electron microscopy
TGA: Thermogravimetric analysis
TM: Transition metals
UHV: Ultrahigh vacuum
UV: Ultraviolet
XAS: X-ray absorption spectroscopy
XRD: X-Ray diffraction

XRR: X-Ray reflectivity

YAO: YAlO_3

YSZ: Yttria-stabilized zirconia, $(\text{ZrO}_2)_{1-x}(\text{Y}_2\text{O}_3)_x$

ZFC: Zero-Field Cooled

Abstract

Perovskites oxides are of strong interest due the huge potential range of applications they offer with a particularly simple structure, such as spintronics, magneto-optic devices, or catalysis, and most of these applications require the use of thin films and heterostructures. Most of the electronic properties of perovskites are determined by the physics associated with the transition metal and the corner-sharing oxygen anions of the BO_6 octahedra therefore, in double perovskite structures, the ordered arrangement of cations in the B-site position is of major relevance.

Chemical solution deposition (CSD) techniques are promising methodologies to achieve epitaxial oxide thin films combining high performance with high easy scalability, environment friendly fabrication and low cost. In this thesis, the polymer-assisted deposition (PAD), an aqueous CSD method, is used to prepare derivatives of lanthanum manganite perovskite films, including $\text{La}_{0.92}\text{MnO}_3$, $\text{La}_{0.7}\text{Sr}_{0.3}\text{MnO}_3$, $\text{La}_2\text{CoMnO}_6$ and $\text{La}_2\text{NiMnO}_6$ films on SrTiO_3 and LaAlO_3 substrates. $\text{La}_{0.92}\text{MnO}_3$ and $\text{La}_{0.7}\text{Sr}_{0.3}\text{MnO}_3$ display ferromagnetic metallic conducting properties, $\text{La}_2\text{CoMnO}_6$ and $\text{La}_2\text{NiMnO}_6$ are ferromagnetic insulating. All these films have Curie temperatures near room temperature.

Firstly, we introduced the basic concepts related to perovskite oxides, including the structure and the magnetic properties, and the methods to grow oxide thin films. Secondly, more detailed processes of PAD method and characterizations will be presented. The third part is a compilation of articles of the $\text{La}_{0.92}\text{MnO}_3$, $\text{La}_2\text{CoMnO}_6$ and $\text{La}_2\text{NiMnO}_6$ films. All the films were prepared by PAD method. The thermal behavior of the mixed metal polymer precursor solution was traced by combining differential scanning calorimetry and thermogravimetric analysis. The structural features were studied by X-ray diffraction. The thickness was measured with X-ray reflectivity. The surface topography of the films was measured by AFM. Static magnetic properties were measured using a SQUID magnetometer. The scanning transmission electron microscopy (STEM) measurements together with electron energy loss spectroscopy (EELS) was used to confirm the full Co/Mn cationic ordering in $\text{La}_2\text{CoMnO}_6$ films, and ALBA synchrotron radiation facilities were used to investigate

the disordering in $\text{La}_2\text{NiMnO}_6$ films. The dynamic magnetic properties of $\text{La}_{0.92}\text{MnO}_3$ thin films and $\text{La}_{0.92}\text{MnO}_3/\text{Pt}$ bilayers as a function of temperature were studied by using a ferromagnetic resonance spectrometer.

The results show that the particular crystallization and growth process conditions of PAD (very slow rate, close to thermodynamic equilibrium conditions) promote high crystallinity and quality of the films, as well as favors spontaneous B-site cationic ordering, almost full B-site cationic ordering can be achieved in $\text{La}_2\text{CoMnO}_6$ while the ordering factor in $\text{La}_2\text{NiMnO}_6$ films is around 80%. The $\text{La}_2\text{CoMnO}_6$ and $\text{La}_2\text{NiMnO}_6$ samples prepared by RTA have similar values of saturation magnetization and Curie temperature to the counterpart films prepared by using conventional annealing processes, indicating a low influence of the annealing heating ramp rate on the B-B' site cationic ordering. However, the magnetic behavior of samples prepared by RTA or conventional annealing is slightly different suggesting a different microstructure. For instance, antiphase boundaries (APB) in RTA samples are easily suppressed by a post-annealing treatment while they are not in samples prepared by conventional annealing process. On the other hand, ferromagnetic resonance (FMR) measurements in $\text{La}_{0.92}\text{MnO}_3$ films and $\text{La}_{0.92}\text{MnO}_3/\text{Pt}$ bilayers indicate a clear increase of the magnetic damping in the later, which may be indicative of the transfer of spin momentum from $\text{La}_{0.92}\text{MnO}_3$ to the Pt layer by spin pumping. This fact demonstrates that PAD technique allows obtaining complex oxide thin films of high microstructural quality suitable for spintronics applications.

Our results make evident the CSD-PAD method can be competitive with physical methods allowing obtaining complex oxide epitaxial thin films of high quality. In particular, the growth conditions of PAD are prone to promote spontaneous B-site cationic ordering in double perovskite oxide.

Table of Contents

Acknowledgments	VII
List of abbreviations	IX
Abstract	XIII
Chapter 1. Introduction	1
1.1 Transition metal oxides	3
1.2 Perovskite crystal structure	5
1.3 Superexchange and double exchange in lanthanum manganite perovskite	8
1.4 Derivative of lanthanum manganite perovskite	11
1.5 Oxide thin films synthesis methods	14
1.5.1 Vapour deposition method	14
1.5.2 Chemical solution deposition (CSD)	18
Chapter 2. Objectives of this thesis	29
Chapter 3. Experimental	33
3.1 Polymer Assisted Deposition (PAD)	35
3.1.1 Solution chemistry of PAD	36
3.1.2 Stability and pH	36
3.1.3 PAD mother solutions preparation	37
3.2 Thermogravimetric analysis of solutions	42
3.3 Substrate treatment for atomically flat surface	44
3.3.1 Structure of substrate	44
3.3.2 Treatment for STO substrates	47
3.3.3 Treatment for LAO substrates	48
3.4 Solution spin-coating	50
3.5 Thermal treatment	53
3.6. Structural characterization and magnetic properties	58
3.6.1 X-ray thin films characterization	58

3.6.2 Atomic force microscopy	62
3.6.3 Magnetic properties characterization	65
3.6.4 Electric transport measurements	69
Chapter 4. Compilation of Articles	77
4.1 La ₂ CoMnO ₆ epitaxial thin films grown by polymer assisted deposition and confirmation of full Co/Mn cationic ordering achievement	79
4.2 La ₂ CoMnO ₆ and La ₂ NiMnO ₆ double perovskite epitaxial thin films grown by polymer assisted deposition, structural and magnetic properties.....	99
4.3 La ₂ CoMnO ₆ and La ₂ NiMnO ₆ thin films prepared by PAD and crystallized by rapid thermal annealing (RTA).....	117
4.4 Dynamic magnetic properties and spin pumping in La _{0.92} MnO ₃ epitaxial thin films prepared by polymer assisted deposition	141
Chapter 5. Discussion	153
5. General discussion of the results	155
Chapter 6. Conclusions.....	159
6. Conclusions.....	161
Chapter 7. Future perspectives	165
7. Future perspectives	167
Appendix.....	A1

Chapter 1

Introduction

1.1 Transition metal oxides

Oxides have a complex crystallo-chemical structure with strong interactions between lattice, spin and charge degrees of freedom and offer a broad variety of functionalities going from high temperature superconductivity to different types of ferroic orderings. Additionally, these materials also offer many different possibilities to tune their properties acting upon their structure: structural distortions (symmetry, bond lengths and bond angles) structural defects (stacking faults, dislocations, vacancies, epitaxial strain) or their doping rate: transition metals (TM) have multiple valence states. For these reasons complex oxides, and especially TM oxides, are both of strong theoretical and technological interest. From the fundamental point of view, they are a unique system to study strongly correlated electron systems, while their physical and chemical properties allow a plethora of technological applications covering from energy harvesting to catalyst or spintronics (Figure 1). For example, TiO_2 , WO_3 , BiVO_4 , $\alpha\text{-Fe}_2\text{O}_3$, and Cu_2O are photocatalysts and can be used for solar water splitting,¹ $\text{La}_{1-x}\text{Sr}_x\text{MnO}_3$, LiNbO_3 , PbTiO_3 , BaTiO_3 , and BiFeO_3 are candidates for non-volatile memory,²⁻³ Cr_2O_3 , Mn_2O_3 , Co_3O_4 , NiO , CuO , SrO , and In_2O_3 are selected for gas sensors,⁴ Cu_2O , TiO_2 , BaTiO_3 , BiFeO_3 , and LiNbO_3 can act as light harvesting materials,⁵ oxides like TiO_x , WO_x , $\text{LaTi}_{1-x}\text{Cu}_x\text{O}_3$, and La_2CuO_4 can catalyze the hydrogenation of carbon oxides to produce organics like olefins or alcohols,⁶ $\text{YBa}_2\text{Cu}_3\text{O}_7$, $\text{HgBa}_2\text{Ca}_2\text{Cu}_3\text{O}_8$, and $\text{Tl}_2\text{Ba}_2\text{Ca}_2\text{Cu}_3\text{O}_{10}$ are high-temperature superconductors⁷⁻⁹, LaMnO_3 , LaCoO_3 , ZrO_2 , LaGaO_3 and CeO_2 are potential materials for the construction of solid oxide fuel cells (SOFCs),¹⁰ and Mn_2O_3 , Co_3O_4 , NiO , CuO , SrO , In_2O_3 , WO_3 , and TiO_2 can be used as thermoelectric generators.¹¹

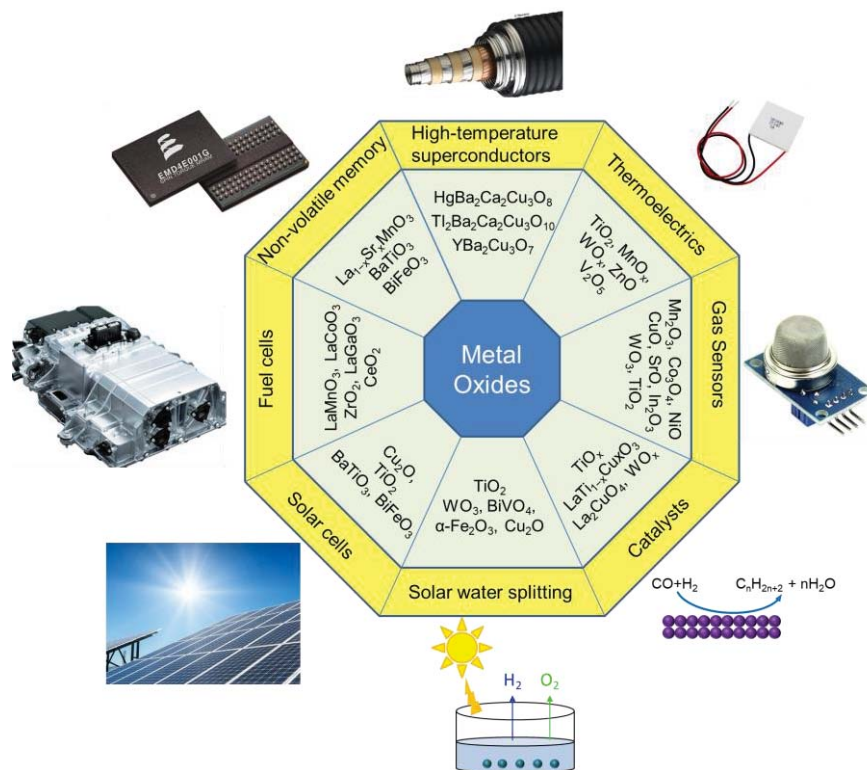


Figure 1. The wide range of applications of metal oxides. (reproduced from Haribabu et al., ref¹²)

Chemical composition and crystal structure can have significant impact on the physical properties of these materials. The common structures of binary oxide materials (i.e., MO, MO₂, M₂O₃, M = metal cation) include rock salt (i.e., VO, CoO and MnO), wurtzite (i.e., ZnO), fluorite (i.e., CeO₂, ThO₂ and ZrO₂), rutile (i.e., TiO₂, IrO₂, and RuO₂), and corundum (i.e., Al₂O₃, V₂O₃, and Cr₂O₃). Common ternary oxides structures include the ilmenite (i.e., FeTiO₃, MnTiO₃ and LiNbO₃), spinel (i.e., MgAl₂O₄, CoFe₂O₄ and LiTi₂O₄), perovskite (i.e., CaTiO₃, SrRuO₃ and BiFeO₃), and perovskite-derived structures such as the Ruddlesden–Popper series and other layered-perovskite structures.¹³ The properties of these metal oxides range from insulators to semiconductors to metals to superconductors and even magnets.

Among the different structures of ternary oxides, perovskites are of strong interest due to the broad variety of possibilities they offer with a particularly simple structure, such as ferroelectricity, magnetism, high temperature superconductivity (HTSC), colossal magnetoresistance (CMR), metal-insulator transitions (MIT), and multiferroicity (coexistence of ferroelectricity and magnetism).¹⁴

In fact, almost half of the elements in the periodic table can be accommodated into the structure at either the A-site or the B-site. The ideal ABO_3 perovskite unit has a cubic structure with a lattice constant of about 4.00 \AA ,¹⁵⁻¹⁸ and most of its electronic properties are determined by the physics associated with the transition metal and the corner-sharing oxygen anions of the BO_6 octahedra. Charge, lattice, spin and orbital degrees of freedom strongly interact with each other¹⁹ and, hence, physical properties of perovskites can be properly tuned by acting upon the interplay between them.

1.2 Perovskite crystal structure

The general composition of perovskite oxides has the formula ABO_3 , where A is usually a large cation, typically an alkali, alkaline earth or rare earth metal and B is usually a medium-sized transition metal. The ABO_3 perovskite structure consists of a three-dimensional network of corner-sharing BO_6 octahedra in which the A-site cations occupy the dodecahedral sites surrounded by twelve oxygen ions. (Figure 2 (a)).²⁰⁻²¹ Thus A-site should be appropriate to 12 coordination, B-site to octahedral coordination and O to linear coordination.

The substitution of the A and B site cations gives rise to a very large number (several hundred) of perovskite derivatives with subtle variations in structure. For example, the presence of more than one cation at A and B sites results in compositions such as $AA'B_2O_6$ (double A-site), $A_2BB'O_6$ (double B-site), where A, A' or B, B' cations order at the respective sublattices.²²⁻²³ Their unit cells are twice that of perovskite, so they are known as double perovskites. Since A-site cations usually act as an electron donor to the BO_6 octahedral and the physical properties are highly dependent on B-site cations, double perovskites usually indicate double B-site perovskites.²⁴

There are 3 types of cation ordering in $A_2BB'O_6$ double perovskites: (1) random, (2) rock-salt, B and B' cations arrange in a chessboard pattern in all the three crystallographic directions (Figure 2 (b)), (3) layered.²⁵ The types of ordering are generally determined by the charge difference between the B-site cations. When the charge difference less than 2, the B-site cations arrange randomly, the possible space groups are cubic ($Pm-3m$) and orthorhombic ($Pbnm$); when the charge difference ≥ 2 ,

the rock-salt ordering dominates, the possible space groups are cubic ($Fm-3m$), tetragonal ($I4/m$) and monoclinic ($P2_1/n$).²⁴ The rock-salt double perovskite is the most abundant and investigated type.

The perovskite oxides are generally approximated as ionic compounds, the charge balance needed to maintain neutrality. In ABO_3 structure, if the charges on the cations are written as q_A and q_B , then $q_A+q_B=6$. In the case of $A_2BB'O_6$, the equation is $2\times q_A+q_B+q_{B'}=12$.

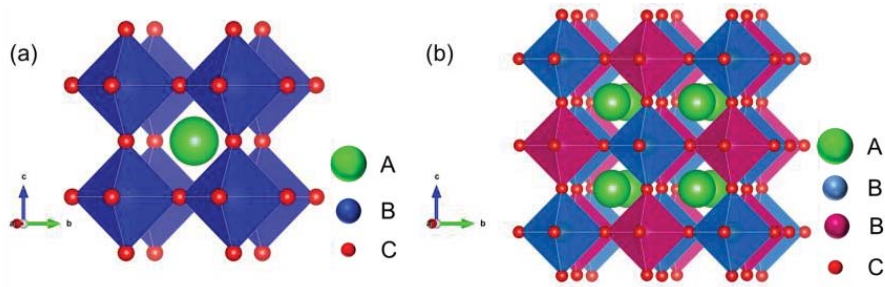


Figure 2. (a) Cubic perovskite ($Pm-3m$) structure, (b) The rock-salt ordered double perovskite ($A_2BB'O_6$) structure ($Fm-3m$)

The ideal stoichiometric ABO_3 structure is cubic ($Pm-3m$), and the space group of a cubic rock-salt $A_2BB'O_6$ double perovskites is $Fm-3m$, the new axes run parallel to the simple cubic perovskite axes, and the lattice parameter is twice the simple cubic lattice parameter a_p , where a_p is the ideal single cubic perovskite cell.

Goldschmidt proposed a tolerance factor to predict the stability and distortion of the perovskite.²⁶ The tolerance factor, t , is defined as

$$t = \frac{r_A + r_O}{\sqrt{2} (r_B + r_O)} \quad \text{Eq. 1}$$

where r_A , r_B and r_O are the ionic radius of the respective A, B and oxygen ions.

For substituted phase $A_{1-x}A_x'BO_3$, t can be written as:²⁷

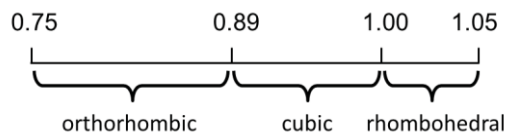
$$t = \frac{(1-x)r_A + xr_{A'} + r_O}{\sqrt{2} (r_B + r_O)} \quad \text{Eq. 2}$$

and in the case of $A_2BB'O_6$:²⁵

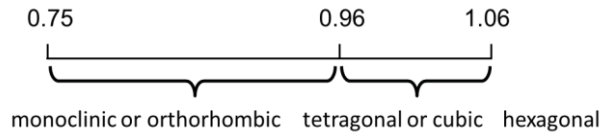
$$t = \frac{r_A + r_O}{\sqrt{2} \left(\frac{r_B + r_{B'}}{2} + r_O \right)} \quad \text{Eq. 3}$$

With the variation in A-site cation ionic radius, the structure adjusts the size of the 12-coordinate site by cooperatively tilting the BO_6 octahedra and bending the B-O-B bonds. This resulting structure deviates from the ideal cubic structure and adopts lower symmetries with a realignment of the unit cell axes.

For a small deviation in t of ABO_3 , the crystal structure changes from cubic to rhombohedral or orthorhombic symmetry:²⁰



and in the case of $\text{A}_2\text{BB}'\text{O}_6$ double perovskite:²⁸



The space groups differences between a random orthorhombic ($Pbnm$) and a rock salt monoclinic ($P2_1/n$) double perovskite are very subtle, diffraction patterns for compounds crystallizing in these space groups are very similar, extreme care must be taken in assigning space groups for them. The only reflection condition that justifies a rock salt arrangement with $P2_1/n$ symmetry is the presence of $0kl: k=2n+1$.²⁹

Many important physical properties of perovskites are determined by the BO_6 octahedra, such as magnetic and electronic properties. This is because these are often mediated by the electron configurations of the B-site cations. The A-site cations tend to be closed-shell ions with a fixed valence and so less responsive to chemical manipulation for tuning the chemical and physical properties.

There are three types of modifications in the structure of the perovskite, namely, B-site cation displacement, BO_6 tilt/rotation and BO_6 distortion. The B-site cation

displacement and BO_6 tilt/rotation are usually associated with the size of the B-site and A-site cations, respectively. The BO_6 distortions are a result of interactions between the cation electron orbitals and the surrounding O anions, typified by the Jahn–Teller effect. These tilts and rotations are also extremely sensitive to external stimuli, including temperature, pressure and strain. This latter aspect is particularly important in the case of thin films epitaxially grown onto a suitable substrate.²⁷

The relationship of the property versus the composition and structure would provide tracks for designing the perovskite materials.

1.3 Superexchange and double exchange in lanthanum manganite perovskite

Most of the CMR oxomanganates are based on the perovskite parent compound LaMnO_3 , an antiferromagnetic (AFM) insulator. Bulk LaMnO_3 exhibits a variation of the electronic correlations (i.e., different strength of the electronic interactions in the system) as a function of temperature. At low temperature the system is a Mott-Hubbard A-type antiferromagnetic (A-AFM) insulator that crystallizes in the Pbnm orthorhombic structure (Figure 3 (a)).³⁰ Ferromagnetically aligned ab -layers are coupled antiferromagnetically along c -axis (Figure 3 (b)).³¹⁻³³ However, at temperatures above $T_{\text{JT}} = 750$ K the system becomes a pseudo-cubic ferromagnetic (FM) metal. The LaMnO_3 has a nominal formula $\text{La}^{3+}\text{Mn}^{3+}\text{O}_3$, containing a population of Mn^{3+} ($3d^4$, $t_{2g}^3 e_g^1$, $S=2$, high-spin (HS)) cations. The Mn^{3+} cation is a Jahn-Teller ion, and the oxygen coordination octahedra are elongated. This results in a distorted perovskite structure. The AFM insulator phases are attributed to superexchange (SE) interactions between the Mn^{3+} cations and the p orbitals of the linking oxygen atoms.³⁴⁻³⁵ The Mn^{3+} cations are in apex-shared octahedra, and the La^{3+} cations in the cage sites between the octahedra and the cation-anion-cation geometry is linear so that the superexchange mechanism suggests that these phases should promote the antiferromagnetic (antiparallel) alignment of the magnetic moments. Schematically (Figure 3 (c)), a cation with an overall spin-up configuration can interact with a spin-down (red arrow) electron in a filled oxygen p orbital, with a consequence that the

other (spin-up, blue arrow) electron in the oxygen p orbital must then induce a favorable exchange to enforce an overall spin-down configuration in the other cation. However, no actual electron exchange takes place between cations and anion, and the exchange is virtual.

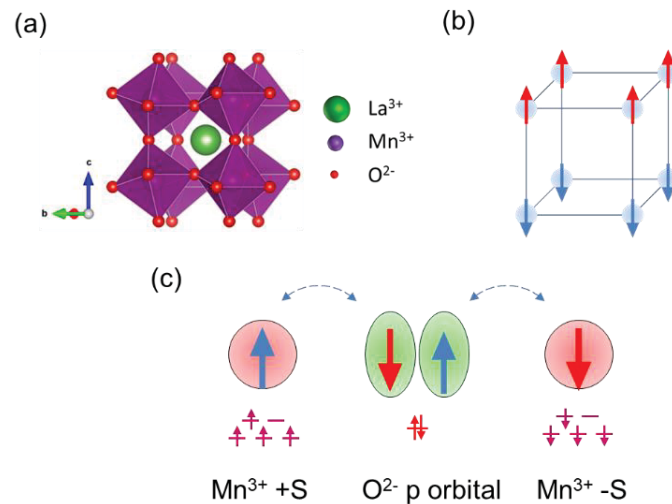


Figure 3. (a) LaMnO_3 ($Pbnm$) crystal structure, (b) A-type $(001)_p$ alignment, (c) Schematic of 180° superexchange between two paramagnetic cations via the filled p orbitals of an intermediate oxygen ion.²⁷

B-site substituted lanthanum manganites have the general formula $\text{LaB}_x\text{Mn}_{1-x}\text{O}_3$ ($B = \text{Fe, Co, Ni, Cu, Zn}$ or Ti),³⁵⁻⁴² when $x = 0.5$ and the B-site cations are ordered, they form the double perovskite structure and are always written as La_2BMnO_6 . Among them, $\text{La}_2\text{CoMnO}_6$ and $\text{La}_2\text{NiMnO}_6$ are more appealing since the charge difference between Co or Ni and Mn is +2, leading to a rock-salt ($P2_1/n$) structure and to unique ferromagnetic and electronic properties. They are ferromagnetic and insulating material due to the B-site ($\text{Ni}^{2+}\text{-O-Mn}^{4+}$ or $\text{Co}^{2+}\text{-O-Mn}^{4+}$) superexchange interactions.⁴³⁻⁴⁵

A-site substituted lanthanum manganites have the general formula $\text{La}_{1-x}\text{A}_x\text{MnO}_3$, or $\text{La}_{1-x}\text{A}_x\text{Mn}_{1-x}^{3+}\text{Mn}_x^{4+}\text{O}_3$ ($A = \text{Ca, Sr, Ba}$, or simply Lanthanum vacancies), the material is generally ferromagnetic and metallic (FMM) below Curie temperatures (T_C) when $0.2 < x < 0.5$.⁴⁶ The generation of Mn^{4+} ($3d^3$, t_{2g}^3 , $S=3/2$) cations to maintain charge neutrality dilutes the Jahn–Teller (J-T) distortions of Mn^{3+} ($3d^4$, $t_{2g}^3e_g^1$, $S=2$). With the

appearance of the Mn mixed valence state ($\text{Mn}^{3+} - \text{Mn}^{4+}$), J-T distortion is partially released and electrons can travel from one Mn cation to another according to the double exchange (DE) mechanism devised by Zener in 1951.⁴⁷⁻⁴⁸ The key in DE mechanism, as in superexchange, is that the interaction between Mn neighbors is mediated by oxygen ions. In double exchange, one Mn^{3+} ion transfers an electron to an adjacent O^{2-} ion, but as this has filled p orbitals, to make this possible, the O^{2-} ion simultaneously transfers one of its electrons to a neighboring Mn^{4+} ion. In essence, the electron hops from Mn^{3+} to Mn^{4+} via intermediate oxygen ions (Figure 4 (b)). In the process the charges on the Mn ions are reversed and because all of the orbitals on the oxygen ion are full and electrons are spin paired, a spin-up electron moving from Mn^{3+} will displace a spin-up electron from O^{2-} onto Mn^{4+} . This DE is only favorable if there are parallel spins on the two Mn cations involved, thus it leads to ferromagnetic alignment of neighbor Mn moments. Note that in DE mechanism, there is an actual electron transfer from one cation to another (in contrast to superexchange interactions in which virtual electrons are interchanged), leading always to ferromagnetic alignment. (Figure 4 (a)).

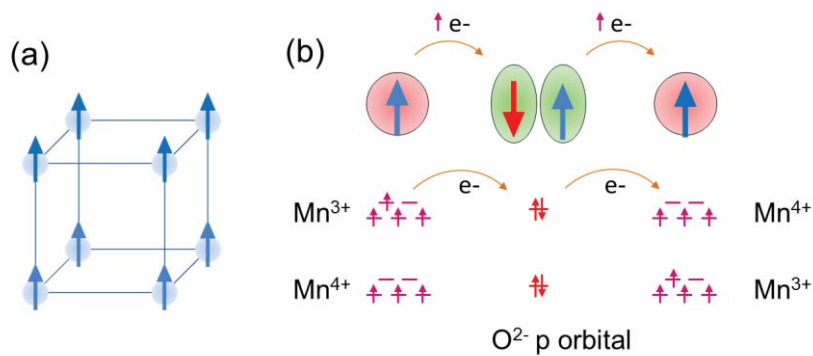


Figure 4. (a) Schematic of Ferromagnetic ordering, (b) Double exchange, schematic: Mn^{3+} ($3d^4, t_{2g}^3 e_g^1, S=2$) cation, left, transfers a spin-up electron to an oxygen p orbital, center (arrow), which simultaneously transfers a spin-up electron, right (arrow), to an empty orbital on the receiving cation Mn^{4+} ($3d^3, t_{2g}^3, S=3/2$), forcing ferromagnetic alignment of spins.²⁷

1.4 Derivative of lanthanum manganite perovskite

The AFM insulator phase limits the applications of LaMnO_3 , introducing a distortion of the MnO_6 octahedra can tune it into a ferromagnetic (FM) metallic conducting phase. However, the stoichiometric LaMnO_3 is a complex system where it is very difficult to disentangle the effects of strain, oxygenation and cation vacancies on the magnetic state.⁴⁹ A relatively easy way to modify the properties of LaMnO_3 consists in substituting part of the La or Mn cations.

In this thesis, we have grown and investigated thin films of the following derivative from LaMnO_3 :

- i) By introducing ion vacancies in La site of the LaMnO_3 , a ferromagnetic metallic conductor phase, $\text{La}_{0.92}\text{MnO}_3$, was obtained (Figure 5 (a));
- ii) Substituting 30% of La by Sr, a ferromagnetic metallic phase $\text{La}_{0.7}\text{Sr}_{0.3}\text{MnO}_3$ with higher T_C was obtained (Figure 5 (b)); and
- iii) By substituting half of the Mn with Co or Ni, ferromagnetic and insulating double perovskites (Figure 5 (c) $\text{La}_2\text{CoMnO}_6$ and (d) $\text{La}_2\text{NiMnO}_6$) were prepared.

The films were deposited on top of different substrates with perovskite structure (SrTiO_3 , LaAlO_3 ,...) by using the PAD technique. Those different materials were selected because they are of potential interest for the implementation of different magnetoelectronic devices due to their ferromagnetic character, high T_C and high saturation magnetization (M_S) values.⁵⁰⁻⁵²

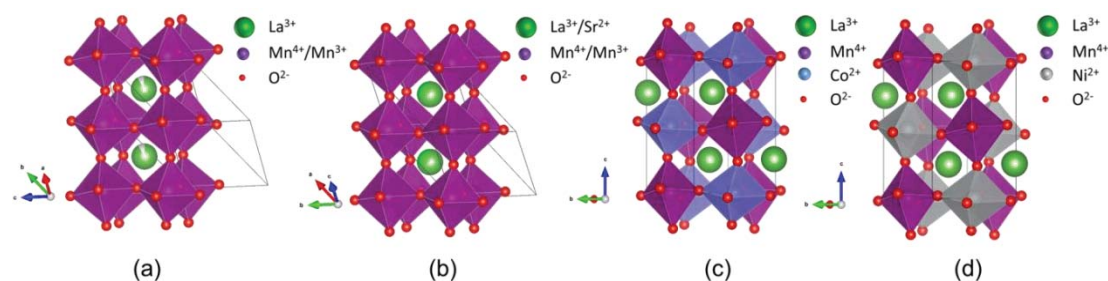


Figure 5. (a) $\text{La}_{0.92}\text{MnO}_3$ (R-3c), (b) $\text{La}_{0.7}\text{Sr}_{0.3}\text{MnO}_3$ (R-3c), (c) $\text{La}_2\text{CoMnO}_6$ ($P2_1/n$), (d) $\text{La}_2\text{NiMnO}_6$ ($P2_1/n$), crystal structures.

Concerning $\text{La}_{0.92}\text{MnO}_3$, an amount of 8% of La vacancies in LaMnO_3 introduces 24% of Mn^{4+} (holes) into the lattice, the nominal valence states are $\text{La}_{0.92}^{3+}\text{Mn}_{0.76}^{3+}\text{Mn}_{0.24}^{4+}\text{O}_3$, this is the same amount of holes that in $\text{La}_{0.76}\text{Ca}_{0.24}\text{MnO}_3$, for instance, although the smaller cationic disorder in $\text{La}_{0.92}\text{MnO}_3$ makes its electronic conductivity much larger, while its Curie temperature increases up to values close to 300 K.⁵³ The appearance of the metallic ferromagnetic behavior is explained by the DE mechanism.

$\text{La}_{0.7}\text{Sr}_{0.3}\text{MnO}_3$, with the nominal valence states of $\text{La}_{0.7}^{3+}\text{Sr}_{0.3}^{2+}\text{Mn}_{0.7}^{3+}\text{Mn}_{0.3}^{4+}\text{O}_3$, is one the most important substituted lanthanum manganite for its high T_C value ($T_C=370$ K).⁵⁴ The ferromagnetic metallic state in this compound is the typical example of the DE mechanism between Mn^{3+} ($3d^4, t_{2g}^3 e_g^1, S=2$) and Mn^{4+} ($3d^3 t_{2g}^3, S=3/2$).

The double perovskites $\text{La}_2\text{CoMnO}_6$ and $\text{La}_2\text{NiMnO}_6$ are much more complicated systems, the degree of ordering of the B-site cations of is crucial to their magnetic and electronic properties. The phases with ordered arrangements of B and B' are in a 'rock salt' fashion in all the three crystallographic directions, the space group is monoclinic $P2_1/n$ at room temperature, at high temperatures, the phase transitions from the monoclinic $P2_1/n$ to the trigonal R-3 takes place.⁵⁵ The average Co-O-Mn and Ni-O-Mn bond angles in ordered phases are close to 160° , which favor SE interactions and FM alignment.⁵⁶⁻⁵⁹ The random distribution results in an orthorhombic structure $Pbnm$ and R-3c.

The ordered phases are ferromagnetic insulator with high Curie temperatures, for example, $T_C(\text{La}_2\text{CoMnO}_6) = 230$ K, and $T_C(\text{La}_2\text{NiMnO}_6) = 270$ K. This behavior could be explained by ferromagnetic (FM) superexchange interactions according to the Goodenough-Kanamori rules. The nominal valence states are $\text{La}_2^{3+}\text{Co}^{2+}\text{Mn}^{4+}\text{O}_6$ ($T_C=230$ K), $\text{La}_2^{3+}\text{Ni}^{2+}\text{Mn}^{4+}\text{O}_6$ ($T_C=270$ K), and the super-exchange interactions are between Co^{2+} ($3d^7, t_{2g}^5 e_g^2, S = 3/2$) and Mn^{4+} ($3d^3, t_{2g}^3, S=3/2$) ions in one case, and between Ni^{2+} ($3d^8, t_{2g}^6 e_g^2, S=1$) and Mn^{4+} ($3d^3, t_{2g}^3, S=3/2$) ions in the other case. The spin only theoretical saturation magnetization value for fully ordered LCMO is $6 \mu_B/\text{f.u.}$, and for LNMO, the value is $5 \mu_B/\text{f.u.}$.^{35, 37-39}

The difference of size and charge of the cations are the major driving force for the B-site ordering.²⁵ It has been established that a large difference in size and charge of the B-B' site cations provides a material with higher degree of ordering.⁶⁰ The ionic radii difference between Ni²⁺ (83.0 pm) and Mn⁴⁺ (67.0 pm) is 16.0 pm, and is 21.5 pm for Co²⁺ (HS, 88.5 pm) and Mn⁴⁺,⁶¹ the energy barrier for the site exchange of Ni²⁺ and Mn⁴⁺ is lower than that of Co²⁺ and Mn⁴⁺, so in LNMO is more difficult to achieve full B-site ordering.

There are two major reasons responsible for the M_s reduction, and the shape changes in the $M-T$ curves and the magnetic hysteresis loops of FM double perovskite, they are anti-site (AS) disorder and antiphase boundary (APB), respectively.

The AS disorder is the situation that B cations partially exchange the sites with B' cations (Figure 6 (a)). The AS disorder and the percentage of ordering are related by the expression: $x = (100-2y)$, where x is the percentage of ordering and y is the percentage of AS disorder. In FM double perovskites, the M_s decreases with increasing AS disorder. In ordered LCMO or LNMO, the FM superexchange between Co²⁺/Ni²⁺ and Mn⁴⁺ (Ni²⁺-O-Mn⁴⁺ or Co²⁺-O-Mn⁴⁺) promotes the M_s , in contrast, AS defects lead to AFM superexchange interactions (Co²⁺-O-Co²⁺, Ni²⁺-O-Ni²⁺, and Mn⁴⁺-O-Mn⁴⁺), and consequently, will reduce the M_s . AS disorder has a direct influence on the magnetic properties of the double perovskites, therefore the departure of the M_s of a given sample from these spin only M_s values is interpreted as a measure of the degree of Co/Mn or Ni/Mn disorder in the structure. For example, if measured M_s of a LNMO film is 4.0 μ_B /f.u., then the percentage of ordering is 80%, and the percentage of AS disorder is 10%.

In ordered La₂CoMnO₆/La₂NiMnO₆, different B-site ordered domains can exist. In one domain, the Mn can be sitting on the B site, while on a B' site in another. An APB is created where two such domains meet, and this leads to AFM Mn⁴⁺-O-Mn⁴⁺ interactions across the interface (Figure 6 (b)). APB is able to explain additional unusual features of magnetization which AS disorder cannot do, namely, the small coercivity and low remanence.⁶² At a zero magnetic field, the FM domains on opposite

sides of the APB will align antiparallel to each other giving rise to a steep reduction of the magnetization.

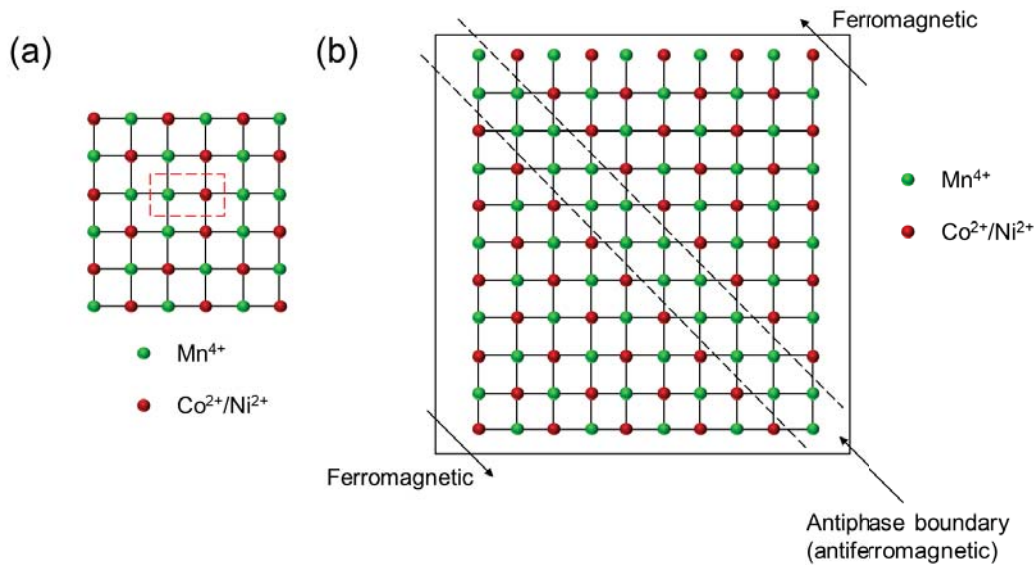


Figure 6. (a) Schematic of anti-site disorder in an (001) plane of $\text{La}_2\text{CoMnO}_6/\text{La}_2\text{NiMnO}_6$. (b) Schematic of an anti-phase boundary in an (001) plane of $\text{La}_2\text{CoMnO}_6/\text{La}_2\text{NiMnO}_6$. (reproduced from Goodenough and Dass, ref⁶²)

Since the size and charge difference of B-site cations are intrinsic effects, more efforts are focused on the reduction of the antisite defects. The generation of antisite defects is temperature sensitive and is influenced by the preparation methods employed.^{35, 37-38} The final amount of antisite defects on the double perovskite structure has consequences for the electronic and magnetic properties of the samples. Therefore, an accurate control of processing temperatures and oxygen pressure is required to prepare high quality LCMO and LNMO films with optimal magnetic properties.

1.5 Oxide thin films synthesis methods

1.5.1 Vapour deposition method

Vapor phase crystal growth methods have been used extensively for the preparation of epitaxial thin films. It describes any process that a film becomes larger in mass due to transference of source material from the vapor onto the surface of a substrate.

Figure 7 schematically illustrates the basic features of evaporative deposition.⁶³ In this process, thermal energy is supplied to a source material, atoms are evaporated and deposit onto a substrate. Single crystal perovskite substrates are usually used for the deposition of perovskite films. The process is normally carried out in a vacuum chamber to enable control of the vapor composition.

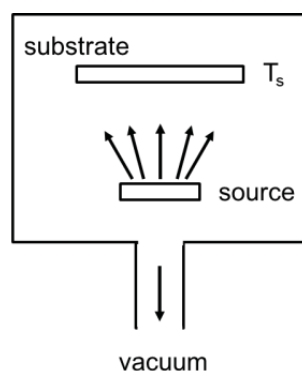


Figure 7. Schematic of the basic features of vapor deposition system⁶³

PVD is the process that the vapor is created by physical method without a chemical reaction, CVD is the process that the material deposited is the product of a chemical reaction.⁶³ Important PVD techniques include sputtering, pulsed laser deposition (PLD), molecular beam epitaxy (MBE). Metalorganic CVD (MOCVD) is the most frequently used CVD methods.

Sputter deposition is a process in which material ejects from a target by the bombardment of high-energy ions condenses onto a substrate in a high vacuum chamber. Figure 8 schematically shows the basic elements of a sputter deposition system. The target is a piece of material with the desired composition of the film, it serves as the cathode. The substrates are placed on a substrate holder which serves as the anode. Low pressure argon (10^{-3} – 10^{-1} Torr) is introduced into the chamber as the sputtering gas. When a voltage of several hundred to a thousand volts is applied between the cathode and the anode, Ar^+ ions are formed, creating a glow discharge in the deposition chamber. The positive Ar^+ ions are accelerated to strike the anode target, surface atoms physically leave the target and form the vapor in the chamber, then condense on the substrate to form a film.⁶⁴⁻⁶⁶

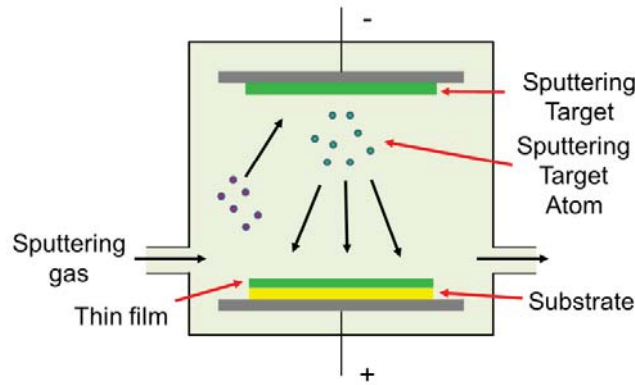


Figure 8. Schematic of the sputtering⁶⁴

PLD is a process that material ejects from a target by the strike of high-energy laser beam, and condenses onto a substrate in a vacuum chamber. Figure 9 schematically shows the basic elements of a PLD system. A pulsed laser beam is focused onto a target of the material to be deposited, vaporizes or ablates a small amount of the material creating a plasma plume. The ablated material is ejected from the target in a highly forward-directed plume, and condenses on a heated substrate forming a thin film with the same composition of the target. The background pressures range from ultrahigh vacuum (UHV) to 1 Torr.⁶⁷

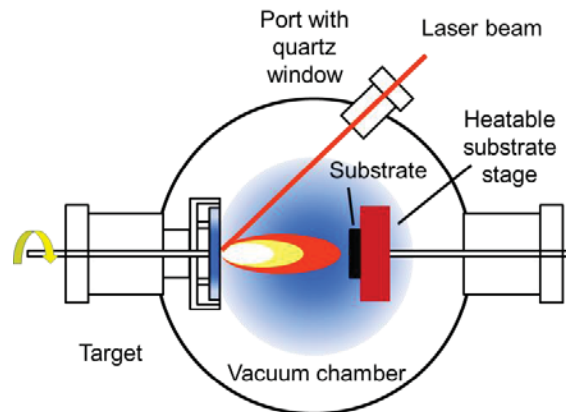


Figure 9. Schematic of the PLD⁶⁴

MBE is a process that pure atoms ejected by a Knudsen cell cross an ultrahigh vacuum (typically below 10^{-10} Torr) chamber and condenses onto a substrate. Figure 10 shows the schematic diagram of a MBE system. Knudsen cells (K-cells) are usually employed as effusion cells for the production of beams from condensed (solid or liquid) materials.

Ultrapure source materials are placed in Knudsen cells and evaporated by radiative heating to produce molecular beams. The substrate is mounted on a heated holder opposite to the effusion cells. Reflection high-energy electron diffraction (RHEED) is often applied for in situ monitoring of the growing process.⁶⁸⁻⁶⁹

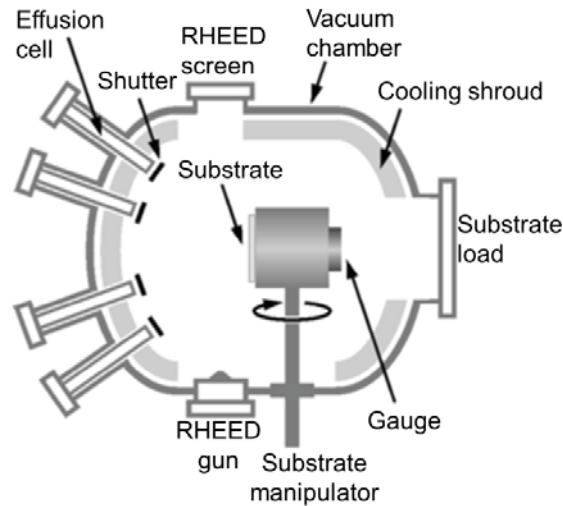


Figure 10. Schematic of the MBE⁶⁸

CVD is a process that the precursors, gases or vapor react or decompose on the substrate at high temperature in a vacuum chamber. The volatile compounds react near the surface of the substrate to form a solid film. Other gaseous by-products are removed by a continuous carrier gas flow.⁷⁰ The MOCVD is a CVD technique using organo-metallic precursors. Figure 11 shows the schematic diagram of a MOCVD system. The precursor solutions are sent in pulsed regime droplets inside the evaporator by using an injector. The droplets are transported to the deposition chamber by a mixture of the carrier gas (Ar, or N₂) and a reactive gas (O₂), and then adsorbed on the substrate surface. The reactive species thus diffuse at the surface and react in heterogeneous phase to form a film.⁷¹

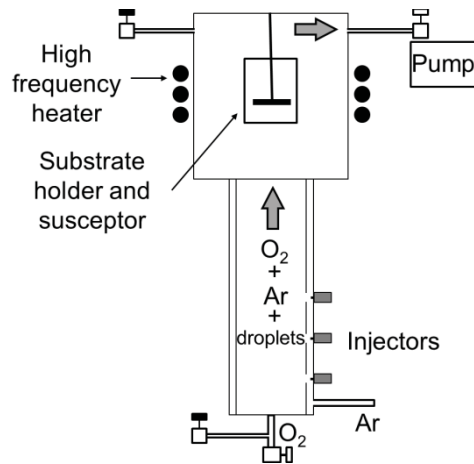


Figure 11. Schematic of the MOCVD⁷²

The advantages of vapor deposition techniques include high crystal quality, precise control of composition and thickness at atomic-scale. However, there are also some drawbacks. For example, all the vapor deposition methods require large capital investment since the vapor depositions are often carried out under vacuum conditions; the size and shape of the sample are limited by the vacuum chamber; the prices of the targets or element sources are very high; and some toxic or corrosive gases may be used.

1.5.2 Chemical solution deposition (CSD)

Among the well-developed deposition techniques, chemical solution deposition (CSD) is noted for its easy setup, low cost, easy scalability, the ability of coating on irregular surfaces, and because the high vacuum system is not necessary. In addition, the thicknesses can be well controlled by the modification of the concentration of the precursor solution, and the desired stoichiometry of the films is easy to control.

Usually, a typical CSD process for thin film deposition includes three steps (Figure 12): precursor solution preparation, surface coating, and thermal treatment.

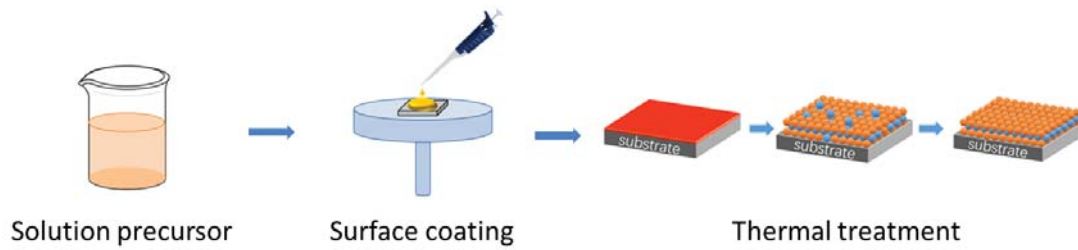


Figure 12. Flow chart of a typical CSD process

Many aspects have to be considered for the choice of synthesis strategy in each step.⁷³

In the solution precursor preparation process, the solubility of the solute should be high enough to form the precursor solution with a high concentration, and the precursor solution should be uniform, stable, and no phase separation should occur.

For surface coating, the wettability and viscosity are important. The wetting between the precursor solution and the substrate should be good and the viscosity of the precursor solution should be properly adjusted for a uniform thickness and crack free surface.

For the thermal treatment, the chemical composition of precursor should be as simple as possible to make sure that all of the chemical elements except the desired cations can be released completely during the annealing.

The most commonly employed methods for metal oxide thin film preparation include sol-gel, chelate, and metallo-organic decomposition (MOD).

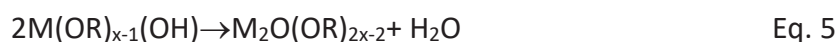
Sol-gel Processes

Sol-gel deposition is a process in which metallic alkoxides are hydrolysed in alcohol solvents with the help of water, and go through a condensation reaction with the elimination of water and alcohol, providing a solid oxide film deposited on a substrate after thermal treatment. The reactions in the sol-gel process result in the formation of oligomeric species and are as follows:

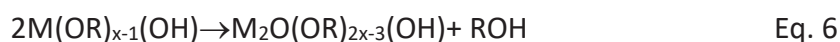
Hydrolysis



Condensation (water elimination)



Condensation (alcohol elimination)



A key point is the control of the amount of water and the process of adding the water to avoid precipitation. The sol-gel method is water sensitive, so the preparation should be conducted in low humidity, inert gas atmosphere or with addition of stabilizing agents.⁷⁴

Chelate Processes

Chelate is a process that relies on the molecular modification of alkoxide compounds through reactions with other reagents, and forms new chemical species that are more stable and possess better film formation behavior. Compounds such as acetic acid, acetylacetone, or amine compounds are often employed in chelate processes, since they are reactive with alkoxides, and the reaction products are less hydrolysis sensitive and can reduce the tendency to excessive polymerization or precipitation. The reaction between a metal alkoxide and acetic acid is shown below:



MOD process

The MOD is a process in which metalorganic compounds are dissolved in a solvent, such as xylene, and combining different solutions to obtain the desired stoichiometry the final solution is then coated onto a substrate. Long-chain carboxylate compounds, such as titanium di-methoxy di-neodecanoate are generally used as the metal precursors in the MOD process. The MOD solution is hydrolysis insensitive There is nearly no reaction among the starting reagents, the final solution is just the simple mixtures of them.⁷⁴

An overview of the starting materials, solvent, process chemistry, and relative advantages and disadvantages of the three principal methods of inorganic thin film preparation is shown in Table 1.

Table 1. Principal Chemical Solution Deposition Methods

	Sol-Gel	Chelate	MOD
Starting materials	Inorganic metal salts or metal organic compounds, typically as metal alkoxides	Multiple metal-organic precursors, such as metal carboxylate, alkoxide, and/or β -diketonate	Long-chain metal carboxylates
Solvent	Alcohol	Acetic acid, acetylacetone or amine compounds	Inert solvents, such as xylene
Mixture state	Molecular shape, extent oligomeric species with M-O-M bonds	Small oligomeric species	Simple mixtures
Ambience humidity	Low humidity, inert gas atmosphere or addition of stabilizing agents	Low humidity, dry box and inert atmosphere conditions	Common ambience
Control (Incr.)	←		
Simplicity (Incr.)	→		

References

- [1] Wang, J.; van Ree, T.; Wu, Y.; Zhang, P.; Gao, L. 8 - Metal oxide semiconductors for solar water splitting. In *Metal Oxides in Energy Technologies*; Wu, Y., Ed.; Elsevier: 2018; pp 205-249.
- [2] Kumar, D.; Aluguri, R.; Chand, U.; Tseng, T. Y. Metal oxide resistive switching memory: Materials, properties and switching mechanisms. *Ceram. Int.* **2017**, *43*, S547-S556.
- [3] Scott, J. F.; Paz de Araujo, C. A. Ferroelectric memories. *Science* **1989**, *246* (4936), 1400-1405.
- [4] Wang, C.; Yin, L.; Zhang, L.; Xiang, D.; Gao, R. Metal oxide gas sensors: sensitivity and influencing factors. *Sensors (Basel)* **2010**, *10* (3), 2088-2106.
- [5] Pérez-Tomás, A.; Mingorance, A.; Tanenbaum, D.; Lira-Cantú, M. Chapter 8 - Metal Oxides in Photovoltaics: All-Oxide, Ferroic, and Perovskite Solar Cells. In *The Future of Semiconductor Oxides in Next-Generation Solar Cells*; Lira-Cantu, M., Ed.; Elsevier: 2018; pp 267-356.
- [6] Fierro, J. L. G. 18-Hydrogenation of Carbon Oxides on Metal Oxides. In *Metal Oxides: Chemistry and Applications*; Fierro, J. L. G., Ed.; Taylor & Francis Inc: 2007; pp 569-589.
- [7] Beno, M. A.; Soderholm, L.; Capone, D. W.; Hinks, D. G.; Jorgensen, J. D.; Grace, J. D.; Schuller, I. K.; Segre, C. U.; Zhang, K. Structure of the single - phase high - temperature superconductor $\text{YBa}_2\text{Cu}_3\text{O}_{7-\delta}$. *Appl. Phys. Lett.* **1987**, *51* (1), 57-59.
- [8] Chu, C. W.; Gao, L.; Chen, F.; Huang, Z. J.; Meng, R. L.; Xue, Y. Y. Superconductivity above 150 K in $\text{HgBa}_2\text{Ca}_2\text{Cu}_3\text{O}_{8+\delta}$ at high pressures. *Nature* **1993**, *365* (6444), 323-325.
- [9] Torardi, C. C.; Subramanian, M. A.; Calabrese, J. C.; Gopalakrishnan, J.; Morrissey, K. J.; Askew, T. R.; Flippen, R. B.; Chowdhry, U.; Sleight, A. W. Crystal Structure of $\text{Tl}_2\text{Ba}_2\text{Ca}_2\text{Cu}_3\text{O}_{10}$, a 125 K Superconductor. *Science* **1988**, *240* (4852), 631-634.
- [10] Wang, P.; Wang, J.; Fu, L.; Wu, Y.; van Ree, T. 2 - Metal oxides in fuel cells. In *Metal Oxides in Energy Technologies*; Wu, Y., Ed.; Elsevier: 2018; pp 17-47.
- [11] Walia, S.; Balendhran, S.; Nili, H.; Zhuiykov, S.; Rosengarten, G.; Wang, Q. H.; Bhaskaran, M.; Sriram, S.; Strano, M. S.; Kalantar-zadeh, K. Transition metal oxides – Thermoelectric properties. *Prog. Mater. Sci.* **2013**, *58* (8), 1443-1489.
- [12] Palneedi, H.; Park, J. H.; Maurya, D.; Peddigari, M.; Hwang, G.-T.; Annapureddy, V.; Kim, J.-W.; Choi, J.-J.; Hahn, B.-D.; Priya, S.; Lee, K. J.; Ryu, J. Laser Processing of Metal Oxides: Laser Irradiation of Metal Oxide Films and Nanostructures: Applications and Advances. *Adv. Mater.* **2018**, *30* (14), 1705148.

- [13] Martin, L. W.; Chu, Y. H.; Ramesh, R. Advances in the growth and characterization of magnetic, ferroelectric, and multiferroic oxide thin films. *Mater. Sci. Eng. R Rep.* **2010**, *68* (4), 89-133.
- [14] Biswas, A.; Yang, C.-H.; Ramesh, R.; Jeong, Y. H. Atomically flat single terminated oxide substrate surfaces. *Prog. Surf. Sci.* **2017**, *92* (2), 117-141.
- [15] Johnsson, M.; Lemmens, P. Perovskites and thin films—crystallography and chemistry. *J. Phys. Condens. Matter* **2008**, *20* (26), 264001.
- [16] Jiang, L. Q.; Guo, J. K.; Liu, H. B.; Zhu, M.; Zhou, X.; Wu, P.; Li, C. H. Prediction of lattice constant in cubic perovskites. *J. Phys. Chem. Solids* **2006**, *67* (7), 1531-1536.
- [17] Verma, A. S.; Jindal, V. K. Lattice constant of cubic perovskites. *J. Alloys Compd.* **2009**, *485* (1), 514-518.
- [18] Kumar, A.; Verma, A. S. Lattice constant of orthorhombic perovskite solids. *J. Alloys Compd.* **2009**, *480* (2), 650-657.
- [19] Angst, M., 12-Strongly correlated electrons. In *JCNS Neutron Lab Course*, Brueckel, T., Heger, G, Richter, D, and Zorn, R, Ed. Forschungszentrum Jülich GmbH, JCNS / RWTH Aachen / Univ. Münster: Jülich/München, Germany, 2012; Vol. 39, pp 12.1 - 12.19.
- [20] WELLS, A. F. *Structural Inorganic Chemistry*, 5th edition ed.; Clarendon Press: Oxford, 1984; p 1382.
- [21] Mitchell, R. H. *Perovskites: modern and ancient*, Thunder Bay, Ont. : Almaz Press: 2002; p 318.
- [22] Longo, J. B. G. a. J. M. In *Landolt-Börnstein Numerical Data and Functional Relationships in Science and Technology, New Series, Group III*; Hellwege, K. H., Ed.; Springer-Verlag: Berlin, 1970; p 125.
- [23] Galasso, F. S. *Perovskites and high- T_c superconductors*, Gordon & Breach: New York, 1990; p 294.
- [24] Yin, W.-J.; Weng, B.; Ge, J.; Sun, Q.; Li, Z.; Yan, Y. Oxide perovskites, double perovskites and derivatives for electrocatalysis, photocatalysis, and photovoltaics. *Energy Environ. Sci.* **2019**, *12* (2), 442-462.
- [25] Anderson, M. T.; Greenwood, K. B.; Taylor, G. A.; Poepelmeier, K. R. B-cation arrangements in double perovskites. *Prog. Solid State Chem.* **1993**, *22* (3), 197-233.
- [26] Goldschmidt, V. M. Die Gesetze der Krystallochemie. *Naturwissenschaften* **1926**, *14* (21), 477-485.
- [27] Tilley, R. J. D. *Perovskites: Structure-Property Relationships*, John Wiley & Sons, Ltd: 2016; p 328.

- [28] Philipp, J. B.; Majewski, P.; Alff, L.; Erb, A.; Gross, R.; Graf, T.; Brandt, M. S.; Simon, J.; Walther, T.; Mader, W.; Topwal, D.; Sarma, D. D. Structural and doping effects in the half-metallic double perovskite A_2CrWO_6 (A=Sr, Ba, and Ca). *Phys. Rev. B* **2003**, *68* (14), 144431.
- [29] Carcano, G.; Ceriani, M.; Soglio, F. Spin Coating with High Viscosity Photoresist on Square Substrates — Applications in the Thin Film Hybrid Microwave Integrated Circuit Field. *Microelectron. Int.* **1993**, *10* (3), 12-20.
- [30] Elemans, J. B. A. A.; Van Laar, B.; Van Der Veen, K. R.; Loopstra, B. O. The crystallographic and magnetic structures of $La_{1-x}Ba_xMn_{1-x}Me_xO_3$ (Me = Mn or Ti). *J. Solid State Chem.* **1971**, *3* (2), 238-242.
- [31] Gor'kov, L. P.; Kresin, V. Z. Manganites at low temperatures and light doping: band approach and percolation. *JETP Letters* **1998**, *67* (11), 985.
- [32] Zhou, J. S.; Goodenough, J. B. Paramagnetic phase in single-crystal $LaMnO_3$. *Phys. Rev. B* **1999**, *60* (22), R15002-R15004.
- [33] Trokiner, A.; Verkhovskii, S.; Gerashenko, A.; Volkova, Z.; Anikeenok, O.; Mikhalev, K.; Eremin, M.; Pinsard-Gaudart, L. Melting of the orbital order in $LaMnO_3$ probed by NMR. *Phys. Rev. B* **2013**, *87* (12).
- [34] Goodenough, J. B. Theory of the Role of Covalence in the Perovskite-Type Manganites $[La, M(II)]MnO_3$. *Phys. Rev.* **1955**, *100* (2), 564-573.
- [35] Dass, R. I.; Yan, J. Q.; Goodenough, J. B. Oxygen stoichiometry, ferromagnetism, and transport properties of $La_{2-x}NiMnO_{6+\delta}$. *Phys. Rev. B* **2003**, *68* (6), 064415.
- [36] Qian, Y.; Wu, H.; Kan, E.; Lu, J.; Lu, R.; Liu, Y.; Tan, W.; Xiao, C.; Deng, K. Biaxial strain effect on the electronic and magnetic phase transitions in double perovskite La_2FeMnO_6 : A first-principles study. *J. Appl. Phys.* **2013**, *114* (6), 063713.
- [37] Dass, R. I.; Goodenough, J. B. Multiple magnetic phases of $La_2CoMnO_{6-\delta}$ ($0 < \delta < 0.05$). *Phys. Rev. B* **2003**, *67* (1), 014401.
- [38] Joly, V. L. J.; Joy, P. A.; Date, S. K.; Gopinath, C. S. Two ferromagnetic phases with different spin states of Mn and Ni in $LaMn_{0.5}Ni_{0.5}O_3$. *Phys. Rev. B* **2002**, *65* (18), 184416.
- [39] Guo, H.; Burgess, J.; Street, S.; Gupta, A.; Calvarese, T. G.; Subramanian, M. A. Growth of epitaxial thin films of the ordered double perovskite La_2NiMnO_6 on different substrates. *Appl. Phys. Lett.* **2006**, *89* (2), 022509.
- [40] Singh, D. N.; Sinha, T. P.; Mahato, D. K. Structural and Dielectric characteristics of La_2CuMnO_6 double perovskite ceramics. *Mater. Today: Proceedings* **2017**, *4* (4), 5640-5646.
- [41] Singh, D. N.; Mahato, D. K.; Sinha, T. P. Structural and electrical characterization of La_2ZnMnO_6 double perovskite. *Physica B Condens. Matter* **2018**, *550*, 400-406.

- [42] Shirazi, P.; Rahbar, M.; Behpour, M.; Ashrafi, M. $\text{La}_2\text{MnTiO}_6$ double perovskite nanostructures as highly efficient visible light photocatalysts. *New J. Chem.* **2020**, *44* (1), 231-238.
- [43] Goodenough, J. B. An interpretation of the magnetic properties of the perovskite-type mixed crystals $\text{La}_{1-x}\text{Sr}_x\text{CoO}_{3-\lambda}$. *J. Phys. Chem. Solids* **1958**, *6* (2-3), 287-297.
- [44] Kanamori, J. Superexchange interaction and symmetry properties of electron orbitals. *J. Phys. Chem. Solids* **1959**, *10* (2-3), 87-98.
- [45] Anderson, P. W. Antiferromagnetism. Theory of Superexchange Interaction. *Phys. Rev.* **1950**, *79* (2), 350-356.
- [46] Kundu, A. K. *Magnetic Perovskites: Synthesis, Structure and Physical Properties*, Springer India: 2016; p 3-5.
- [47] Zener, C. Interaction Between the d-Shells in the Transition Metals. *Phys. Rev.* **1951**, *81* (3), 440-444.
- [48] Zener, C. Interaction between the d-Shells in the Transition Metals. II. Ferromagnetic Compounds of Manganese with Perovskite Structure. *Phys. Rev.* **1951**, *82* (3), 403-405.
- [49] Wang, H.; Pomar, A.; Martín-Rio, S.; Frontera, C.; Mestres, N.; Martínez, B. Dynamic magnetic properties and spin pumping in polymer-assisted-deposited $\text{La}_{0.92}\text{MnO}_3$ thin films. *J. Mater. Chem. C* **2019**, *7* (40), 12633-12640.
- [50] López-Mir, L.; Frontera, C.; Aramberri, H.; Bouzehouane, K.; Cisneros-Fernandez, J.; Bozzo, B.; Balcells, L.; Martinez, B. Anisotropic sensor and memory device with a ferromagnetic tunnel barrier as the only magnetic element. *Sci. Rep.* **2018**, *8* (1), 861.
- [51] Lan, C.; Zhao, S.; Xu, T.; Ma, J.; Hayase, S.; Ma, T. Investigation on structures, band gaps, and electronic structures of lead free $\text{La}_2\text{NiMnO}_6$ double perovskite materials for potential application of solar cell. *J. Alloys Compd.* **2016**, *655*, 208-214.
- [52] Sun, L.-P.; Li, H.; Li, Q.; Huo, L.-H.; Zhao, H.; Bassat, J.-M.; Rougier, A.; Fourcade, S.; Grenier, J.-C. Evaluation of $\text{La}_{2-x}\text{NiMnO}_{6-\delta}$ as cathode for intermediate temperature solid oxide fuel cells. *J. Power Sources* **2018**, *392*, 8-14.
- [53] Vila-Fungueiriño, J. M.; Rivas-Murias, B.; Rodríguez-González, B.; Rivadulla, F. Interface Magnetic Coupling in Epitaxial Bilayers of $\text{La}_{0.92}\text{MnO}_3/\text{LaCoO}_3$ Prepared by Polymer-Assisted Deposition. *Chem. Mater.* **2014**, *26* (3), 1480-1484.
- [54] Kwon, C.; Robson, M. C.; Kim, K. C.; Gu, J. Y.; Lofland, S. E.; Bhagat, S. M.; Trajanovic, Z.; Rajeswari, M.; Venkatesan, T.; Kratz, A. R.; Gomez, R. D.; Ramesh, R. Stress-induced effects in epitaxial $(\text{La}_{0.7}\text{Sr}_{0.3})\text{MnO}_3$ films. *J. Magn. Magn. Mater.* **1997**, *172* (3), 229-236.

- [55] Bull, C. L.; Gleeson, D.; Knight, K. S. Determination of B-site ordering and structural transformations in the mixed transition metal perovskites $\text{La}_2\text{CoMnO}_6$ and $\text{La}_2\text{NiMnO}_6$. *J. Phys. Condens. Matter* **2003**, *15* (29), 4927-4936.
- [56] Baidya, S.; Saha-Dasgupta, T. Electronic structure and phonons in $\text{La}_2\text{CoMnO}_6$: A ferromagnetic insulator driven by Coulomb-assisted spin-orbit coupling. *Phys. Rev. B* **2011**, *84* (3).
- [57] Murthy, J. K.; Chandrasekhar, K. D.; Murugavel, S.; Venimadhav, A. Investigation of the intrinsic magnetodielectric effect in $\text{La}_2\text{CoMnO}_6$: role of magnetic disorder. *J. Mater. Chem. C* **2015**, *3* (4), 836-843.
- [58] Zhang, C.; Zhang, T.; Ge, L.; Wang, S.; Yuan, H.; Feng, S. Hydrothermal synthesis and multiferroic properties of Y_2NiMnO_6 . *RSC Adv.* **2014**, *4* (92), 50969-50974.
- [59] Zhao, H. J.; Chen, X. M. First-principles study on the differences of possible ferroelectric behavior and magnetic exchange interaction between $\text{Bi}_2\text{NiMnO}_6$ and $\text{La}_2\text{NiMnO}_6$. *AIP Advances* **2012**, *2* (4), 042143.
- [60] Vasala, S.; Karppinen, M. $\text{A}_2\text{B}'\text{B}''\text{O}_6$ perovskites: A review. *Prog. Solid State Chem.* **2015**, *43* (1-2), 1-36.
- [61] Shannon, R. D. Revised effective ionic radii and systematic studies of interatomic distances in halides and chalcogenides. *Acta Cryst. A* **1976**, *32* (5), 751-767.
- [62] Goodenough, J. B.; Dass, R. I. Comment on the magnetic properties of the system $\text{Sr}_{2-x}\text{Ca}_x\text{FeMoO}_6$, $0 \leq x \leq 2$. *Int. J. Inorg. Mater.* **2000**, *2* (1), 3-9.
- [63] Freund, L. B.; Suresh, S. *Thin Film Materials: Stress, Defect Formation and Surface Evolution*, Cambridge University Press: Cambridge, 2004.
- [64] Bellardita, M.; Di Paola, A.; Yurdakal, S.; Palmisano, L. Chapter 2 - Preparation of Catalysts and Photocatalysts Used for Similar Processes. In *Heterogeneous Photocatalysis*; Marci, G.; Palmisano, L., Eds.; Elsevier: 2019; pp 25-56.
- [65] Gudmundsson, J. T.; Lundin, D. 1 - Introduction to magnetron sputtering. In *High Power Impulse Magnetron Sputtering*; Lundin, D.; Minea, T.; Gudmundsson, J. T., Eds.; Elsevier: 2020; pp 1-48.
- [66] Herman, M. A.; Richter, W.; Sitter, H. *Epitaxy*, 1 ed.; Springer-Verlag Berlin Heidelberg: 2004; p XV, 525.
- [67] Norton, D. P. Pulsed Laser Deposition of Complex Materials: Progress Toward Applications. In *Pulsed Laser Deposition of Thin Films*; Eason, R., Ed.; John Wiley & Sons, Inc.: Hoboken, New Jersey, 2006; Chapter 1, pp 1-31.

- [68] Pohl, U. W. Methods of Epitaxy. In *Epitaxy of Semiconductors: Introduction to Physical Principles*; Pohl, U. W., Ed.; Springer Berlin Heidelberg: Berlin, Heidelberg, 2013; pp 275-313.
- [69] Martín-Palma, R. J.; Lakhtakia, A. Chapter 15 - Vapor-Deposition Techniques. In *Engineered Biomimicry*; Lakhtakia, A.; Martín-Palma, R. J., Eds.; Elsevier: Boston, 2013; pp 383-398.
- [70] Pottathara, Y. B.; Grohens, Y.; Kokol, V.; Kalarikkal, N.; Thomas, S. Chapter 1 - Synthesis and Processing of Emerging Two-Dimensional Nanomaterials. In *Nanomaterials Synthesis*; Beeran Pottathara, Y.; Thomas, S.; Kalarikkal, N.; Grohens, Y.; Kokol, V., Eds.; Elsevier: 2019; pp 1-25.
- [71] Niu, G.; Saint-Girons, G.; Vilquin, B. Chapter 18 - Epitaxial systems combining oxides and semiconductors. In *Molecular Beam Epitaxy*; Henini, M., Ed.; Elsevier: Oxford, 2013; pp 451-475.
- [72] Galindo, V.; Sénateur, J. P.; Abrutis, A.; Teiserskis, A.; Weiss, F. High quality $\text{YBa}_2\text{Cu}_3\text{O}_{7-\delta}/\text{PrBa}_2\text{Cu}_3\text{O}_{7-\delta}$ multilayers grown by pulsed injection MOCVD. *J. Cryst. Growth* **2000**, *208* (1), 357-364.
- [73] Ji, Y.; Lin, Y. Nanostructural Thin Film Development with Chemical Solution Deposition. In *Advanced Nano Deposition Methods*; 2016; pp 159-177.
- [74] Schwartz, R. W.; Narayanan, M. Chemical Solution Deposition—Basic Principles. In *Solution Processing of Inorganic Materials*; Mitzi, D. B., Ed.; 2008; pp 33-76.

Chapter 2

Objectives

2. Objectives of this thesis

Among the large amount of materials and combinations of materials with potential functionalities, metal oxides constitute a vast and interesting family, exhibiting numerous properties already in the bulk state. Ferroelectric, ferromagnetic multiferroic or superconducting are some of the behaviors found among the large variety of metal oxides, which range from rather simple binary oxides such as Fe_3O_4 , TiO_2 , ZrO_2 , or ZnO , to more complex materials like binary and ternary metal perovskites or spinels (LaMnO_3 , SrTiO_3 , $\text{La}_{0.7}\text{Sr}_{0.3}\text{MnO}_3$, $\text{La}_2\text{CoMnO}_6$, $\text{La}_2\text{NiMnO}_6$, BiFeO_3 , CoFe_2O_4 , ...). Nowadays, most of the new technological applications of materials require the use of thin films and heterostructures to take advantage of the varied benefits of miniaturization.

In the context of stoichiometry control, scalability and high throughput required for application purposes, chemical solution deposition approaches to grow thin films offer a great potential. In addition, in the actual circumstances where the demand for sustainable and environmentally friendly reactants and processes steadily increases, polymer assisted deposition (PAD) is very attractive, since it is based on using aqueous solutions of environmentally friendly metal salts and commercially available polymers. However, serious concerns have been raised on the control of surface and interfacial quality of films grown by chemical solution deposition, limiting their use in emergent applications relying in flat sharp interfaces, for example, for spintronics.

In the present thesis we undertake the challenge of realizing and exploring different high-quality perovskite oxide thin films, namely LCMO, LNMO, LSMO and LMO on STO and LAO substrates by the PAD approach. The results of LCMO, LNMO, and LMO films were published. The physical properties of these materials are strongly dependent on the ordered arrangement of cations, especially the B-site ordering in the double perovskite structure. Therefore, these materials constitute an excellent playground to investigate the influence of the PAD growth process on the structure and properties of complex oxides. On the other hand, bilayer films are necessary in devices based on the spin transfer torque effect and the surface/interface roughness or magnetic inhomogeneities strongly impact their properties. As a result, the requirements for a

good functional film include high crystallinity, low surface roughness, good electric properties, and good magnetic properties.

The first objective has been to optimize the preparation of the mixed metal polymer mother solution for each cation, which will be used afterwards to prepare the precursor solution for each oxide compound with the desired stoichiometry. In addition to the effort done in controlling the growth of these complex oxides on STO and LAO substrates, we have also explored them in depth performing a comprehensive characterization of their surface morphology, crystallography, microstructure and magnetic and transport properties.

The magnetic properties of LCMO films ($M_S \approx 6 \mu_B/\text{f.u.}$ and $T_C \approx 230 \text{ K}$) prepared by PAD are indicative of almost full Co/Mn B-site cationic ordering, favored by the particular grow conditions of PAD, very slow rate, close to thermodynamic equilibrium conditions. The double perovskite cationic arrangement was investigated by high resolution scanning transmission electron microscopy (STEM) images. For LNMO epitaxial thin films, complete ordering is more difficult to attain due to the smaller ionic radii difference between Ni^{2+} and Mn^{4+} . Consequently, saturation magnetization values are depleted compared with the expected spin-only theoretical value ($M_S = 5 \mu_B/\text{f.u.}$). The oxidation state of the transition metal cations was determined by synchrotron x-ray absorption studies. Further, the effect of fast heating rates on the magnetic properties of LCMO and LNMO epitaxial thin films was analyzed.

The static and dynamic magnetic properties of high-quality LMO thin films on STO were prepared by PAD were investigated. Ferromagnetic resonance measurements in LMO films and LMO/Pt bilayers indicate the transfer of spin momentum from LMO to the Pt layer by spin pumping, which demonstrate that the PAD technique allows obtaining complex oxide thin films of high microstructural and interfacial quality suitable for spintronic applications.

Chapter 3

Experimental

3.1 Polymer Assisted Deposition (PAD)

Polymer-assisted deposition (PAD) was first introduced in 2004 by Jia et. al.¹ to prepare metal-oxide films. Different from the CSD methods mentioned above, it employs water as the solvent. PAD is a wet chemical method that uses water-soluble polymers to bind metal ions as film precursors. The key to PAD is that the polymer controls the viscosity and binds metal-ions, resulting in a homogeneous distribution of metal precursors in the solution and the formation of uniform metal-organic precursor films. The latter feature makes it possible to grow simple and complex epitaxial metal-oxides with desired physical and structural properties. The PAD process is illustrated in Figure 13.

As PAD itself is a chemical solution deposition method, it has the traditional advantages of CSD. Importantly, the precursors are stable, and they can be coated by spin, dip, or spray on to the substrate. Furthermore, it has features, such as binding metals directly to the polymer, that prevent the pre-formation of metal-oxide in the solution before the polymer is decomposed.²The precursor solutions are very stable and not sensitive to the ambience humidity, a common hood is enough almost for all the process. Compared with the CSD methods in Table 1, the PAD process is simpler and easier.

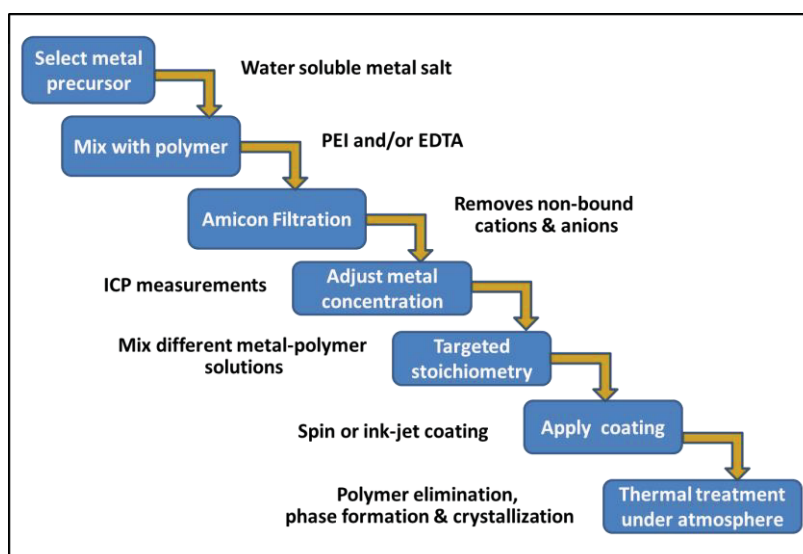


Figure 13. Flow chart of the polymer assisted deposition process

3.1.1 Solution chemistry of PAD

The PAD solutions contain water, salt(s), and polymer(s). The salts are water soluble metallic salts (nitrate, chloride, acetate, oxalate, etc) and their hydrate. The most used polymer is polyethylenimine (PEI) due to its large amount of terminal amino ($-NH_2$) groups, the simple PEI polymer binds well to the first row transition metals.³ Some hard metals, such as titanium or strontium, cannot bind directly to PEI. There are two ways to improve the coordination ability of PEI. One way is to chemically modify the PEI polymer, such as carboxylated polyethylenimine (CPEI), phosphorylated polyethylenimine (PPEI), sulfonated polyethylenimine (SPEI).⁴ Another method is to use ethylenediaminetetraacetic acid (EDTA) to coordinate with metals to form anionic metal complexes, and then coordinate to protonated PEI. The major advantage of the EDTA route is that EDTA forms stable complexes with almost all metals. The EDTA complexes bind to the PEI via a combination of hydrogen bonding and electrostatic attraction as seen in Figure 14. Metal polymer solution with over 45 different elements are able to be produced using either pure PEI or PEI-EDTA.³

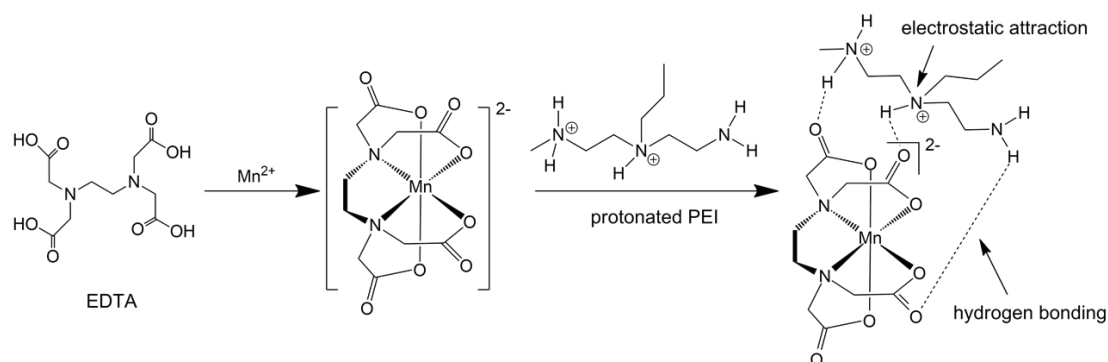


Figure 14. Schematic of the formation of $[M-EDTA]-PEI$ complex, illustrated by Mn^{2+} . The cation chelates with EDTA to form a complex with negative charge, then combine with protonated PEI.

3.1.2 Stability and pH

The pH plays a very important role in the formation of $[M-EDTA]-PEI$ complexes. The PEI used in this thesis is branched with a molecular weight of 25,000. In the aqueous PEI solution, the pK_a for primary, secondary and tertiary amines are 10.5, 6.4 and 4.2, respectively⁵. The enhancement of electrostatic interactions, particularly hydrogen

bonds, takes place at lower values of pH, where most of amines of PEI are protonated.⁵ The hydrolysis of cations occurs at very high value of pH, and precipitations of metal hydroxides appear. For instance, La^{3+} hydrolysis occurs at $\text{pH} \approx 8.5$ ⁶ while a $\text{pH} \approx 7$ is enough to hydrolyze Mn^{2+} .⁷ But when the pH value is too low, the chelating ability of EDTA will be weakened.

Another situation that should be considered is the mixing of different mother solutions according to the targeted stoichiometry. Their pH values should be similar to avoid precipitations during the mixing process. After all the situations were taken into consideration, the pH values of the different mother solutions prepared in this work were set up to be close to 6.

3.1.3 PAD mother solutions preparation

The main solution preparation process is the same with other CSD, the differences are the use of ultrafiltration to remove unbound low molecular weight cations or anions, and inductively coupled plasma-atomic emission spectroscopy (ICP-AES) to measure the concentration of the cations. Figure 15 is the schematic of precursor solution preparation process of $\text{La}_2\text{CoMnO}_6$ solution.

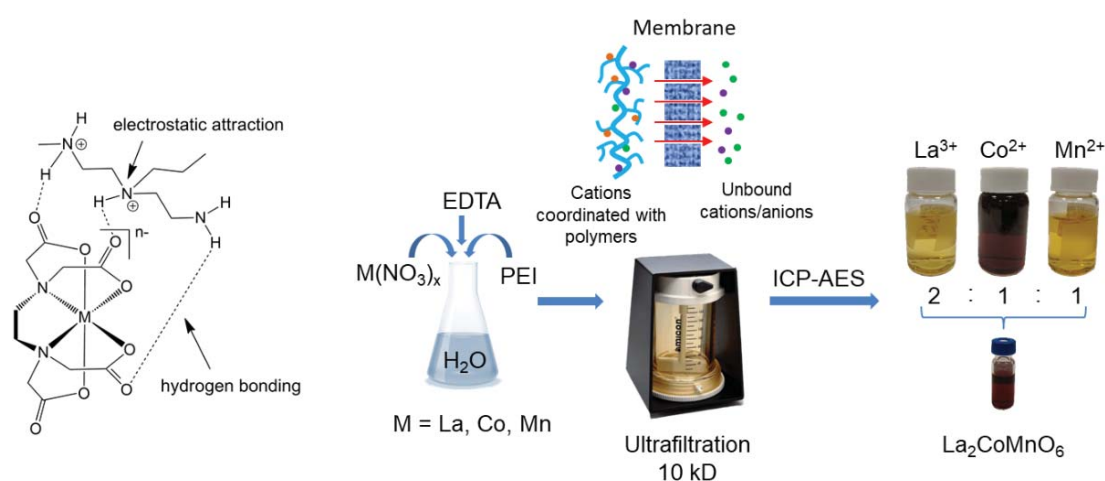


Figure 15. Schematic of precursor solution preparation process of $\text{La}_2\text{CoMnO}_6$

3.1.3.1 Precursor solution preparation

EDTA is not easy to dissolve in water directly. Usually, 2 g PEI are dissolved in 40 mL water firstly obtaining a basic solution of $\text{pH} \approx 11$, then EDTA is added into the solution, and the pH value decreases. The pH value is measured with pH-meter, and ammonia or nitric acid were used to adjust the pH value to around 6. High purity metal nitrates or chlorides were used as cations sources. After the metal salts were dissolved in the EDTA-PEI solution, the final pH values were adjusted again. Since EDTA is a polydentate ligand, and the cations used in this thesis are polycordinationable, the molar ratios of metal and EDTA were set up to 1:1. The mass ratios of EDTA and PEI were 1:1 or 1:2, which resulted in different binding degrees and viscosities. The solutions were heated at 50 °C for a few hours with stirring to ensure all the chemicals were dissolved completely. After preparation of a given solutions, they were kept several hours before filtration, just to confirm that no precipitate is formed. The solutions were filtered through a syringe membrane filter with a pore size of 0.22 μm PTFE filter to remove undissolved chemicals or impurities introduced during the preparation process like dust. The same filtration will be repeated before and after the ultrafiltration, since all the processed are perform in a common laboratory.

3.1.3.2 Ultrafiltration

One of the key features of the precursor solution of PAD is the use of an Amicon[®] filtration unit to remove non-coordinated cation and anion species. The solution is passed through a membrane to wash out cations and anions not coordinated with polymers. This is possible because of the large difference in molecular weight and size between the polymer and the cations. Filtering the solution prevents precipitation and therefore yields a homogeneous solution (and ultimately a homogeneous coating) at the molecular level. Filtration plays an important role in the growth of high quality epitaxial films. This step is especially critical in the growth of epitaxial complex materials where two or more cations are involved.⁸

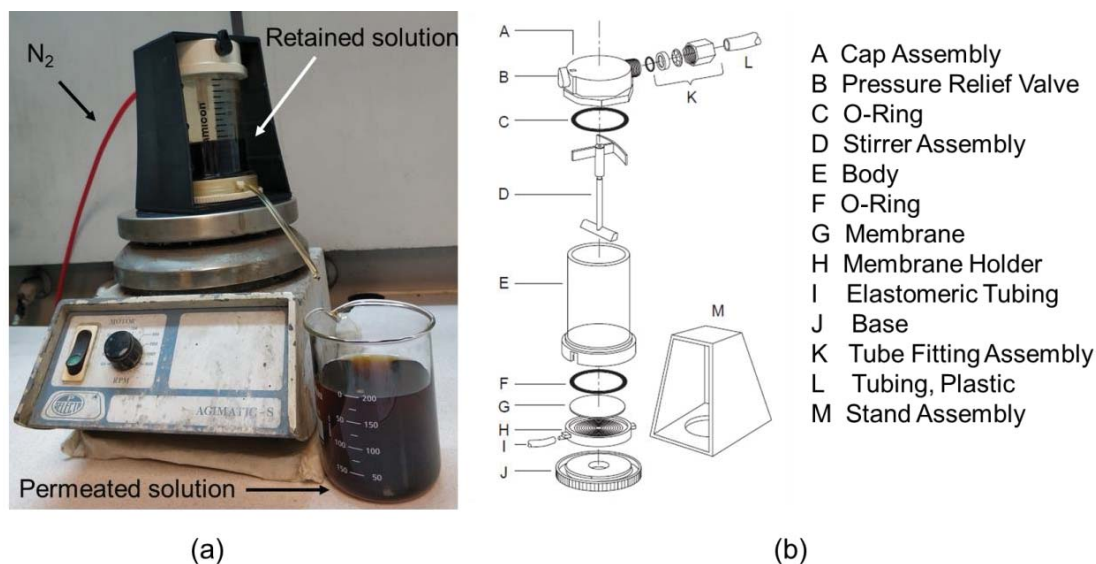


Figure 16. (a) Photo of an Amicon ultrafiltration cell used in the experiments. (b) Amicon stirred cell model 8200, capacity 200 mL.

Firstly, the Amicon filtration unit model 8200 (Figure 16) was assembled from the bottom to the top. Secondly, 40 mL metal polymer solution were transferred into the cell, and 110 mL Milli-Q water were added, the total volume of the solution was 150 mL. Then the cell was closed with the cap and mounted in the stand assembly. Finally, the pressure relief valve was closed, and the N_2 inlet valve opens (0.5~1.0 bar) to increase the pressure in the cell and let the solution overpass the membrane filter drop by drop until a final volume of less than 20 mL was reached.

The operation was repeated two to three times, adding Milli-Q water up to 150 mL before each filtration. The filtration ends up to attaining the desired volume 20~25 mL, the concentration of PEI is about 0.1 g/mL. The stirring speed is controlled by a magnetic stirrer under the cell, usually operated at 60 rpm.

The membranes had a cut-off molecular weight of 10 kDa, only cations and EDTA which are coordinated to polymers over this molecular weight value will retain in the cell. The retained and permeated solutions were collected for concentration measurements. All the retained solutions were kept in a refrigerator.

3.1.3.3 ICP-AES

Metal concentration analysis was conducted using inductively coupled plasma-atomic emission spectrometer (ICP-AES), located at the Servei d'Anàlisi Química of the UAB. The efficiency of the interaction of PEI to metals and to anionic complexes can be studied by comparing the yield between retained and permeated portions during Amicon filtration. The efficiency of PEI to coordinate different metals was quantified through the degree of retention of metal ions after ultrafiltration of the solutions. In order to calculate the degree of retention, the retained and permeated volumes must be taken into account, besides the molar concentration, so that the ratio between the number of moles (n) is obtained.

$$Retention = \frac{n_{retained}}{n_{retained} + n_{permeated}} = \frac{[Retained] \cdot V_{ret.}}{[Retained] \cdot V_{ret.} + [Permeated] \cdot V_{perm.}} \quad \text{Eq. 8}$$

The higher the formation of the metal complex polymer species the higher the degree of retention, because in order to remain into the retained portion of the filtered solution, the metal or the complex metal necessarily must be coordinated to PEI. The degree of retention after ultrafiltration, as well as the pH value of metal polymer solutions is summarized in Table 2. The degree of retention of different ions prepared in this thesis, and pictures of precursor solutions are shown in Figure 17. The viscosity of the solutions were measured with a DMA 4100m Anton Paar densimeter with a micro-viscometer module Lovis 2000 ME, the viscosity values range from 3 to 4 MPa·s.

Table 2. Degree of retention of different ions at their corresponding pH value in solutions. The proportion of EDTA with respect to metal, and the proportion of EDTA to PEI, is also indicated.

Cation	Salt	pH	c(mmol/l)	Retention (%)	M:EDTA molar ratio	EDTA:PEI mass ratio
La ³⁺	La(NO ₃) ₃ ·6H ₂ O	6.03	230.37	76.69	1:1	1:1
Sr ²⁺	Sr(NO ₃) ₂	5.34	125.54	46.95	1:1	1:1
Ni ²⁺	NiCl ₂ ·6H ₂ O	6.48	168.67	66.5	1:1	1:1
Co ²⁺	Co(NO ₃) ₂ ·6H ₂ O	8.01	146.44	53.31	1:1	1:2
Mn ²⁺	Mn(NO ₃) ₂ ·5H ₂ O	5.29	176.38	67.05	1:1	1:1
Ru ³⁺	RuCl ₃ ·xH ₂ O	7.90	11.0	85.25	1:1	1:1.5

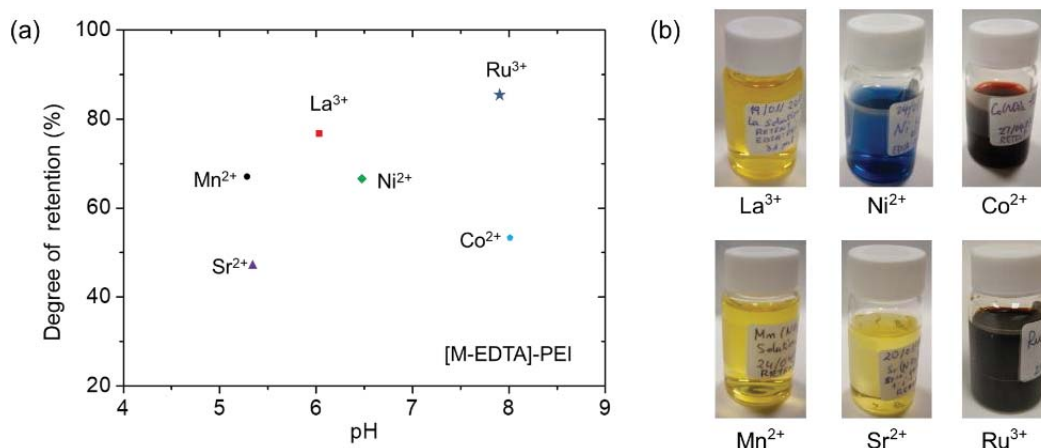


Figure 17. (a) Degree of retention of different ions prepared in this thesis, (b) Pictures of different precursor solutions.

3.1.3.4 Preparation of precursor solution for a given compound according to stoichiometry

PAD can be used for the synthesis of poly-cationic compounds because polymer coordination prevents any undesired reaction in the solution due to differences in chemical reactivity among metals. As mentioned above, the pH values of the metal polymer solutions were adjusted to be close to 6, so no precipitation occurred during mixing, and the final mixture solutions could be stable for months. The purified solutions of each individual cation are then mixed according to the final desired stoichiometry.

In this thesis, nine different poly-cationic solutions were prepared; they are La_{0.92}MnO₃, La₂CoMnO₆, La₂NiMnO₆, LaNiO₃, La_{0.7}Sr_{0.3}MnO₃, La_{0.5}Sr_{0.5}CoO₃, LaCoO₃, SrCoO₃ and SrRuO₃.

As an example, below we show the characteristic data for mixing of individual solutions with a given molar concentration for obtaining 2 mL of the solution for La_{0.92}MnO₃ in a concentration of 56.7 mM with respect to Mn:

Table 3. Mixing of individual La and Mn solutions to obtain a La_{0.92}MnO₃ precursor solution

Cation	Stoichiometry	pH	Molar concentration (mM)	Volume (μL)
La	0.92	6.03	230.37	798.7
Mn	1	5.29	176.38	1133.9

Typical film thickness obtained with this solution concentration was around 10 nm. For the formation of films with a thickness of 25 nm, the solution was concentrated to around 130 mM reaching a final volume of 0.91 mL prior to spin-coating.

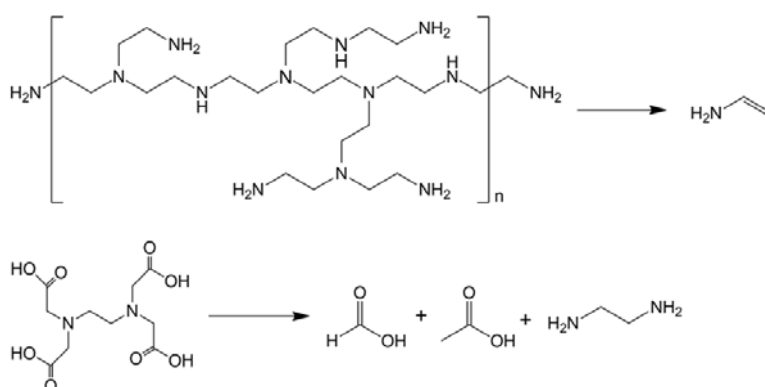
The different precursor solutions are transferred by using micropipettes with low-retention tips for a higher accuracy. After mixing, the final solution is usually evaporated or diluted for increasing or decreasing the molar concentration. The concentration is an important parameter in spin-coating at the time of varying the thickness layer. The relation between the thickness and solution concentration varies with the composition of the solution. At a speed of 4000 rpm for the spin coater, in the cases of LCMO and LNMO, if the concentration of the solution is about 20 mM, then the thickness of the grown film was around 5 nm. Increasing the concentration to about 60 mM, the thickness increased to be about 20 nm. But for LSMO films, a concentration of 150 mM is necessary to produce a film of 20 nm. It has to be aware that the viscosity is related to the concentration, so the concentration-thickness relationship is not necessarily linear.

3.2 Thermogravimetric analysis of solutions

The last step of the PAD process is the thermal treatment, it mainly consists of the decomposition of organics (<600 °C) and crystallization of metal oxides (700-1000 °C). The thermal behavior of the poly-cationic solutions was analyzed by means of thermogravimetry (TG) and differential thermal analysis (DTA). The temperature range from room temperature to 500 °C, provides information on water loss and on the thermal stability of the polymer. In the solutions, besides water there are metal nitrates, PEI, and EDTA. From room temperature to ~ 250 °C, the weight loss corresponds to the process of evaporation of residual water and dehydration.⁹ Pure EDTA decomposes to acetic acid, formic acid, and ethylenediamine in water at a temperature range from 200°C to 260 °C.¹⁰ When EDTA chelates with metal ions, such as Fe, Ni, the decomposition temperature will increase to 230-310 °C.¹¹ PEI starts to decompose from 230 °C, loses more than 80% mass at about 450 °C, and it will be removed completely above 550 °C. An important aspect of PEI is that this polymer undergoes de-polymerization instead of a combustion, the only reaction product is

$\text{CH}_2=\text{CHNH}_2$.⁸ The decomposition processes of PEI and EDTA are shown in Figure 18 (a), all the organics are decomposed to small volatile molecules and removed from the film, as a result, only metal oxides remain. Furthermore, before completely decomposed, the polymer keeps the homogenous mixing of the metals and inhibits the crystallization of the oxides as a result, high quality complex metal-oxide films without second phase inclusions are formed at higher temperatures.¹²

As an example, we show the thermogravimetric analysis performed on a $\text{La}_{0.7}\text{Sr}_{0.3}\text{MnO}_3$ precursor solution. Before the measurement, the solution was dried at $80\text{ }^\circ\text{C}$ to remove most of the water to form a powder mixture. Figure 18 (b) shows the TG and DTA curves of the sample. The mass loss step with no peak on the DTA curve upon heating to about $200\text{ }^\circ\text{C}$ is due to evaporation of water. Between $250\text{ }^\circ\text{C}$ and $350\text{ }^\circ\text{C}$, the major mass loss step with the strong exothermic DTA peak at about $310\text{ }^\circ\text{C}$ comes from the decomposition of the PEI and EDTA. The residual organics continue to decompose until $500\text{ }^\circ\text{C}$. The mass loss from 310 to $500\text{ }^\circ\text{C}$ with the small exo-peak close to $440\text{ }^\circ\text{C}$ comes from PEI with higher molecular weight. Finally, the mass loss is close to 90%. The actual thermal behavior of the metal-polymer film may be different from the powder, but the thermogravimetric analysis is still helpful for the understanding of the decomposition process and the proper selection for crystallization temperature of the film.



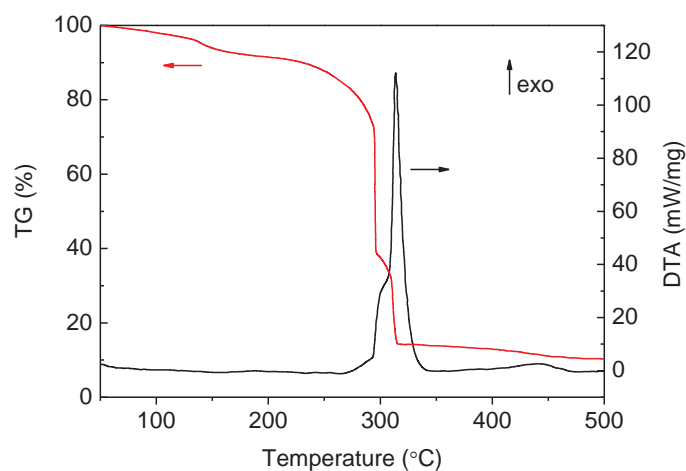


Figure 18. (a) Decomposition of PEI and EDTA, (b) The TG/DTA curves of $\text{La}_{0.7}\text{Sr}_{0.3}\text{MnO}_3$ precursor. The precursor solution was dried at 80°C prior analysis. The analyses were performed in flowing air atmosphere with a $20^\circ\text{C}/\text{min}$ heating rate. The sample mass was about 5.69 mg.

3.3 Substrate treatment for atomically flat surface

3.3.1 Structure of substrate

Epitaxial growth refers to the process of growing a single-crystalline film with a structural coherence, crystallographic orientation and lattice matching to the structure of the crystal substrate (Figure 19). To grow an epitaxial perovskite film, the requirements for substrate include perovskite crystal structure, lattice match as well as chemical compatibility, especially, substrates with atomically flat and chemically homogeneous surfaces, i.e., surfaces with the step-terrace structure of one-unit cell step height and also of single chemical termination, are indispensable for the growth of high quality epitaxial thin films with atomically controlled interface.

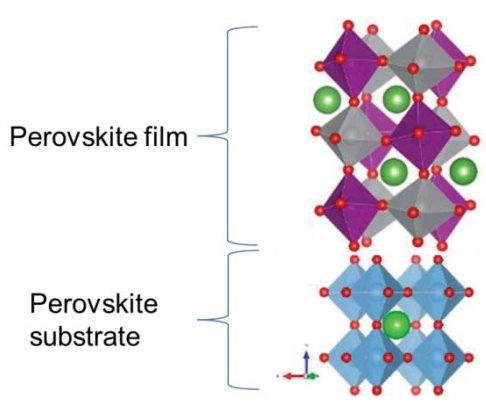


Figure 19. Epitaxial growth

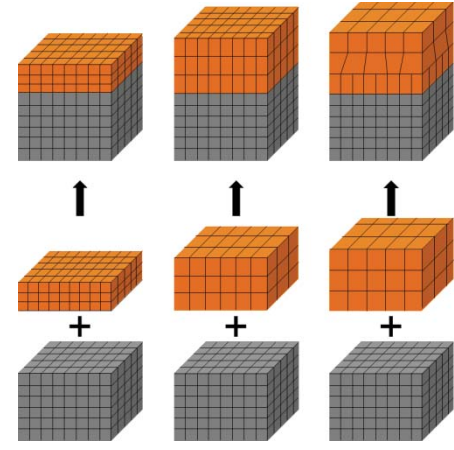


Figure 20. Schematics of epitaxial growing attending to lattice parameter mismatch, f . (a) $f < 0$, tensile; (b) $f > 0$, compressive; (c) $f \gg 0$, relaxed

The strain introduced by the substrate helps to modulate the unit of the upper film cell both in tensile or compressive way (Figure 20). The mismatch between the lattice constant of the substrate ($a_{substrate}$) and the film (a_{film}) can be quantified by a parameter, f .

$$f = (a_{film} - a_{substrate}) / a_{substrate} \times 100 \quad \text{Eq. 9}$$

The diversity of substrates as evident from Figure 21 means that for a given material a very close to lattice-match substrate can be chosen to produce a film in its most natural state with almost no structural strain. It also means that either compressive or tensile strain can be induced in the film by choosing appropriate lattice-mismatched substrates to alter the functionalities.

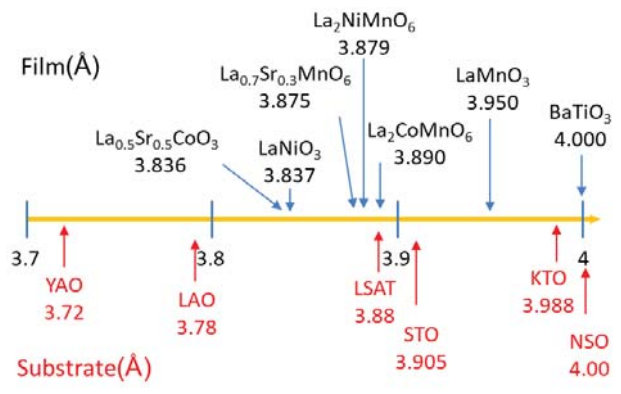


Figure 21. Comparative cubic or pseudocubic lattice constant (Å) of various perovskite thin films and commercially available substrates, STO and LAO are used in this thesis.¹³⁻²⁰

Table 4 includes the list of some commercially available single crystal metal oxide substrates. We can see that structure and lattice constant of substrate and film maybe not the same. The lattice parameters of the film are measured by X-ray diffraction, if the film is not a cubic structure, it should be simplified by reference to a pseudocubic structure. For example, the pseudo-cubic lattice constant for a rhombohedral (R-3c) $\text{La}_{0.7}\text{Sr}_{0.3}\text{MnO}_3$ film is $a_p \approx \sqrt{2}a_r/(1+\cos\alpha_r)$, $\alpha_p = \arccos[(1-2\cos\alpha_r)/(2\cos\alpha_r-3)]$, where a_r and α_r are lattice constant and angles of rhombohedral structures, respectively.²¹ For a monoclinic ($P2_1/n$) $\text{La}_2\text{CoMnO}_6$ film, $a_p \approx a/\sqrt{2} \approx b/\sqrt{2} \approx c/2$, $\beta \approx 90^\circ$.

Table 4. List of commercially available single crystal metal oxide substrates with preferable orientations used for thin film growth.¹³

Substrate	Orientation	Structure	Lattice constants (Å)	Cubic (pseudo) lattice constant (Å)
NdScO_3 (NSO)	(110)	Orthorhombic	a = 5.57 b = 5.77 c = 7.99	4.00
KTaO_3 (KTO)	(001)	Cubic	a = 3.988	3.988
SrTiO_3 (STO)	(001)	Cubic	a = 3.905	3.905
LaAlO_3 (LAO)	(001)	Rhombohedral	a = 3.78	3.78
$\text{La}_{0.18}\text{Sr}_{0.82}$ $\text{Al}_{0.59}\text{Ta}_{0.41}\text{O}_3$ (LSAT)	(001)	Cubic	a = 3.88	3.88
YAIO_3 (YAO)	(110)	Orthorhombic	a = 5.18 b = 5.33 c = 7.37	3.72

Commercially available substrate crystals usually come with mechanically polished surfaces of low miscut angle, typically less than 0.1° (Figure 22 (a)).¹³ Along the [001] direction, a perovskite ABO_3 crystal consists of alternate stacking of AO and BO_2 layers, and the surface of as-received substrates is always composed of a mixed layer of AO and BO_2 (Figure 22 (b)).²² The surface is far from being flat and homogeneous with step height from 0.2 nm to 0.6 nm.

The terminating plane of the substrate determines the stacking sequence of the film. Suppose that the substrate has the following $-AO-BO_2-AO-BO_2-$ structure in the (001) direction. When growing a thin film of say $A'O-B'O_2$, the most favorable order in the film would be dictated by the order in the substrate for reasons of charge neutrality leading to $-AO-BO_2-AO-BO_2-A'O-B'O_2-$. However, if the termination is not unique, schematically indicated in Figure 22 (b), regions of the thin film have the slightly different order $-AO-BO_2-AO-B'O_2-A'O-$. This order will perpetuate in each subsequent layer applied. Therefore, one must ensure a single-terminated surface.²²

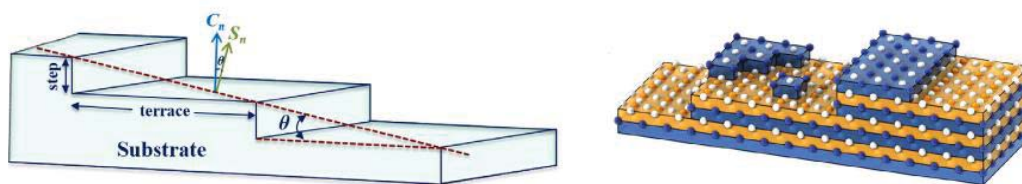


Figure 22. (a) Schematic representation of a substrate. Miscut angle (θ) of a substrate, defined as the angle between surface normal (S_n) and the crystal plane normal (C_n), determines step height and terrace width. It is seen that the step height would increase with an increase in miscut angle.¹³ (b) A schematic representation of a mixed-terminated surface with steps of 0.2, 0.4, and 0.6 nm high.²²

Following, we are going to describe the treatment performed in the different used commercial substrates in order to obtain flat and single terminated substrates.

3.3.2 Treatment for STO substrates

In the case of STO, TiO_2 termination is more stable than the SrO termination, and re-etching the substrate after the high temperature annealing in an O_2 environment produces a nearly perfect atomically flat surface. Homogenous termination on a TiO_2 surface will favor the preferential deposition of AO (A-site) layer of the perovskite (ABO_3) film, thus forming an epitaxial TiO_2 -AO interface.

Buffered hydrofluoric acid (BHF) and “aqua regia” are used in the etching process.²³⁻²⁹ BHF is more toxic and should be used in clean room, so we choose the “aqua regia” to etch STO, all the process could be performed in an ordinary hood. The original recipe is from Kareev et al..²⁹

Initially, the 5x5 mm² crystals were soaked for 20~25 min in de-ionized (DI) water at 70 °C to create soluble hydroxide complexes Sr(OH)_x+xH₂O at the surface. Next, 20 min of wet etching in HCl-HNO₃ (3:1) acidic solution was applied to remove the surface SrO layer. Further, the substrates were thoroughly rinsed out with DI water to remove the acidic contamination and cleaned in acetone and methanol.

Finally, the etched samples were annealed at 1000 °C for 30 min in the 0.5 l/min O₂ flux to facilitate the recrystallization of the surface.

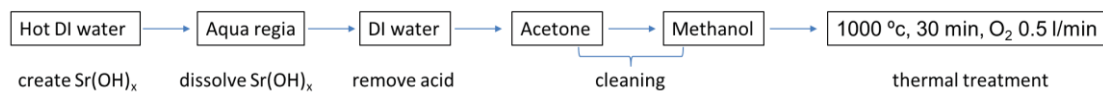


Figure 23. Substrate treatment process for STO substrates

3.3.3 Treatment for LAO substrates

High temperature annealing can produce singly AlO₂-terminated LAO (001) surfaces.³⁰⁻
³¹ The substrates were annealed at 900 °C for 300 min in the 0.5 l/min O₂ flux to facilitate the surface re-crystallization to get AlO₂ terminated atomically flat substrates with terraces.

After treating substrates according to the surface treatment procedures described above, atomic force microscopy (AFM) was used to ensure structural flatness of the surface. The surface of an as-received (001) substrate would be far from being flat and homogeneous (Figure 24 (a), (d)). After the prescribed treatment procedures, the substrate surface turns into a step-terrace structure (Figure 24 (b), (e)) and the line profiles show the height of the terraces.

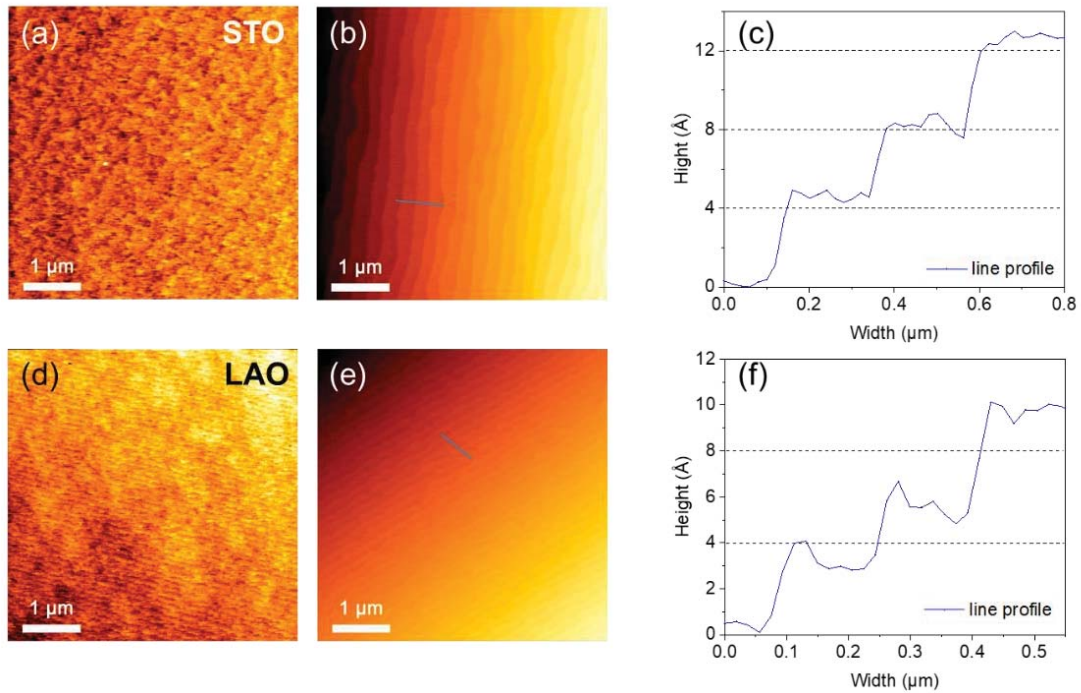


Figure 24. (a) $5 \times 5 \mu\text{m}^2$ AFM topography image of an as received STO (001) substrate from CrysTec GmbH, $\text{RMS} \sim 0.1 \text{ nm}$ (b) AFM image of the same sample after treatment, clearly displaying flat terraces, $\text{RMS} \sim 0.1 \text{ nm}$. (c) Line profile along the terraces, demonstrating that their height is very close to lattice parameter of $\sim 0.4 \text{ nm}$. (d) $5 \times 5 \mu\text{m}^2$ AFM topography image of an as received LAO (001) substrate from CrysTec GmbH, $\text{RMS} \sim 0.1 \text{ nm}$. (e) AFM image of the same sample after treatment, clearly displaying flat terraces, $\text{RMS} \sim 0.1 \text{ nm}$. (f) Line profile along the terraces, demonstrating that their height is very close to lattice parameter of $\sim 0.4 \text{ nm}$.

Except for the chemical challenges, one of the foremost problems in water-based chemical solution deposition is the poor affinity of polar aqueous solutions to the substrate surface. The reasons may be the intrinsic hydrophobic surface properties or organic contamination. In most cases, a surface-wetting reagent was added to the precursor solution in order to adjust its viscosity and surface tension. Also a physical UV/ozone technique has been reported³². For this cleaning procedure, the substrate is placed in a closed container where continuously ozone is produced and destroyed by the illumination of oxygen with UV radiation of two different wavelengths. During this process, atomic oxygen is formed as an intermediate product, which being a very strong oxidizer, is able to decompose all organic contaminants from the substrate by oxidation.³³ In the case of Si substrate, during the UV/ozone treatment process, hydroxyl-rich oxide film can be generated on Si surface, which increases the

hydrophilicity.³⁴⁻³⁵ It also works on other substrates like Pt, Ir, or IrO₂.³² The UV/ozone treatment process increases the wettability of the surfaces of perovskite substrates in the same way.

Therefore, an important step process for the substrates before spin-coating of the precursor solution is surface cleaning. Firstly, they are cleaned and dried with methanol and cleanroom wipers. Next they are put in the UV/ozone cleaner (UVO cleaner model No. 42-220 from Jelight Company Inc.) for 20 minutes to increase surface wettability (Figure 25).



Figure 25. UV/O₃ treatments reduce the contact angle of water to almost zero. It allows excellent wetting behavior of (most) water based precursor solutions on different types of substrates.

After the solution and substrate are prepared, the next step is spin-coating the precursor solution on top of the substrate, followed by a thermal treatment at high temperature in a tube furnace.

3.4 Solution spin-coating

The most commonly used technique in the laboratory for solution deposition on top of a substrate is spin coating (Figure 26). The substrate is first fixed on the holder of the spinner by a double faced tape at the backside. The precursor solution is dropped on the substrate by the help of a micropipette, typical dispensed volume is (12 μ l). The optimized spin coating conditions are the following: substrate rotation speed of 4000–6000 rpm with a total time of 90 seconds, including an acceleration and deceleration time of 1 second, respectively. The thickness of the as-prepared wet film can be controlled by rotation speed, spinning time, and solution concentration and viscosity.

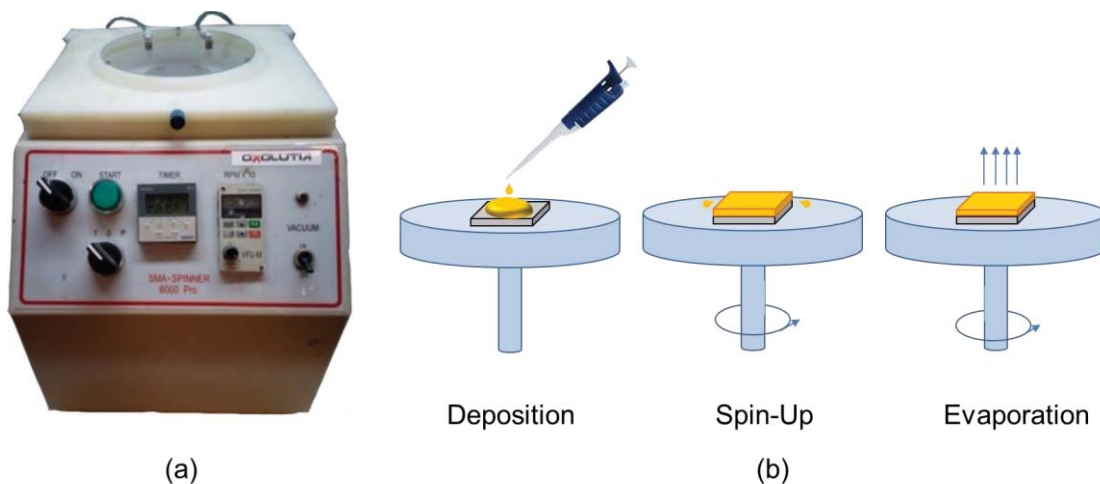


Figure 26. (a) Spin-coater SMA SPINNER 6000 Pro used in this work. (b) Steps involved in deposition: (1) dispense of the coating solution, (2) fluid flow dominated thinning, and (3) solvent evaporation and coating “set”.

Spin speed is one of the most important factors in spin coating. The speed affects the degree of radial (centrifugal) force applied to the liquid solution as well as the velocity.³⁶ In particular, the high-speed spin step generally defines the final film thickness. Theoretically it was predicted for spin-coating of polymers that the film thickness would vary according to the relationship $t = A \cdot c^n \cdot \omega^m$, where t is the film thickness, c is the concentration of the solution and ω is the rotation velocity³⁷⁻³⁸. Film thickness is largely a balance between the force applied to shear the fluid solution towards the edge of the substrate and the drying rate which affects the viscosity of the solution. The viscosity increases as the solution dries, until the radial force can no longer move the solution over the surface. At this point, the film thickness will not decrease significantly with increased spin time.³⁹

The acceleration of the substrate can also affect the properties of the coated film. In some processes, 50% of the solvents in the solution will be lost due to evaporation in the first few seconds of the process.³⁹ Relatively high acceleration benefits the uniformity of the film.

The comets, environmental sensitivity, and edge effects are common defects encountered in the spin coating process.

The comets usually occur when relatively large solid particles impede the normal flow patterns of the solution on the substrate.⁴⁰ The comets can be avoided by solution filtration and substrate cleaning.

Environmental sensitivity effects are mainly caused by the humidity of the surrounding air. The PAD solutions are water based with low viscosity and relatively limited vapor pressure at room temperature, which are less sensitive to the environment and allow a uniform evaporation and a good solution spread.

In fact, for us the most difficult problem is the edge effect. Since the substrates are square, the air flow over the protruding parts (corners) will be perturbed, resulting in non-uniformity in coating thickness in the corner areas (5%~20% of the surface). These patterns occur when spin coating on a squared substrate outside the circumference of the inscribed circle, where radial uniformity is lost.⁴¹

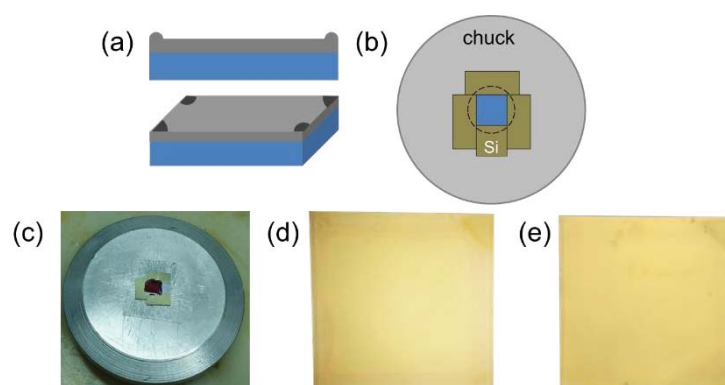


Figure 27. (a) Schematic (side view and top view) of the solution accumulation at the corners of the substrate due to the edge effect. (b) Silicon pieces "puzzle" around the substrate (in blue), to minimize the edge effect. (c) The photo of the puzzle. (d) The photo of a metal polymer film with edge effect. (e) The photo of the same sample with (d), after the thermal treatment.

Edge effect is almost inevitable in the spin-coating process on square substrates (Figure 27), especially at low speed. It makes troubles for the obtaining of precise results of further characterizations, for instance, the saturation magnetization of ferromagnetic films. A framework made of silicon pieces is used to overcome this situation, the idea is let the edge effect occurs on the framework, instead of the substrate we need. The Si pieces have the same thickness and the same length of the

shorter edge as the perovskite substrates; they are cleaned, and put in the UV/ozone cleaner to make sure the surface wettability is similar. After a tight puzzle of the substrates is mounted properly, the precursor solution is dropped on top of it, covers the whole perovskite substrate, and part of Si framework. The schematics of the Si puzzle are shown in Figure 27 (b) and (c). A metal polymer film with an upper right corner is shown in Figure 27 (d). A very important condition is that all the pieces in the puzzle should be on the same plane. This method cannot produce a perfect film every time, but improves a lot reducing the edge effects. The Si pieces used are also substrate grade with super high quality, they are chosen just for its low price compared with the perovskite substrates.

3.5 Thermal treatment

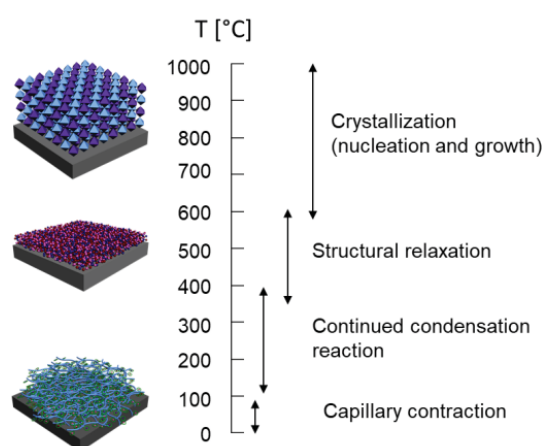


Figure 28. Approximate temperature ranges for processes contributing to densification and crystallization of thin films by PAD processed at moderate ramp rates ($\sim 5\text{--}50$ °C/min).⁴²

Following deposition by spin coating, the film may be described as a viscoelastic solid consisting of a polymer network with bound metal ions (the skeleton) and some residual water in the film. Both the organics and the water must be removed from the film prior to conversion to the crystalline state. This requires significant structural rearrangement, which occurs through a variety of chemical and physical processes at a variety of length scales over a range of temperatures. The processes involved in the transformation from the as-deposited into the crystalline state, as well as typical temperature ranges in which they occur, are illustrated in Figure 28. The process could

be roughly divided into decomposition of organics (<600 °C) and crystallization of metal oxides (700-1000 °C) with some overlaps. In practice, the thermal treatment is performed in a tube oven with O₂ flux. As described in the TG/DTA analysis of LSMO precursor, the polymers decompose completely above 550 °C. In the case of films, at this temperature, the organics are removed from the M-O-M backbone, and the amorphous network condenses with 90% weight loss or more. As the temperature increases above 600 °C, the structural rearranges with concomitant decrease in the free energy of the material. After crystallization at high temperature (700-1000 °C) with dwell time, the perovskite phase stabilizes in the cooling process. Various other factors, such as substrate, ramp rate, heat treatment atmosphere, film thickness, and film composition may each impact the temperature regime in which the processes noted in Figure 28 will occur. The extent of overlap of these processes, film crystallization behavior, microstructure, orientation and epitaxial growth are all influenced by these parameters.

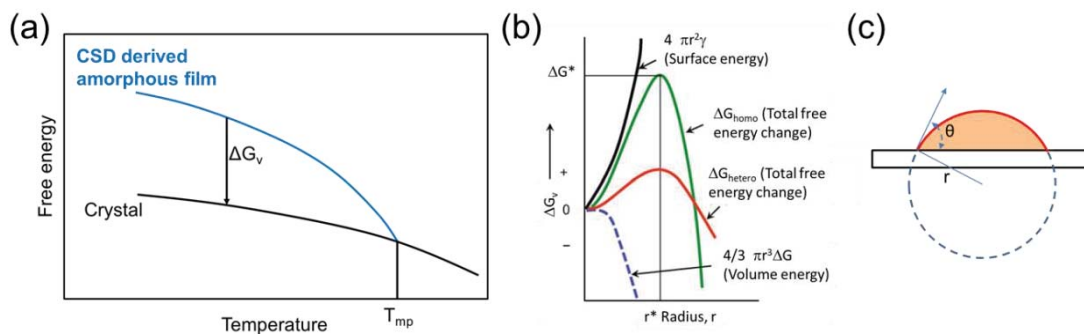


Figure 29. (a) Schematic of free energy vs. temperature for crystalline and chemically derived amorphous materials. Also indicated is the thermodynamic driving force for the transformation, ΔG_v . (Adapted from ref. ⁴³⁻⁴⁴) (b) Volume and surface energy contributions to the barriers for homogeneous and heterogeneous nucleation.⁹ (c) Schematic representation of the liquid-drop model used for the calculation of the Gibbs free energy.

The decomposition behavior has been discussed above. The other important step is the crystallization. The free energy map of free energy vs. temperature has been used to understand the crystallization behavior of PAD thin films. This process starts with amorphous oxide film, ends up with crystalline perovskite. Since there is no special theory for PAD process, the crystallization behavior of sol-gel process is used here (see

Figure 29). Figure 29 (a) shows that the free energy of the CSD amorphous thin film is greater than that of the crystalline state. The difference in the free energy between the amorphous film and the crystallized thin film is ΔG_v (volumetric free energy; J/m³). The driving force associated with the nucleation of the crystalline phase is dependent on both the crystallization temperature and the free energy of the amorphous state. Chemical, physical and structural factors can each contribute to the free energy of the film.

The phase transformation in the films is described by using the classic nucleation and growth theory. The governing equation for homogeneous nucleation of a spherical crystalline nucleus (Figure 29 (c)), with radius 'r', in a uniform amorphous host is given by:

$$\Delta G = -\frac{4}{3}\pi r^3 \Delta G_v + 4\pi r^2 \gamma \quad \text{Eq. 10}$$

where the first and second terms are known as "volume" and "surface" free energy, respectively. ΔG_v , the Gibbs free energy per unit volume, is the driving force for crystallization, which is the difference in the free energies of the amorphous and crystalline states, and γ is the surface energy per unit area associated with the formation of the nucleus.

Figure 29 (b) shows the change in the volume, surface and total free energy as a function of the radius of the nucleus. It can be seen that there exists a critical radius (r^*) below which the newly formed nucleus is not stable, while for $r > r^*$, the nucleus is stable and continues to grow. The energy barrier, ΔG^* , that the nucleation process must overcome to form a stable nucleus is given by:

$$\Delta G^* = \frac{16\pi\gamma^3}{3(\Delta G_v)^2} \quad \text{Eq. 11}$$

In heterogeneous nucleation, the above equation may be multiplied by a contact angle term that is dependent on the surface energies of the interfaces associated with the growth surface (which for CSD films is most often the substrate), crystal and amorphous phases, as:

$$\Delta G_{hetero}^* = \Delta G^* \cdot f(\theta) \quad \text{Eq. 12}$$

$$f(\theta) = \frac{2-3\cos\theta+\cos^3\theta}{4} \quad \text{Eq. 13}$$

where, θ is the contact or wetting angle measured between crystal and the substrate surface (Figure 29 (c)). Energetically, heterogeneous nucleation will always be preferred (see Figure 29 (b)), because preferential nucleation sites, such as the substrate surface, impurity phases or grain boundaries require less energy due to a lower effective surface energy.

The free energies of the amorphous and crystalline states, and γ are related to the composition and structure of the film and substrate. Once the precursor solution and the substrate are chosen, the most important parameter for the driving force ΔG_v is the temperature.

In the context of thermal treatment of CSD films, Vila-Funqueiriño et al. prepared $\text{La}_{0.92}\text{MnO}_3$ and $\text{La}_{0.7}\text{Sr}_{0.3}\text{MnO}_3$ films on STO by PAD at 950 °C, in air.^{5, 45-47} Xie et al. prepared $\text{La}_{0.9}\text{MnO}_3$ films on LAO at 700 - 1000 °C, in air, found that the films grown at 800 - 950 °C showed higher metal-insulator transition temperatures and lower resistance⁴⁸. Jain et al. prepared $\text{La}_{0.67}\text{Sr}_{0.33}\text{MnO}_3$ films on LAO by PAD at 750, 850, and 950 °C, in oxygen atmosphere. The results showed that as the annealing temperature was increased to 950°C, the homogeneity in the film improves, resulting in a sharper transition in $M-T$ curves.⁴⁹⁻⁵⁰ Jian et al. prepared $\text{La}_{0.7}\text{Sr}_{0.3}\text{MnO}_3$ films on LAO by CSD at 1000 °C, in O_2 atmosphere. The solution was prepared with metal-acetate and propionic acid was used as solvent.⁵¹ Hasenkox et al. prepared $\text{La}_{0.7}\text{Sr}_{0.3}\text{MnO}_3$, films on LAO by CSD at 850 °C, in oxygen atmosphere. The solution was prepared by dissolving metal propionates of La, Sr, Ca and Mn in propionic acid.⁵² Hassini et al. prepared $\text{La}_{0.7}\text{Sr}_{0.3}\text{MnO}_3$ films on STO by CSD at 900-1000 °C. The solution was prepared with metal propionates of La, Sr, Ca and Mn, the solvent was propionic acid. The results showed that good physical properties were achieved above annealing temperatures of 900 °C.⁵³ Xie et al. prepared $\text{La}_2\text{NiMnO}_6$ films on LAO by PAD at 900 °C, in air.⁵⁴

Most of the thermal treatments are carried out in air or O_2 flux, the oxidizing atmosphere is very important for the valence of the B site in the perovskite. The inert or reducing gases are also used to investigate the effects of the atmosphere on the structure and properties of the film. Nasui et al. prepared $\text{La}_{0.66}\text{Sr}_{0.33}\text{MnO}_3$ films on

STO by CSD in O₂ and air. The T_C of the LSMO thin films is about 320 K and 350 K for the films annealed in oxygen and air, respectively.⁵⁴ Wang et al. prepared polycrystalline La₂NiMnO₆ films on LAO by CSD at 900 °C for 2h in different atmosphere. The solution was prepared with metal acetate of La, Ni, and Mn, propionic acid was used as chelating agent and butyl alcohol was used as solvent. The T_C of the LNMO films annealed in O₂, air and N₂ are 277 K, 268 K, and 132 K, respectively.⁵⁵

Another important parameter is the heating ramp. Two kinds of ramps were used in this thesis, the conventional annealing (≤ 15 °C/min) and rapid thermal annealing (≥ 20 °C/s) (Figure 30).

At slow heating ramps, specimens are gradually heated up, and thus, removal of organic species and crystallization take place at significantly separated temperatures (Figure 28). In practice, a step at 350-500 °C was set for the decomposition of the organics for the conventional annealing process (Figure 30 (a)). The ramps are less than 15 °C/min, the most used ramp is 2 °C/min. The crystallization will not start until the organics are decomposed completely; the final decomposition temperature is very close to the crystallization temperature, with a slow heating ramp, the process is very close to thermodynamic equilibrium conditions, which is beneficial for the high crystallinity¹² and B-site ordering.

Higher ramp rates tend to delay structural changes to higher temperature, the temperature regime over which organic removal, densification and crystallization processes occur is further compressed. RTA can facilitate densification prior to the onset of crystallization,⁹ and the nucleation occurs at high temperature in a situation similar to that of isothermal annealing, which leads to a more homogeneous texture and grain size distribution.⁵⁶ Additionally, short dwell time at high temperature may avoid segregations and the possible diffusion reactions between films and substrate.⁵⁷

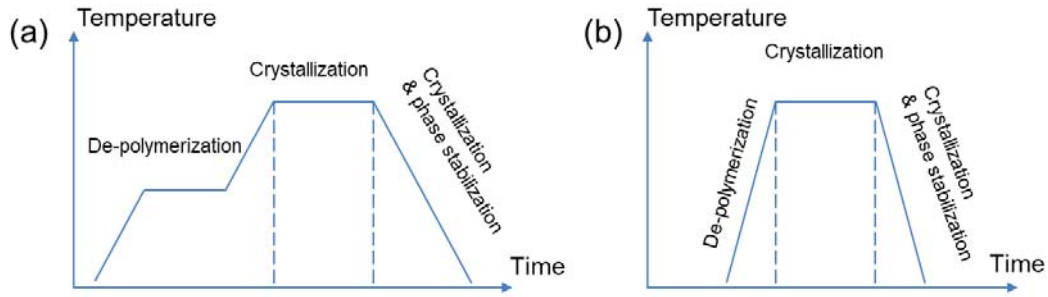


Figure 30. (a) Schematic drawing of the thermal treatment profile used in the PAD process. Polymer PEI is depolymerized at a temperature 350 - 500 °C. Oxides crystallize at 700 - 1000 °C. Heat and cooling ramps are less than 15 °C/min. (b) Rapid thermal annealing profile. Heat and cooling ramps are higher than 20 °C/s. The organic removal, densification and crystallization processes are compressed to high temperature at 700 - 1000 °C.

3.6. Structural characterization and magnetic properties

3.6.1 X-ray thin films characterization

X-ray diffraction and reflectivity are very useful techniques for the structural characterization of thin films. Different type of experimental setups, including θ - 2θ scans, rocking curve measurements, reciprocal space map, and reflectivity allow obtaining valuable information regarding the structural features of the films. θ - 2θ scans provide information about the composition; the orientation and the lattice mismatch between the film and the substrate and therefore provide information regarding structural strain and stress. Rocking curves are used to determine the crystalline perfection, the strain inside the film, the type and parameter of defects, and the sharpness of the interface between the film and the substrate. Reciprocal space maps (RSM) provide information about the tilt, strain, mismatch, and relaxation. X-ray reflectivity (XRR) measurements provide information about thickness, roughness, and density of the films.

The structural properties of the epitaxial films were studied by X-ray diffraction and reflectivity using a D5000 (Siemens) diffractometer, an X'Pert MRD (PANalytical) four-angle diffractometer with monochromatic Cu- $K_{\alpha 1}$ radiation (1.54060 Å) and a Bruker D8 Advance GADDS system.

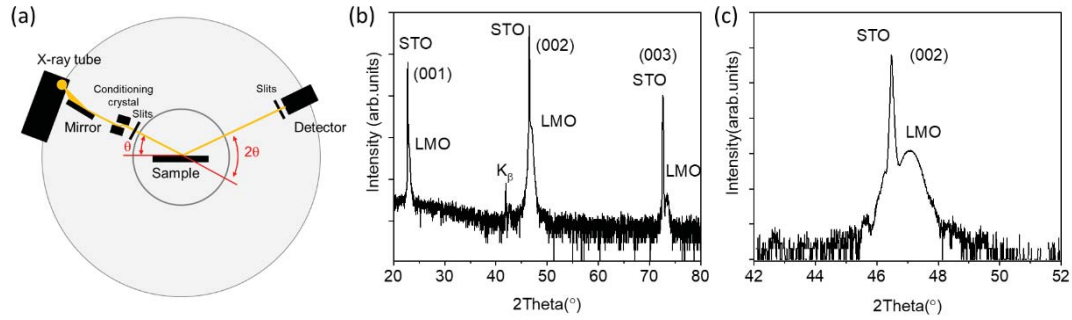


Figure 31. (a) Bragg-Brentano ($\theta-2\theta$) geometry. The X-ray tube is fixed, the sample and detector rotate. (b) $\theta-2\theta$ scan of the $\text{La}_{0.92}\text{MnO}_3$ thin film (22 nm) on a STO substrate. (c) Details of the $\theta-2\theta$ scan around the (002) STO

The X-ray diffraction measurement is based on the Bragg's law:

$$\lambda = 2d \sin \theta \quad \text{Eq. 14}$$

where λ is the wavelength of the incident X-ray, d is the distance between each adjacent crystal layer, and θ is the angle between the incident X-ray and the sample surface.

A $\theta-2\theta$ instrumental setup is shown in Figure 31 (a). The sample is mounted on the holder in the center of the instrument, the X-ray tube is fixed, the sample and the detector rotate. The sample-detector distance R is kept constant in the scan to avoid affecting the scattered intensity. If the angle between the incident beam and the sample surface is defined as θ_{in} , and the angle between the scattered beam and the sample surface is defined as θ_{out} , then during the whole scan, $\theta_{in} = \theta_{out}$. The angle between the scattered beam and the extended incident beam is 2θ , that's why the measurement procedure is called $\theta-2\theta$ scan. The detector measures the intensity of the scattered beam throughout the scan. The results are typically presented as a function of photon intensity versus 2θ .

The usual $\theta-2\theta$ ranges used in this thesis are from 20° to 80° , and from 42° to 52° (Figure 31 (b), (c)). Figure 31 (b) demonstrate that LMO thin film is in a single phase with only (001) peaks. Figure 31 (c) shows the detail of (002) reflection peak.

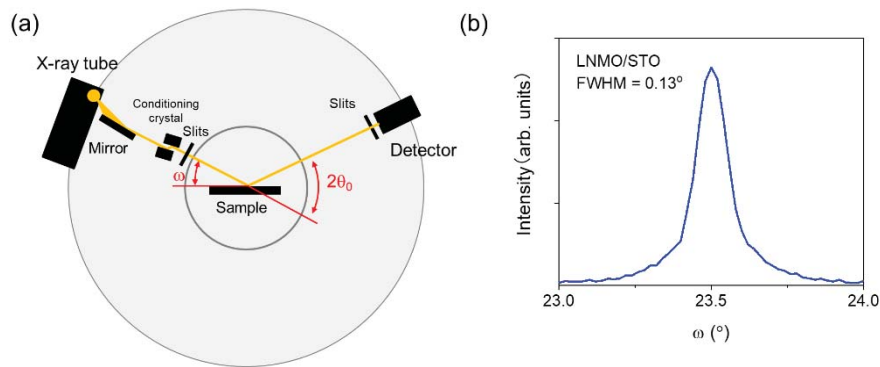


Figure 32. (a) A schematic representation of the setup of the rocking curve imaging. The sample is tilted while the detector is set in an angle (only ω changes). (b) The rocking curve obtained around the (002) reflection of LNMO/STO film (20 nm) exhibiting a FWHM=0.13°.

A rocking curve, or ω scan, consists in a ω (incidence angle) scan around a fixed $2\theta_0$ value (diffraction angle) of a particularly intense peak (usually those oriented to the substrate with a low index value), while the sample is tilted on the θ circle (“rocked”) in the vicinity of the Bragg angle θ_0 . In this configuration ω is decoupled to θ . The result is a plot of X-ray intensity versus ω . It provides information about the degree of crystallinity, texture, and mosaicity, attending to the Full Width at Half Maximum (FWHM). The lower the FWHM value the higher the film crystallinity; for single-crystals the FWHM value is usually less than 0.1°. A broadening of the curve can be related to the presence of mosaicity, dislocation, or curvature in the sample. The Figure 32 (b) shows the rocking curve of a LNMO/STO film, with a FWHM value of 0.13°. This relatively small FWHM value indicates that the grown film has a good crystallinity with some mosaicity.

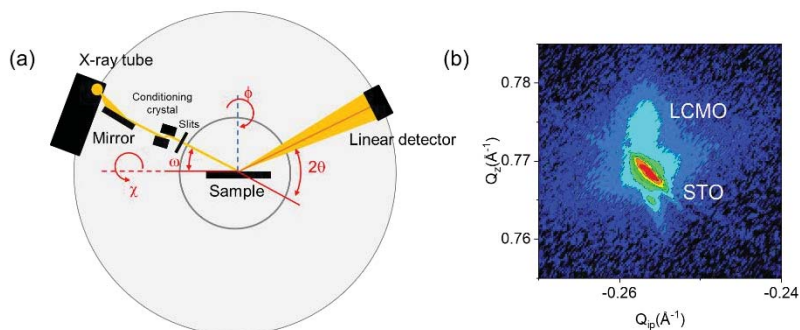


Figure 33. RSM configuration. (a) Schematic view of a four-axes diffractometer with a linear detector (1D). (b) Reciprocal space map around (103) reflections for LCMO/STO film (20 nm).

A reciprocal space map (RSM) consists in performing various rocking curves with increasing scattering angle 2θ , or makes use of successive radial scans and map directly in reciprocal space. To get information about the lattice parameters, the scan axis must be changed from θ and ω to the wave vectors parallel to the surface Q_x and perpendicular to the surface Q_z with the following relations:⁵⁸

$$Q_x = \frac{2\pi}{\lambda} [\cos(\theta - \omega) - \cos(\theta + \omega)] \quad \text{Eq. 15}$$

$$Q_z = \frac{2\pi}{\lambda} [\sin(\theta - \omega) + \cos(\theta + \omega)] \quad \text{Eq. 16}$$

where Q_x and Q_z are the equivalent reciprocal space distances on the equivalent real space distances.

Absolute values of in-plane a , and out of plane parameter c can be extracted from the position of the peak, again corrected by a ω and θ shift deduced from the substrate peaks with:

$$a = \frac{h}{Q_x} \quad \text{Eq. 17}$$

$$c = \frac{l}{Q_z} \quad \text{Eq. 18}$$

where h and l are the Miller reflection indexes of the peak.

Typical RSM were scanned around the (103) reflections of substrate and films. The coordinates system is oriented with the horizontal axis, $Q_x//[100]$, parallel to the substrate interface and the vertical axis, $Q_z//[010]$, perpendicular to the substrate.

Figure 33 (b) shows the reciprocal space map around (103) reflections for a LCMO film on STO. It reveals that the film is fully strained without any measurable difference of the in-plane lattice parameters.

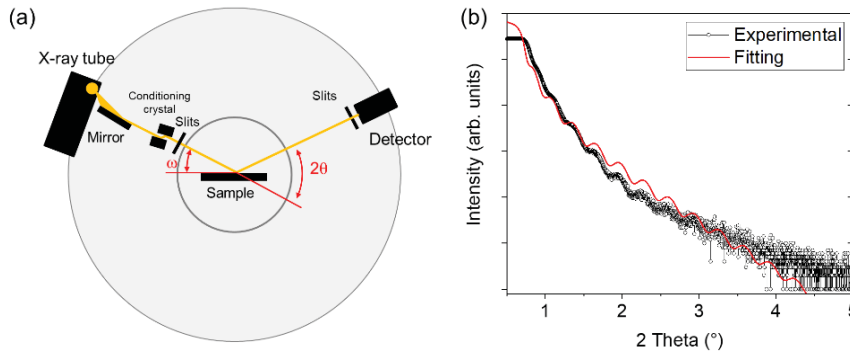


Figure 34. (a) A schematic representation of the setup of the XRR. 2θ ranges from $0.5-5^\circ$. (b) XRR pattern of a $\text{La}_{0.7}\text{Sr}_{0.3}\text{MnO}_3$ (26.3 nm) film and the corresponding fit.

XRR consists in a $\omega/2\theta$ scan in symmetric configuration in a similar way to a typical $\theta/2\theta$ scan, but with much smaller 2θ angles ($0.5-5^\circ$) (Figure 34). Below a critical incidence angle θ_c (depending on the material density), the X-Rays are completely reflected leading to a total external reflection, above this critical angle the beam penetration increases and due to interference phenomena of the scattered X-rays the curve shows characteristic intensity oscillations. The period of those oscillations is related to the film thickness. The relationship between the thickness t and the distance between two adjacent fringes for $2\theta_{m+1}$ and $2\theta_m$ is:⁵⁹

$$2\theta_{m+1} - 2\theta_m \approx \lambda/t \quad \text{Eq. 19}$$

where m is an index to each oscillation maximum.

The Figure 34 (b) shows the XRR pattern from 0.5° to 5° , of a $\text{La}_{0.7}\text{Sr}_{0.3}\text{MnO}_3$ film, which extracted thickness was 26.3 nm, the data was fitted by the program GenX 2.3.5. In practice, the XRR works when the RMS value is less than 5 nm.

3.6.2 Atomic force microscopy

Atomic force microscopy (AFM) is a powerful technique for characterizing surface topography properties of materials within a range from few nanometers to few micrometers. In this thesis AFM experiments have been performed in thin films in the range 4-80 nm with an MFP-3D Asylum Research AFM (Oxford Instruments).

The basic components include a stand AFM head, an X-Y scanner, and a base, shown in Figure 35 (a). All these components are connected to the controller and computer.⁶⁰

The base is the metal plate on which the head and scanner sit. It contains critical signal conditioning electronics for the scanner and acts as the electronic hub for connecting the controller to the scanner and head. The X-Y scanner holds the sample and scans it laterally in X and Y beneath the tip. It contains piezoelectric actuators, flexure based translations stages, and high resolution position sensors. The head holds the cantilever chip and contains the optical lever detection system, and electronics and the vertical (Z) motion actuator and sensor. In short, it moves the cantilever vertically as the sample moves laterally beneath it. It also contains optics for illuminating and optically imaging the sample and cantilever from above.

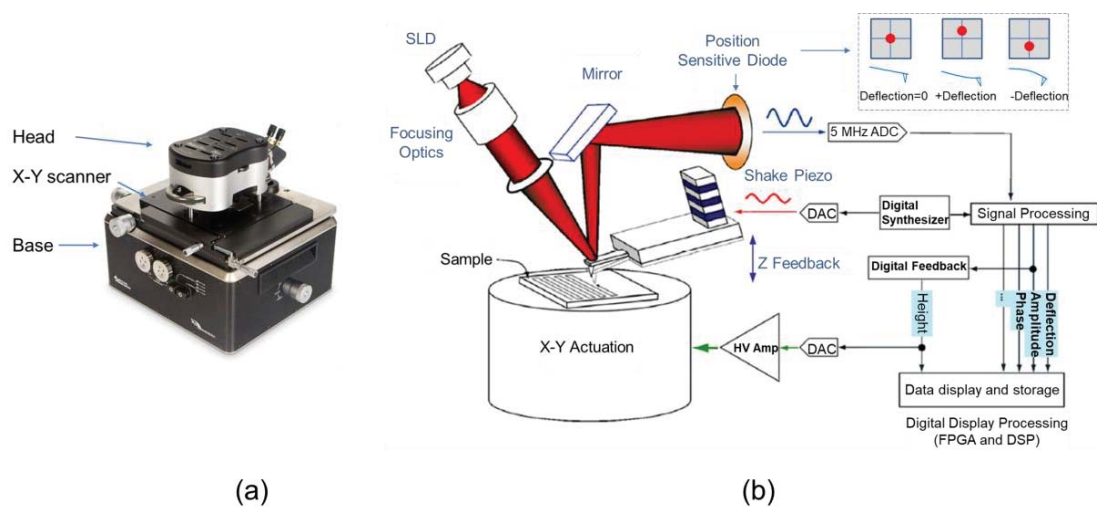


Figure 35. (a) Basic AFM Components, (b) Simplified schematic of MFP-3D system.⁶⁰

All the AFM images in this thesis were measured in non-contact mode, the cantilever is used as a mechanical resonator and brought to oscillate very close (~ 12 nm) to the surface, the mechanical interaction between the cantilever tip and the sample is exploited to yield surface topography. Inside the head, the optical lever detection (Figure 35 (b)) is used to sense the force on the cantilever. Optical techniques are used to measure the bending of a flexible cantilever as it responds to mechanical interactions with the surface of the film. An SLD (super luminescent diode) shines onto the back of the reflective cantilever which is mounted at roughly eleven degrees with respect to the sample plane. A lens focuses the light beam from the SLD at the lever. The light reflects off the cantilever and up to a re-collimation lens and mirror to the

position sensitive detector. The measured cantilever deflection is used to generate the topographical image of the sample surface.

During the scanning process, the movements of the sample in X-Y direction is recorded with the X-Y scanner, the head records the height data of the surface, namely, the AFM scans over a sample and maps out the surface topography in three dimensions. The AFM system can plot 3D images of the surface of the sample, and calculate the surface roughness. The roughness typically expressed by the root mean square (RMS). RMS is the square root of the distribution of surface height; it describes the finish of optical surfaces.

The AFM topography images of LMO films displayed in Figure 36 show flat surfaces with an RMS surface roughness value of <1 nm, thus indicating that the samples have a high microstructural quality. The terrace-like morphology imposed by the conformal growth on top of the substrate steps.

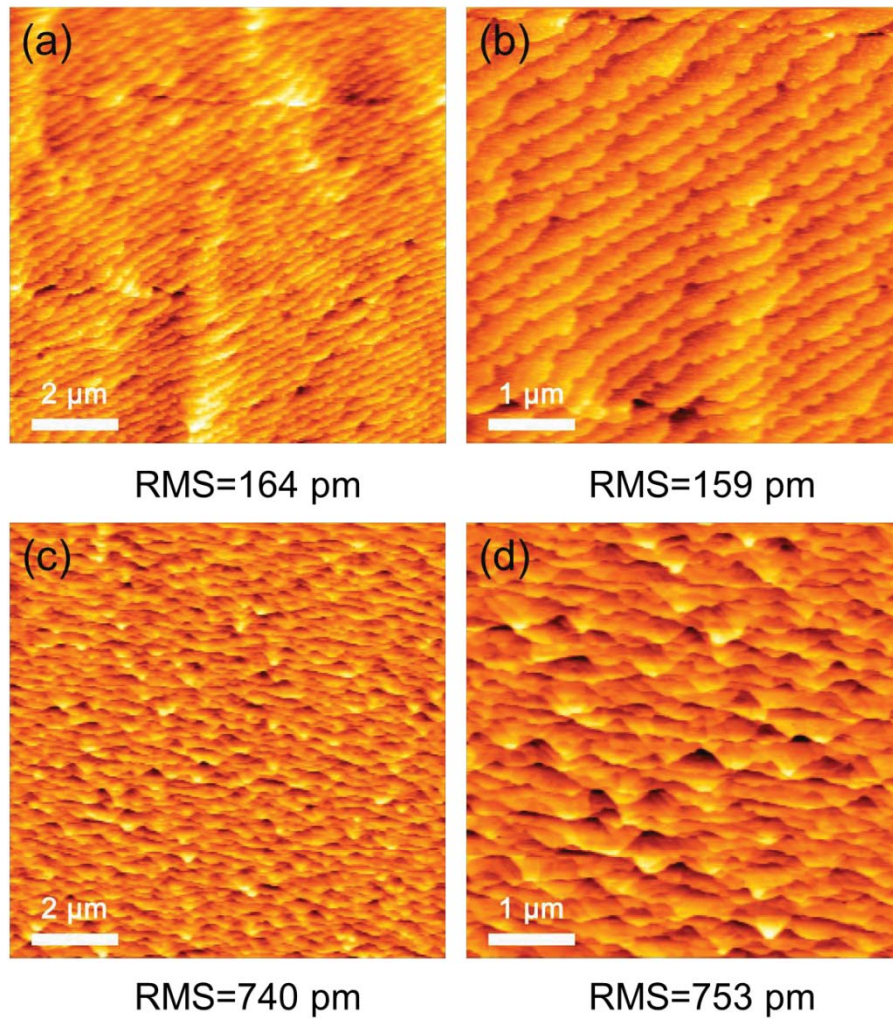


Figure 36. Atomic force microscopy surface topography images ($10 \times 10 \mu\text{m}^2$, and $5 \times 5 \mu\text{m}^2$) of representative $\text{La}_{0.92}\text{MnO}_3$ thin film samples on top of STO substrates with different thicknesses. Films thermally treated in conventional annealing conditions, $2 \text{ }^\circ\text{C}/\text{min}$ heating ramp, dwell time 60 min at $990 \text{ }^\circ\text{C}$ with an oxygen flow of $0.1 \text{ l}/\text{min}$. (a) and (b), 10 nm thick film; (c) and (d), 23 nm thick film.

3.6.3 Magnetic properties characterization

Magnetization measurements were performed using Magnetic Property Measurement System (MPMS XL-7T) from Quantum Design, with a radio frequency superconducting quantum interference device (RF SQUID) (Figure 37). The temperature is controlled with combination of cold helium gas, and heaters, the temperature range is from 2 K to 400 K. The external axial magnetic field, from -7 Tesla to +7 Tesla, is provided by a superconducting solenoid.

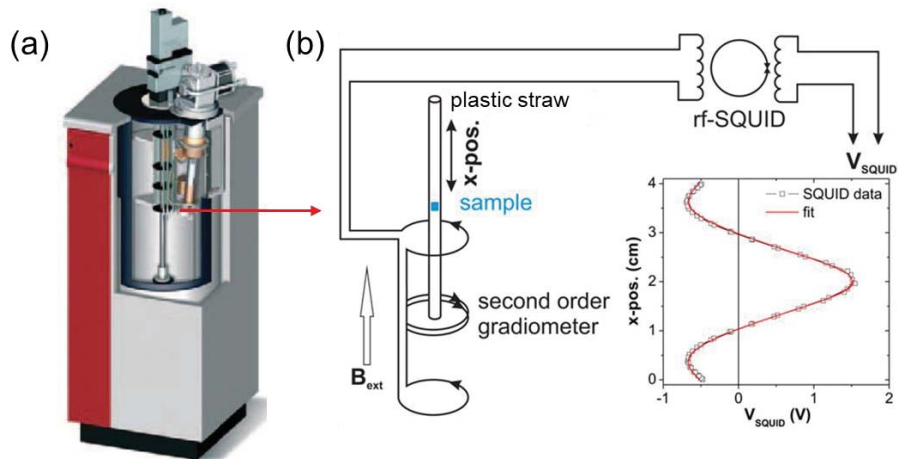


Figure 37. (a) MPMS XL-7T system, (b) Schematic setup of a SQUID magnetometer with 2nd order gradiometer. The inset shows the SQUID response V_{SQUID} versus sample position ($x\text{-pos.}$)⁶¹.

SQUID magnetometers usually detect the change of magnetic flux created by mechanically moving the sample through a superconducting pick-up coil which is converted to a voltage V_{SQUID} . For the MPMS, the position is denoted as the x direction which is parallel to the external magnetic field B_{ext} so that one obtains raw data where V_{SQUID} is plotted versus $x\text{-pos.}$ as shown in Figure 37 (b). To suppress the influence of all kinds of external magnetic fields, the pick-up coils are made with a configuration of second order gradiometer. The entire detection system is sketched in Figure 37 (b) and the inset exemplarily shows a single SQUID scan where the maximum of V_{SQUID} at $x\text{-pos.}$ of 2 cm corresponds to the sample directly positioned in-between the double coil of the pick-up gradiometer. The output data contains temperature, field, and moment, which can be calculated and give the relationship of magnetization vs. field and magnetization vs. temperature. The signal for thin films is generally weak (of the order of 10^{-5} emu) with a diamagnetic contribution coming from the substrate which is not negligible. When measuring hysteresis loops, the diamagnetic contribution gives a negative slope at high magnetic fields. This slope should be subtracted by adjusting the slope of the cycle at high fields.

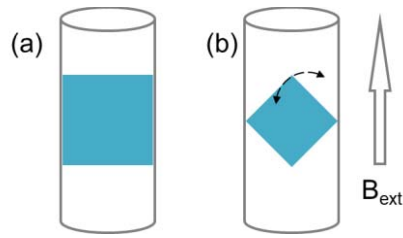


Figure 38. Sketch of a low-background sample mounting inside a transparent disposable plastic straw. (a) Geometry if only in-plane magnetization curves are to be measured. (b) Square-shaped sample size which can be rotated from in-plane (ip) to out-of-plane (op) geometry.⁶¹

Transparent disposable plastic straws serve as sample holder where the sample is held in place by no other means than clamping it in-between the walls of the straw (see Figure 38). If the external magnetic field is parallel to the film plane, it's called in plane (IP) geometry; and when the external magnetic field is perpendicular to the film plane is the out of plane (OP) geometry.

In order to properly quantify the magnetization of a grown thin film (in units of emu/cm^3 or $\mu_B/\text{f.u.}$), it is necessary to precisely determine the volume of the film. The film thickness can be measured with XRR. However, as discussed in the spin-coating process section, some films may have some irregular corners with accumulated material on them due to the border effect. This fact will introduce large error to the volume determination.

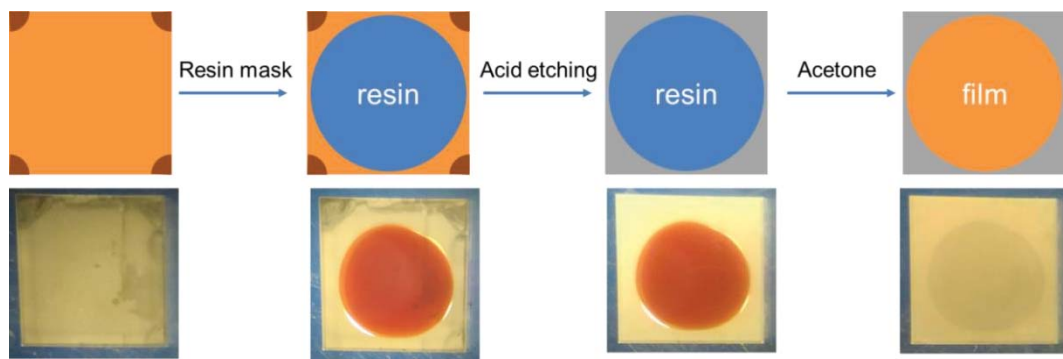


Figure 39. Piranha solution etching

In order to overcome this inconvenient, a piranha solution etching method is used to remove the corners. Figure 39 shows a schematic of the process. The piranha solution

is a mixture solution of 30% H₂O₂ and 98% H₂SO₄ with a volume ratio of 32:1. The 10% piranha water solution is enough for the etching. The piranha solution can dissolve the film, but can't hurt the substrate. A resin (Shipley 1813 photoresist) is used to protect the film. Firstly, the resin is deposited on the film with the help of a pipette, covering the uniform area of the film, and leaving the corners outside. Next the film is put in a ventilated electric oven at 120 °C for 10 minutes to cure the resin. In this way, the resin is dried and converted into a solid resistant to the piranha solution. Then the film is soaked in the 10% piranha solution for less than 1 minute, to etch away the corners without hurting the protected region of the film. After the corners were removed completely, the film is soaked in water to stop the etching. Finally, the sample is washed with acetone in an ultrasonic bath in order to remove the resin, leaving only the film part with uniform thickness. The estimated error in the volume determination of our films is around 5 - 8 %.

Two kinds of experimental procedures were used to measure *M-T* curves in this thesis. One is a simple field cooled procedure to determine the T_C , a magnetic field (ip or op) usually of 1 kOe was applied to the film while cooling from RT to 10K, and the magnetic moment of the film is measured while temperature increases from 10 K to 400 K, above the T_C . The other procedure is the well-known zero field cooling / field cooling (ZFC/FC) process. In a ZFC process, the sample is firstly cooled down from above T_C down to 10 K in zero field, then an external field of 1kOe is applied and the data are collected in the warming up process. Once the temperature is above T_C , keeping the external field constant at 1 kOe, the sample is cooled down to 10 K, and then data are collected in the warming up process. This is the so-called FC process. From the thermal dependence of ZFC/FC magnetization curves, T_C and magnetic anisotropy effect can be obtained.

Hysteresis loops were usually collected at 10 K, along the easy magnetization axis of the film, in a range field of ± 7 T. The IP/OP *M-H* loops allow determining the magnetic anisotropy of the film on different substrates.

Figure 40 shows the field cooled *M-T* curve and *M-H* loop of a 20 nm La_{0.92}MnO₃/STO film. The T_C of the film is 325 K, the M_S is 360 emu/cm³.

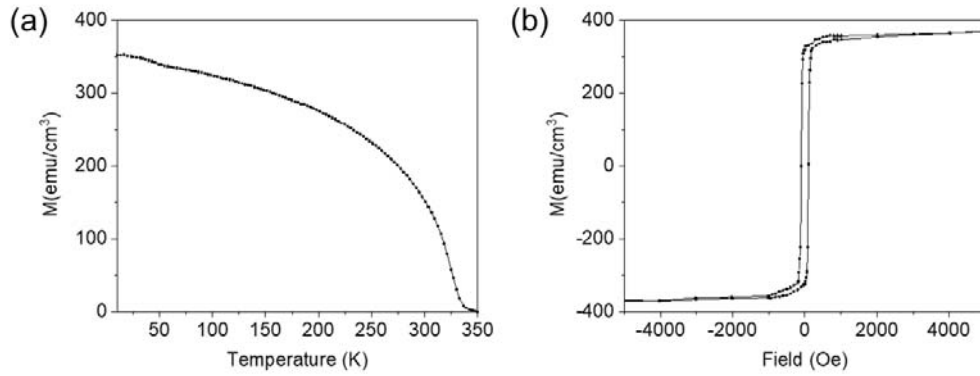


Figure 40. (a) Temperature dependence of the magnetization measured at 1 kOe (field-cooled) for a 20 nm LMO/STO film, magnetic field applied in plane. (b) M - H loop of the same LMO/STO film measured at 10 K, magnetic field applied in plane. The film was grown at 990 °C for 60 min in air.

3.6.4 Electric transport measurements

Electric transport measurements on the films have been performed using a Physical Property Measurement System (PPMS) from Quantum Design. The four corners of the film are connected to a standard puck for PPMS with silver paint and silver wires. The four-point contact configuration allows avoiding the contribution of contact resistivity. The four contacts were connected to 2 channels of the puck with 8 silver wires at the same time; see Figure 41 (a). Firstly, the current is applied to channel 1 through 2 contacts (C and D) and voltage is measured on the other 2 (A and B). Then, a second measurement is performed by applying current to channel 2 through 2 other contacts (A and D) and voltage is measured on the remaining ones (B and C).

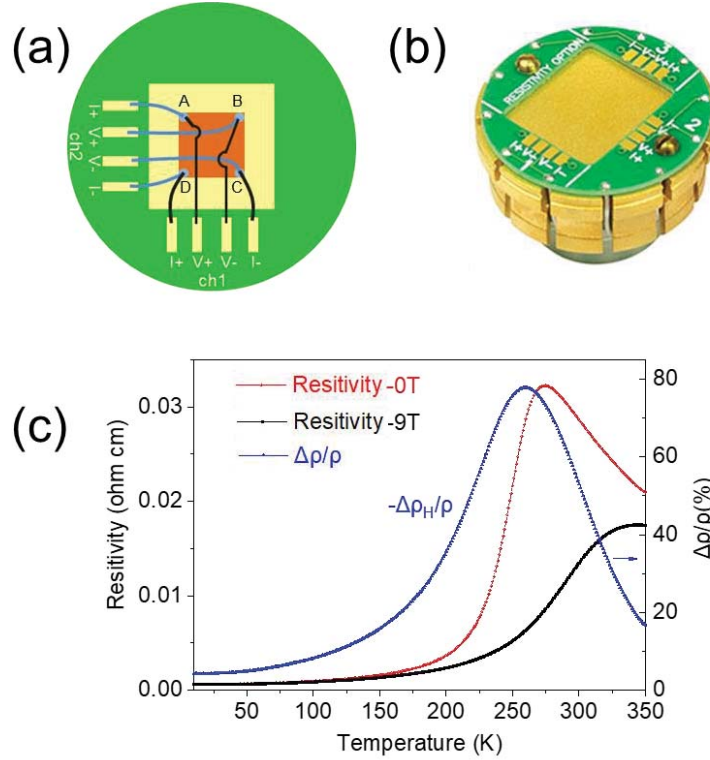


Figure 41. (a) Van der Pauw configuration employed to perform resistivity measurements, (b) Standard puck for DC resistance measurement, (c) Resistivity vs temperature curves of a 10.8 nm $\text{La}_{0.92}\text{MnO}_3$ film on LAO, measures at 0T and 9T and the extracted magnetoresistance curve

The film resistivity is calculated with the following van der Pauw method,⁶²

$$\rho = \frac{\pi t}{\ln 2} \frac{R_{ch1} + R_{ch2}}{2} f \quad \text{Eq. 20}$$

where $R_{ch1} = (V_A - V_B) / I_{CD}$ and $R_{ch2} = (V_B - V_C) / I_{AD}$ are the resistances for the 2 measurements, t is the thickness of the sample, and f is the multiplying factor between 0 and 1 and depends on the ratio $\frac{R_{ch1}}{R_{ch2}}$.

The resistivity is always measured from 10 K to a temperature higher than T_C , with a field of 9 T or with zero field. The magnetoresistance value is given by:

$$\%MR = \frac{\rho(H) - \rho(0)}{\rho(0)} \times 100 \quad \text{Eq. 21}$$

Figure 41 (c) shows the resistivity versus temperature curves of a 10.8 nm $\text{La}_{0.92}\text{MnO}_3$ film on LAO, measured at 0 T and 9 T. The magnetoresistance value is 77% at the metal-insulator transition temperature, near 250 K.

References

- [1] Jia, Q. X.; McCleskey, T. M.; Burrell, A. K.; Lin, Y.; Collis, G. E.; Wang, H.; Li, A. D.; Foltyn, S. R. Polymer-assisted deposition of metal-oxide films. *Nat. Mater.* **2004**, *3* (8), 529-532.
- [2] Schneller, T.; Waser, R.; Kosec, M.; Payne, D. Chemical Solution Deposition of Functional Oxide Thin Films. Springer-Verlag Wien: 2013; pp 1-796.
- [3] Burrell, A. K.; Mark McCleskey, T.; Jia, Q. X. Polymer assisted deposition. *Chem. Commun.* **2008**, (11), 1271-1277.
- [4] Zou, G. F.; Zhao, J.; Luo, H. M.; McCleskey, T. M.; Burrell, A. K.; Jia, Q. X. Polymer-assisted-deposition: a chemical solution route for a wide range of materials. *Chem. Soc. Rev.* **2013**, *42* (2), 439-449.
- [5] Vila-Fungueiriño, J. M.; Rivas-Murias, B.; Rodríguez-González, B.; Txoperena, O.; Ciudad, D.; Hueso, L. E.; Lazzari, M.; Rivadulla, F. Room-Temperature Ferromagnetism in Thin Films of LaMnO₃ Deposited by a Chemical Method Over Large Areas. *ACS Appl. Mater. Interfaces* **2015**, *7* (9), 5410-5414.
- [6] Yakubovich, Y. Y.; Alekseev, V. G. Hydrolysis constants of tervalent lanthanum and lanthanide ions in 0.1 M KNO₃ solution. *Russ. J. Inorg. Chem.* **2012**, *57* (6), 911-915.
- [7] Perrin, D. D. 421. The hydrolysis of manganese (II) ion. *J. Chem. Soc.* **1962**, (0), 2197-2200.
- [8] McCleskey, T. M.; Shi, P.; Bauer, E.; Highland, M. J.; Eastman, J. A.; Bi, Z. X.; Fuoss, P. H.; Baldo, P. M.; Ren, W.; Scott, B. L.; Burrell, A. K.; Jia, Q. X. Nucleation and growth of epitaxial metal-oxide films based on polymer-assisted deposition. *Chem. Soc. Rev.* **2014**, *43* (7), 2141-2146.
- [9] Schwartz, R. W.; Schneller, T.; Waser, R. Chemical solution deposition of electronic oxide films. *C. R. Chim.* **2004**, *7* (5), 433-461.
- [10] Martell, A. E.; Motekaitis, R. J.; Fried, A. R.; Wilson, J. S.; MacMillan, D. T. Thermal Decomposition of EDTA, NTA, and Nitrilotrimethylenephosphonic Acid in Aqueous Solution. *Can. J. Chem.* **1975**, *53* (22), 3471-3476.
- [11] Motekaitis, R. J.; Cox Iii, X. B.; Taylor, P.; Martell, A. E.; Miles, B.; Tvedt Jr, T. J. Thermal degradation of EDTA chelates in aqueous solution. *Can. J. Chem.* **1982**, *60* (10), 1207-1213.
- [12] Vila-Fungueiriño, J. M.; Rivas-Murias, B.; Rubio-Zuazo, J.; Carretero-Genevri, A.; Lazzari, M.; Rivadulla, F. Polymer assisted deposition of epitaxial oxide thin films. *J. Mater. Chem. C* **2018**, *6* (15), 3834-3844.
- [13] Biswas, A.; Yang, C.-H.; Ramesh, R.; Jeong, Y. H. Atomically flat single terminated oxide substrate surfaces. *Prog. Surf. Sci.* **2017**, *92* (2), 117-141.

- [14] Kim, M. K.; Moon, J. Y.; Choi, H. Y.; Oh, S. H.; Lee, N.; Choi, Y. J. Investigation of the magnetic properties in double perovskite R_2CoMnO_6 single crystals (R = rare earth: La to Lu). *J. Phys. Condens. Matter.* **2015**, *27* (42), 426002.
- [15] Guo, H.; Burgess, J.; Street, S.; Gupta, A.; Calvarese, T. G.; Subramanian, M. A. Growth of epitaxial thin films of the ordered double perovskite La_2NiMnO_6 on different substrates. *Appl. Phys. Lett.* **2006**, *89* (2), 022509.
- [16] Detemple, E.; Ramasse, Q. M.; Sigle, W.; Cristiani, G.; Habermeier, H.-U.; Benckiser, E.; Boris, A. V.; Frano, A.; Wochner, P.; Wu, M.; Keimer, B.; Aken, P. A. v. Polarity-driven nickel oxide precipitation in $LaNiO_3$ - $LaAlO_3$ superlattices. *Appl. Phys. Lett.* **2011**, *99* (21), 211903.
- [17] Gazquez, J.; Bose, S.; Sharma, M.; Torija, M. A.; Pennycook, S. J.; Leighton, C.; Varela, M. Lattice mismatch accommodation via oxygen vacancy ordering in epitaxial $La_{0.5}Sr_{0.5}CoO_{3-\delta}$ thin films. *APL Mater.* **2013**, *1* (1), 012105.
- [18] Kotomin, E. A.; Evarestov, R. A.; Mastrikov, Y. A.; Maier, J. DFT plane wave calculations of the atomic and electronic structure of $LaMnO_3$ (001) surface. *Physical Chemistry Chemical Physics* **2005**, *7* (11), 2346-2350.
- [19] Lebedev, O. I.; Verbeeck, J.; Van Tendeloo, G.; Dubourdieu, C.; Rosina, M.; Chaudouët, P. Structure and properties of artificial $[(La_{0.7}Sr_{0.3}MnO_3)_m(SrTiO_3)_n]_{15}$ superlattices on (001) $SrTiO_3$. *J. Appl. Phys.* **2003**, *94* (12), 7646-7656.
- [20] Wang, J. J.; Meng, F. Y.; Ma, X. Q.; Xu, M. X.; Chen, L. Q. Lattice, elastic, polarization, and electrostrictive properties of $BaTiO_3$ from first-principles. *J. Appl. Phys.* **2010**, *108* (3), 034107.
- [21] Vaillionis, A.; Boschker, H.; Siemons, W.; Houwman, E. P.; Blank, D. H. A.; Rijnders, G.; Koster, G. Misfit strain accommodation in epitaxial ABO_3 perovskites: Lattice rotations and lattice modulations. *Phys. Rev. B* **2011**, *83* (6), 064101.
- [22] Kleibeuker, J. E.; Koster, G.; Siemons, W.; Dubbink, D.; Kuiper, B.; Blok, J. L.; Yang, C.-H.; Ravichandran, J.; Ramesh, R.; ten Elshof, J. E.; Blank, D. H. A.; Rijnders, G. Atomically Defined Rare-Earth Scandate Crystal Surfaces. *Adv. Funct. Mater.* **2010**, *20* (20), 3490-3496.
- [23] Kawasaki, M.; Takahashi, K.; Maeda, T.; Tsuchiya, R.; Shinohara, M.; Ishiyama, O.; Yonezawa, T.; Yoshimoto, M.; Koinuma, H. Atomic Control of the $SrTiO_3$ Crystal Surface. *Science* **1994**, *266* (5190), 1540.
- [24] Kawasaki, M.; Ohtomo, A.; Arakane, T.; Takahashi, K.; Yoshimoto, M.; Koinuma, H. Atomic control of $SrTiO_3$ surface for perfect epitaxy of perovskite oxides. *Appl. Surf. Sci.* **1996**, *107*, 102-106.

- [25] Koster, G.; Kropman, B. L.; Rijnders, G. J. H. M.; Blank, D. H. A.; Rogalla, H. Quasi-ideal strontium titanate crystal surfaces through formation of strontium hydroxide. *Appl. Phys. Lett.* **1998**, *73* (20), 2920-2922.
- [26] Koster, G.; Rijnders, G.; Blank, D. H. A.; Rogalla, H. Surface morphology determined by (001) single-crystal SrTiO₃ termination. *Physica C: Superconductivity* **2000**, *339* (4), 215-230.
- [27] Leca, V.; Rijnders, G.; Koster, G.; Blank, D. H. A.; Rogalla, H. Wet Etching Methods for Perovskite Substrates. *MRS Proceedings* **2011**, *587*, O3.6.
- [28] Zhang, J.; Dou, D.; Merz, T.; Chakhalian, J.; Kareev, M.; Liu, J.; Brillson, L. J. Depth-resolved subsurface defects in chemically etched SrTiO₃. *Appl. Phys. Lett.* **2009**, *94* (9), 092904.
- [29] Kareev, M.; Prosandeev, S.; Liu, J.; Gan, C.; Kareev, A.; Freeland, J. W.; Xiao, M.; Chakhalian, J. Atomic control and characterization of surface defect states of TiO₂ terminated SrTiO₃ single crystals. *Appl. Phys. Lett.* **2008**, *93* (6), 061909.
- [30] van der Torren, A. J. H.; van der Molen, S. J.; Aarts, J. Formation of a mixed ordered termination on the surface of LaAlO₃ (001). *Phys. Rev. B* **2015**, *91* (24), 245426.
- [31] Lanier, C. H.; Rondinelli, J. M.; Deng, B.; Kilaas, R.; Poeppelmeier, K. R.; Marks, L. D. Surface Reconstruction with a Fractional Hole: ($\sqrt{5} \times \sqrt{5}$) R 26.6 degrees LaAlO₃ (001). *Phys Rev Lett* **2007**, *98* (8), 086102.
- [32] Nelis, D.; Van Bael, M. K.; Van Den Rul, H.; Mullens, J.; Van Poucke, L. C.; Vanhoyland, G.; D'Haen, J.; Laureyn, W.; Wouters, D. J. Ferroelectric SrBi₂Nb₂O₉ Thin Films by Aqueous Chemical Solution Deposition. *Integr. Ferroelectr.* **2002**, *45* (1), 205-213.
- [33] Kern, W. *Handbook of Semiconductor Wafer Cleaning Technology: Science, Technology, and Applications*, Noyes Publications: 1993; p 623.
- [34] Wang, H.; Yu, B.; Jiang, S.; Jiang, L.; Qian, L. UV/ozone-assisted tribochemistry-induced nanofabrication on Si(100) surfaces. *RSC Adv.* **2017**, *7* (63), 39651-39656.
- [35] McIntyre, N. S.; Davidson, R. D.; Walzak, T. L.; Williston, R.; Westcott, M.; Pekarsky, A. Uses of ultraviolet/ozone for hydrocarbon removal: Applications to surfaces of complex composition or geometry. *J. Vac. Sci. Technol. A* **1991**, *9* (3), 1355-1359.
- [36] Emslie, A. G.; Bonner, F. T.; Peck, L. G. Flow of a Viscous Liquid on a Rotating Disk. *J. Appl. Phys.* **1958**, *29* (5), 858-862.
- [37] Ricote, J.; Holgado, S.; Ramos, P.; Calzada, M. L. Piezoelectric ultrathin lead titanate films prepared by deposition of aquo-diol solutions. *IEEE Trans. Ultrason. Ferroelectr. Freq. Control* **2006**, *53* (12), 2299-2304.

- [38] Walsh, C. B.; Franses, E. I. Ultrathin PMMA films spin-coated from toluene solutions. *Thin Solid Films* **2003**, *429* (1), 71-76.
- [39] Tyona, M. D. A theoretical study on spin coating technique. *Adv. Mat. Res.* **2013**, *2* (4), 195-208.
- [40] Hanaor, D. A. H.; Triani, G.; Sorrell, C. C. Morphology and photocatalytic activity of highly oriented mixed phase titanium dioxide thin films. *Surf. Coat. Technol.* **2011**, *205* (12), 3658-3664.
- [41] Carcano, G.; Ceriani, M.; Soglio, F. Spin Coating with High Viscosity Photoresist on Square Substrates — Applications in the Thin Film Hybrid Microwave Integrated Circuit Field. *Microelectron. Int.* **1993**, *10* (3), 12-20.
- [42] Schwartz, R. W.; Narayanan, M. Chemical Solution Deposition—Basic Principles. In *Solution Processing of Inorganic Materials*; Mitzi, D. B., Ed.; 2008; pp 33-76.
- [43] Larry L. Hench, D. R. U. *Science of Ceramic Chemical Processing*, Wiley: 1986; p 624.
- [44] Roy, R. Gel Route to Homogeneous Glass Preparation. *J. Am. Ceram. Soc.* **1969**, *52* (6), 344-344.
- [45] Vila-Funqueiriño, J. M.; Rivas-Murias, B.; Rodríguez-González, B.; Rivadulla, F. Interface Magnetic Coupling in Epitaxial Bilayers of $\text{La}_{0.92}\text{MnO}_3/\text{LaCoO}_3$ Prepared by Polymer-Assisted Deposition. *Chem. Mater.* **2014**, *26* (3), 1480-1484.
- [46] Vila-Funqueiriño, J. M.; Rivas-Murias, B.; Rivadulla, F. Strong interfacial magnetic coupling in epitaxial bilayers of $\text{LaCoO}_3/\text{LaMnO}_3$ prepared by chemical solution deposition. *Thin Solid Films* **2014**, *553*, 81-84.
- [47] Lucas, I.; Vila-Funqueiriño, J. M.; Jiménez-Cavero, P.; Rivas-Murias, B.; Magén, C.; Morellón, L.; Rivadulla, F. Tunnel Conduction in Epitaxial Bilayers of Ferromagnetic $\text{LaCoO}_3/\text{La}_{2/3}\text{Sr}_{1/3}\text{MnO}_3$ Deposited by a Chemical Solution Method. *ACS Appl. Mater. Interfaces* **2014**, *6* (23), 21279-21285.
- [48] Xie, C.; Shi, L.; Zhao, J.; Zhou, S.; Li, Y.; Guo, J. Insight into the enhancement of transport property for oriented $\text{La}_{0.9}\text{MnO}_3$ films. *J. Phys. D: Appl. Phys.* **2017**, *50* (20), 205306.
- [49] Jain, M.; Li, Y.; Hundley, M. F.; Hawley, M.; Maiorov, B.; Campbell, I. H.; Civale, L.; Jia, Q. X.; Shukla, P.; Burrell, A. K.; McCleskey, T. M. Magnetoresistance in polymer-assisted deposited Sr- and Ca-doped lanthanum manganite films. *Appl. Phys. Lett.* **2006**, *88* (23), 232510.
- [50] Jain, M.; Shukla, P.; Li, Y.; Hundley, M. F.; Wang, H.; Foltyn, S. R.; Burrell, A. K.; McCleskey, T. M.; Jia, Q. X. Manipulating Magnetoresistance Near Room Temperature in

- La_{0.67}Sr_{0.33}MnO₃/La_{0.67}Ca_{0.33}MnO₃ Films Prepared by Polymer Assisted Deposition. *Adv. Mater.* **2006**, *18* (20), 2695-2698.
- [51] Jian, H.; Zhang, Z.; Wang, Y.; Tang, X.; Yang, J.; Hu, L.; Chen, L.; Zhu, X.; Sun, Y. Preparation of La_{0.7}Sr_{0.3}Mn_{1+x}O_y (1 ≤ x ≤ 4) thin films by chemical solution deposition: Dual epitaxy and possible spinodal growth. *J. Alloys Compd.* **2013**, *561*, 95-100.
- [52] Hasenkox, U.; Mitze, C.; Waser, R.; Arons, R. R.; Pommer, J.; Güntherodt, G. Chemical Solution Deposition of Epitaxial La_{1-x}(Ca, Sr)_xMnO₃ Thin Films. *J. Electroceramics* **1999**, *3* (3), 255-260.
- [53] Hassini, A.; Pomar, A.; Gutiérrez, J.; Coll, M.; Romà, N.; Moreno, C.; Ruyter, A.; Puig, T.; Obradors, X. Atomically flat MOD La_{0.7}Sr_{0.3}MnO₃ buffer layers for high critical current YBa₂Cu₃O₇ TFA films. *Supercond. Sci. Technol.* **2007**, *20* (9), S230-S238.
- [54] Xie, C.; Shi, L.; Zhou, S.; Zhao, J.; Liu, H.; Li, Y.; Yao, D. Structural characteristics, magnetic properties of Re₂NiMnO₆ (Re=La, Pr, Nd, Sm, Y) thin films on (001) LaAlO₃ by simple polymer assisted deposition. *Surf. Coat. Technol.* **2015**, *277*, 222-226.
- [55] Wang, T.; Fang, X.; Dong, W.; Tao, R.; Deng, Z.; Li, D.; Zhao, Y.; Meng, G.; Zhou, S.; Zhu, X. Fabrication of polycrystalline La₂NiMnO₆ thin films on LaAlO₃ (100) substrates by chemical solution deposition. *J. Cryst. Growth* **2008**, *310* (14), 3386-3390.
- [56] Schwartz, R. W. Chemical Solution Deposition of Perovskite Thin Films. *Chem. Mater.* **1997**, *9* (11), 2325-2340.
- [57] Gunawan, R.; Jung, M. Y. L.; Seebauer, E. G.; Braatz, R. D. Optimal control of rapid thermal annealing in a semiconductor process. *J. Process Control* **2004**, *14* (4), 423-430.
- [58] Birkholz, M.; Fewster, P. F. High-Resolution X-ray Diffraction. In *Thin Film Analysis by X-Ray Scattering*; Birkholz, M., Ed.; Wiley-VCH: 2006; pp 297-341.
- [59] Birkholz, M. Grazing Incidence Configurations. In *Thin Film Analysis by X-Ray Scattering*; Birkholz, M., Ed.; Wiley-VCH: 2006; pp 143-182.
- [60] Asylum MFP-3D manual Version 04_08. Asylum Research, Inc: 2008; p. 270.
- [61] Buchner, M.; Höfler, K.; Henne, B.; Ney, V.; Ney, A. Tutorial: Basic principles, limits of detection, and pitfalls of highly sensitive SQUID magnetometry for nanomagnetism and spintronics. *J. Appl. Phys.* **2018**, *124* (16), 161101.
- [62] Van der Pauw, L. J. A Method of Measuring the Resistivity and Hall Coefficient on Lamellae of Arbitrary Shape. *Philips Techn. Rev.* **1958**, *2*.

Chapter 4

Compilation of Articles

4.1 La₂CoMnO₆ epitaxial thin films grown by polymer assisted deposition and confirmation of full Co/Mn cationic ordering achievement

Double perovskite La₂CoMnO₆ (LCMO) oxides are of interest because of their physical properties; being ferromagnetic insulating oxides with a high Curie temperature ($T_C \approx 230$ K) have important applications in fields as diverse as spintronics, magneto-optic devices, or catalysis. However, these properties are strongly dependent on the ordered arrangement of Co and Mn cations in the double perovskite structure. In this work, we have shown that slow growth rates close to thermodynamic equilibrium conditions in polymer assisted deposition-based growth methods are advantageous promoting spontaneous B-site cationic ordering.

The PAD process includes precursor solution preparation, spin-coating, and thermal annealing for phase formation and crystallization. Individual solutions were prepared by using metal salts of lanthanum (III) nitrate, cobalt (II) nitrate, and Mn (II) nitrate. In the initial step PEI-EDTA–Metal complexes stables in water were prepared. Each individual solution was filtered by using Amicon filtration units (10 kDa), and retained portions were analyzed by inductively coupled plasma. The solutions were mixed according to the desired La:Co:Mn 2:1:1 final stoichiometry. After, polymeric layers were deposited on SrTiO₃ (STO) single crystal substrates and then they were annealed in a horizontal tube furnace (800 °C to 950 °C) under an oxygen flow.

XRD patterns and reciprocal space maps reveal that the LCMO films grow epitaxial, cube-on-cube and fully strained with the STO substrate. The AFM topography images show flat surfaces with an RMS surface roughness value below 1 nm, thus indicating that grown films have a high microstructural quality.

Ferromagnetic ordering in LCMO double perovskites is explained by superexchange interaction between Mn⁴⁺ and Co²⁺ cations via the oxygen ions, and it is very sensitive to the cationic ordering in the B-sublattice of the double perovskite structure. LCMO films show saturation magnetization values close to 6 μ_B /f.u., the corresponding spin-only theoretical value of saturation magnetization; and a $T_C \approx 230$ K, thus indicating

full cationic ordering of $\text{Co}^{2+}/\text{Mn}^{4+}$ in the B sublattice. Confirmation of full Co/Mn cationic ordering is found by detailed scanning transmission electron microscopy (STEM) measurements together with electron energy loss spectroscopy (EELS) maps, performed in collaboration with researchers at Oak Ridge National Laboratory (USA).

This study demonstrates the advantage of the chemical solution deposition PAD method over physical methods (far from thermodynamic equilibrium growth) to optimize B-site ordering as well as the desirable physical properties of functional double perovskite oxide thin films. In addition, in the context where the demand for sustainable and environmentally friendly reactants and processes steadily increases, PAD is based on using aqueous solutions of environmentally friendly metal salts and commercially available polymers.

npg **asia materials**

Spontaneous cationic ordering in chemical solution-grown $\text{La}_2\text{CoMnO}_6$ double perovskite thin films

Hailin Wang¹, Jaume Gazquez¹, Carlos Frontera¹, Matthew F. Chisholm², Alberto Pomar¹, Benjamín Martínez¹ and Narcís Mestres¹

1.- Institut de Ciència de Materials de Barcelona (ICMAB), Consejo Superior de Investigaciones Científicas (CSIC), Campus UAB, 08193 Bellaterra, Spain

2.- Materials Science and Technology Division, Oak Ridge National Laboratory,
Oak Ridge, TN 37831, USA

Correspondence: Narcis Mestres (narcis.mestres@icmab.es)

MENU

Search | E-alert | Submit | Login



Featured Article: Thin films: Perfectly flat ceramics unleash their magnetism
Using polymers to control the growth of ceramic thin films can make it easier to produce materials for spintronic applications, which use electron spin instead of charge to carry information.

Call for Papers - Special Issue on Energy-related Materials
We invite researchers to submit original research articles, perspectives and reviews for this issue. Manuscripts... [show more](#)

Latest Review: Biomaterials: Brushing up on polymers
Attaching long polymer molecules to a surface by one end creates a brush-like feature that can provide... [show more](#)

LATEST REVIEW

Latest Perspective: Spin transport in antiferromagnetic insulators: progress and challenges
Spin transport is a key process in the operation of spin-based devices that has been the focus of spintronics... [show more](#)

LATEST PERSPECTIVE

ARTICLE

Open Access

Spontaneous cationic ordering in chemical-solution-grown $\text{La}_2\text{CoMnO}_6$ double perovskite thin films

Hailin Wang¹, Jaume Gazquez¹, Carlos Frontera¹, Matthew F. Chisholm², Alberto Pomar¹, Benjamin Martinez¹ and Narcis Mestres¹

Abstract

Double perovskite oxides are of interest because of their electric, magnetic, and elastic properties; however, these properties are strongly dependent on the ordered arrangement of cations in the double perovskite structure. Therefore, many efforts have been made to improve the level of cationic ordering to obtain optimal properties while suppressing antisite defect formation. Here, epitaxial double perovskite $\text{La}_2\text{CoMnO}_6$ thin films were grown on top of (001)-STO oriented substrates by a polymer-assisted deposition chemical solution approach. Confirmation of the achievement of full Co/Mn cationic ordering was found by scanning transmission electron microscopy (STEM) measurements; EELS maps indicated the ordered occupancy of B–B' sites by Co/Mn cations. As a result, optimal magnetic properties ($M_{\text{sat}} \approx 6 \mu_{\text{B}}/\text{f.u.}$ and $T_{\text{C}} \approx 230 \text{ K}$) are obtained. We show that the slow growth rates that occur close to thermodynamic equilibrium conditions in chemical solution methods represent an advantageous alternative to physical deposition methods for the preparation of oxide thin films in which complex cationic ordering is involved.

Introduction

Complex oxides are a class of materials with a plethora of physical properties of strong interest for many different technological applications from catalysis to spintronics^{1,2}. In addition, there are many possibilities to tune their final physical properties by changing their microstructure (structural strain, microstructural defects, and vacancies) and doping rate. On the other hand, the spectacular advance of thin film preparation and characterization techniques has opened the possibility of engineering physical properties of oxides on the atomic scale, which allows the design of devices with new functionalities^{3,4}.

In this context, transition metal oxides with a double perovskite structure have attracted considerable attention because of their unique electrical, magnetic, and elastic

properties^{5–7}. The simple ABO_3 chemical formula of perovskites allows for high structural and compositional flexibility, as both A and B sites can accommodate a wide variety of atomic combinations. As a result, in double perovskite $(\text{AA}')(\text{BB}')\text{O}_3$ compounds, in which the A and B sites contain more than one element, cation ordering can play an important role in determining the material properties. In particular, $\text{A}_2\text{BB}'\text{O}_6$ double perovskite physical properties are strongly affected by the cationic ordering of B and B'-site sublattices, which in turn is very sensitive to the particular synthesis conditions. $\text{La}_2\text{CoMnO}_6$ (LCMO) exemplifies the challenges associated with structure-property engineering of multi-component oxide systems^{8–11}. When full cationic ordering is achieved, LCMO is a ferromagnetic (FM) semiconductor with a relatively high FM Curie temperature, $T_{\text{C}} \approx 230 \text{ K}$, making it very attractive for thermoelectric and spintronic applications^{12,13}. FM ordering is explained by the superexchange interaction between Mn^{4+} and Co^{2+} according to the Goodenough–Kanamori

Correspondence: Narcis Mestres (narcis.mestres@icmab.es)

¹Institut de Ciència de Materials de Barcelona (ICMAB), Consejo Superior de Investigaciones Científicas (CSIC), Campus UAB, 08193 Bellaterra, Spain

²Materials Science and Technology Division, Oak Ridge National Laboratory, Oak Ridge, TN 37831, USA

© The Author(s) 2019



Open Access This article is licensed under a Creative Commons Attribution 4.0 International License, which permits use, sharing, adaptation, distribution and reproduction in any medium or format, as long as you give appropriate credit to the original author(s) and the source, provide a link to the Creative Commons license, and indicate if changes were made. The images or other third party material in this article are included in the article's Creative Commons license, unless indicated otherwise in a credit line to the material. If material is not included in the article's Creative Commons license and your intended use is not permitted by statutory regulation or exceeds the permitted use, you will need to obtain permission directly from the copyright holder. To view a copy of this license, visit <http://creativecommons.org/licenses/by/4.0/>.

rules^{14–16}, and it is very sensitive to the cationic ordering in the B-sublattice¹⁷. Spontaneous cationic ordering of the B, B'-site sublattice is difficult to attain, and tedious annealing processes under a controlled atmosphere are usually required. Currently, there is no clear agreement in the literature regarding the most convenient strategy to achieve full cationic ordering, and the benefits and drawbacks of crystal growth close to/far from thermodynamic equilibrium conditions have been discussed¹⁸.

Films prepared by chemical solution deposition methods have the final amount of material with the required stoichiometry already deposited on the substrate at the very beginning of the growth process (ex situ growth process). Therefore, it is expected that the film growth will proceed close to thermodynamic equilibrium conditions, which should promote the high crystallinity and quality of the films¹⁹. In contrast, physical deposition methods such as pulsed laser deposition (PLD) or radio-frequency (RF) magnetron sputtering deposition are nonequilibrium growth techniques owing to the continuous deposition of material and to the high electronic excitation, degree of ionization, and kinetic energies of the flux of atomic species incident on the substrate¹⁸.

Specifically, in the case of LCMO, most of the results reported in the literature correspond to epitaxial thin films grown by PLD. As mentioned above, crystal growth occurs under conditions far from equilibrium, and ordered occupancy of the B and B' positions is difficult to attain. Usually, as-grown LCMO films prepared by PLD do not exhibit high cationic ordering, making additional annealing processes in ambient oxygen necessary^{10,20,21}. Strategies based on structural strain effects leading to the formation of two different sized B-site spaces in a rock salt arrangement have been recently proposed as a way to induce spontaneous cationic ordering of the B, B'-site sublattice in epitaxial thin films;²² however, the results are not conclusive. High-quality LCMO thin films have also been prepared by using RF magnetron sputtering. A very narrow window for the growth of the ordered phase was identified; however, an annealing process at sufficiently high temperatures ($\sim 900^\circ\text{C}$) in an oxygen-rich atmosphere ($P_{\text{O}_2} > 400$ Torr) is necessary to obtain optimal magnetic properties, which are indicative of a high cationic ordering²³.

Therefore, the precise physicochemical mechanisms that promote spontaneous B-site cationic ordering are still unknown. In this regard, control of the growth kinetics has been proposed as an effective tool to achieve spontaneous cationic ordering because B-site differences may be enhanced at the growth front²⁴. For this reason, the use of chemical methods that allow thin film growth close to equilibrium conditions, in contrast to physical growth methods (PLD and sputtering), might be an interesting alternative for obtaining spontaneous cationic

ordering. In fact, the growth of LCMO on (111)-SrTiO₃ (STO) substrates has been explored using metal-organic aerosol deposition (MAD)²⁵, and excellent saturation magnetization (*M_{sat}*) and Curie temperature values indicative of high cationic ordering have been obtained.

Polymer-assisted deposition (PAD) is an affordable and environmentally friendly chemical solution deposition technique with great potential for the preparation of complex oxide thin films. In the PAD technique, stable metal-polymer solutions are used as film precursors, and the polymer not only controls the solution viscosity but also binds the metal ions to form a homogeneous solution^{26–28}. As a chemical solution route, PAD provides an attractive opportunity to grow films close to thermodynamic equilibrium conditions. The characteristic growth conditions of PAD have already been shown to be advantageous for the stabilization of materials with complex structures or chemical composition, such as misfit cobalt oxides²⁹ and Y₃Fe₅O₁₂ yttrium iron garnet³⁰. On the other hand, PAD might also be useful to clarify the role of structural strain in stimulating spontaneous cationic ordering because it has been shown that structural strain accommodation may proceed in a different way in samples prepared by PAD. As demonstrated in epitaxial La_{0.7}Sr_{0.3}MnO₃ thin films grown on STO, structural accommodation through complex rotation of the MnO₆ octahedra is different in films grown by PLD and PAD³¹.

Since material properties and hence functionality strongly depend on the preparation method and processing steps, in the present work, we report the successful epitaxial growth of highly ordered LCMO double perovskite thin films on (001)-STO substrates by PAD. Epitaxial films with thicknesses in the range of 3–30 nm with excellent magnetic properties (*M_{sat}* $\approx 6 \mu_{\text{B}}/\text{f.u.}$ and *T_c* ≈ 230 K) were prepared. Films are in-plane (IP) fully strained with a flat surface displaying root mean squared (RMS) surface roughness values of < 1 nm. No signals were detected from secondary phases. A powerful confirmation of the spontaneous B-site cationic ordering was obtained through aberration-corrected scanning transmission electron microscopy (STEM) measurements. Atomically resolved elemental electron energy loss spectroscopy (EELS) maps made evident the ordered occupancy of B-B' sites by Co-Mn cations, as inferred from the optimal values of the *M_{sat}* and Curie temperature.

materials and methods

Thin film growth

The PAD technique relies on the use of water-soluble polymers with functional $-\text{NH}_2$ groups that coordinate cations and prevent their hydrolysis. The polymers used should be compatible with the metal precursors and should undergo clean decomposition upon heating²⁷. The

precursor solution for the growth of the LCMO thin film was prepared by mixing three separate aqueous solutions of La, Co, and Mn bound to polymers. Separate solutions were prepared using high-purity (>99.9%) metal salts of lanthanum(III) nitrate, cobalt(II) nitrate, and Mn(II) nitrate. The polymer used in the experiment was branched polyethyleneimine (PEI), average $M_w \sim 25,000$, and ethylenediaminetetraacetic acid (EDTA) was used as a complexing agent; both were from Sigma Aldrich. Water used in the solution preparation was purified using a Milli-Q water treatment system.

In detail, individual solutions of the different metal ions were prepared by dissolving the corresponding nitrate salts in water and EDTA (1:1 molar ratio). PEI was incorporated into the solution in a 1:1 mass ratio with EDTA. Each individual solution was filtrated using Amicon® filtration units (10 kDa), and retained portions were analyzed by inductively coupled plasma (ICP) (*Optima 4300™ DV ICP-OES Perkin-Elmer*). The final concentrations of the solutions used in this work were $[La] = 230.4$ mM, $[Co] = 146.4$ mM, and $[Mn] = 176.4$ mM. The solutions were mixed according to the desired La:Co:Mn 2:1:1 final stoichiometry and concentrated to reach a final cation concentration of ≈ 61 mM with respect to Mn. These conditions were adjusted to produce films in the range of ≈ 20 – 30 nm. Similarly, more diluted solutions were adjusted to obtain films in the range of a few nm (3–5 nm).

The precursor solutions obtained in this way were spin coated on top of 0.5×0.5 cm² (001)-STO substrates from *Crystec*, GmbH, Germany. Prior to deposition, the as-received substrates were chemically etched and thermally treated to create TiO₂-terminated substrates with atomically flat terraces³². After the polymeric layer was deposited, it was annealed in a horizontal tube furnace under an oxygen flow to eliminate the presence of oxygen vacancies. The precursor films were slowly heated from room temperature to 500 °C, and the ramp was stopped for 60 min to ensure that the solvent was evaporated and the polymer decomposed at a slow rate to avoid the formation of pinholes and cracks. PEI decomposes at ≈ 550 °C, i.e., immediately before the crystallization of the inorganic film. The metal ions are released to form oxides after polymer decomposition, and higher substrate temperatures will lead to the growth of epitaxial films^{27,28}. Therefore, after the step, the samples were heated at a ramp rate of 3 °C/min from 800 °C to 950 °C for film crystallization. The cooling ramp was also set at 3 °C/min.

Characterization of the structural and physical properties

The structural properties of the epitaxial films were studied by X-ray diffraction and reflectivity using a D5000 (Siemens) diffractometer, an X'Pert MRD (PANalytical) four-angle diffractometer with monochromatic Cu-K α 1

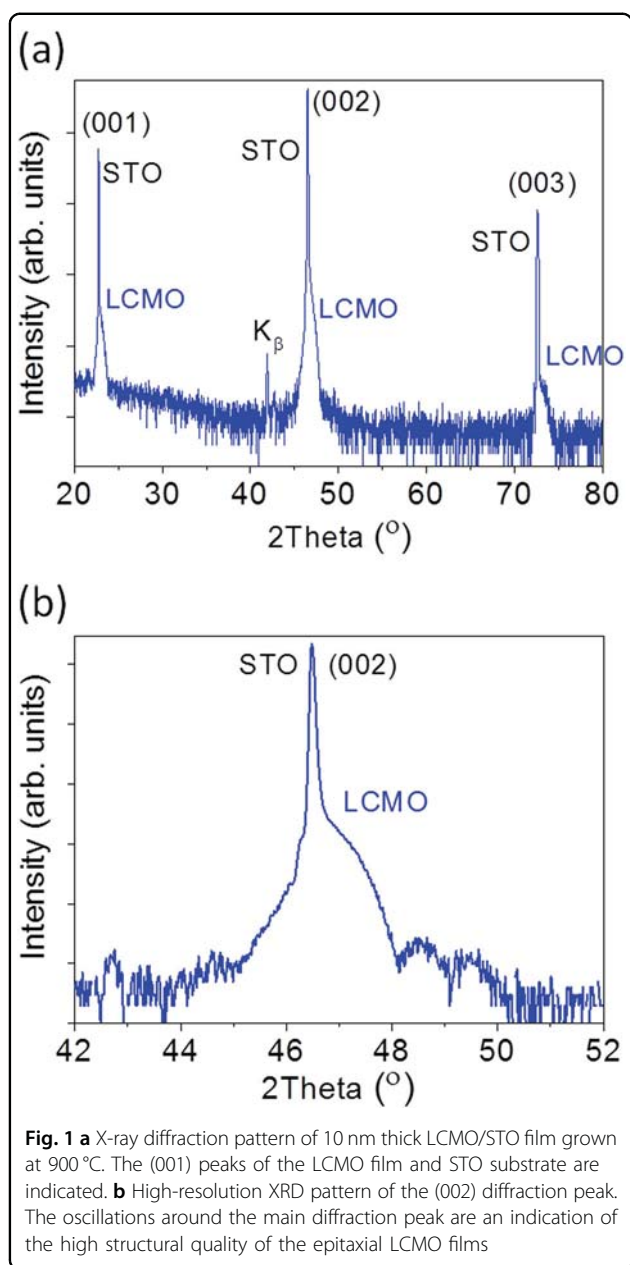
radiation (1.54060 Å) and a Bruker D8 Advance GADDS system. Magnetization measurements were performed using a superconducting quantum interference device (SQUID; Quantum Design) as a function of temperature and magnetic field. External magnetic fields were applied both parallel (IP configuration) and perpendicular (OP configuration) to the sample plane. The diamagnetic contribution of the substrate and other instrumental contributions were properly corrected³³. The relative error in the determination of the M_{sat} was $\sim 5\%$ and was mostly attributable to the error in the estimation of the film volume. The surface topography of the films was investigated by atomic force microscopy (AFM) using an Asylum Research MFP-3D microscope in tapping mode. The microstructure of the LCMO film and the B-site ordering at the atomic scale were studied using STEM in combination with EELS. Specimens for STEM were prepared by conventional methods, grinding, and Ar-ion milling. The STEM images and EELS spectral images were acquired with an aberration-corrected Nion Ultra-STEMTM 200 operated at 200 kV and equipped with a 5th order Nion aberration corrector. The particular geometry of these microscopes allows for the simultaneous acquisition of different signals from two singular detectors.

Results and discussion

After a careful optimization process (see Supporting Information), we determined the ideal growth conditions (growth temperature of 900 °C, annealing time of ~ 1 h, and oxygen flow above 0.3 l/min) to obtain the optimal magnetic properties, which were close to the theoretically expected values. Samples prepared under other conditions show depressed magnetization values.

A typical XRD pattern corresponding to an LCMO film annealed at 900 °C on an STO substrate is shown in Fig. 1. The corresponding film thickness, extracted from the X-ray reflectivity measurements, is ~ 10 nm (Supporting Information, Fig. S1). The epitaxial nature of the LCMO film is evidenced by the detection of only (001) peaks along with the corresponding STO-(001) peaks originating from the STO-(001) substrate and the K_β reflection (see Fig. 1a). An out-of-plane lattice parameter $c = 3.859$ Å is estimated from the high-resolution X-ray diffraction pattern of the (002) diffraction peak (see Fig. 1b).

The film is IP fully strained with a lattice mismatch of $\sim 0.4\%$. The 3D reciprocal space tomography reveals the presence of superstructure peaks of the type $(hk\frac{l}{2})$ ($l = \text{odd}$), and the absence of reflections of the type $(\frac{h}{2}kl)$ ($h = \text{odd}$) and $(h\frac{k}{2}l)$ ($k = \text{odd}$) indicates that the cell of LCMO ($\sqrt{2}a_p \times \sqrt{2}a_p \times 2a_p$, with $a_p = \text{primitive perovskite}$) is oriented with the c -direction out of plane (OP) (Supporting Information, Fig. S2). The epitaxial nature of the LCMO films is further confirmed by the reciprocal space maps around the STO-(103) reflection that reveal that the



films grow epitaxially, cube-on-cube and fully strained with the STO substrate (Supporting Information, Fig. S3).

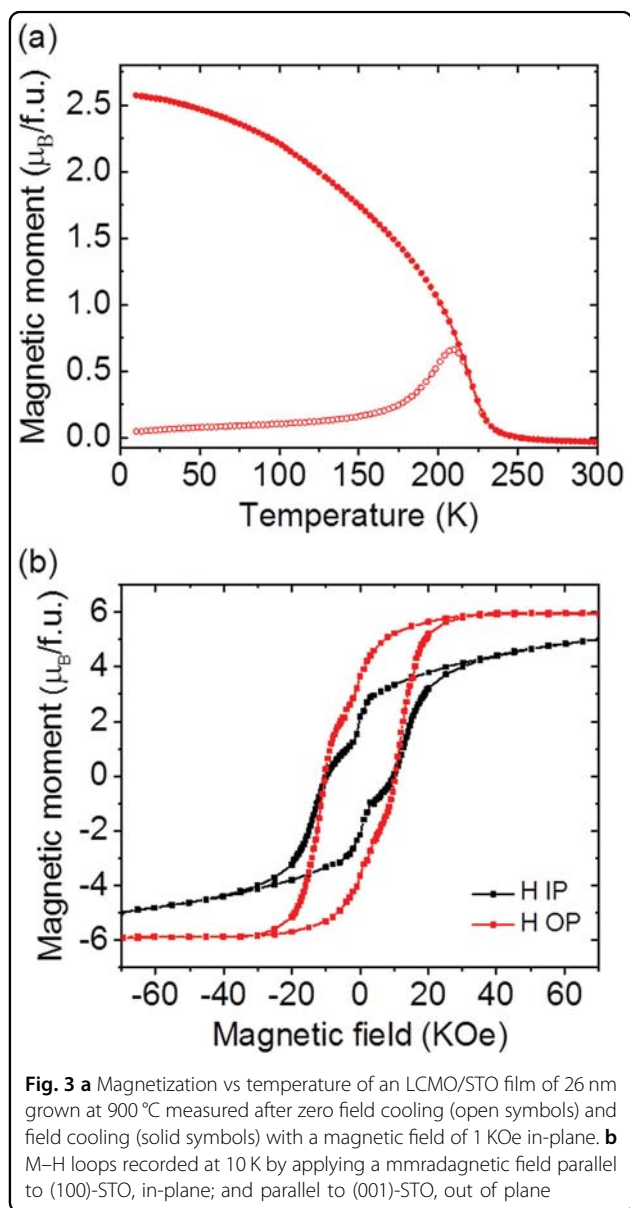
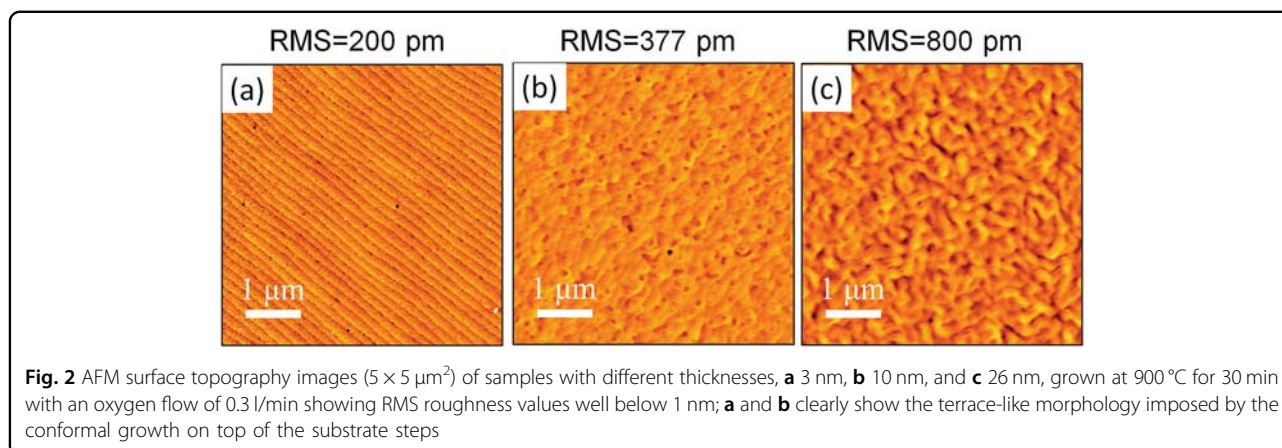
In addition, the AFM topography images displayed in Fig. 2 show flat surfaces with an RMS surface roughness value of <1 nm, thus indicating that the samples have a high microstructural quality. Fig. 2a, b clearly shows the terrace-like morphology imposed by the conformal growth on top of the substrate steps.

The magnetic properties of a 26-nm-thick LCMO/STO thin film grown at 900 °C for 60 min with an oxygen flow of 0.3 l/min are shown in Fig. 3. Figure 3a shows the temperature dependence of magnetization (zero field

cooling and field cooling measurements) in the temperature range from 10 K to 300 K under a magnetic field of $H = 1$ kOe applied along the IP direction. The Curie temperature $T_C = 230$ K was estimated from the minimum of the function $(1/M)(dM/dT)$. No signals for the coexistence of different FM phases, as usually occurs in oxygen-deficient samples prepared by PLD or sputtering^{10,23}, are detected; thus, we assume that the samples are fully oxygenated. In Fig. 3b, the measured low temperature (10 K) $Msat \approx 5.9 \mu_B/f.u.$ and IP coercive field of $H_c \approx 10$ kOe agree well with the data reported for B-site ordered LCMO bulk³⁴ and thin film samples^{20,23,25}. On the other hand, samples not grown under optimal conditions show depressed magnetization values (Supporting Information, Fig. S4). Even though the XRD data cannot provide information regarding B-site cationic ordering, in addition to the improvement in the magnetic properties, the degree of crystallinity and the microstructural film quality also improve with increasing annealing time and oxygen flux, as shown in the reciprocal space maps displayed in Fig. S3 in the Supporting Information.

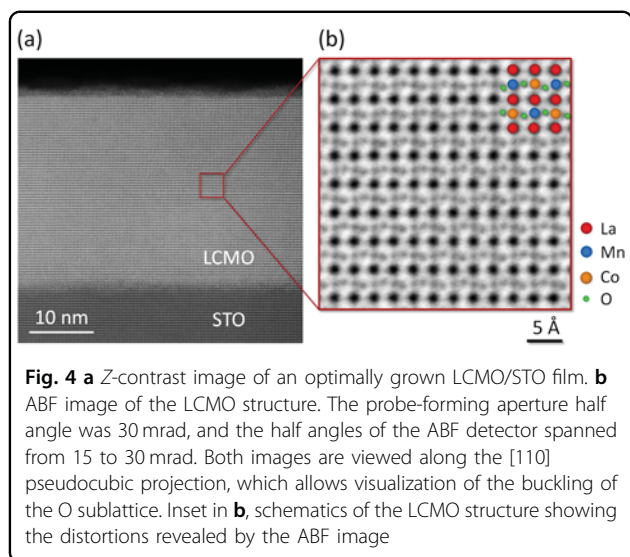
The high values of $Msat$ and T_C indicate a high degree of Co/Mn cationic ordering. As mentioned previously, both values are very sensitive to cationic ordering and are substantially reduced in disordered samples. As indicated above, FM ordering in the insulating LCMO originates from the superexchange interaction between Co^{2+} ions in the high spin state ($3d^7: t_{2g}^5 e_g^2$) with half-filled e_g orbitals and the overall spin $S = 3/2$ and Mn^{4+} ions ($3d^3: t_{2g}^3 e_g^0$) with empty e_g orbitals and $S = 3/2$ mediated by oxygen anions, according to the Goodenough–Kanamori–Anderson rules^{14–16}. As a result, a large theoretical saturation spin only moment, $Msat = 6 \mu_B/f.u.$ and a relatively high value of $T_C \sim 230$ K are predicted. In this scenario, cationic disorder promotes the appearance of $Mn^{4+}-O-Mn^{4+}$ and $Co^{2+}-O-Co^{2+}$ bonding, generating antiferromagnetic superexchange interactions and lowering both the $Msat$ and the Curie temperature in partially disordered samples.

Figure 3b also shows the strong anisotropic behavior of the samples. When the magnetic field is applied perpendicular to the sample plane (the OP configuration), saturation is reached at ~ 30 kOe, while when the field is applied parallel to the sample plane (the IP configuration), saturation is not reached even at 80 kOe. Thus, the perpendicular-to-plane direction is the easy magnetization direction, as previously observed in samples grown by RF magnetron sputtering^{23,35}. Our previous results for samples prepared by RF sputtering indicate that the Co^{2+} valence state is preferentially stabilized irrespective of the structural strain even in nonstoichiometric samples³⁶. In addition, it was also shown that anisotropy in LCMO films is mainly driven by spin-orbit coupling of Co^{2+} and is strain-dependent. Under tensile strain, as in LCMO films grown on STO, a strong increase in the angular



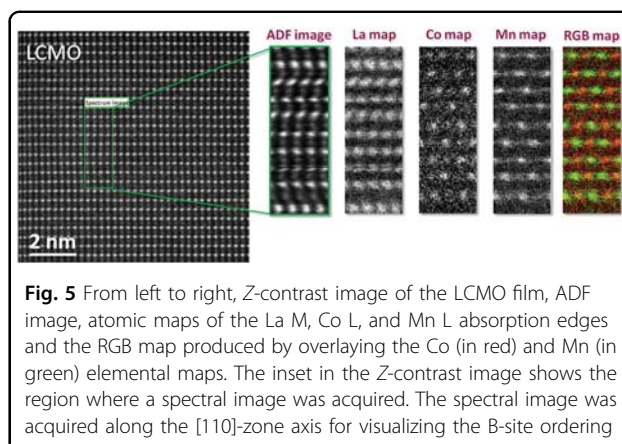
contribution to the magnetic moment of Co^{2+} occurs and generates a strong perpendicular magnetic anisotropy^{35,36}, as in the present case. On the other hand, $M(H)$ in Fig. 3b show the typical bi-loop shape recurrent in many cases reported in the literature^{10,22}. The origin of this sudden drop in the remanent magnetization at $H = 0$, which has been erroneously attributed in some cases to the existence of two magnetic domains possessing different coercivities¹⁰, is due to the existence of antiphase boundaries. Antiphase boundaries appear because the nucleation of Co^{2+} and Mn^{4+} cationic ordering may occur at different positions in different regions of the sample, and when regions with inverted Co^{2+} and Mn^{4+} positions relative to the other merge together, an antiphase boundary is formed. As noted by Dass and Goodenough⁸, at the antiphase interface of $\text{Co}^{2+}\text{-O-Co}^{2+}$ or $\text{Mn}^{4+}\text{-O-Mn}^{4+}$, AF interactions occur; thus, lowering the field from saturation at $H = 0$ causes any antiphase regions to revert back to an antiparallel orientation with a 180° change in the spin orientation across an antiphase boundary, which would produce the observed sudden drop in the remnant magnetization. This drop is more pronounced in thinner films (Supporting Information, Fig. S5), indicating a larger contribution of antiphase boundaries on the magnetic hysteresis loops. Accordingly, the bi-loop features of the hysteresis cycle are not observed in samples without extended antiphase boundaries or with ordered regions separated by a blurred disordered boundary region²⁵. Therefore, from the magnetic measurements, we conclude that our LCMO films present almost full $\text{Mn}^{4+}\text{-Co}^{2+}$ cationic ordering.

Aberration-corrected STEM images obtained for optimally grown films give further support to the high B-site cationic ordering degree of films grown by the PAD approach. As mentioned above, the particular geometry of the microscope used allows for acquiring different signals simultaneously from two singular detectors in such a way that electrons that are scattered at high angles are



recorded with a high angle annular detector that produces a contrast interpretable in terms of the atomic number Z of the different atomic species. Thus, this is an effective structure imaging mode specifically for the atomic scale³⁷. Simultaneously, those electrons that are scattered at much lower angles can be collected by an annular bright field (ABF) detector, which is a direct beam disk that allows the imaging of light and heavy atoms in a single STEM image, thus probing the A , B , and O sublattices of the ABO_3 -perovskite structure^{38,39}. The coherent interference of such electrons results in a phase image that presents an inverted contrast with respect to the Z -contrast images. Fig. 4a, b show a Z -contrast image of the 30-nm-thick LCMO film and a higher magnification ABF image of the LCMO structure. Both images were acquired along the [110] pseudocubic projection, which allows visualization of the BO_6 octahedral rotation and the buckling of the O sublattice of LCMO, as clearly seen in Fig. 4b. Such rippling is due to the presence of octahedral tilts along the $[100]_{pc}$ and $[010]_{pc}$ directions^{8,34}. The structure and chemistry of the material can be probed simultaneously by using another imaging detector, such as an electron energy loss spectrometer, together with the high angle annular detector.

Figure 5 shows from left to right the Z -contrast image of the LCMO structure from which the spectrum image (see marked area in green) was acquired, the simultaneously acquired annular dark field (ADF) image, the atomic resolution maps of the La M , Co L , and Mn L absorption edges and the RGB image produced by overlaying the Co (in red) and Mn (in green) elemental maps. Whereas the La elemental map shows a continuous A-site contrast, both Co and Mn maps show an intensity variation in every other B-site atomic column, consistent with ordering. Indeed, the checkerboard pattern evidenced by the



RGB map unambiguously demonstrates the Co/Mn ordering of the LCMO phase. Therefore, STEM images provide powerful confirmation that PAD growth promotes the desired double perovskite cationic ordering, as inferred from the optimal values of the M_{sat} and Curie temperature.

To date, there is no clear knowledge regarding the mechanism controlling B-site cationic ordering, and efforts to attain it have been mainly focused on obtaining two well-differentiated B-sites so that different cations will spontaneously choose one of them according to steric or charge distribution criteria. In this regard, it was recently claimed that a high degree of cationic ordering can be obtained by growing LCMO on (111)-STO substrates instead of the commonly used (001)-STO²².

It was argued that (111)-substrate growth induces an “in-plane” strain that combined with the intrinsically tilted oxygen octahedra, following the $a^-a^-c^+$ scheme of the $P2_1/n$ (monoclinic) space group⁴⁰, generates the formation of two different sized B-site spaces in a rock salt arrangement. This particular arrangement would promote the desired double perovskite cationic ordering, resulting in excellent magnetic properties. However, authors in ref. 22 report fully strained epitaxial growth on the (111) substrate incompatible with the monoclinic crystal system but compatible with the trigonal one. It is worth mentioning that many single perovskites crystallize in the rhombohedral $R\bar{3}c$ space group (e.g., $LaCoO_3$ ⁴¹, $LaNiO_3$ ⁴², and $La_{2/3}Sr_{1/3}MnO_3$ ⁴³). Thus, this crystal system can naturally accommodate the strain imposed by the (111) orientation of the substrate with the $a^-a^-a^-$ octahedral tilting scheme without creating two differently sized B-site cages. In addition, it is important to remark that the conclusion regarding the higher degree of cationic ordering in samples prepared on (111)-STO substrates was derived by comparing magnetization values measured with the magnetic field applied parallel to the sample plane and that, in the case of the (001)-STO samples, corresponds to the hard magnetization direction.

Therefore, the lower values of the magnetization obtained in the (001)-STO samples do not necessarily imply a lower cationic ordering but result from the strong perpendicular magnetic anisotropy present in the (001)-oriented LCMO thin films³⁵.

It has also been proposed that growth instabilities at the growth front may be a possible alternative to induce spontaneous B-site cationic ordering. The notable differences between thermal evaporation methods and CSD techniques represent clearly different approaches. Undoubtedly, in CSD techniques, the microstructure and orientation of the thin films can be significantly influenced by the solution and material chemistry, substrate characteristics, and annealing conditions. Moreover, in the PAD method, the direct binding between the metal and polymer stabilizes the metal complexes so that they do not experience preformation in the solution prior to polymer decomposition⁴⁴, thus increasing the lifetime of the solution and preventing early metal oxide formation during the deposition stage. Thermogravimetric analysis indicated complete degradation of the polymer above ≈ 550 °C, and the high thermal stability of PEI prevents the formation of the oxide film phase below this temperature. Consequently, the removal of the organic material and the crystallization of the film both take place at the same temperature^{27,28}. Furthermore, the slow decomposition of the polymer promotes the formation of the inorganic film at a very slow rate close to thermodynamic equilibrium conditions and promotes its high crystallinity and quality. Thus, the nucleation and growth processes in PAD films are substantially different from those occurring in films prepared by thermal evaporation. In the latter case, atomic species arrive at the substrate surface, typically at a temperature close to 900 °C, with kinetic energies in the range from tens of eV to a few hundred eV, and they have to thermalize. Therefore, crystallization and film growth occur far from thermodynamic equilibrium conditions⁴⁵; i.e., surface diffusion is high and atomic species can move easily, which might make B-site cationic ordering difficult and require the use of ulterior high temperature annealing processes to improve it. In contrast, the formation and crystallization of a solid phase from liquid-based solutions requires a much smaller thermodynamic-driving force than thermal evaporation methods¹⁸. Thus, in films prepared by PAD, crystallization of the oxide takes place near the decomposition temperature of the polymer, i.e., 550 °C, i.e., close to thermodynamic equilibrium conditions. The slow growth conditions of PAD can be much more favorable for attaining spontaneous B-site cationic ordering, as observed in our case. In fact, PAD has been revealed as a very appropriate method to prepare complex oxide phases with complex cationic ordering²⁸.

Conclusions

High-quality epitaxial LCMO films have been prepared with a single one-step growth process using the PAD technique on top of STO (001)-oriented substrates. The magnetic properties of the films ($M_{sat} \approx 6 \mu_B/f.u.$ and $T_c \approx 230$ K) are indicative of almost full Co/Mn B-site cationic ordering. Further support for the existence of full Co/Mn cationic ordering is obtained by STEM measurements; EELS maps indicate the ordered occupancy of B–B' sites by Co/Mn cations. The magnetic properties of LCMO are highly sensitive to B-site cationic ordering; therefore, obtaining full cationic ordering is fundamental for potential technological applications. To date, there is no clear knowledge regarding the mechanism controlling B-site cationic ordering, and different strategies relying on structural strain and growth instabilities have been proposed but without conclusive results. In this work, we show that the particular crystallization and growth process conditions of PAD (very slow rate, close to thermodynamic equilibrium conditions) promote the high crystallinity and quality of the films, as well as B-site cationic ordering. We believe that the obtained results show the advantage of the CSD–PAD method over physical methods (far from thermodynamic equilibrium growth) to optimize B-site ordering as well as the desirable physical properties of functional double perovskite oxide thin films. In addition, in the context where the demand for sustainable and environmentally friendly reactants and processes steadily increases, PAD is based in aqueous solutions of environmentally friendly metal salts and commercially available polymers.

Acknowledgements

We acknowledge financial support from the Spanish Ministry of Economy and Competitiveness through the Severo Ochoa Programme for Centres of Excellence in R&D (SEV-2015-0496), COACHSUPENERGY project (MAT2014-51778-C2-1-R) and MAT2015-71664-R, cofinanced by the European Regional Development Fund. Support from the European Union's Horizon 2020 Research and Innovation Programme under the Marie Skłodowska-Curie grant agreement no. 645658 (DAFNEOX Project) is also acknowledged. H.W. acknowledges financial support from the China Scholarship Council (CSC). J.G. also acknowledges the Ramon y Cajal program (RYC-2012-11709). The STEM–EELS analysis was sponsored by the U.S. Department of Energy, Office of Science, Basic Energy Sciences, Materials Sciences and Engineering Division. The authors would like to thank Anna Crespi and Francesc Xavier Campos for assistance with the 3D reciprocal space tomography and reciprocal space map measurements.

Conflict of interest

The authors declare no conflict of interest.

Publisher's note

Springer Nature remains neutral with regard to jurisdictional claims in published maps and institutional affiliations.

Supplementary information is available for this paper at <https://doi.org/10.1038/s41427-019-0144-8>.

Received: 13 February 2019 Revised: 2 May 2019 Accepted: 18 May 2019
Published online: 02 August 2019

References

- Tokura, Y. & Hwang, H. Y. Condensed-matter physics: complex oxides on fire. *Nat. Mater.* **7**, 694–695 (2008).
- Rondinelli, J. M. & Spaldin, N. A. Structure and properties of functional oxide thin films: insights from electronic-structure calculations. *Adv. Mater.* **23**, 3363–3381 (2011).
- Martin, L. W., Chu, Y. H. & Ramesh, R. Advances in the growth and characterization of magnetic, ferroelectric, and multiferroic oxide thin films. *Mater. Sci. Eng. R Rep.* **68**, 89–133 (2010).
- Ohtomo, A. & Hwang, H. Y. A high-mobility electron gas at the $\text{LaAlO}_3/\text{SrTiO}_3$ heterointerface. *Nature*. **427**, 423–426 (2004).
- Moritomo, Y. et al. Electronic structure of double-perovskite transition-metal oxides. *Phys. Rev. B*. **61**, R7827–R7830 (2000).
- Hua, B. et al. The excellence of both worlds: developing effective double perovskite oxide catalyst of oxygen reduction reaction for room and elevated temperature applications. *Adv. Funct. Mater.* **26**, 4106–4112 (2016).
- Vasala, S. & Karppinen, M. $\text{A}_2\text{B}'\text{B}''\text{O}_6$ perovskites: a review. *Prog. Solid State Chem.* **43**, 1–36 (2015).
- Dass, R. I. & Goodenough, J. B. Multiple magnetic phases of $\text{La}_2\text{CoMnO}_{6-\delta}$ ($0 < \delta < \sim 0.05$). *Phys. Rev. B*. **67**, 014401 (2003).
- Kyömen, T., Yamazaki, R. & Itoh, M. Correlation between Magnetic Properties and Mn/Co Atomic Order in $\text{LaMn}_{0.5}\text{Co}_{0.5}\text{O}_{3+\delta}$: I. Second-Order Nature in Mn/Co Atomic Ordering and Valence State. *Chem. Mater.* **15**, 4798–4803 (2003).
- Guo, H. Z., Gupta, A., Zhang, J., Varela, M. & Pennycook, S. J. Effect of oxygen concentration on the magnetic properties of $\text{La}_2\text{CoMnO}_6$ thin films. *Appl. Phys. Lett.* **91**, 202509 (2007).
- Truong, K. D., Laverdière, J., Singh, M. P., Jandl, S. & Fournier, P. Impact of Co/Mn cation ordering on phonon anomalies in $\text{La}_2\text{CoMnO}_6$ double perovskites: Raman spectroscopy. *Phys. Rev. B*. **76**, 132413 (2007).
- Mao, Y. Facile molten-salt synthesis of double perovskite La_2BMnO_6 nanoparticles. *RSC Adv.* **2**, 12675–12678 (2012).
- López-Mir, L. et al. Anisotropic sensor and memory device with a ferromagnetic tunnel barrier as the only magnetic element. *Sci. Rep.* **8**, 861 (2018).
- Goodenough, J. B. An interpretation of the magnetic properties of the perovskite-type mixed crystals $\text{La}_{1-x}\text{Sr}_x\text{CoO}_{3-x}$. *J. Phys. Chem. Solids*. **6**, 287–297 (1958).
- Kanamori, J. Superexchange interaction and symmetry properties of electron orbitals. *J. Phys. Chem. Solids*. **10**, 87–98 (1959).
- Anderson, P. W. Antiferromagnetism. Theory of superexchange interaction. *Phys. Rev.* **79**, 350–356 (1950).
- Goodenough, J. B., Wold, A., Arnett, R. J. & Menyuk, N. Relationship between crystal symmetry and magnetic properties of ionic compounds containing Mn^{3+} . *Phys. Rev.* **124**, 373–384 (1961).
- Koster, G., Huijben, M. & Rijnders, G. Chemical solution deposition techniques for epitaxial growth of complex oxides. in *Epitaxial Growth of Complex Metal Oxides*, Ch. 4 (Woodhead Publishing, Cambridge, UK, 2015) 69–93.
- Schneller, T., Waser, R., Kosec, M. & Payne, D. *Chemical Solution Deposition of Functional Oxide Thin Films*. (Springer-Verlag, Wien, 2013) 1–796.
- Guo, H. Z., Gupta, A., Calvarese, T. G. & Subramanian, M. A. Structural and magnetic properties of epitaxial thin films of the ordered double perovskite $\text{La}_2\text{CoMnO}_6$. *Appl. Phys. Lett.* **89**, 262503 (2006).
- Singh, M. P., Charpentier, S., Truong, K. D. & Fournier, P. Evidence of bidomain structure in double-perovskite $\text{La}_2\text{CoMnO}_6$ thin films. *Appl. Phys. Lett.* **90**, 211915 (2007).
- Kleibecker, J. E. et al. Route to achieving perfect B-site ordering in double perovskite thin films. *NPG Asia Mater.* **9**, e406 (2017).
- Galceran, R. et al. Engineering the microstructure and magnetism of $\text{La}_2\text{CoMnO}_{6-\delta}$ thin films by tailoring oxygen stoichiometry. *Appl. Phys. Lett.* **105**, 242401 (2014).
- Chakraverty, S., Yu, X. Z., Kawasaki, M., Tokura, Y. & Hwang, H. Y. Spontaneous B-site order and metallic ferrimagnetism in LaSrVMoO_6 grown by pulsed laser deposition. *Appl. Phys. Lett.* **102**, 222406 (2013).
- Egoavil, R. et al. Phase problem in the B-site ordering of $\text{La}_2\text{CoMnO}_6$: impact on structure and magnetism. *Nanoscale*. **7**, 9835–9843 (2015).
- Jia, Q. X. et al. Polymer-assisted deposition of metal-oxide films. *Nat. Mater.* **3**, 529–532 (2004).
- Zou, G. F. et al. Polymer-assisted-deposition: a chemical solution route for a wide range of materials. *Chem. Soc. Rev.* **42**, 439–449 (2013).
- Vila-Fungueiriño, J. M. et al. Polymer assisted deposition of epitaxial oxide thin films. *J. Mater. Chem. C*. **6**, 3834–3844 (2018).
- Rivas-Murias, B., Vila-Fungueiriño, J. M. & Rivadulla, F. High quality thin films of thermoelectric misfit cobalt oxides prepared by a chemical solution method. *Sci. Rep.* **5**, 11889 (2015).
- Lucas, I. et al. Chemical solution synthesis and ferromagnetic resonance of epitaxial thin films of yttrium iron garnet. *Phys. Rev. Mater.* **1**, 074407 (2017).
- Vila-Fungueiriño, J. M. et al. Thermodynamic conditions during growth determine the magnetic anisotropy in epitaxial thin-films of $\text{La}_{0.7}\text{Sr}_{0.3}\text{MnO}_3$. *J. Phys. D*. **49**, 315001 (2016).
- Kareev, M. et al. Atomic control and characterization of surface defect states of TiO_2 terminated SrTiO_3 single crystals. *Appl. Phys. Lett.* **93**, 061909 (2008).
- Stamenov, P. & Coey, J. M. D. Sample size, position, and structure effects on magnetization measurements using second-order gradiometer pickup coils. *Rev. Sci. Instrum.* **77**, 015106 (2006).
- Baron-Gonzalez, A. J., Frontera, C., Garcia-Munoz, J. L., Rivas-Murias, B. & Blasco, J. Effect of cation disorder on structural, magnetic and dielectric properties of $\text{La}_2\text{MnCoO}_6$ double perovskite. *J. Phys. Condens. Matter*. **23**, 496003 (2011).
- Galceran, R. et al. Strain-induced perpendicular magnetic anisotropy in $\text{La}_2\text{CoMnO}_{6-x}$ thin films and its dependence on film thickness. *Phys. Rev. B*. **93**, 144417 (2016).
- López-Mir, L. et al. Magnetic anisotropy and valence states in $\text{La}_2\text{Co}_{1-x}\text{Mn}_{1+x}\text{O}_6$ ($x \approx 0.23$) thin films studied by x-ray absorption spectroscopy techniques. *Phys. Rev. B*. **95**, 224434 (2017).
- Nellist, P. D. & Pennycook, S. J. Incoherent imaging using dynamically scattered coherent electrons. *Ultramicroscopy*. **78**, 111–124 (1999).
- Okunishi, E. et al. Visualization of light elements at ultrahigh resolution by STEM annular bright field microscopy. *Microsc. Microanal.* **15**(S2), 164–165 (2009).
- Ishikawa, R. et al. Direct imaging of hydrogen-atom columns in a crystal by annular bright-field electron microscopy. *Nat. Mater.* **10**, 278–281 (2011).
- Woodward, P. M. Octahedral tilting in perovskites. I. geometrical considerations. *Acta Crystallogr. Sect. B Struct. Sci.* **53**, 32–43 (1997).
- Thornton, G., Tofield, B. C. & Hewat, A. W. A neutron diffraction study of LaCoO_3 in the temperature range $4.2 < T < 1248$ K. *J. Solid State Chem.* **61**, 301–307 (1986).
- García-Muñoz, J. L., Rodríguez-Carvajal, J., Lacorre, P. & Torraine, J. B. Neutron-diffraction study of RNiO_3 ($R = \text{La, Pr, Nd, Sm}$): electronically induced structural changes across the metal-insulator transition. *Phys. Rev. B*. **46**, 4414–4425 (1992).
- Radaelli, P. G. et al. Structural effects on the magnetic and transport properties of perovskite $\text{A}_{1-x}\text{A}'_x\text{MnO}_3$ ($x = 0.25, 0.30$). *Phys. Rev. B*. **56**, 8265–8276 (1997).
- Burrell, A. K., Mark McCleskey, T. & Jia, Q. X. Polymer assisted deposition. *Chem. Commun.* **11**, 1271–1277 (2008).
- Greene, J. E. Thin film nucleation, growth, and microstructural evolution: an atomic scale view. in *Handbook of Deposition Technologies for Films and Coatings* 3rd edn (ed. Martin, P. M.) Ch. 12 (William Andrew Publishing, Boston, 2010) 554–620.

npg **asia materials**

Supporting Information

for Wang et al. NPG Asia Materials (2019) 11:44

Spontaneous cationic ordering in chemical solution-grown $\text{La}_2\text{CoMnO}_6$ double perovskite thin films

Hailin Wang¹, Jaume Gazquez¹, Carlos Frontera¹, Matthew F. Chisholm², Alberto Pomar¹, Benjamín Martínez¹ and Narcís Mestres¹

Supporting Information

Spontaneous cationic ordering in chemical solution grown $\text{La}_2\text{CoMnO}_6$ double perovskite thin films

Hailin Wang¹, Jaume Gazquez¹, Carlos Frontera¹, Matthew F. Chisholm², Alberto Pomar¹, Benjamin Martinez¹, Narcis Mestres^{1}*

¹Institut de Ciència de Materials de Barcelona (ICMAB), Consejo Superior de Investigaciones Científicas (CSIC), Campus UAB, 08193 Bellaterra, Spain

²Materials Science and Technology Division, Oak Ridge National Laboratory, Oak Ridge, Tennessee 37831, USA

*E-mail: narcis.mestres@icmab.es

S1. X-ray reflectivity spectra of epitaxial LCMO/STO thin films

S2. 3D reciprocal space tomography of LCMO/STO films

S3. Reciprocal space maps of samples grown under different conditions

S4. Magnetization vs. temperature of films grown under different conditions

S5. $M(H)$ hysteresis loops of epitaxial LCMO/STO thin films of different thickness

S1. X-ray reflectivity spectra of epitaxial LCMO/STO thin films

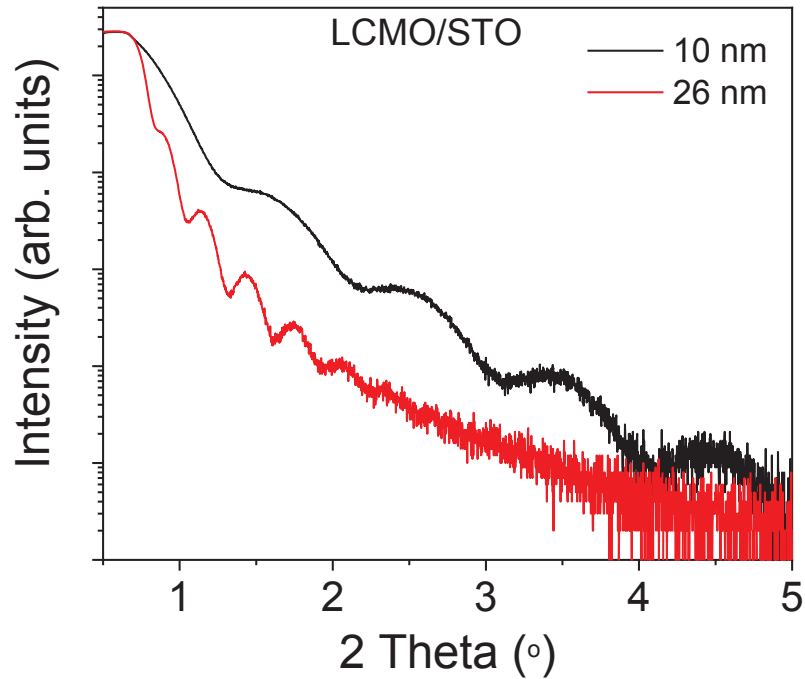


Figure S1: X-ray reflectivity spectra of two LCMO/STO films of thickness 10 nm (black line) and 26 nm (red line) respectively

S2. 3D reciprocal space tomography of LCMO/STO films

3D reciprocal space tomography was done by collecting diffracted intensity using a Bruker D8 advance diffractometer equipped with a 2D GADDS detector (four-circles). Phi-scans were performed at small steps ($\Delta\phi = 0.5^\circ$) for two different values of Ψ angle (28° , 63°) and two different values of α angle ($\alpha \equiv 2\theta$ at the center of the detector, 25° , 45°). Figure S2 shows the collected intensity at two cuts of the reciprocal space, perpendicular to (001) direction at values of $q_z \sim 1/a_{\text{STO}}$ (S2(a)) and $q_z \sim 1/2a_{\text{STO}}$ (S2(b)).

In figure S2(a) all diffraction peaks have integer indices, no peaks indexed as $(h/2k1)$ ($h=\text{odd}$) or $(hk/21)$ ($k=\text{odd}$) can be seen (indices are referred to primitive cubic reciprocal lattice). Besides, diffraction peaks indexed as $(hk\frac{1}{2})$ can be seen in figure S2(b) but not in figure S2(a). This shows that LCMO is orientated with c perpendicular to the film.¹

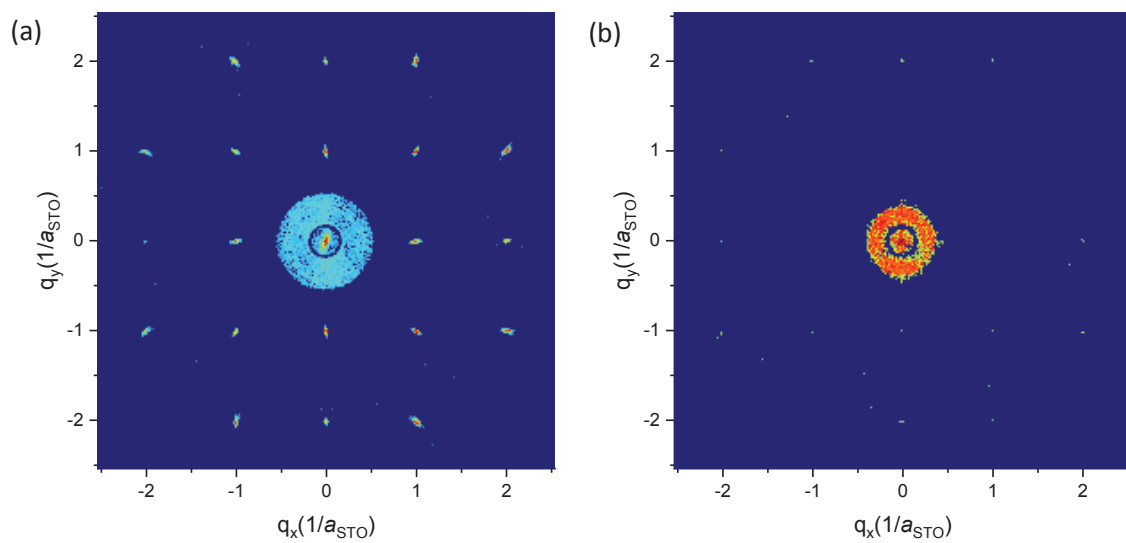


Figure S2: Cuts of the reciprocal space at around (a) $l=1$ ($q_z \sim 1/a_{\text{STO}}$) and (b) $l= \frac{1}{2}$ ($q_z \sim 1/2a_{\text{STO}}$).

S3. Reciprocal space maps of samples grown under different conditions

Reciprocal space maps of two 26 nm thick samples prepared under different annealing conditions are shown in Figure S3. Sample (a) exhibits very good magnetization properties and has been prepared with a long annealing time at high oxygen flow, while sample (b) has been annealed for a short time under low oxygen flow. In both cases LCMO films grow epitaxial cube-on-cube and fully strained with the substrate. XRD spectra of different samples indicate that the degree of crystallinity and the microstructural film's quality improves with increasing annealing time and oxygen flow.

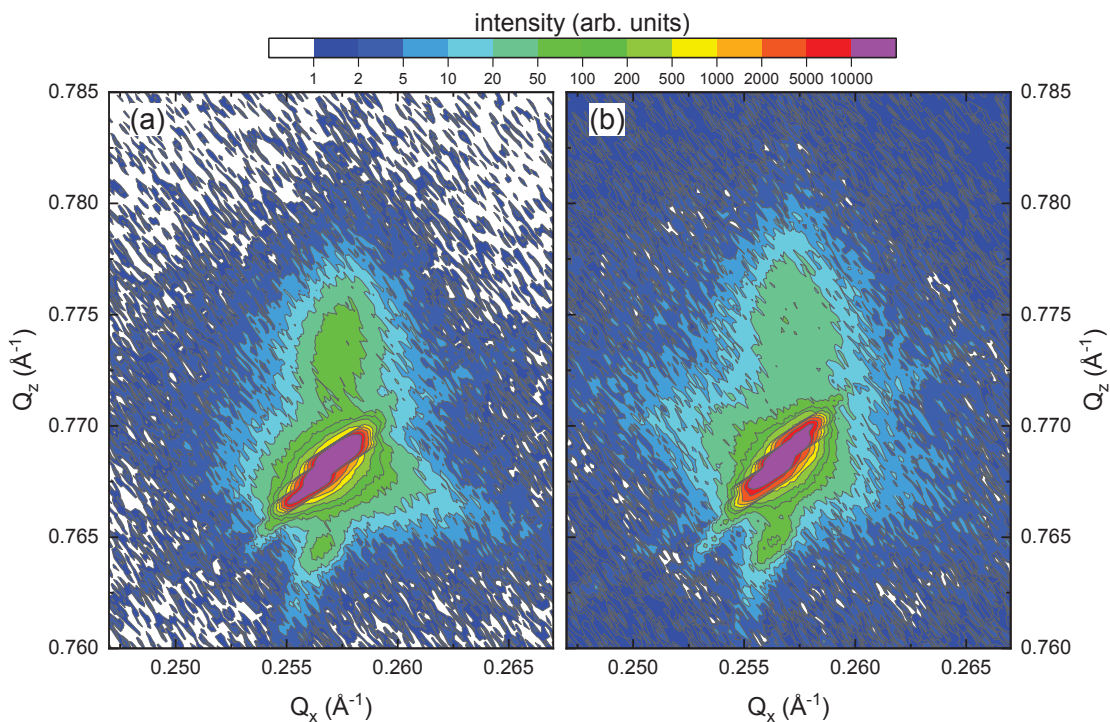


Figure S3: Reciprocal space maps around STO-(103) reflection for two samples prepared at: (a) 900 °C, with long annealing time (60 min) and high oxygen flow (0.3 l/min); and (b) 900 °C, with short annealing time (15 min) and low oxygen flow (0.1 l/min).

S4. Magnetization Vs. temperature of films grown under different conditions

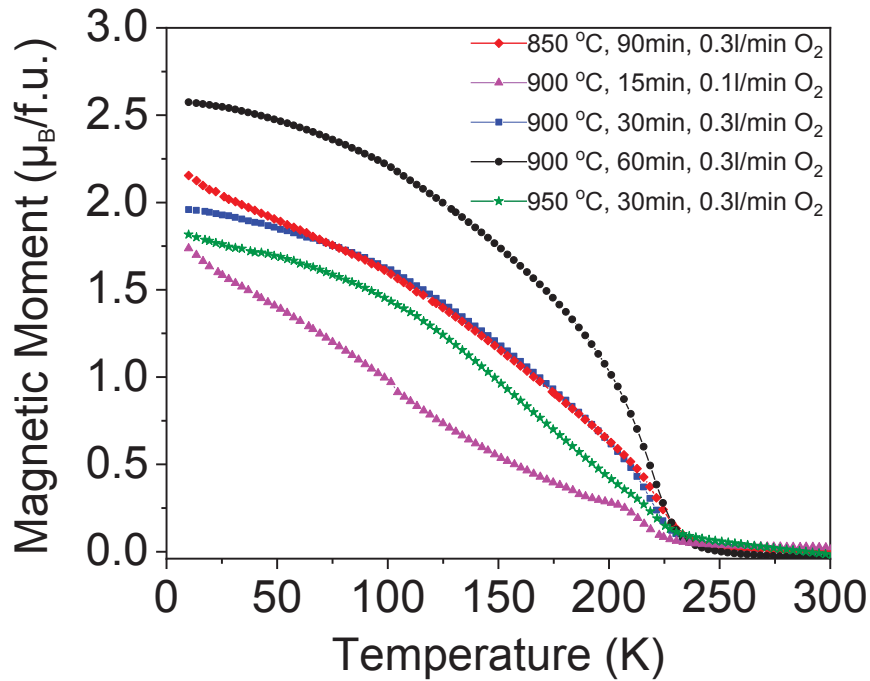


Figure S4: Magnetization vs. temperature of different films grown under different conditions, measured under an applied magnetic field $H=1$ kOe.

From figure S4, it is evidenced that to obtain good magnetic ordering it is necessary to attain high enough temperatures (900 °C), long annealing times (60 min) and high oxygen flow (0.3 l/min). Samples grown under lower oxygen flow (0.1 l/min) or shorter annealing times show lower magnetization values. In concomitance with the improvement in magnetic properties, the degree of crystallinity and the micro-structural film's quality also improves with increasing annealing time and oxygen flux, as it can be appreciated from Figure S3.

S5. $M(H)$ hysteresis loops of epitaxial LCMO/STO epitaxial thin films of different thickness

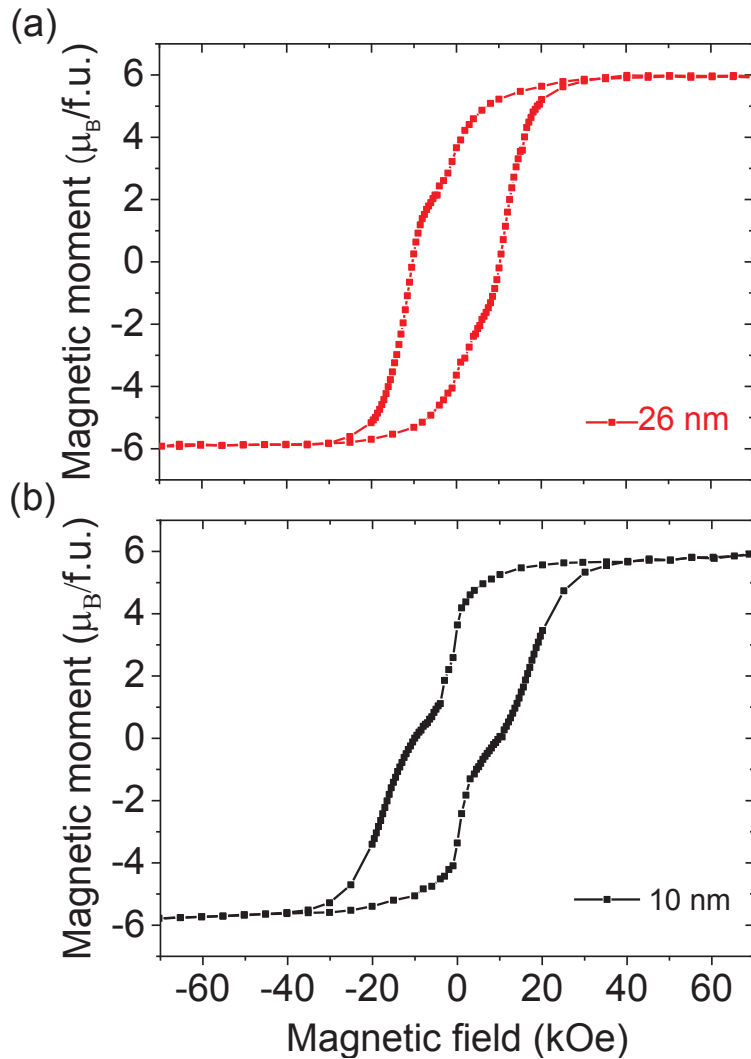


Figure S5: Out of plane $M(H)$ hysteresis loops at 10K for two LCMO films grown on STO of different thickness (a) 26 nm, (b) 10 nm.

$M(H)$ loops in Figure S5 show the typical biloop shape. The origin of this sudden drop of the remanent magnetization at $H=0$, is due to the existence of antiphase boundaries. Antiphase boundaries appear because nucleation of Co^{2+} and Mn^{4+} cationic ordering may occur at different positions in different regions of the sample,

when regions with inverted Co^{2+} and Mn^{4+} positions relative to the other merge together an antiphase boundary is formed. As pointed out by Dass and Goodenough,² at the antiphase interface $\text{Co}^{2+}\text{-O-Co}^{2+}$ or $\text{Mn}^{4+}\text{-O-Mn}^{4+}$ AF interactions occur, on lowering field from saturation, at $H=0$, any antiphase regions would revert back to an antiparallel orientation with a 180° change of spin orientation across an antiphase boundary, which would produce the observed sudden drop of the remanent magnetization. This drop is more pronounced in thinner films indicating a larger contribution of antiphase boundaries on the magnetic hysteresis loops.

References:

1. Galceran, R; Frontera, C; Balcells, Ll.; Cisneros-Fernandez, J; Lopez-Mir, L; Roqueta, J; Santiso, J; Bagues, N; Bozzo, B; Pomar, A; Sandiumenge, F; and Martinez, B; Engineering the microstructure and magnetism of $\text{La}_2\text{CoMnO}_{6-\delta}$ thin films by tailoring oxygen stoichiometry *Appl. Phys. Lett.* (2014) 105, 242401.
2. Dass R.I. and Goodenough J.B.; Multiple magnetic phases of $\text{La}_2\text{CoMnO}_6$, *Phys. Rev. B: Condens. Matter* (2003) 67, 014401.

4.2 La₂CoMnO₆ and La₂NiMnO₆ double perovskite epitaxial thin films grown by polymer assisted deposition, structural and magnetic properties

Chemical solution deposition techniques are appearing as a very promising methodology to achieve epitaxial oxide thin films combining high performance with high throughput and low cost. As already mentioned in the previous chapter, complex oxides with double perovskite structure (A₂BB'O₆) exhibit a breadth of multifunctional properties with a vast potential range of applications in many different fields of technological interest. Moreover, the physical properties of these materials are strongly dependent on the ordered arrangement of cations in the B sublattice of the double perovskite structure, which is hard to attain. Thus, promoting spontaneous cationic ordering has become a very relevant issue. This work represents the extension of the knowledge gained in the polymer assisted deposition (PAD) of La₂CoMnO₆/SrTiO₃ epitaxial thin films (see previous article) and we investigate the growth of epitaxial ferromagnetic insulating double perovskite La₂CoMnO₆ (LCMO) and La₂NiMnO₆ (LNMO) thin films on SrTiO₃ (STO) and LaAlO₃ (LAO) single-crystal substrates by using the PAD method.

Stable complexes of PEI-EDTA–Metal in water were prepared for each single metal. After careful filtering and inductive coupled plasma analysis, precursor solutions with the desired composition and stoichiometry were prepared. The heating ramps were optimized by analyzing the precursor solution decomposition by combined differential scanning calorimetry (DSC) and thermogravimetric (TG) analysis in collaboration with Grup de Recerca en Materials i Termodinàmica (Universitat de Girona). Atomic force microscopy (AFM) and scanning electron microscopy (SEM) images showed that the surfaces of the films are flat and that the composition is uniform across the whole surface area. The reciprocal space maps and high-resolution $\theta/2\theta$ scans allow determining the lattice parameters making evident that LCMO/STO and LNMO/STO thin films grow epitaxially and fully strained on top of STO substrates. In contrast, in the case of LAO substrates LCMO films grow fully relaxed while LNMO films grow partially relaxed.

The magnetic properties of LCMO epitaxial films, saturation magnetization $M_S \approx 5.9 \mu_B/\text{f.u.}$ and Curie temperature $T_C \approx 230 \text{ K}$, are indicative of almost full Co/Mn B-site cationic ordering, in good agreement with previous scanning transmission electron microscopy (STEM) studies. LNMO epitaxial thin films, on their side, display T_C values about 270 K, but saturation magnetization values $M_S \approx 4 \mu_B/\text{f.u.}$, are depleted compared with the expected spin-only theoretical value ($M_S = 5 \mu_B/\text{f.u.}$), which suggest the existence of anti-site disorder (ASD) at the Ni/Mn sublattice.

By using X-ray absorption spectroscopy measurements performed at ALBA synchrotron radiation facilities, we have verified that the oxidation state of Ni is +2, and that of Mn is +4, irrespective to the structural strain and the amount of ASD of the samples. Therefore, since no other than Mn^{4+} and Ni^{2+} valence states are present in the samples, we conclude that the reduction of magnetic moment in the LNMO samples is linked to the disordered Ni-Mn occupancy of the B sublattice, i.e. introducing ASD. ASD give place to $\text{Ni}^{2+}\text{-O}^{2-}\text{-Ni}^{2+}$ and $\text{Mn}^{4+}\text{-O}^{2-}\text{-Mn}^{4+}$ superexchange antiferromagnetic interactions reducing the saturation magnetization, M_S , value by a factor of $(1-2X_{\text{ASD}})$, with X_{ASD} being the fraction of ASD.

The observed differences in the B'-site cationic ordering between LCMO and LNMO thin films are attributed to the larger ionic radii difference between Co^{2+} and Mn^{4+} compared to that of Ni^{2+} and Mn^{4+} , making B-site cationic ordering in the LCMO system more favorable than for LNMO.

Aqueous Chemical Solution Deposition of Functional Double Perovskite Epitaxial Thin Films

Hailin Wang,^[a] Carlos Frontera,^[a] Javier Herrero-Martín,^[b] Alberto Pomar,^[a] Pere Roura,^[c] Benjamín Martínez,^{*[a]} and Narcís Mestres^{*[a]}

[a] H. Wang, Dr. C. Frontera, Dr. A. Pomar, Prof. B. Martínez, Dr. N. Mestres

Institut de Ciència de Materials de Barcelona, ICMAB

Consejo Superior de Investigaciones Científicas, CSIC

Campus de la UAB 08193 Bellaterra, Barcelona (Spain)

E-mail: benjamin.martinez@icmab.es

narcis.mestres@icmab.es

[b] Dr. J. Herrero-Martín

ALBA Synchrotron Light Source

C. de la Llum 2–26, 08920 Cerdanyola del Vallés (Spain)

[c] Prof. P. Roura

Universitat de Girona

Campus Montilivi, Edif. PII

17071 Girona, Catalonia (Spain)

Double Perovskites

SPECIAL ISSUE

Aqueous Chemical Solution Deposition of Functional Double Perovskite Epitaxial Thin Films

Hailin Wang,^[a] Carlos Frontera,^[a] Javier Herrero-Martín,^[b] Alberto Pomar,^[a] Pere Roura,^[c] Benjamín Martínez,^{*[a]} and Narcis Mestres^{*[a]}

Abstract: Double perovskite structure ($A_2BB'O_6$) oxides exhibit a breadth of multifunctional properties with a huge potential range of applications in fields as diverse as spintronics, magneto-optic devices, or catalysis, and most of these applications require the use of thin films and heterostructures. Chemical solution deposition techniques are appearing as a very promising methodology to achieve epitaxial oxide thin films combining high performance with high throughput and low cost. In addition, the physical properties of these materials are strongly dependent on the ordered arrangement of cations in the double perovskite structure.

Thus, promoting spontaneous cationic ordering has become a relevant issue. In this work, our recent achievements by using polymer-assisted deposition (PAD) of environmentally friendly, water-based solutions for the growth of epitaxial ferromagnetic insulating double perovskite La_2CoMnO_6 and La_2NiMnO_6 thin films on $SrTiO_3$ and $LaAlO_3$ single-crystal substrates are presented. It is shown that the particular crystallization and growth process conditions of PAD (very slow rate, close to thermodynamic equilibrium conditions) promote high crystallinity and quality of the films, as well as favors spontaneous B-site cationic ordering.

Introduction

Complex oxides are a class of materials of strong technological relevance because they not only present a broad variety of physical properties of technological interest but there are also several different mechanisms to modify these physical properties at convenience. In particular, the crystalline structure and aspects related to it (strain, defects, vacancies, cationic ordering, ...) are an important playground to tune material properties. A common structure in oxide materials is the perovskite structure; ideal ABO_3 perovskite structure has a cubic symmetry and most of the electronic properties are determined by the physics associated with the transition metal and the


corner-sharing oxygen anions of the BO_6 octahedra. The double perovskite structure of the $A_2BB'O_6$ -type, made of stacking single perovskite units, have attracted considerable attention because of their unique electrical, magnetic, and elastic properties. In the ideal double perovskite structure, in which A is an alkaline earth or a rare-earth metal cation and B and B' are transition metal cations, there exists a 3D network of alternating BO_6 and $B'O_6$ octahedra.^[1] As a result of this, the final physical properties are strongly affected by the B-site cationic ordering.^[2] Achieving full cationic ordering is challenging because the alternative occupancy of the B/B'-site ions can be influenced by several factors, such as synthesis conditions and ionic features. As a general rule, a large difference in size and charge of the B/B'-site cations provides a material with a higher degree of ordering.^[1]


In particular, La_2MMnO_6 ($M=Co, Ni$) compounds with B-site ordering display high Curie temperatures,^[3] which has been explained by ferromagnetic (FM) superexchange interactions according to the Goodenough–Kanamori rules.^[4] In addition, these oxides combine their high-temperature FM with insulating behavior.^[5] Dielectric properties close to room temperature^[6] and large magnetic field induced changes in the electric resistivity have also been reported.^[7] These properties make La_2MMnO_6 double perovskites interesting candidates for potential thin-film spin-based electronics,^[8] lead-free materials for use in solar cells^[9] and more recently, for cathode materials in intermediate temperature solid-oxide fuel cells.^[10] However, some of these properties critically depend on the degree of cationic ordering. In particular, the lack of cationic ordering results in competing ferro- and antiferromagnetic interactions and depressed saturation magnetization,^[5a] making the mag-

[a] H. Wang, Dr. C. Frontera, Dr. A. Pomar, Prof. B. Martínez, Dr. N. Mestres
 Institut de Ciència de Materials de Barcelona, ICMA B
 Consejo Superior de Investigaciones Científicas, CSIC
 Campus de la UAB
 08193 Bellaterra, Barcelona (Spain)
 E-mail: benjamin.martinez@icmab.es
 narcis.mestres@icmab.es

[b] Dr. J. Herrero-Martín
 ALBA Synchrotron Light Source
 C. de la Llum 2–26, 08920 Cerdanyola del Vallès (Spain)

[c] Prof. P. Roura
 Universitat de Girona
 Campus Montilivi, Edif. PII
 17071 Girona, Catalonia (Spain)

 Supporting information and the ORCID identification number(s) for the author(s) of this article can be found under:
<https://doi.org/10.1002/chem.202000129>

 Part of a Special Issue on Low Temperature Solution Route Approaches to Oxide Functional Nanoscale Materials.

netic behavior a good indicator for the degree of cation ordering.

As oxides are increasingly applied as thin films or nanostructures to harness the varied benefits of miniaturization, convenient film deposition methods have to be developed. Although high-vacuum methods like molecular beam epitaxy,^[11] radiofrequency sputtering,^[12] and pulsed laser deposition (PLD)^[13] provide, in general, unquestionable advantages for the growth of metal oxide thin films including high crystal quality, precise control of composition and thickness at the atomic-scale, more affordable alternatives are desirable. In this context, solution-based fabrication methods are being pursued as an alternative for economically viable and large-scale production of functional ceramic oxide thin films, nanoparticles, mesoporous solids films, or bulk ceramics.^[14] The main advantage of this chemical solution deposition (CSD) methodology is the low cost, and easy scalability, associated with the process because the use of high vacuum systems is no longer required. In addition, the precursor solution can be modified in terms of solvent and molarity to tune different desirable thicknesses. Another advantage is the easy control of the desired final stoichiometry and the in situ doping feasibility, simply by adding a doping agent to the precursor solution. The trend nowadays is the development of solution-based processes that are environmentally friendly and processes that can be used with low-temperature techniques such as self-combustion and deep-ultraviolet photochemical activation, enabling the direct integration of metal oxide layers on low melting point polymeric substrates for flexible electronic systems.^[15] Despite these achievements, the mechanism transforming combustion-precursors into oxides is under debate and several authors have cast doubts that combustion really occurs in thin films.^[16] Recent results by means of photocatalytically assisted decomposition of liquid precursors of metal oxides show the successful integration of crystalline metal oxides on flexible substrates at temperatures as low as 325 °C.^[17]

Concerning environmentally friendly precursor solutions, water is well recognized as an ideal and green solvent. However, with metal ions that are easy to hydrolyze (e.g., La^{3+} , Sr^{2+}), it is difficult to form a stable solution in water.^[18] Moreover, it is hard to control the real metal ion concentration of the aqueous precursor solution, which often results in nonstoichiometric growth of the thin film compound. These problems have been solved by the approach proposed by Jia et al.,^[19] which involved preparing a stable metal-ion aqueous system, based on a homogeneous metal-polymer complex solution. A water-soluble polymer is used to bind and stabilize the metal ions in the precursor solution and, at the same time, facilitate the film coating. Specifically, the metal ions (usually nitrate salts or chloride salts) are coordinated with lone-pair electrons of the nitrogen atoms in the polyethyleneimine (PEI) polymer, preventing in this way hydrolysis of metal ions and hence forming stable metal-polymer complexes.^[19,20] In some cases, the use of an additional complexing agent like ethylenediaminetetraacetic acid (EDTA) is required to improve the coordination of metal cations to the polymer. To recapitulate, the polymer-assisted deposition (PAD) route is only composed of metal

nitrate, multidentate polymers, and deionized water, and consequently it is considered to be free of health risks and environmentally friendly. Moreover, PAD solutions are highly stable over time and allow preparation of a library of a large number of metal cations, which can be subsequently mixed according to the desired stoichiometry. As a surfactant-assisted synthesis method, the PEI present in the solution controls the viscosity and binds metal ions, resulting in homogeneous mixing of metal ions in the gel and the formation of uniform metal-organic films, providing a facile chemical approach to both simple and complex crack-free epitaxial metal oxide films.

Despite the scientific and technological interest in $\text{La}_2\text{CoMnO}_6$ and $\text{La}_2\text{NiMnO}_6$ double perovskites, more effort is needed to bring them from laboratory research to applications. Towards this end, it is essential to search for synthesis routes able to provide thin films of target products with low cost and good control of the composition, cation ordering, and cation charge and coupling. In this context, the above-mentioned specificities of PAD have proven to be very beneficial for the growth of complex oxide layers^[21] and, recently, we have demonstrated the PAD growth of B-site ordered $\text{La}_2\text{CoMnO}_6/\text{SrTiO}_3$ double perovskite epitaxial thin films, with perfect crystallinity and a high degree of B-site cationic ordering.^[22]

In the present work, we report the epitaxial growth of $\text{La}_2\text{CoMnO}_6$ (LCMO) and $\text{La}_2\text{NiMnO}_6$ (LNMO) compounds on (001)- SrTiO_3 (STO) and (001)- LaAlO_3 (LAO) substrates by the PAD technique. We have investigated the influence of the substrate, on the structure and magnetic properties of the films. LCMO epitaxial thin films exhibit a single magnetic phase with high saturation magnetization (M_s) values, indicative of full $\text{Co}^{2+}/\text{Mn}^{4+}$ B-site cationic ordering, whereas the LNMO films showed a more complex magnetic behavior suggesting the persistence of anti-site defects lowering M_s with respect to the spin-only maximum theoretical value.

Results and Discussion

To trace the thermal behavior of the mixed metal polymer precursor solution thin films during the annealing in a conventional tube furnace, we used thermogravimetric analysis combined with differential scanning calorimetry (TGA/DSC). Films of several hundreds of nanometers were obtained by the free spreading of a microdrop containing the precursor solution on glass substrates. High purity oxygen and synthetic air at a flow rate around 50 mL min^{-1} were used to control the furnace atmosphere with a heating rate of $20^\circ\text{C min}^{-1}$. Figure 1 shows the TGA curve for a $\text{La}_2\text{NiMnO}_6$ precursor solution film. It can be seen that the sample begins to decompose at 220 °C, and that there is gradual mass loss (PEI, EDTA, and nitrates loss) that finishes at around 550 °C. This suggests that the polymer and nitrate compound is completely decomposed and that the $\text{La}_2\text{NiMnO}_6$ phase may be obtained above this temperature. The heat of decomposition has been measured by DSC and an exothermic signal has been recorded with an exchanged heat of approximately 7.500 J g^{-1} , which is consistent with the redox reaction between the polymer and the nitrate groups.

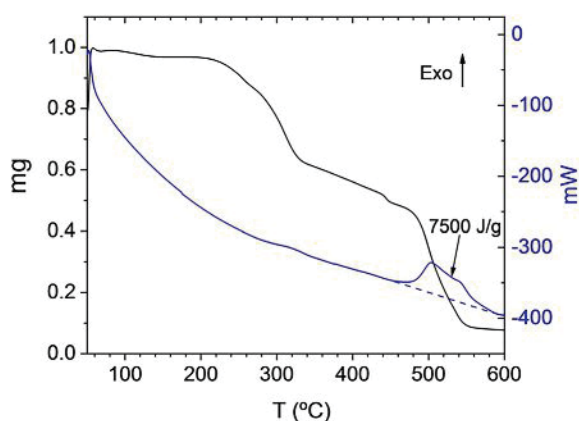


Figure 1. TGA and DSC curves of the thermal decomposition of $\text{La}_2\text{NiMnO}_6$ precursors, made from nitrate precursors, EDTA, and PEI.

In the PAD process, the coordination between the polymers and the metal cations prevents premature nucleation below the temperature of decomposition of the polymers. In this way, the metal cations are inactive before the polymers are thermally decomposed.^[20a,21] Thus, crystallization of the oxide takes place near the decomposition temperature of the polymer and nitrates, that is, close to thermodynamic equilibrium conditions; and it has been proposed that these particular growth conditions of PAD are much more favorable for attaining spontaneous B-site cationic ordering.^[22]

Figure 2 shows atomic force microscopy topography images in tapping mode of representative LCMO and LNMO films grown on top of STO and LAO substrates (film thickness $d \approx 25$ nm). Samples were grown at 900°C , with heating and cooling ramps of $3^\circ\text{C}\text{min}^{-1}$, dwell time 60 min, and oxygen flow 0.3 Lmin^{-1} . Topography shows a high-quality flat surface with root-mean-square (rms) values of surface roughness below 2 nm in all cases. For samples grown on STO substrates the RMS values are below 1 nm. This fact may be related to the lower lattice mismatch between LCMO and LNMO and STO substrates, which favors coherent growth (see below). Samples with thicknesses below 10 nm clearly show the terrace-like morphology imposed by the conformal growth on top of the substrate steps.^[22] Sample uniformity across the whole surface area has been demonstrated by field-emission scanning electron microscopy, visualizing secondary electron

images (information on topography) as well as backscattered electron images (sensitive to differences in composition).

The structural features of LCMO and LNMO films grown on STO and LAO substrates have been studied by X-ray diffraction. The epitaxial nature of the films was evidenced by the detection of only (001) peaks along with the corresponding (001) peaks originating from the (001)-STO and -LAO substrates, and the K_β reflection. No superlattice peaks as a result of cation ordering were observed in the measured XRD spectra. These peaks are expected to be within the noise level in the present case^[23] owing to the fact that Co/Mn and Ni/Mn have a very similar number of electrons; and consequently, their form factors are too similar to give a sizeable contrast in X-ray diffraction.

Reciprocal space maps of LCMO films around the (103) substrate peaks (Figure 3(a) and (b)) reveal that the films on STO substrates grow fully strained without any measurable difference of the in-plane lattice parameters, as illustrated by Figure 3(a). An out-of-plane lattice parameter $c = 3.872 \text{ \AA}$ is estimated from the high-resolution X-ray diffraction pattern of the (002) diffraction peak (see Figure 3(c)). These measurements performed in new samples confirm our previous results on the LCMO/STO system^[22] and make evident the high stability of the precursor solutions and the reproducibility of the samples. On the other hand, LCMO films grown on LAO were fully relaxed, and the in-plane parameter estimated from the reciprocal space map is about $a = 3.89 \text{ \AA}$, Figure 3(b). The high-resolution $\theta/2\theta$ scan around the (002) substrate peak (Figure 3(d)) was used to estimate an out-of-plane lattice parameter $c = 3.886 \text{ \AA}$. These values are consistent with a fully relaxed LCMO/LAO film.

A similar analysis was conducted on LNMO films. Reciprocal space maps of LNMO films around (103) substrate peaks (Figure 4(a) and (b)) show that the films grown on STO substrates are fully strained (Figure 4(a)). An out-of-plane lattice parameter $c = 3.854 \text{ \AA}$ is estimated from the high-resolution X-ray diffraction pattern of the (002) diffraction peak (see Figure 4(c)), which is shorter than the corresponding in-plane lattice parameter. In contrast, the peak position of the (103) reflection of the LNMO films grown on LAO is clearly shifted from that of the LAO substrate along the Q_{100} axis (Figure 4(b)). Although LNMO films are also grown epitaxially on LAO substrates, the large lattice mismatch (-2.61%) between the films and the

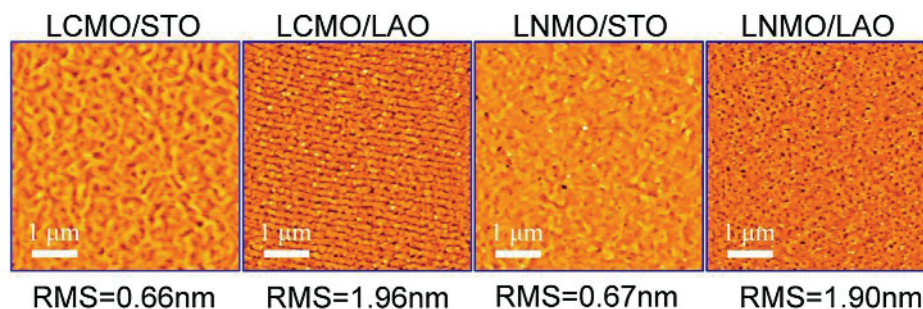


Figure 2. Atomic force microscopy surface topography images ($5 \times 5 \mu\text{m}^2$) of representative La_2MnO_6 thin film samples with thickness values close to 25 nm, on top of STO and LAO substrates. Root-mean-square (RMS) roughness values are below 2 nm in all cases.

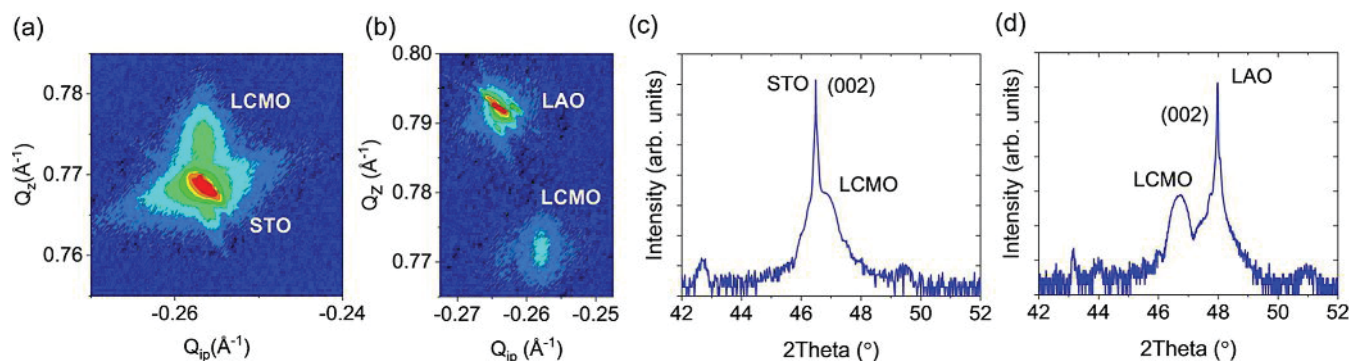


Figure 3. Reciprocal space maps around (103) reflections for LCMO films grown on a) STO and b) LAO. c, d) High-resolution $\theta/2\theta$ XRD scans of the (002) reflections for the same samples.

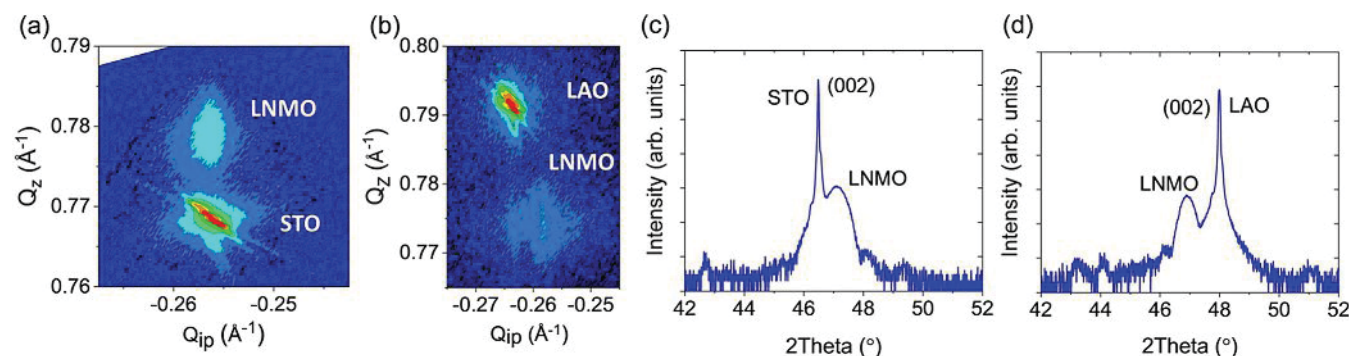


Figure 4. Reciprocal space maps around the (103) reflections for LNMO films grown on a) STO and b) LAO. c, d) High-resolution $\theta/2\theta$ XRD scans of the (002) reflections for the same samples.

LAO substrate causes a relaxation of the film structure. In addition, the larger broadening of the LNMO film peak on LAO indicates that part of the sample is fully relaxed and some part is not.

As the lattice parameters of pseudocubic bulk $\text{La}_2\text{CoMnO}_6$ ($a_{\text{pc}}=3.89 \text{ \AA}$)^[24] and $\text{La}_2\text{NiMnO}_6$ ($a_{\text{pc}}=3.879 \text{ \AA}$)^[25] are close to the lattice parameters of the STO substrate ($a=3.905 \text{ \AA}$), epitaxial $\text{La}_2\text{CoMnO}_6$ and $\text{La}_2\text{NiMnO}_6$ thin films grow coherently on this substrate. However, owing to the large nominal lattice mismatch of the LCMO/LAO (-2.61%) and LNMO/LAO (-2.31%) systems, LCMO grows fully relaxed and LNMO partially relaxed on LAO substrates for film thickness of approximately 20 nm.

Our previous results on LCMO thin films prepared by sputtering indicate that irrespective of the structural strain (tensile or compressive), the oxidation states of Co and Mn ions are Co^{2+} and Mn^{4+} .^[26] According to the Goodenough–Kanamori rules,^[4] superexchange interaction between high spin Co^{2+} ($3d^7$, $t_{2g}^5e_g^2$, $S=3/2$) and Mn^{4+} ($3d^3$, $t_{2g}^3e_g^0$, $S=3/2$) cations promotes ferromagnetic ordering in fully ordered LCMO films. Consequently, a Curie temperature, $T_C \approx 230 \text{ K}$, and a spin-only theoretical saturation magnetization, $M_S = 6 \mu_B/\text{f.u.}$ is observed.^[5,6] However, Co and Mn ions may interchange their crystallographic sites, giving place to what is known as anti-site disorder (ASD). As ASD will promote the appearance of $\text{Co}^{2+}\text{-O-Co}^{2+}$ and $\text{Mn}^{4+}\text{-O-Mn}^{4+}$ antiferromagnetic (AFM) inter-

actions, the saturation magnetization, M_S , will be reduced by a factor $(1-2X_{\text{ASD}})$ with X_{ASD} the fraction of ASD disorder.^[27] Therefore, $M_S = (1-2X_{\text{ASD}}) 6 \mu_B/\text{f.u.}$ is a very sensitive indicator of the degree of B-site cationic ordering. Recently, we have shown that the particular growth conditions of PAD (very slow rate and close to thermodynamic equilibrium conditions) are prone to promote high quality, as well as B-site ordered, LCMO/STO epitaxial thin films.^[22] Accordingly, the magnetic properties extracted from measurements in optimized LCMO/STO new samples (growth temperature 900°C for 60 min with an oxygen flow of 0.3 l min^{-1}) confirm the previous results obtained in ref. [22], and exhibit a Curie temperature of $T_C = 230 \text{ K}$ (see Figure 5(a)). Moreover, no signals for the coexistence of different FM phases, as usually occurs in oxygen-deficient samples prepared by PLD or sputtering^[12b,28] are detected. In Figure 5(b), the measured low-temperature (10 K) saturation magnetization $M_S \approx 5.9 \mu_B/\text{f.u.}$ and a coercive field of $H_C \approx 10 \text{ kOe}$ for an external magnetic field applied perpendicular to the substrate plane (OP-configuration) agree well with data reported for B-site ordered LCMO bulk^[29] and thin film samples.^[12b,30]

Additionally, multiple nucleation sites can generate zones with alternated Co/Mn local ordering. When two of these zones merge together, deviations from the ideal Co/Mn ordering appear at the interface giving rise to $\text{Co}^{2+}\text{-O-Co}^{2+}$ and $\text{Mn}^{4+}\text{-O-Mn}^{4+}$ AFM interactions generating an antiphase bound-

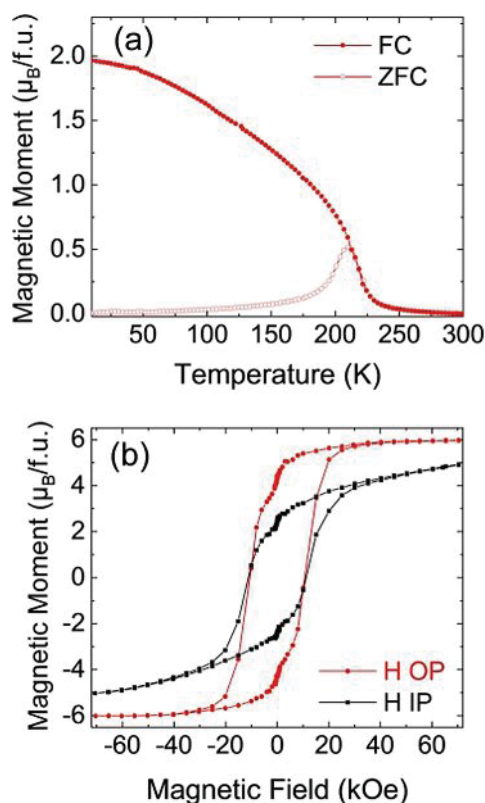


Figure 5. a) Magnetization versus temperature of an LCMO/STO film of 26 nm grown at 900 °C measured after zero-field cooling (open symbols) and field cooling (solid symbols) with a magnetic field of 1 kOe applied in-plane. b) M - H loops recorded at 10 K by applying a magnetic field parallel to the (100)-STO (in-plane) and parallel to (001)-STO (out-of-plane).

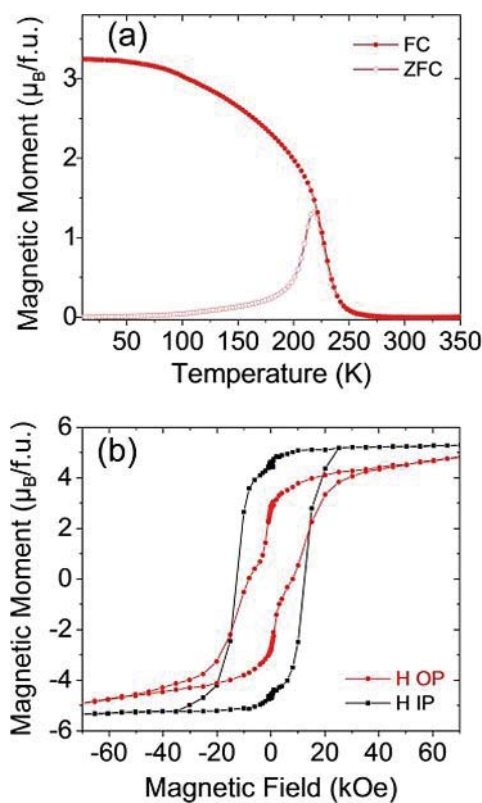


Figure 6. a) Magnetization versus temperature of an LCMO/LAO film of 20 nm grown at 900 °C measured after zero field cooling (open symbols) and field cooling (solid symbols) with a magnetic field of 1 kOe applied in-plane. b) M - H loops recorded at 10 K by applying a magnetic field parallel to (100)-LAO (in-plane) and parallel to (001)-LAO (out-of-plane).

dary (APB). APBs also promote a reduction of the saturation magnetization; however, their effect is very much smaller than that of ASD. They act as domain walls between the FM domains, within which a $\text{Co}^{2+}/\text{Mn}^{4+}$ ordering exists,^[2d,4b] and their signature appears as a sudden drop in the remnant magnetization at $H=0$, as observed in Figure 5(b).^[5a,22] This figure also makes evident the strong anisotropic behavior of the LCMO/STO thin film samples, as the OP direction is the easy magnetization direction, in agreement with theoretical prediction and experimental evidence reported in previous work.^[12b,26]

The same behavior is observed for LCMO/LAO thin films (see Figure 6). The temperature dependence of the magnetization for a 20 nm thick sample grown at a temperature of 900 °C with an oxygen flux of 0.3 L min^{-1} , measured in IP configuration under a field of 1 kOe is shown in Figure 6(a). A Curie temperature of 230 K was observed with no signals of any secondary phase, indicating optimum oxygen content and high film quality.

One can also infer from the $M(H)$ curves in Figure 6(b) that IP is the easy magnetization direction as expected for LCMO films under in-plane tensile strain.^[26b] On the other hand, Figure 6(b) shows that IP saturation magnetization almost reaches the spin-only saturation value of $6 \mu_{\text{B}}/\text{f.u.}$, therefore indicating full B-site cationic ordering as in the case of LCMO/STO films.

As in the previous case, clear signatures of the existence of APB are also evident in Figure 6(b).

We move now to the analysis of the magnetic properties of LNMO thin film samples. In contrast to the LCMO system, the $M(T)$ curves of the LNMO samples exhibit a more complex structure, which in some cases has been considered as indicative of the existence of different magnetic phases^[31] with two distinct magnetic transition temperatures at $T_{\text{C1}} \approx 270$ K and $T_{\text{C2}} \approx 150$ K (see Figure 7(a)). The sharp transition at $T_{\text{C1}} \approx 270$ K was attributed to the Ni^{2+} -O- Mn^{4+} superexchange interaction between Ni^{2+} ($3d^8$, $t_{2g}^6 e_g^2$, $S=1$) and Mn^{4+} ($3d^3$, $t_{2g}^3 e_g^0$, $S=3/2$) ions owing to Ni/Mn cation ordering. At the same time, the broad transition at T_{C2} about 150 K was ascribed to the Ni^{3+} -O- Mn^{3+} superexchange interaction between low-spin Ni^{3+} ($3d^7$, $t_{2g}^6 e_g^1$, $S=1/2$) and high-spin Mn^{3+} ($3d^4$, $t_{2g}^3 e_g^1$, $S=2$) cations.^[32] However, recent results indicate that this particular shape of the $M(T)$ curve is not indicative of different magnetic phases but may well be related to the existence of ASD (i.e., disordered occupancy of the Ni/Mn sites).^[33] Accordingly, featureless $M(T)$ curves should be indicative of a smaller amount of ASD (see Figure 7(a)). Nevertheless, it is worth noting that $M(T)$ curves of the Ni/Mn system are always much flatter than those of the Co/Mn system, which could be indicative of a higher degree of cationic disorder. This fact is also confirmed by a smaller saturation magnetization with respect to the spin-

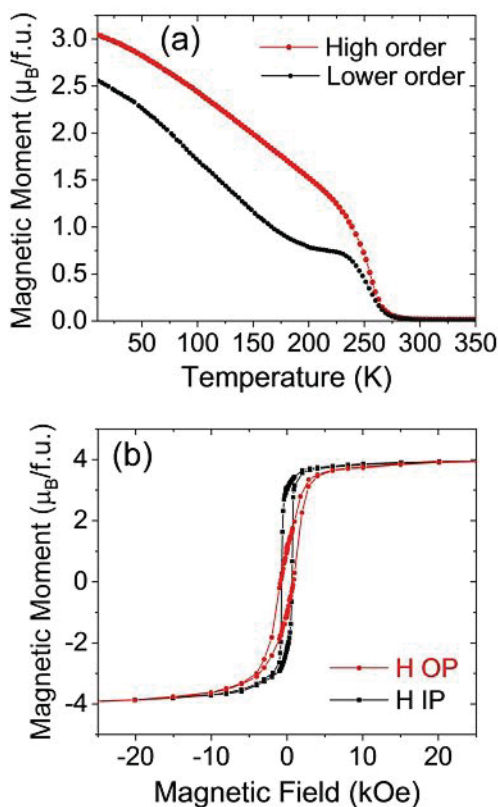


Figure 7. a) Magnetization versus temperature of two LNMO/STO films with different amounts of ASD, measured after field cooling with a magnetic field of 1 kOe applied in-plane. b) M - H loops of the more ordered LNMO/STO film in a) recorded at 10 K by applying a magnetic field H parallel to (100)-STO (in-plane) and parallel to (001)-STO (out-of-plane).

only theoretical value of the LNMO system ($M_s = 5 \mu_B/f.u.$; see Figure 7(b)). Figure 7(a) also shows that the FM transition temperature is $T_C \approx 270$ K, irrespective to the amount of ASD in the sample, as T_C is proportional to the strength of the superexchange FM interactions, which are stronger in the LNMO system than in LCMO.

Similar results are obtained for LNMO films grown on top of LAO substrates. $M(T)$ curves are very alike the LNMO/STO samples with a FM transition temperature $T_C \approx 270$ K. As in the previous case, samples with a larger amount of ASD exhibit a non-monotonic $M(T)$ curve with a local minimum around $T \approx 150$ K (see Figure 8(a)). This is further supported by the smaller saturation magnetization values obtained for these samples.

Comparison between LCMO and LNMO magnetization curves (see Figures 5(b), 6(b), 7(b), and 8(b)) make evident that LCMO samples exhibit strong perpendicular magnetic anisotropy, which is absent in LNMO samples. It is worth mentioning that LNMO samples show small in-plane anisotropy. Another interesting difference between $M(H)$ in LCMO and LNMO systems is the absence of APB in the latter. The typical sudden drop of the magnetization at $H=0$ observed very often in $M(H)$ curves of LCMO samples, associated with the existence of APB, is completely absent in the case of LNMO samples. However, LNMO samples show clear evidence of ASD. The appear-

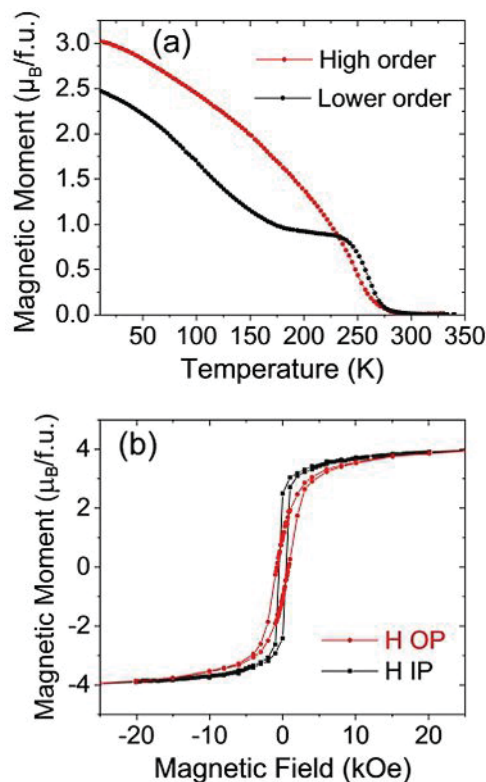


Figure 8. a) Magnetization versus temperature of two LNMO/LAO films with different amounts of ASD, measured after field cooling with a magnetic field of 1 kOe applied in-plane. b) M - H loops of the more ordered LNMO/LAO film in a) recorded at 10 K by applying a magnetic field H parallel to (100)-LAO (in-plane) and parallel to (001)-LAO (out-of-plane).

ance of ASD, where Ni and Mn ions interchange their crystallographic sites, would mask the effect of multiple nucleation sites generating zones with alternated Ni/Mn local ordering, thus precluding the formation of APB.

On the other hand, the obtained value of $M_s \sim 4 \mu_B/f.u.$ corresponds to a concentration of ASD of about 10% [$M_s = (1 - 2X_{ASD}) \times 5 \mu_B/f.u.$], which is among the best of those reported in the literature.^[33b,c,34] Therefore, we should conclude that the particular growth conditions of this PAD technique promote a high degree of spontaneous B-site cationic ordering.

A way to discard the existence of secondary phases in our samples is to determine the oxidation state of Ni and Mn ions. For that purpose, an X-ray absorption spectroscopy (XAS) study has been performed. XAS spectra were recorded across the Ni and Mn $L_{2,3}$ edges by using a Si-drift fluorescence detector in the BL29-BOREAS beamline at the ALBA Synchrotron Light Source (Barcelona, Spain).^[35] This technique is a very sensitive local probe, ideal to study the valence state^[36] and spin^[37] of the ions under analysis.

Figure 9 shows the partial fluorescence yield (PFY) spectra corresponding to two LNMO samples with different amounts of ASD (see Figure 7(a)) in the energy range 845–875 eV. As indicated, La- M_4 and Ni- $L_{2,3}$ absorption edges are in this range of energies. Two important features can be observed for Ni edges. First, the two maxima of the Ni- L_3 edge show very different amplitudes and second, there is a clear split of the Ni- L_2

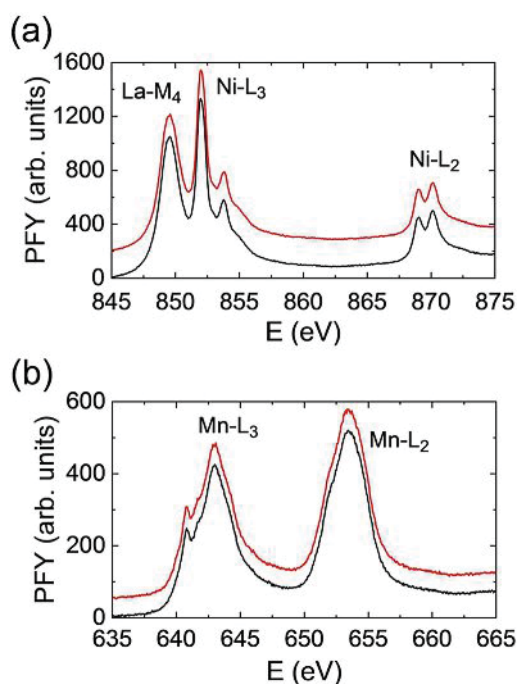


Figure 9. Partial fluorescence yield (PFY) of Ni- $L_{2,3}$ and Mn- $L_{2,3}$ edges measured in the two LNMO/STO thin films displayed in Figure 7 (a), with different amounts of ASD. Red line: high ordered sample, black line: lower ordered sample.

edge (see Figure 9(a)). These two features have been identified as evidence of Ni in a +2 oxidation state in both $\text{LaNiO}_3/\text{LaMnO}_3$ multilayers^[38] and in $\text{La}_2\text{NiMnO}_6$ bulk samples.^[33b,c] Figure 9(b) shows the absorption of the same sample in the region corresponding to Mn- $L_{2,3}$ edges. The position of the L_3 maxima (643 eV) coincides quite well with that reported in ref. [33b] for bulk samples of LNMO in which the valence of Mn is identified as +4. Moreover, the feature visible at 640.8 eV was identified as having a strong d^3 character of the Mn electronic state Mn^{4+} .^[39]

As evident from the figure, spectra corresponding to samples with different amounts of ASD are very much alike. Therefore, XAS measurements confirm that the formal oxidation states of Ni and Mn ions in our samples are Ni^{2+} and Mn^{4+} , irrespective of the structural strain, and in spite of the different values of the saturation magnetization, that is, the amount of ASD, in agreement with previous reports.^[33b,c] So, we can conclude that the features observed in the $M(T)$ curves in the LNMO system are not due to the existence of different magnetic phases but to different amounts of disorder.

The final amount of ASD in a given sample can be influenced by several factors including oxygen and cationic non-stoichiometry, and synthesis and processing conditions.^[40] From a material synthesis standpoint, it has been shown that a large difference between the ionic size and electronegativity of the B/B' cations is crucial to promote ordering.^[1] XAS analysis allows us to conclude that in both LCMO and LNMO systems the oxidation states of Co, Ni, and Mn are Co^{2+} , Ni^{2+} , and Mn^{4+} , therefore no mayor differences are expected from this

aspect. However, the ionic radii difference between Co^{2+} and Mn^{4+} is larger than that between Ni^{2+} and Mn^{4+} ^[41] (21.5 pm and 16.0 pm, respectively), which makes B-site cationic ordering in the LCMO system more favorable than for LNMO, as experimentally observed.

Conclusion

We have synthesized high-quality $\text{La}_2\text{CoMnO}_6$ and $\text{La}_2\text{NiMnO}_6$ epitaxial thin films on STO and LAO substrates by using a polymer-assisted deposition technique. The physical properties of these oxide compounds, in particular magnetic properties, are very sensitive to the presence of long-range B-site cationic ordering; therefore, obtaining full cationic ordering is fundamental for potential technological applications. In this work, we show that the particular growth process and crystallization conditions of PAD (very slow rate, close to thermodynamic equilibrium conditions) promote the high crystallinity and quality of the films, as well as favoring high B-site cationic ordering.

The magnetic properties of $\text{La}_2\text{CoMnO}_6$ films ($M_s \approx 5.9 \mu_B/\text{f.u.}$ and $T_C \approx 230 \text{ K}$) are indicative of almost full Co/Mn B-site cationic ordering. However, signals indicating the presence of antiphase boundaries are detected. In the case of $\text{La}_2\text{NiMnO}_6$ epitaxial thin films, superexchange interactions are a bit stronger, leading to a ferromagnetic transition temperature of $T_C \approx 270 \text{ K}$. However, saturation magnetization values are depleted compared with the expected spin-only theoretical value ($M_s = 5 \mu_B/\text{f.u.}$), which suggest the existence of anti-site disorder at the Ni/Mn sublattice. Values around $M_s \sim 4 \mu_B/\text{f.u.}$ are obtained, indicating around 10% ASD, which compares very well with previous reports. The observed differences between LCMO and LNMO are attributed to the ionic radii difference between Co^{2+} and Mn^{4+} and that of Ni^{2+} and Mn^{4+} making B-site cationic ordering in the LCMO system more favorable than for LNMO. By using X-ray absorption spectroscopy, we have verified that the oxidation state of Ni is +2, and that of Mn is +4, irrespective of the structural strain and the amount of ASD of the samples. We conclude that the reduction of magnetic moment in the LNMO samples is linked to the introduction of $\text{Ni}^{2+}-\text{O}^{2-}-\text{Ni}^{2+}$ and $\text{Mn}^{4+}-\text{O}^{2-}-\text{Mn}^{4+}$ superexchange AF interactions at anti-sites reducing the saturation magnetization, M_s , by a factor of $(1-2X_{\text{ASD}})$, with X_{ASD} being the fraction of ASD disorder.

Our results make evident the advantage of the CSD-PAD method over physical methods (far from thermodynamic equilibrium growth) to optimize spontaneous B-site cationic ordering as well as the desirable physical properties of functional double perovskite oxide thin films. In addition, in the context where the demand for sustainable and environmentally friendly reactants and processes steadily increases, PAD is based on using aqueous solutions of environmentally friendly metal salts and commercially available polymers.

Experimental Section

Chemicals and solvents

The PAD technique relies on the use of water-soluble polymers with functional $-NH_2$ groups that coordinate cations and prevent their hydrolysis. The precursor solution for the growth of the LCMO and LNMO thin films were prepared by mixing three separate aqueous solutions of La, Co, Mn and La, Ni, Mn, respectively, bound to polymers. Separate solutions were prepared by using high-purity ($>99.9\%$) metal salts of lanthanum(III) nitrate, cobalt(II) nitrate, nickel(II) chloride, and Mn^{II} nitrate. The polymer used was branched PEI, with an average $M_w \approx 25,000$, and EDTA was used as a complexing agent; both were from Sigma–Aldrich. Water used in the solution preparation was purified by using a Milli-Q water treatment system.

Precursor solutions preparation

In detail, individual solutions of the different metal ions were prepared by dissolving the corresponding nitrate salts in water and EDTA (1:1 molar ratio). PEI was incorporated into the solution in a 1:1 mass ratio with EDTA. The electrostatic interactions of the protonated amino groups of PEI with the $[EDTA-Metal]^{n-}$ complex are crucial for further successful deposition of a homogeneous film. As the direct bonding between PEI and metal is too weak, the chelate ligand EDTA is used to form the EDTA–metal complexes, which can establish hydrogen-bonding and electrostatic interactions with protonated PEI. The pH value plays an important role in the formation of stable individual solutions of different metals. The enhancement of electrostatic interactions, particularly hydrogen bonds, takes place at lower values of pH, where most of the amines of PEI are protonated. The formation of more stable EDTA–metal complexes prefers higher values of pH, whereas the hydrolysis of some cations occurs at relatively high pH. For instance, a $pH \approx 7$ is enough to hydrolyze Mn^{2+} . The pH values of all the initial solutions for each individual cation in this work were adjusted to near 6 to balance all these situations, and prevent the precipitation when mixing them to prepare the final multicationic solutions.

Subsequently, the non-coordinated cations of each single metal solution can be easily removed by filtration processes to prepare a homogeneous precursor solution for each single cation. Each individual solution was filtered by using Amicon filtration units (10 kDa), and retained portions were analyzed by inductively coupled plasma (ICP; Optima 4300 DV ICP-OES PerkinElmer), for careful determination of the cation concentration in the primary solutions. The final concentrations of the solutions used in this work were $[La] = 230.4$ mM, $[Co] = 146.4$ mM, $[Ni] = 272.6$ mM, and $[Mn] = 176.4$ mM. From these primary solutions, the final aqueous precursor solutions with the desired La/Co/Mn 2:1:1 and La/Ni/Mn 2:1:1 final stoichiometry were prepared, and concentrated to reach a final cation concentration of 61–65 mM with respect to Mn. These conditions were adjusted to produce films in the range of 16–26 nm. Similarly, more diluted solutions were adjusted to obtain films in the range of a few nm (3–5 nm). Typical viscosity values were in the range $\eta \approx 3$ –4 MPas (measured with a DMA 4100 M Anton Paar densimeter, with a micro-viscometer module Lovis 2000 ME).

Thermal characterization

Thermal analysis experiments were carried out with a Mettler Toledo TGA85^{LF} thermobalance. Complementary experiments were carried out with a differential scanning calorimeter (DSC)

from TA Instruments (Q2000 apparatus). Films of several hundreds of nanometers were obtained by the free spreading of a microdrop containing the precursor solution on glass substrates. High-purity oxygen and synthetic air at a flow rate of around 50 mL min^{-1} were used to control the furnace atmosphere with heating rate of 20 °C min^{-1} .

Thin films growth

The precursor solutions obtained in this way were spin-coated on top of 0.5×0.5 cm² (001)-STO and 0.5×0.5 cm² (001)-LAO substrates from Crystec GmbH, Germany. Prior to deposition, the as-received STO substrates were chemically etched and thermally treated to create TiO_2 -terminated substrates with atomically flat terraces,^[42] and the LAO substrates were thermally treated to create AlO_2 -terminated substrates with atomically flat terraces.

The last step is the thermal annealing of the spin-coated films under oxygen flow for elimination of the organic components at lower temperatures, and phase formation and crystallization at higher temperatures. Thermal annealing was performed by using a tube furnace with heating rates of several degrees Celsius per minute, under oxygen flow (flow rates between 100 and 600 mL min^{-1}) to avoid the formation of oxygen vacancies. Good quality samples were obtained for optimized growth conditions (growth temperatures above 850 °C, annealing time of ≈ 1 h, and oxygen flow above 0.3 L min^{-1}).

Characterization of structural and physical properties

The structural properties of the epitaxial films were studied by X-ray diffraction and reflectivity by using a D5000 (Siemens) diffractometer, an X'Pert MRD (PANalytical) four-angle diffractometer with monochromatic $Cu_{K\alpha 1}$ radiation (1.54060 Å) and a Bruker D8 Advance GADDS system. Magnetization measurements were performed by using a superconducting quantum interference device (SQUID; Quantum Design) as a function of temperature and magnetic field. External magnetic fields were applied both parallel (IP configuration) and perpendicular (OP configuration) to the sample plane. The diamagnetic contribution of the substrate and other instrumental contributions were properly corrected.^[43] The relative error in the determination of the saturation magnetization (M_s) was approximately 5% and was mostly attributable to the error in the estimation of the film volume. The surface topography of the films was investigated by atomic force microscopy by using an Asylum Research MFP-3D microscope in tapping mode.

X-ray absorption spectroscopy (XAS) and X-ray magnetic circular dichroism (XMCD) were investigated at the Ni and Mn- $L_{2,3}$ edges in the BL29-BOREAS beamline at ALBA Synchrotron Light Source (Barcelona, Spain). The spectra were measured in both the total electron yield (TEY) mode and by partial fluorescence yield (PFY), under ultrahigh vacuum conditions (2×10^{-10} mbar). PFY was measured by using a large area silicon drift detector collecting the non-resonant emission of the O K-edge (energy window of about 100 eV) and applying the inverse partial fluorescence yield technique.^[44] The applied magnetic field (parallel to the X-ray beam) was 2 T. XAS measures were performed at $T = 150$ K.

Acknowledgments

We acknowledge financial support from the Spanish Ministry of Science, Innovation and Universities through Severo Ochoa (SEV-2015–04969), SUMATE (RTI2018-095853-B-C21), and SPIN-

CURIOX (RTI2018-099960-B-I00) projects co-financed by the European Regional Development Fund. Hailin Wang acknowledges financial support from the China Scholarship Council (CSC). This work has been performed in the framework of the Ph.D. program in Materials Science of the Universitat Autònoma de Barcelona (UAB), through the CSC/UAB Joint Scholarship. The authors thank the ALBA Synchrotron (Spain) for the provision of beamtime. The authors also thank Dr. B. Bozzo and F. J. Campos for their technical support during magnetic and X-ray diffraction measurements.

Conflict of interest

The authors declare no conflict of interest.

Keywords: B-site cationic ordering · chemical growth methods · double perovskites · ferromagnetism · polymer-assisted deposition

- [1] a) M. T. Anderson, K. B. Greenwood, G. A. Taylor, K. R. Poeppelmeier, *Prog. Solid State Chem.* **1993**, *22*, 197–233; b) S. Vasala, M. Karppinen, *Prog. Solid State Chem.* **2015**, *43*, 1–36.
- [2] a) K. I. Kobayashi, T. Kimura, H. Sawada, K. Terakura, Y. Tokura, *Nature* **1998**, *395*, 677–680; b) Y. Moritomo, S. Xu, A. Machida, T. Akimoto, E. Nishibori, M. Takata, M. Sakata, *Phys. Rev. B* **2000**, *61*, R7827–R7830; c) M. García-Hernández, J. L. Martínez, M. J. Martínez-Lope, M. T. Casais, J. A. Alonso, *Phys. Rev. Lett.* **2001**, *86*, 2443–2446; d) A. T. Lee, C. A. Marianetti, *Phys. Rev. B* **2018**, *97*, 045102.
- [3] a) G. Blasse, *J. Phys. Chem. Solids* **1965**, *26*, 1969–1971; b) G. H. Jonker, *J. Appl. Phys.* **1966**, *37*, 1424–1430.
- [4] a) J. B. Goodenough, *Phys. Rev.* **1955**, *100*, 564–573; b) J. Kanamori, *J. Phys. Chem. Solids* **1959**, *10*, 87–98.
- [5] a) R. I. Dass, J. B. Goodenough, *Phys. Rev. B* **2003**, *67*, 014401; b) R. I. Dass, J. Q. Yan, J. B. Goodenough, *Phys. Rev. B* **2003**, *68*, 064415.
- [6] M. P. Singh, K. D. Truong, P. Fournier, *Appl. Phys. Lett.* **2007**, *91*, 042504.
- [7] R. N. Mahato, K. Sethupathi, V. Sankaranarayanan, *J. Appl. Phys.* **2010**, *107*, 09D714.
- [8] L. López-Mir, C. Frontera, H. Aramberri, K. Bouzehouane, J. Cisneros-Fernández, B. Bozzo, L. Balcells, B. Martínez, *Sci. Rep.* **2018**, *8*, 861.
- [9] C. Lan, S. Zhao, T. Xu, J. Ma, S. Hayase, T. Ma, *J. Alloys Compd.* **2016**, *655*, 208–214.
- [10] L.-P. Sun, H. Li, Q. Li, L.-H. Huo, H. Zhao, J.-M. Bassat, A. Rougier, S. Fourcade, J.-C. Grenier, *J. Power Sources* **2018**, *392*, 8–14.
- [11] a) A. Y. Cho, J. R. Arthur, *Prog. Solid State Chem.* **1975**, *10*, 157–191; b) D. G. Schlom, *APL Mater.* **2015**, *3*, 062403.
- [12] a) I. Safi, *Surf. Coat. Technol.* **2000**, *127*, 203–218; b) R. Galceran, C. Frontera, L. Balcells, J. Cisneros-Fernández, L. López-Mir, J. Roqueta, J. Santiso, N. Bagués, B. Bozzo, A. Pomar, F. Sandiumenge, B. Martínez, *Appl. Phys. Lett.* **2014**, *105*, 242401.
- [13] a) D. H. A. Blank, G. Koster, G. A. J. H. M. Rijnders, E. van Setten, P. Slycke, H. Rogalla, *J. Cryst. Growth* **2000**, *211*, 98–105; b) M. Opel, *J. Phys. D* **2012**, *45*, 033001.
- [14] a) R. W. Schwartz, T. Schneller, R. Waser, *C. R. Chim.* **2004**, *7*, 433–461; b) T. Schneller, R. Waser, M. Kosec, D. Payne, *Chemical Solution Deposition of Functional Oxide Thin Films*, 1st ed., Springer, Wien, **2013**, pp. 1–796; c) M. L. Calzada in *The Sol-Gel Handbook* (Ed.: D. L. M. Zayat), Wiley-VCH, Weinheim, **2015**, pp. 841–882; d) J. E. ten Elshof in *Epitaxial Growth of Complex Metal Oxides*, 1st ed., Woodhead Publishing, Sawston, **2015**, pp. 69–93; e) N. Bassiri-Gharb, Y. Bastani, A. Bernal, *Chem. Soc. Rev.* **2014**, *43*, 2125–2140.
- [15] a) M. G. Kim, M. G. Kanatzidis, A. Facchetti, T. J. Marks, *Nat. Mater.* **2011**, *10*, 382–388; b) P.-C. Wu, Y.-H. Chu, *J. Mater. Chem. C* **2018**, *6*, 6102–6117; c) I. Bretos, R. Jimenez, J. Ricote, M. L. Calzada, *Chem. Soc. Rev.* **2018**, *47*, 291–308.
- [16] a) D. Sanchez-Rodriguez, J. Farjas, P. Roura, S. Ricart, N. Mestres, X. Obradors, T. Puig, *J. Phys. Chem. C* **2013**, *117*, 20133–20138; b) E. A. Cochran, K. N. Woods, D. W. Johnson, C. J. Page, S. W. Boettcher, *J. Phys. Chem. A* **2019**, *7*, 24124–24149.
- [17] I. Bretos, R. Jimenez, D. Perez-Mezcua, N. Salazar, J. Ricote, M. L. Calzada, *Adv. Mater.* **2015**, *27*, 2608–2613.
- [18] G. Wulfsberg, *Principles of Descriptive Inorganic Chemistry*, Brooks/Cole, Monterey, **1987**.
- [19] Q. X. Jia, T. M. McCleskey, A. K. Burrell, Y. Lin, G. E. Collis, H. Wang, A. D. Li, S. R. Foltyn, *Nat. Mater.* **2004**, *3*, 529–532.
- [20] a) A. K. Burrell, T. M. McCleskey, Q. X. Jia, *Chem. Commun.* **2008**, 1271–1277; b) G. F. Zou, J. Zhao, H. M. Luo, T. M. McCleskey, A. K. Burrell, Q. X. Jia, *Chem. Soc. Rev.* **2013**, *42*, 439–449.
- [21] J. M. Vila-Funqueiriño, B. Rivas-Murias, J. Rubio-Zuazo, A. Carretero-Genievrier, M. Lazzari, F. Rivadulla, *J. Mater. Chem. C* **2018**, *6*, 3834–3844.
- [22] H. Wang, J. Gazquez, C. Frontera, M. F. Chisholm, A. Pomar, B. Martínez, N. Mestres, *NPG Asia Mater.* **2019**, *11*, 44.
- [23] a) D. Waasmaier, A. Kirfel, *Acta Crystallogr. Sect. A* **1995**, *51*, 416–431; b) V. Shabadi, M. Major, P. Komissinskiy, M. Vafaei, A. Radetinac, M. B. Yazdi, W. Donner, L. Alff, *J. Appl. Phys.* **2014**, *116*, 114901.
- [24] M. K. Kim, J. Y. Moon, H. Y. Choi, S. H. Oh, N. Lee, Y. J. Choi, *J. Phys. Condens. Matter* **2015**, *27*, 426002.
- [25] H. Guo, J. Burgess, S. Street, A. Gupta, T. G. Calvarese, M. A. Subramanian, *Appl. Phys. Lett.* **2006**, *89*, 022509.
- [26] a) R. Galceran, L. López-Mir, B. Bozzo, J. Cisneros-Fernández, J. Santiso, L. Balcells, C. Frontera, B. Martínez, *Phys. Rev. B* **2016**, *93*, 144417; b) L. López-Mir, R. Galceran, J. Herrero-Martín, B. Bozzo, J. Cisneros-Fernández, E. V. Pannunzio Miner, A. Pomar, L. Balcells, B. Martínez, C. Frontera, *Phys. Rev. B* **2017**, *95*, 224434.
- [27] L. Balcells, J. Navarro, M. Bibes, A. Roig, B. Martínez, J. Fontcuberta, *Appl. Phys. Lett.* **2001**, *78*, 781–783.
- [28] H. Z. Guo, A. Gupta, J. Zhang, M. Varela, S. J. Pennycook, *Appl. Phys. Lett.* **2007**, *91*, 202509.
- [29] A. J. Barón-González, C. Frontera, J. L. García-Munoz, B. Rivas-Murias, J. Blasco, *J. Phys. Condens. Matter* **2011**, *23*, 496003.
- [30] a) H. Z. Guo, A. Gupta, T. G. Calvarese, M. A. Subramanian, *Appl. Phys. Lett.* **2006**, *89*, 262503; b) R. Egoavil, S. Huhn, M. Jungbauer, N. Gauqueilin, A. Beche, G. Van Tendeloo, J. Verbeeck, V. Moshnyaga, *Nanoscale* **2015**, *7*, 9835–9843.
- [31] a) K. D. Truong, M. P. Singh, S. Jandl, P. Fournier, *Phys. Rev. B* **2009**, *80*, 134424; b) M. P. Singh, C. Grygiel, W. C. Sheets, P. Boullay, M. Hervieu, W. Prellier, B. Mercey, C. Simon, B. Raveau, *Appl. Phys. Lett.* **2007**, *91*, 012503; c) M. P. Singh, S. Charpentier, K. D. Truong, P. Fournier, *Appl. Phys. Lett.* **2007**, *90*, 211915.
- [32] a) V. L. J. Joly, P. A. Joy, S. K. Date, C. S. Gopinath, *Phys. Rev. B* **2002**, *65*, 184416; b) J. Blasco, M. C. Sánchez, J. Pérez-Cacho, J. García, G. Subías, J. Campo, *J. Phys. Chem. Solids* **2002**, *63*, 781–792.
- [33] a) D. Choudhury, P. Mandal, R. Mathieu, A. Hazarika, S. Rajan, A. Sundaresan, U. V. Waghmare, R. Knut, O. Karis, P. Nordblad, D. D. Sarma, *Phys. Rev. Lett.* **2012**, *108*, 127201; b) S. Pal, G. Sharada, M. Goyal, S. Mukherjee, B. Pal, R. Saha, A. Sundaresan, S. Jana, O. Karis, J. W. Freeland, D. D. Sarma, *Phys. Rev. B* **2018**, *97*, 165137; c) M. Nasir, S. Kumar, N. Patra, D. Bhattacharya, S. N. Jha, D. R. Basaula, S. Bhatt, M. Khan, S.-W. Liu, S. Biring, S. Sen, *ACS Appl. Electron. Mater.* **2019**, *1*, 141–153.
- [34] a) S. R. Spurgeon, Y. Du, T. Droubay, A. Devaraj, X. Sang, P. Longo, P. Yan, P. G. Kotula, V. Shutthanandan, M. E. Bowden, J. M. LeBeau, C. Wang, P. V. Sushko, S. A. Chambers, *Chem. Mater.* **2016**, *28*, 3814–3822; b) M. Nasir, M. Khan, S. Kumar, S. Bhatt, N. Patra, D. Bhattacharya, S. N. Jha, S. Biring, S. Sen, *J. Magn. Magn. Mater.* **2019**, *483*, 114–123.
- [35] A. Barla, J. Nicolas, D. Cocco, S. M. Valvidares, J. Herrero-Martín, P. Gargiani, J. Moldes, C. Ruget, E. Pellegrin, S. Ferrer, *J. Synchrotron Radiat.* **2016**, *23*, 1507–1517.
- [36] C. Mitra, Z. Hu, P. Raychaudhuri, S. Wirth, S. I. Csizsar, H. H. Hsieh, H. J. Lin, C. T. Chen, L. H. Tjeng, *Phys. Rev. B* **2003**, *67*, 092404.
- [37] S. Ray, A. Kumar, D. D. Sarma, R. Cimino, S. Turchini, S. Zennaro, N. Zema, *Phys. Rev. Lett.* **2001**, *87*, 097204.
- [38] C. Piamonteze, M. Gibert, J. Heidler, J. Dreiser, S. Rusponi, H. Brune, J. M. Triscone, F. Nolting, U. Staub, *Phys. Rev. B* **2015**, *92*, 014426.
- [39] M. Abbate, F. M. de Groot, J. C. Fuggle, A. Fujimori, O. Strebel, F. Lopez, M. Domke, G. Kaindl, G. A. Sawatzky, M. Takano, Y. Takeda, H. Eisaki, S. Uchida, *Phys. Rev. B* **1992**, *46*, 4511–4519.

- [40] M. P. Singh, K. D. Truong, S. Jandl, P. Fournier, *J. Appl. Phys.* **2010**, *107*, 09D917.
- [41] R. D. Shannon, *Acta Crystallogr. Sect. A* **1976**, *32*, 751–767.
- [42] M. Kareev, S. Prosandeev, J. Liu, C. Gan, A. Kareev, J. W. Freeland, M. Xiao, J. Chakhalian, *Appl. Phys. Lett.* **2008**, *93*, 061909.
- [43] P. Stamenov, J. M. D. Coey, *Rev. Sci. Instrum.* **2006**, *77*, 015106.
- [44] A. J. Achkar, T. Z. Regier, H. Wadati, Y. J. Kim, H. Zhang, D. G. Hawthorn, *Phys. Rev. B* **2011**, *83*, 081106.

Manuscript received: January 10, 2020

Accepted manuscript online: February 26, 2020

Version of record online: May 11, 2020

Chemistry A European Journal

 **Chemistry
Europe**
European Chemical
Societies Publishing

Supporting Information

for Chem. Eur. J. 2020, 26, 9338 – 9347

Aqueous Chemical Solution Deposition of Functional Double Perovskite Epitaxial Thin Films

Hailin Wang,^[a] Carlos Frontera,^[a] Javier Herrero-Martín,^[b] Alberto Pomar,^[a] Pere Roura,^[c] Benjamín Martínez,^{*[a]} and Narcís Mestres^{*[a]}

Chemistry–A European Journal

Supporting Information

Aqueous Chemical Solution Deposition of Functional Double Perovskite Epitaxial Thin Films

Hailin Wang,^[a] Carlos Frontera,^[a] Javier Herrero-Martín,^[b] Alberto Pomar,^[a] Pere Roura,^[c] Benjamín Martínez,^{*[a]} and Narcis Mestres^{*[a]}

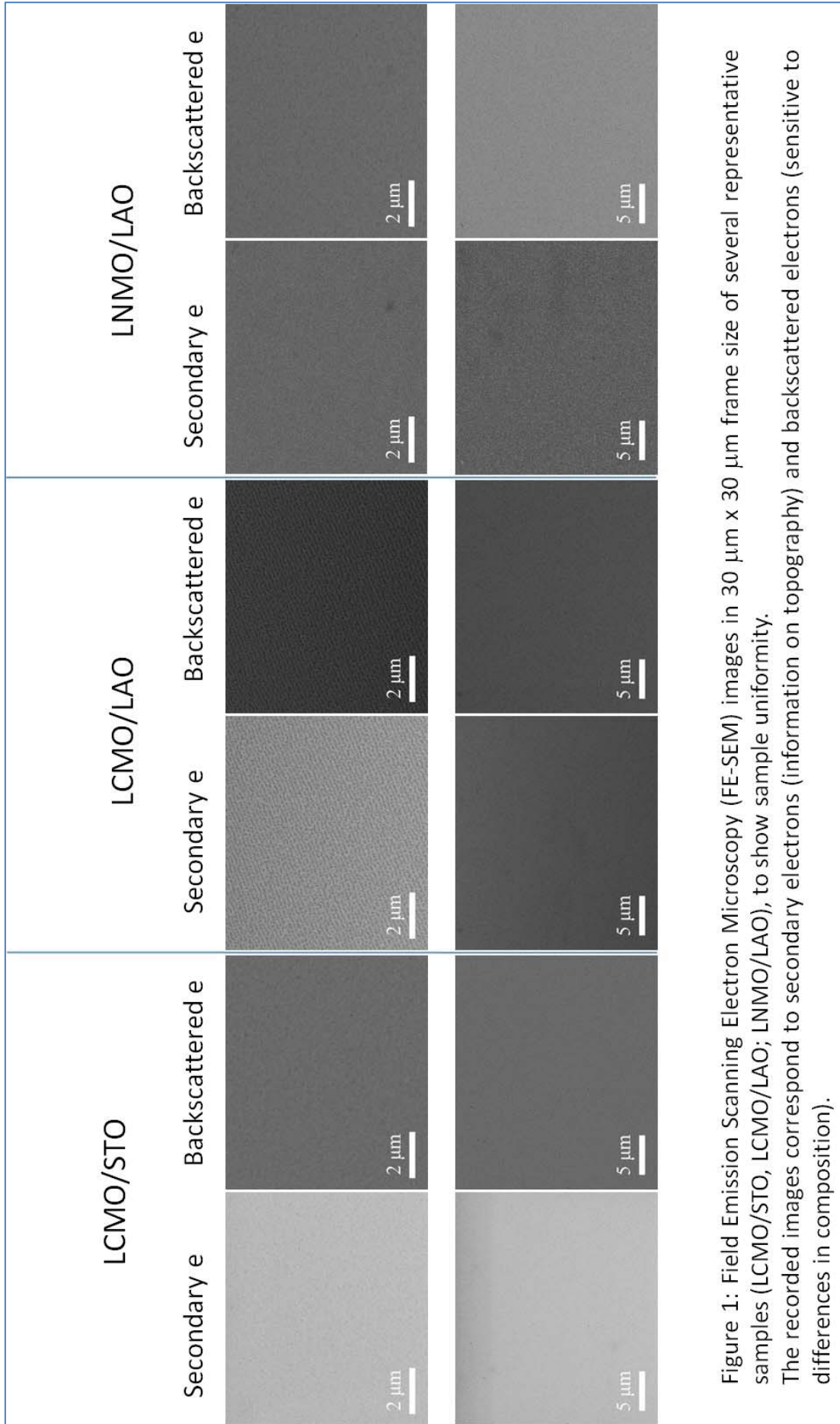


Figure 1: Field Emission Scanning Electron Microscopy (FE-SEM) images in 30 μm x 30 μm frame size of several representative samples (LCMO/STO, LCMO/LAO; LNMO/LAO), to show sample uniformity. The recorded images correspond to secondary electrons (information on topography) and backscattered electrons (sensitive to differences in composition).

4.3 La₂CoMnO₆ and La₂NiMnO₆ thin films prepared by PAD and crystallized by rapid thermal annealing (RTA)

An important step, common to all chemical solution deposition (CSD) film growth methods, is the annealing process since the microstructure of the films can be severely affected by the precise features of the thermal processing. It is well known that crystallization usually begins during heating to the final annealing temperature. On the other hand, nucleation is delayed to higher temperatures when a rapid heating rate is used. As a consequence, when a low heating rate is used, it is expected that some disordered phases will nucleate during the heating process. On the contrary, if a rapid heating rate is used, the nucleation will be delayed, which in its turn should be beneficial for ordered phase nucleation, resulting in an enhancement of the ordered phase.

In this work we have investigated the effect of fast heating rates (10-50 °C/s) on the structural and magnetic properties of manganese based double perovskite La₂CoMnO₆ and La₂NiMnO₆ thin films synthesized by using the polymer assisted deposition (PAD) approach. Results obtained in RTA samples are compared with those obtained in samples prepared by using conventional thermal processes, (heating rates 2-10 °C/min). Stable polymer based precursor solutions were prepared and spin coated as described previously.

It is found that samples prepared by RTA have similar values of saturation magnetization and Curie temperature to the counterpart prepared by using conventional thermal processes, thus indicating a low influence of the heating ramp rate on the B-B' site cationic ordering of the A₂BB'O₆ double perovskite structure that is mainly controlled by charge difference and steric effects. However, a deeper analysis suggested a different microstructure. In the case of the LCMO system, samples prepared by RTA present almost full B-B' site cationic ordering with M_s values close to the spin-only theoretical value of 6 μ_B /f.u.; $M-H$ loops exhibit the sudden drop of the remnant magnetization at H=0 indicative of the existence of anti-phase boundaries (APBs). In contrast to what is observed in samples prepared by

conventional annealing method, APBs in RTA samples are easily suppressed by a post-annealing treatment under oxygen flow which indicates differences in the microstructure of the samples.

In the case of the LNMO system full B-B' site cationic ordering is harder to attain since the ionic radii difference between Ni^{2+} and Mn^{4+} is too small. The existence of an important amount of ASDs in LNMO samples precludes the appearance of APBs since the magnetic disorder already generated blurs out clear frontiers between zones with inverted Ni/Mn ordering. However, the values of M_s obtained both in LNMO/STO and LNMO/LAO after a post-RTA thermal treatment are among the best reported in the literature. In the case of the LNMO system, as previously mentioned, the existence of ASDs precludes the formation of APBs making difficult to detect differences in the magnetic behavior between RTA and conventionally annealed samples. However, the approach to magnetic saturation in $M-H$ loops and irreversibility in zero field cooling-field cooling $M-T$ curves also suggest some differences.

Rapid Thermal Annealing of Double Perovskite Thin Films Formed by Polymer Assisted Deposition

by  Hailin Wang ,  Carlos Frontera ,  Benjamín Martínez  and  Narcís Mestres 

Institut de Ciència de Materials de Barcelona, ICMAB, Consejo Superior de Investigaciones Científicas, CSIC, Campus UAB, 08193 Bellaterra, Barcelona, Spain

* Authors to whom correspondence should be addressed.

Materials **2020**, *13*(21), 4966; <https://doi.org/10.3390/ma13214966> (registering DOI)

Received: 4 October 2020 / Revised: 2 November 2020 / Accepted: 3 November 2020 / Published: 4 November 2020

[View Full-Text](#)

[Download PDF](#)

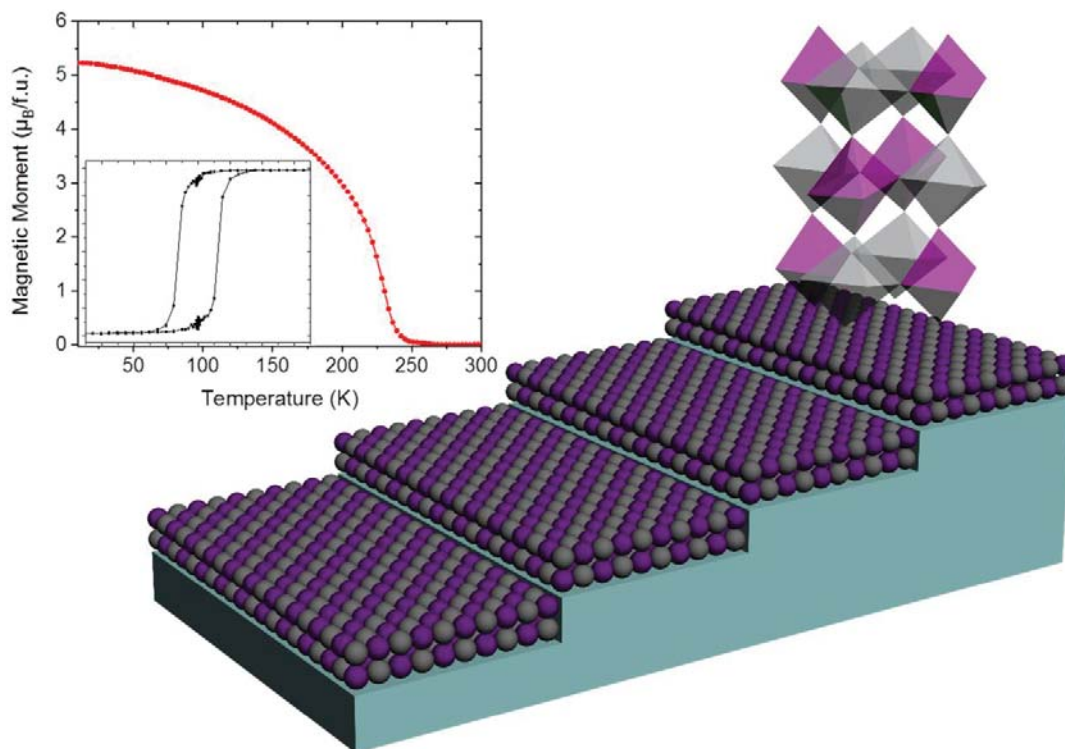
[Browse Figures](#)

[Cite This Paper](#)

Abstract

The annealing process is an important step common to epitaxial films prepared by chemical solution deposition methods. It is so because the final microstructure of the films can be severely affected by the precise features of the thermal processing. In this work we analyze the structural and magnetic properties of double perovskite $\text{La}_2\text{CoMnO}_6$ and $\text{La}_2\text{NiMnO}_6$ epitaxial thin films prepared by polymer-assisted deposition (PAD) and crystallized by rapid thermal annealing (RTA). It is found that samples prepared by RTA have similar values of saturation magnetization and Curie temperature to their counterparts prepared by using conventional thermal annealing (CTA) processes, thus indicating low influence of the heating rates on the B-B' site cationic ordering of the $\text{A}_2\text{BB}'\text{O}_6$ double perovskite structure. However, a deeper analysis of the magnetic behavior suggested some differences in the actual microstructure of the films. [View Full-Text](#)

Keywords: functional oxides; double perovskites; B-site ordering; ferromagnetism; chemical growth methods; polymer-assisted deposition



Article

Rapid Thermal Annealing of Double Perovskite Thin Films Formed by Polymer Assisted Deposition

Hailin Wang, Carlos Frontera, Benjamín Martínez * and Narcís Mestres *

Institut de Ciència de Materials de Barcelona, ICMA B, Consejo Superior de Investigaciones Científicas, CSIC, Campus UAB, 08193 Bellaterra, Barcelona, Spain; hwang@icmab.es (H.W.); frontera@icmab.es (C.F.)

* Correspondence: benjamin.martinez@icmab.es (B.M.); narcis.mestres@icmab.es (N.M.)

Received: 4 October 2020; Accepted: 3 November 2020; Published: 4 November 2020

Abstract: The annealing process is an important step common to epitaxial films prepared by chemical solution deposition methods. It is so because the final microstructure of the films can be severely affected by the precise features of the thermal processing. In this work we analyze the structural and magnetic properties of double perovskite $\text{La}_2\text{CoMnO}_6$ and $\text{La}_2\text{NiMnO}_6$ epitaxial thin films prepared by polymer-assisted deposition (PAD) and crystallized by rapid thermal annealing (RTA). It is found that samples prepared by RTA have similar values of saturation magnetization and Curie temperature to their counterparts prepared by using conventional thermal annealing (CTA) processes, thus indicating low influence of the heating rates on the B-B' site cationic ordering of the $\text{A}_2\text{BB}'\text{O}_6$ double perovskite structure. However, a deeper analysis of the magnetic behavior suggested some differences in the actual microstructure of the films.

Keywords: functional oxides; double perovskites; B-site ordering; ferromagnetism; chemical growth methods; polymer-assisted deposition

1. Introduction

Most of the new technological applications of materials need to utilize thin films and heterostructures to take advantage of the varied benefits of miniaturization. Thus, preparation and characterization of thin films and heterostructures has become a very active area of research in which traditional high-vacuum deposition methods rival with more affordable chemical deposition methods. While traditional high-vacuum techniques, such as molecular beam epitaxy [1,2], radiofrequency sputtering [3,4], and pulsed laser deposition [5,6], offer clear benefits for growing thin films of metal oxides with high crystalline quality and excellent control over thickness and composition at the atomic-scale, chemical solution deposition (CSD) methods represent a more affordable alternative for extensive production of high quality functional oxide thin films [7–9]. The main benefits of this CSD methodology are the cheap and facile scalability of the deposition process. Additionally, CSD methods allow an easy control of the desired stoichiometry and film thickness with in situ doping possibilities, via the addition of a dopant to the precursor solution. Polymer-assisted deposition (PAD) is one of the CSD methods with major projection. PAD is based on very stable and homogeneous metal-polymer complex aqueous solutions. Towards this end, a water soluble polymer is employed to bind and stabilize the metal cations in the precursor solutions on the one hand and also to regulate the solution viscosity determining the film coating [10].

An important step, common to all CSD film growth methods, is the annealing process since the microstructure of the films can be severely affected by the precise features of the thermal processing [11–13]. In particular, the annealing ramp rate is significant for materials with a wide range of nucleation energies. In contrast to more usual low ramp rate (2–10 °C/min) annealing methods, in rapid thermal annealing (RTA) with heating rates 10–50 °C/s, the physical processes leading to

densification and crystallization of the film are delayed to higher temperatures. On the contrary, when using slow heating ramps nucleation and growth start at lower temperatures and progresses as the temperature increases. This broad processing window often results in a wide nucleation range and distinct grain growth rates, which determine the final film microstructure and may lead to incoherently textured films. Conversely, if the film is rapidly heated, simultaneous nucleation occurs at high temperatures in a situation similar to that of isothermal annealing, which leads to a more uniform texture and grain size distribution [14].

Additionally, it is also expected that the RTA process will minimize possible diffusion reactions between films and substrates while enhancing the film densification and preventing the stabilization of intermediate phases, as already observed in the microelectronics industry where RTA is conventionally used [15]. According to these features, RTA might also be of interest to tune the final physical properties of complex oxide thin films, in particular it could be very interesting in the case of double perovskite oxides in which B-site cationic ordering plays a crucial role in their final physical properties. Double perovskite structures of the type $A_2BB'O_6$ are made of stacking single perovskite units and the unit cell is twice that of the perovskite. In the ideal double perovskite structure, in which A is a rare-earth metal or an alkaline earth metal cation and B and B' are transition metal cations, a 3-D network of alternating BO_6 and $B'O_6$ octahedra exists. These materials have attracted considerable attention because of their particular ferromagnetic, electrical, and elastic properties [16]. Attaining a complete cationic ordering is demanding since the alternative occupancy of the B-B'-site cations can be influenced by several factors, such as processing conditions and ionic characteristics. It has been established that the larger the difference in size and charge of the B-B' site cations, the more easy it is to grow a material with a higher degree of ordering [16]. Correspondingly, the final physical properties are strongly influenced by the degree of B-B' site cationic ordering [17].

As previously shown [18,19], the PAD technique has been successfully used for the growth of high-quality double perovskite oxide thin films (La_2CoMnO_6 (LCMO) and La_2NiMnO_6 (LNMO)) with magnetic properties close to the optimal ones. It is well known that the magnetic properties of these compounds are extremely sensitive to B-B' site cationic ordering of Mn^{4+} and Co^{2+}/Ni^{2+} ions.

In this work we have investigated the effect of fast heating rates on the magnetic properties of manganese-based double perovskite La_2CoMnO_6 and La_2NiMnO_6 thin films synthesized by using the PAD method. Results obtained from RTA samples are compared with those obtained in samples prepared by using conventional thermal annealing (CTA) processes. It is found that samples prepared by RTA have similar values of saturation magnetization and Curie temperature to those prepared by using CTA, thus indicating the low influence of the heating rates on the B-B' site cationic ordering of the $A_2BB'O_6$ double perovskite structure. However, a deeper analysis of the magnetic properties suggests a slightly different microstructure. In particular, it is observed that antiphase boundaries in LCMO samples prepared by RTA can be easily suppressed by a subsequent annealing in an oxygen rich atmosphere, in contrast to what is observed in the counterpart samples processed by conventional annealing methods. In parallel with this, different behavior after zero field cooling-field cooling processes in $M(T)$ curves is also observed, mainly in LNMO, thus also pointing to a different microstructure from that of samples prepared by using a conventional annealing process.

2. Materials and Methods

2.1. Precursor Solutions Preparation

The precursor solutions for the LCMO and LNMO thin films growth were produced by mixing previously synthesized solutions of La, Co, Mn and La, Ni, Mn respectively, bound to polymers using water as the solvent. First, individual solutions were prepared by using lanthanum(III) nitrate, cobalt(II) nitrate, nickel(II) chloride, and Mn(II) nitrate metal salts of high-purity (>99.9%). Branched polyethylenimine PEI, from Sigma Aldrich, Steinheim, Germany (average Mw ~25,000) was used as the binding polymer; and Ethylenediaminetetraacetic acid (EDTA), also provided by Sigma Aldrich, (Steinheim, Germany) was the complexing agent used. The different metal ion solutions were prepared by dissolving the proper metal salts in Milli-Q water and EDTA in a 1:1 molar ratio. The

amount of PEI added to the solution was in a 1:1 mass ratio with EDTA. Each separate solution was filtrated using an Amicon® filtration unit (Merck, Darmstadt, Germany) and 10 kDa filters, to remove non-coordinated cations and polymer fractions, and to obtain a homogeneous precursor solution. The retained fractions were analyzed by inductively coupled plasma (ICP) using Optima 4300™ DV ICP-OES Perkin-Elmer (Waltham, MA, USA) equipment, to precisely determine the cation concentration in the primary solutions.

The obtained concentrations of the used solutions were $[La] = 230.4$ mM, $[Co] = 146.4$ mM, $[Ni] = 272.6$ mM, and $[Mn] = 176.4$ mM. From these primary solutions, the final precursor solutions with the desired La:Co:Mn 2:1:1, and La:Ni:Mn 2:1:1 stoichiometries were prepared and concentrated. The final cation concentration was adjusted to be 60–65 mM with respect to Mn. These conditions were chosen to be able to produce films in the 15–25 nm thickness range. Typical viscosity values were $\eta \approx 3\text{--}4$ mPa s (measured with a DMA 4100 M Anton Paar (Ashland, VA, USA) densimeter, with a micro-viscometer module Lovis 2000 ME).

2.2. Thin Films Growth

The prepared precursor solutions were spin-coated on top of 0.5×0.5 cm² (001)-SrTiO₃ (STO) or (001)-LaAlO₃ (LAO) substrates from Crystec, GmbH (Berlin, Germany). Previously, to create TiO₂-terminated substrates with atomically flat terraces the as-received STO substrates were chemically etched and thermally treated [20]. Similarly, to create AlO₂-terminated substrates with atomically flat terraces, the LAO substrates were thermally treated at high temperatures (950 °C) under oxygen flow.

The last step for the film growth is the thermal treatment of the spin-coated films under oxygen flow. This thermal annealing leads to elimination of the organic components at low temperatures, and to phase formation and crystallization at high temperatures. Rapid thermal annealing was achieved using an AS-Micro RTA furnace from Annealsys (Montpellier, France) under a controlled and stagnant oxygen atmosphere (loaded at 5 L/min for 2 min), and at temperatures from 800 to 1000 °C with dwell times in the 10 to 30 min range, and heating rates from 0.5 to 20 °C/s. Conventional thermal annealing was accomplished by using a tube furnace and heating ramps of several degrees Celsius per minute under oxygen flow to elude the formation of oxygen vacancies (oxygen flow rates between 100 and 600 mL/min).

2.3. Characterization of Structural and Physical Properties

The structural properties of the grown films were studied by X-ray diffraction and reflectivity employing a Bruker D8-Discover (Billerica, MA, USA) and a D5000-Siemens (Madison, WI, USA) diffractometers, with Cu-K_{α1} monochromatic radiation (1.5406 Å). The surface morphology of the epitaxial films was analyzed by atomic force microscopy (AFM) performed in tapping mode using an Asylum Research MFP-3D (Wiesbaden, Germany) microscope. DC magnetization measurements as a function of temperature and magnetic fields were performed using a superconducting quantum interference device (SQUID) from Quantum Design (San Diego, CA, USA). External magnetic fields were applied either parallel (in-plane (IP) configuration) or perpendicular (out-of-plane (OP) configuration) to the film/sample plane. The diamagnetic contribution of the substrate and other instrumental contributions were properly corrected [21]. The possible relative error when determining the saturation magnetization (M_s) was estimated to be approximately 5–8% and is predominantly ascribed to the error in the determination of the volume of the films. Once the thin film is grown, in most cases it is necessary to remove the accumulated material in the corners by chemical etching, to quantify with greater precision the values of the magnetic properties, and this introduces a non-negligible source of error. These patterns occur outside the circumference of the inscribed circle when spin coating on a square substrate, where radial uniformity vanishes [22].

3. Results and Discussion

3.1. Structural Characterization

The surface morphology of the films was studied by atomic force microscopy (AFM). Figure 1 shows topography images of ~20 nm thick LCMO and LNMO thin films grown by RTA on top of STO and LAO substrates. All the films present flat surfaces with low values of RMS (below 2 nm), as indicated in the figure. This fact confirms that the PAD method using RTA thermal treatment is able to produce films with surface roughness similar to the ones obtained by pulsed laser deposition (PLD) or sputtering deposition methods.

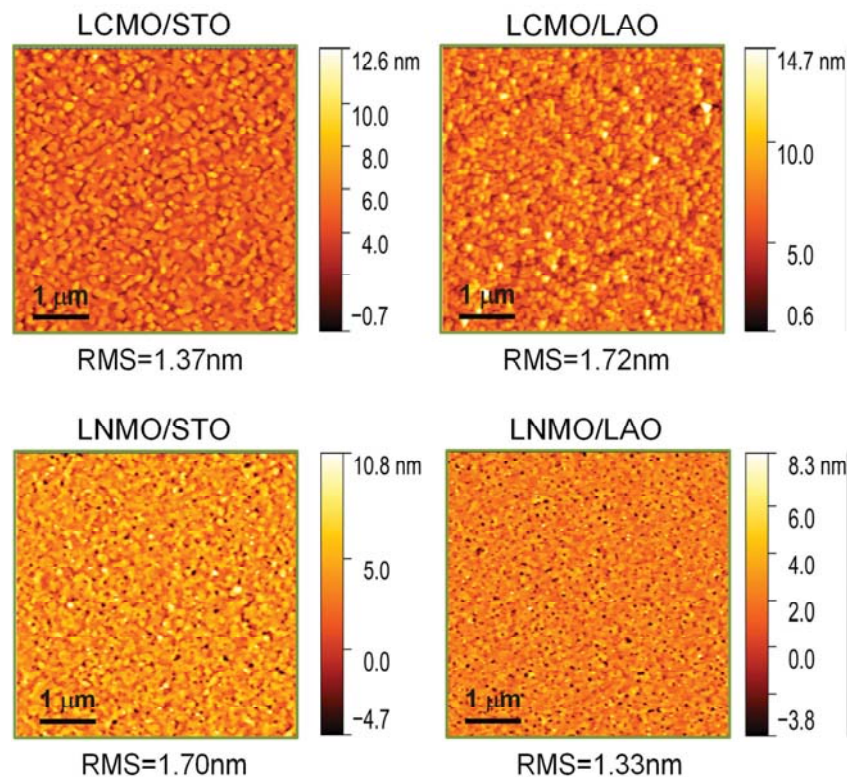


Figure 1. Atomic force microscopy surface topography images ($5 \times 5 \mu\text{m}^2$) of representative $\text{La}_2\text{CoMnO}_6$ and $\text{La}_2\text{NiMnO}_6$ thin films, with thickness values of about 20 nm, on top of SrTiO_3 (STO) and LaAlO_3 (LAO) substrates. Films thermally treated in rapid thermal annealing (RTA) conditions, $20 \text{ }^\circ\text{C/s}$ heating ramp, dwell time 20 min at $900 \text{ }^\circ\text{C}$ in static oxygen. In all cases, root mean square (RMS) roughness values are below 2 nm.

The in-plane strain degree of the grown epitaxial films has been investigated by means of reciprocal space maps adjacent to the (103) substrate signal. Reciprocal space maps of LCMO films grown on STO substrate (not shown) reveal that these films grew fully strained without any measurable difference of the in-plane lattice parameters of film and substrate. Conversely, LCMO films grown on LAO were fully relaxed (see Figure 2a), and the in-plane lattice parameter extracted from the reciprocal space map is about $a = 3.88 \text{ \AA}$.

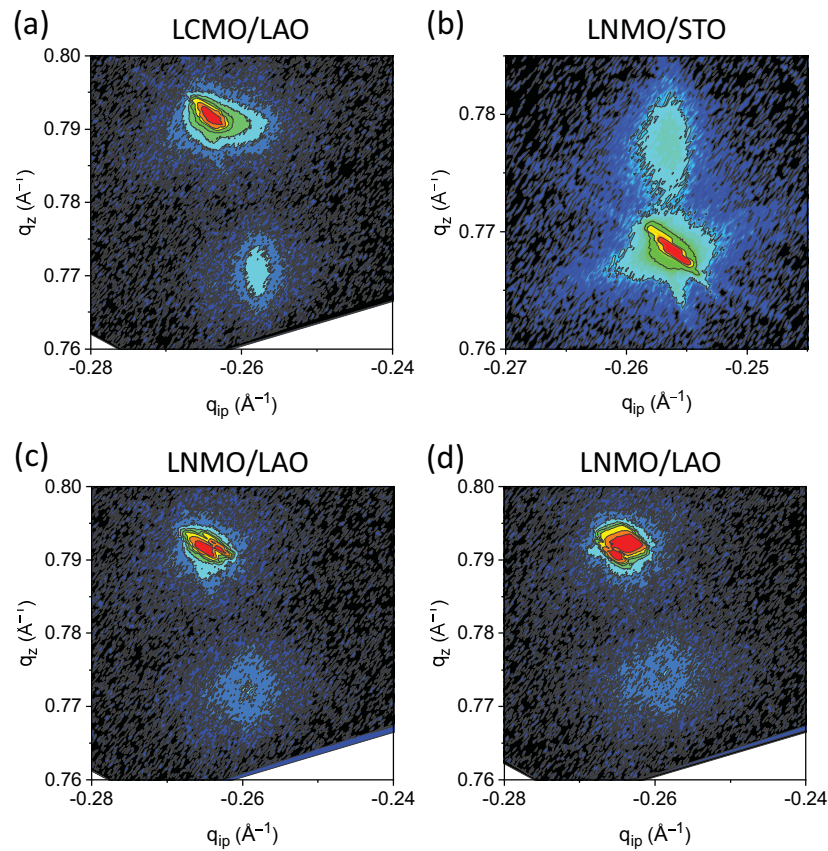


Figure 2. Reciprocal space maps around the (103) substrate reflections for (a) LCMO film grown on LAO; (b) LNMO film grown on STO; (c) LNMO film grown on LAO; treated in RTA conditions, 20 °C/s heating ramp, dwell time 20 min at 900 °C in static oxygen (d) LNMO film grown on LAO in RTA conditions, and subsequent high temperature conventional annealing in oxygen flux (5 °C/min, 750 °C, 120 min, 0.5 L/min oxygen).

A parallel analysis was performed on LNMO films. Reciprocal space map examination shows that LNMO films grown on STO substrates are fully strained (Figure 2b). On the contrary, when the LNMO films are grown on LAO, the peak position of (103) reflection is clearly shifted from that of the LAO substrate along the q_{-100} axis (see Figure 2c). This fact is a direct consequence of the large lattice mismatch between the LNMO films and the LAO substrate (−2.31%), that causes a relaxation of the films structure. Moreover, the larger broadening observed in the LNMO film peak indicates that part of the film is fully relaxed and that some part is not. As can be observed in Figure 2d, this strained state is maintained even after a subsequent anneal at a high temperature under oxygen flow.

The measured strain behavior is similar to the one observed in PAD grown films using conventional thermal annealing [19] (see supplementary information Figure S1, for θ -2 θ XRD spectra of representative LCMO/LAO and LNMO/LAO epitaxial thin films). Namely, epitaxial $\text{La}_2\text{CoMnO}_6$ and $\text{La}_2\text{NiMnO}_6$ thin films grow coherently and tensile strained on STO substrate owing to the fact that the lattice parameters of pseudo-cubic bulk $\text{La}_2\text{CoMnO}_6$ ($a_{pc} = 3.89 \text{ \AA}$) [23] and $\text{La}_2\text{NiMnO}_6$ ($a_{pc} = 3.879 \text{ \AA}$) [24], are close to the lattice parameter of STO ($a = 3.905 \text{ \AA}$). On the contrary, due to the large nominal lattice mismatch of the LCMO/LAO (−2.61%) and LNMO/LAO (−2.31%) arrangements, for film thickness values close to 20 nm, LCMO grows fully relaxed on LAO substrates ($a_{pc} = 3.791 \text{ \AA}$), and LNMO grows partially relaxed on the same substrate.

Moreover, rocking curves measured on the (002) reflections of the films have full width at half maximum (FWHM) values in the range of 0.12–0.17 degrees (see supplementary information Figure

S2 for representative LNMO/STO and LNMO/LAO films). These relatively small FWHM values indicate that the RTA-grown films have a good crystallinity with some mosaicity.

3.2. Magnetic Properties

Ferromagnetic (FM) ordering in LCMO and LNMO double perovskites is generated by super-exchange interactions between Mn^{4+} and Co^{2+} (Ni^{2+}) ions according to the Goodenough–Kanamori rules [25–27]. The corresponding spin-only theoretical values of saturation magnetization, M_s , of LCMO (Co^{2+} ($3d^7$, $t_{2g}^5 e_g^2$; $S = 3/2$) and Mn^{4+} ($3d^3$, $t_{2g}^3 e_g^0$; $S = 3/2$)) and LNMO (Ni^{2+} ($3d^8$, $t_{2g}^6 e_g^2$; $S = 1$) and Mn^{4+} ($3d^3$, $t_{2g}^3 e_g^0$; $S = 3/2$)) are 6 and 5 $\mu_B/f.u.$ respectively. However, if there is some disorder in the B–B' site occupancy among Mn^{4+} and Co^{2+} (Ni^{2+}) ions generating anti-site defects (ASD), i.e., a portion of Co (Ni) and Mn ions have their crystallographic sites interchanged, Co^{2+} –O– Co^{2+} (Ni^{2+} –O– Ni^{2+}) and Mn^{4+} –O– Mn^{4+} antiferromagnetic (AFM) interactions are introduced lowering the saturation magnetization value by a factor $(1-2 \cdot X(ASD))$, where $X(ASD)$ is the fraction of ASD disorder [28]. Therefore, magnetic measurements are a very sensitive sensor to determine the amount of B–B' site cationic ordering. The ordered occupancy of the B sublattice by Mn and Co (Ni) ions is difficult to achieve because it is affected by different factors, such as ionic characteristics and synthesis circumstances. In general, it is observed that the larger the difference in charge and ionic radii of the B-site cations, the higher the grade of ordering achieved. According to this, we will proceed to analyze both the temperature dependence, $M(T)$, and the magnetic field dependence, $M(H)$, of magnetization in samples prepared by RTA in comparison with similar samples prepared by traditional thermal processing.

Table 1 summarizes the different RTA growth conditions and the subsequent CTA treatments for the samples investigated, together with the extracted values of Curie temperature T_c and saturation magnetization M_s .

Table 1. List of samples whose magnetic properties have been analyzed, with the corresponding RTA growth conditions and the parameters of the subsequent CTA treatment. The extracted values for T_c and M_s are also displayed.

Sample	Annealing Conditions Ramp, Temperature, Dwell Time, Oxygen	Curie Temperature, T_c (K)	Saturation Magnetization, M_s ($\mu_B/f.u.$)
LCMO/STO–1	RTA 20 °C/s, 900 °C, 20 min, static oxygen	230	5.7
LCMO/STO–1R	CTA 5 °C/min, 700 °C, 240 min, 0.5 L/min O ₂	240	5.9
LCMO/LAO–1	RTA 20 °C/s, 900 °C, 10 min, static oxygen	225	5.7
LCMO/LAO–1R	CTA 5 °C/min, 700 °C, 240 min, 0.5 L/min O ₂	240	5.8
LNMO/STO–1	RTA 20 °C/s, 900 °C, 20 min, static oxygen	255	3.7
LNMO/STO–1R	CTA 5 °C/min, 800 °C, 180 min, 0.5 L/min O ₂	270	4.3
LNMO/LAO–1	RTA 20 °C/s, 900 °C, 10 min, static oxygen	265	3.5
LNMO/LAO–1R	CTA 5 °C/min, 800 °C, 180 min, 0.5 L/min O ₂	275	4.2

We will analyze first the results obtained in the LCMO system. In Figure 3 $M(T)$ and $M(H)$ curves corresponding to the LCMO/STO-1 sample processed in static oxygen atmosphere with a heating ramp of 20 °C/s and a dwell time of 20 min at 900 °C are reported. The field cooled temperature dependence of the magnetization $M(T)$ under an external magnetic field of 1 kOe applied along the easy magnetization direction, that for the LCMO samples is perpendicular to the film plane, i.e., out-of-plane (OP) configuration, is shown in Figure 3a. The $M(T)$ curve exhibits a non-monotonic behavior with a local minimum around $T \approx 200$ K and a paramagnetic to ferromagnetic transition temperature $T_c \approx 230$ K, which often has been interpreted as a proof of the existence of two different phases in the sample [29–31]. Nevertheless, it is worth mentioning here that the existence of two different magnetic phases will require different oxidation states of Mn and Co from that of Mn^{4+} and Co^{2+} . However, our previous results on LCMO thin films prepared by sputtering, obtained from synchrotron XPS measurements, indicate that regardless of the structural strain (compressive or tensile) the oxidation states of Co and Mn ions are Co^{2+} and Mn^{4+} [32,33]. On the other hand, X-ray absorption spectroscopy analysis in LNMO samples prepared by PAD also confirm that the actual oxidation states are Ni^{2+} and Mn^{4+} [19]. In parallel with this, the obtained saturation magnetization values, slightly below the theoretical spin only saturation value, $6\mu_B/f.u.$ in LCMO and close to $5\mu_B/f.u.$ in LNMO, give further support to this idea, thus precluding the presence of several magnetic phases in the sample, in agreement with previous reports on samples prepared by sol-gel methods [34–36].

The origin of the specific shape of the $M(T)$ curve is not clearly established and it should be related to the existence of some kind of magnetic disorder. This magnetic disorder may have two main different origins. On one side, the presence of anti-site disorder (ASD) (i.e., a portion of Co and Mn cations have their crystallographic sites interchanged) will trigger the appearance of $Co^{2+}-O-Co^{2+}$ and $Mn^{4+}-O-Mn^{4+}$ antiferromagnetic (AFM) interactions reducing the M_s value [19,28] and introducing competition of magnetic interactions, frustration and disorder. On the other side, multiple nucleation sites in the film can produce zones with alternating Co/Mn local ordering. When two of these zones merge together, at its interface deviations from the ideal Co/Mn ordering appear generating again $Co^{2+}-O-Co^{2+}$ and $Mn^{4+}-O-Mn^{4+}$ AFM interactions, giving rise to an antiphase boundary (APB) [37,38]. APBs appear as kind of domain walls between two FM domains, within which a Co^{2+}/Mn^{4+} arrangement exists and their identification shows up as a sudden drop in the remnant magnetization at $H = 0$, as noticed in Figure 3b. Since $M_s \approx 5.7 \mu_B/f.u.$, i.e., nearby the ideal $6 \mu_B/f.u.$ spin-only saturation value (see Figure 3b), the amount of ASD in the sample should be very small, i.e., indicating that almost full B-B' site cationic ordering has been achieved. On the other hand, Figure 3b also makes evident the existence of APBs (note the sudden drop of the remnant magnetization at $H = 0$). Therefore, it seems that the observed flattened $M(T)$ curve should be associated with the existence of some amount of magnetic disorder in the sample mainly attributable in this case to APBs. Similar results were obtained in LCMO/STO samples prepared by conventional annealing [18]; however, $M(T)$ curves in RTA seem to indicate a higher degree of magnetic disorder, which suggests a different microstructure, at least from the magnetic point of view.

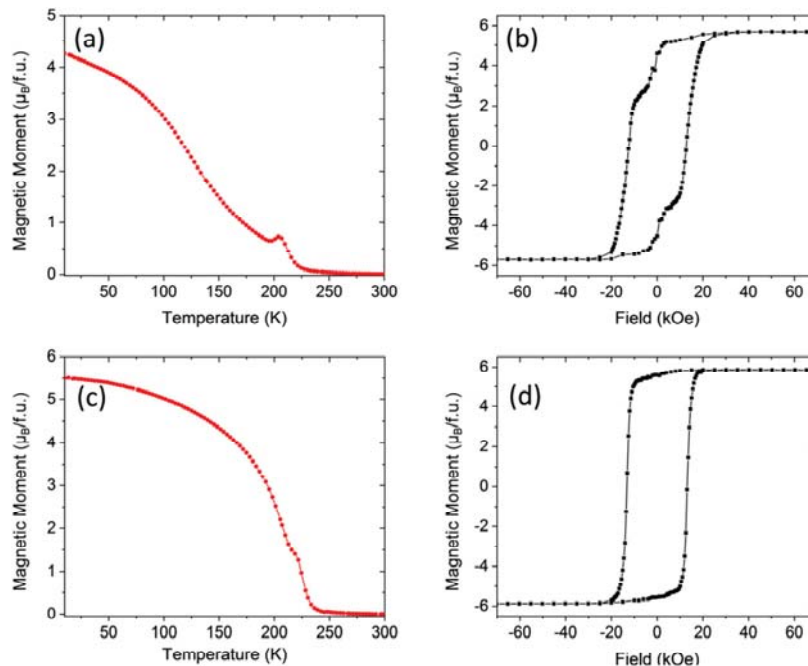


Figure 3. (a) Magnetization vs. temperature of LCMO/STO-1 film measured after field cooling with a magnetic field of 1 kOe applied parallel to (001)-STO (out of plane). (b) M-H loop of the same sample recorded at 10 K, magnetic field H applied out of plane. (c) Temperature dependence of the magnetization under an applied magnetic field of 1 kOe (out of plane), of sample LCMO/STO-1R. (d) M-H loop of sample LCMO/STO-1R recorded at 10 K, magnetic field H applied out of plane.

Post-growth annealing in an oxygen-rich atmosphere has proved to be an effective method to modify the microstructure reducing structural defects and oxygen vacancies in double perovskite ceramic samples and thin films [39,40]. The effect of a post-growth thermal treatment in a conventional tube furnace on the magnetic properties of the RTA grown sample (700 °C temperature, 4 h dwell time, 5 °C/min ramp, under an oxygen flow of 0.5 L/min) film LCMO/STO-1R, is evidenced in Figure 3c,d.

The temperature dependence of the magnetization, under an applied magnetic field of 1 kOe, shows that ferromagnetism decays at a slower rate, and that only a single T_c at a slightly higher temperature $T_c = 240$ K with a sharper FM-PM transition is present. On the other hand, the sudden drop of the remnant magnetization at $H = 0$, indicative of the existence of APBs, has been completely suppressed while $M_s \approx 5.9 \mu_B/f.u.$, is slightly higher than in the as-grown sample. Therefore, the conventional post-growth annealing process is consistent with an overall suppression of the APBs reducing magnetic disorder as reflected in the $M(T)$ curve.

Similar results are obtained in the case of LCMO samples grown on top of LAO substrates as can be appreciated in Figure 4. Figure 4a shows the field cooled temperature dependence of the magnetization $M(T)$ under an applied external magnetic field of 1 kOe in the in-plane (IP) configuration for the LCMO/LAO-1 sample processed in a static oxygen atmosphere with a heating ramp of 20 °C/s and a dwell time of 10 min at 900 °C. Compared to LCMO/STO samples, the $M(T)$ curve is featureless but flattened with $T_c \approx 225$ K, indicative of a smaller amount of magnetic disorder (see Figure 3a). The magnetic hysteresis loop recorded at 10 K, and displayed in Figure 4b, shows a magnetization saturation value near 5.7 $\mu_B/f.u.$, slightly smaller than in a fully ordered sample and indicating almost full cationic ordering. Moreover, the typical drop of the remnant magnetization at $H = 0$, signature of APBs, is also observed, thus indicating that magnetic disorder is mainly introduced by APBs as in the previous case.

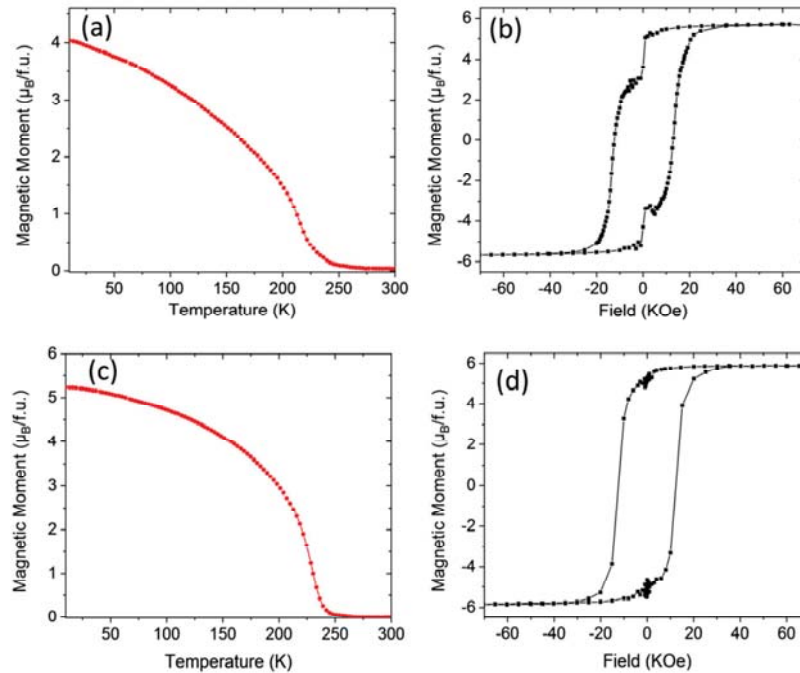


Figure 4. (a) Magnetization vs. temperature of the LCMO/LAO–1 film thermally treated in RTA conditions, measured after field cooling with a magnetic field of 1 kOe applied parallel to (100)-LAO, (in-plane). (b) M–H loop of the same sample recorded at 10 K by applying the magnetic field H in-plane. (c) Temperature dependence of the magnetization under an in-plane applied magnetic field of 1 kOe, of sample LCMO/LAO–1R. (d) M–H loop of sample LCMO/LAO–1R recorded at 10 K by applying the magnetic field H in-plane.

A post-growth thermal treatment in oxygen flow, sample LCMO/LAO–1R (700 °C temperature, 4 h dwell time, 5 °C/min ramp, and oxygen flow of 0.5 L/min) equivalent to that performed in LCMO/STO samples, clearly modifies the $M(T)$ curve, showing a slower decay rate of the magnetization and an increase of T_c of up to about 240 K (see Figure 4c). At the same time, the magnetic hysteresis loop recorded at 10 K and displayed in Figure 4d makes it evident that the annealing has fully suppressed APBs, while a slight increase of the saturation magnetization M_s value to about 5.8 $\mu_B/f.u.$ was also found.

We move now to the analysis of the LNMO system. As evidenced in our previous studies in LNMO samples prepared by using conventional annealing processes [19], full B–B' site cationic ordering is not achieved basically because the ionic radii difference between Ni^{2+} and Mn^{4+} is too small (16.0 pm as compared to 21.5 pm for Co^{2+} and Mn^{4+} [41]), so the amount of ASDs is substantially larger than in the LCMO samples. Therefore, the magnetic disorder linked to the introduction of $Ni^{2+}-O^{2-}-Ni^{2+}$ and $Mn^{4+}-O^{2-}-Mn^{4+}$ AFM interactions at anti-sites is larger than in LCMO samples, as can be clearly appreciated in Figure 5.

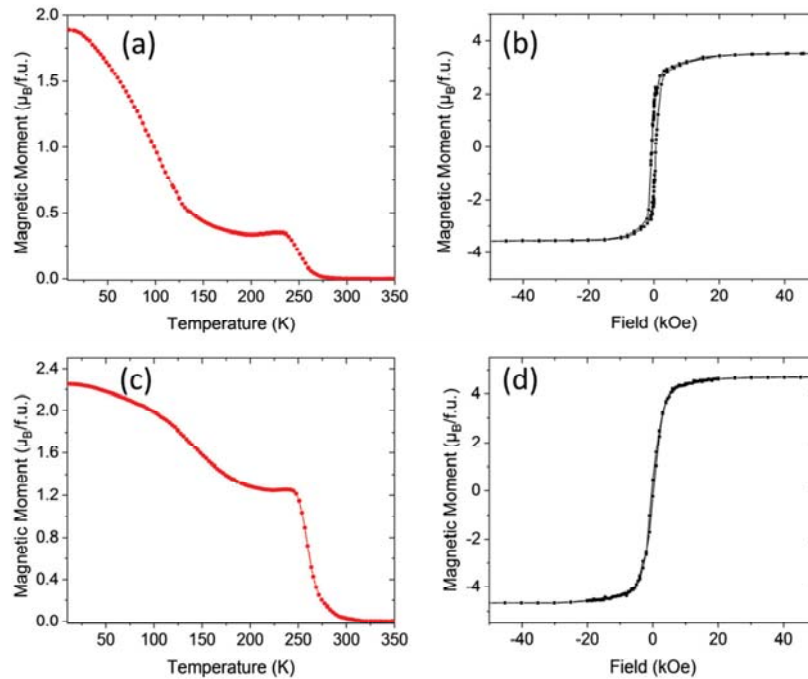


Figure 5. (a) Magnetization vs. temperature of an LNMO/STO-1 film thermally treated in RTA conditions, measured after field cooling with a magnetic field of 1 kOe applied parallel to (100)-SrTiO₃, (in-plane). (b) M–H loop of the same sample recorded at 10 K by applying the magnetic field H in-plane. (c) Temperature dependence of the magnetization under an in-plane applied magnetic field of 1 kOe, of sample LNMO/STO-1R. (d) M–H loop of sample LNMO/STO-1R recorded at 10 K by applying the magnetic field H in-plane.

Figure 5a displays the temperature dependence of the magnetization $M(T)$ under an applied external magnetic field of 1 kOe in the IP configuration for the LNMO/STO-1 thin film sample processed in static oxygen environment with a heating ramp of 20 °C/s and a dwell time of 20 min at 900 °C. As in the LCMO/STO case, the $M(T)$ curve exhibits a non-monotonic behavior with a local minimum around $T \approx 200$ K and a paramagnetic to ferromagnetic transition temperature $T_c \approx 255$ K, which reflects the existence of magnetic disorder due to ASD involving Ni and Mn atoms [19,28]. The magnetic hysteresis loop recorded at 10 K is displayed in Figure 5b, and shows a depressed magnetization saturation value near 3.6–3.7 $\mu_B/f.u.$, smaller than the value expected in a sample with full cationic ordering (5 $\mu_B/f.u.$), thus corroborating the existence of ASDs. It is worth mentioning here that the existence of several ASDs in the sample precludes the formation of APBs, since the magnetic disorder already generated blurs out the clear frontiers between zones with inverted Ni/Mn ordering.

As already observed in LCMO thin films, a post-growth thermal treatment in oxygen flow (800 °C temperature, 3 h dwell time, 5 °C/min ramp, and oxygen flow of 0.5 L/min), sample LNMO/STO-1R, clearly modified the $M(T)$ curve, showing a slower decay rate of the magnetization and an increase of T_c up to about 270 K (see Figure 5c). At the same time, the magnetic hysteresis loop recorded at 10 K shown in Figure 5d displays an unequivocal increase in the saturation magnetization M_s value, up to about $M_s \sim 4.3$ $\mu_B/f.u.$, closer to the value expected in a fully ordered sample, therefore indicating a reduction in the ASD disorder density induced by the post-growth annealing in an oxygen rich atmosphere. The reduction of the magnetic disorder introduced by ASDs can also be appreciated in the reduction of the coercive fields (see Figure 5b,d).

The effects of the RTA process were also investigated in LNMO samples grown on LAO substrates and the results are compiled in Figure 6. The temperature dependence of the magnetization of sample LNMO/LAO-1 thermally treated with a heating ramp of 20 °C/s and a dwell time of 10 min at 900 °C in a static oxygen environment is shown in Figure 6a. As in the case of LNMO/STO samples, the $M(T)$

curve exhibits a non-monotonic behavior with a pronounced local minimum at a temperature $T \approx 175$ K and a paramagnetic to ferromagnetic transition temperature of $T_c \approx 265$ K, indicative of the existence of a magnetic disorder. In agreement with this, the $M(H)$ curve displayed in Figure 6b shows a slow approach to the saturation characteristic of a large magnetic disorder with a saturation value slightly below $3.5 \mu_B/\text{f.u.}$, which indicates the large amount of ASD that generates this disorder. This shape of $M(H)$ curves was neither observed for LNMO/STO samples (see previous section), nor for LNMO/LAO samples grown in a conventional oven [19] and suggests a different microstructure. A post RTA thermal treatment under oxygen flow, sample LNMO/LAO-1R (800 °C temperature, 3 h dwell time, 5 °C/min ramp, and oxygen flow of 0.5 L/min), slightly improves the $M(T)$ curve that is less flattened, and at the same time promotes an upward shift of the Curie temperature up to $T_c = 275$ K (see Figure 6c). In parallel, a slight increase of the M_s value up to about $4.1\text{--}4.2 \mu_B/\text{f.u.}$ was also observed, which would indicate a small decrease of the ASDs. However the line-shape of the $M(H)$ curve is still clearly different from $M(H)$ curves observed in the LCMO system and in that of LNMO/STO samples.

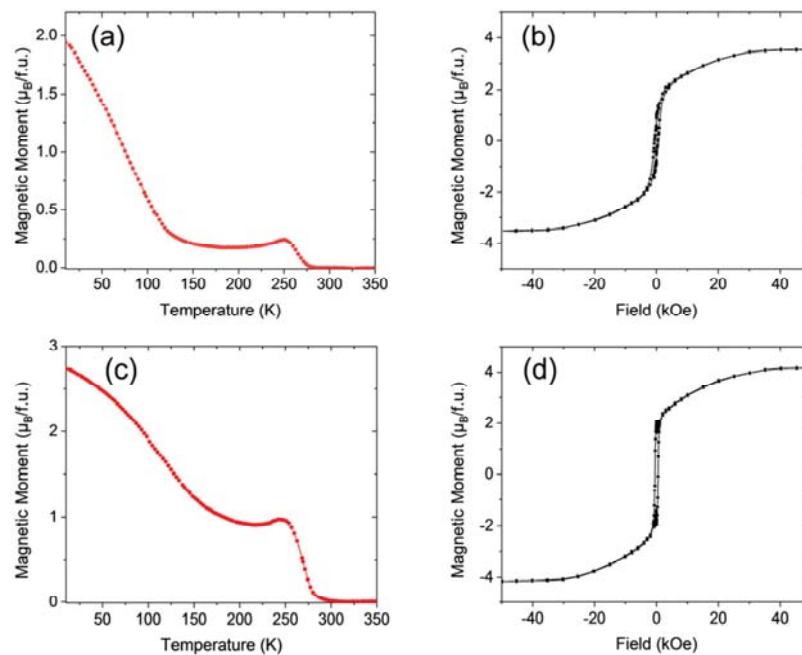


Figure 6. (a) Magnetization vs. temperature of a LNMO/LAO-1 epitaxial film thermally treated in RTA conditions, measured after field cooling with a magnetic field of 1 kOe applied parallel to (100)-LAO, (in-plane). (b) M-H loop of the same sample recorded at 10 K by applying the magnetic field H in-plane. (c) Temperature dependence of the magnetization under an in-plane applied magnetic field of 1 kOe, of sample LNMO/LAO-1R. (d) M-H loop of sample LNMO/LAO-1R recorded at 10 K by applying the magnetic field H in-plane.

In the case of LNMO epitaxial films, the values of M_s obtained both in LNMO/STO and LNMO/LAO, around $4.3 \mu_B/\text{f.u.}$, after a post-RTA thermal treatment are among the best reported in the literature [35,36,40,42], corresponding to an ASD concentration below 10%. $M(T)$ curves suggest a larger magnetic disorder. To gain a deeper insight into the nature of this disorder, $M(T)$ curves have been analyzed after a zero field cooling-field cooling process (ZFC-FC). As shown in Figure 7 in RTA samples irreversibility at low T remains for applied magnetic fields well above the coercive field, while this irreversibility is fully suppressed in samples prepared by a conventional annealing process (see supplementary information, Figures S3 and S4). Therefore, LNMO samples prepared by RTA exhibit a spin glass-like behavior similar to that reported in [34].

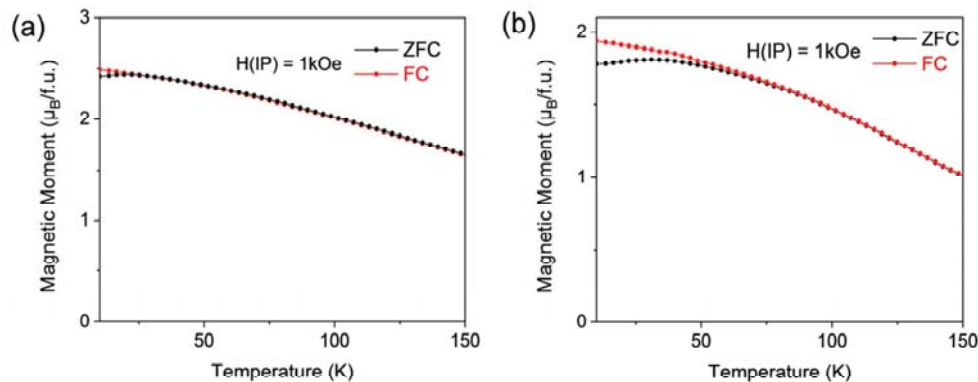


Figure 7. Zero-field-cooled (ZFC) and field-cooled (FC) magnetization curves measured at fields of 1 kOe for LNMO/STO epitaxial thin film samples grown by: (a) conventional thermal annealing (CTA) with 2 °C/min heating and cooling ramps, dwell time 30 min at 875 °C under oxygen flow, 0.4 L/min; (b) RTA conditions, 20 °C/s heating ramp, dwell time 20 min at 900 °C.

As previously mentioned, both ASD and APB introduce $\text{Ni}^{2+}\text{-O-Ni}^{2+}$ and $\text{Mn}^{4+}\text{-O-Mn}^{4+}$ AFM interactions generating competition of magnetic interactions and magnetic disorder. Moreover, microstructural features (stacking faults, twins, vacancies) can contribute to pin magnetization making harder to achieve full magnetic saturation as observed in LNMO/LAO samples.

Comparing the LNMO/STO and LNMO/LAO films, the results seem to indicate that cationic ordering is easier to attain in strained films, in good agreement with recently published results [43].

4. Conclusions

The influence of the annealing process on the microstructural and magnetic properties of LCMO and LNMO double perovskites prepared by PAD is analyzed. It is found that, irrespective of the structural strain, samples prepared by RTA exhibit similar values of T_c and M_s to their counterparts prepared by the conventional annealing process. Therefore, the heating ramp rate seems to have only a minor influence on the B-B' site cationic ordering that is mainly controlled by charge difference and steric effects. In the case of the LCMO system, samples prepared by RTA present almost full B-B' site cationic ordering with M_s values close to the spin-only theoretical value of $6 \mu_B/\text{f.u.}$ $M(H)$ loops exhibit the sudden drop of the remnant magnetization at $H = 0$, indicative of the existence of APBs. In the case of the LNMO system, full B-B' site cationic ordering is harder to attain since the ionic radii difference between Ni^{2+} and Mn^{4+} is too small. However, the values of M_s obtained both in LNMO/STO and LNMO/LAO, after a post-RTA thermal treatment, are among the best reported in the literature, suggesting state-of-the-art samples. The existence of an important amount of ASDs in LNMO samples precludes the appearance of APBs, since the magnetic disorder already generated blurs out the clear frontiers between zones with inverted Ni/Mn ordering. Nevertheless, it is worth mentioning that the magnetic behavior observed in samples prepared by RTA is different from that observed in samples prepared by a conventional annealing process, suggesting a different microstructure. Specifically, in the case of the LCMO system, it is observed that APBs in RTA samples are easily suppressed by a post-annealing treatment in contrast to what is observed in samples prepared by conventional annealing methods. However, X-ray microstructural analysis, i.e., rocking curves and reciprocal space maps, do not show relevant differences between samples prepared by RTA or by conventional processes. In samples prepared using a fast heating rate, a simultaneous nucleation occurs at high temperatures in a situation similar to that of isothermal annealing, which leads to a more homogeneous texture and grain size distribution and thus, there are few microstructural defects to pin APBs that are easily suppressed after a post-growth annealing.

In the case of the LNMO system, as previously mentioned, the existence of ASDs precludes the formation of APBs, making it difficult to detect differences in the magnetic behavior between RTA and conventionally annealed samples. However, the approach to magnetic saturation in $M(H)$ curves also suggest some differences. In fact, $M(T)$ curves measured after a ZFC-FC process show the existence of irreversibility at low temperatures, for magnetic fields well above the coercive field, in RTA samples that is not detected in samples prepared by conventional annealing. This irreversibility indicates the existence of a magnetic disorder attributable to the disorder generated by the simultaneous nucleation of grains and their interaction with ASD in RTA samples.

Supplementary Materials: The following are available online at www.mdpi.com/1996-1944/13/21/4966/s1, Figure S1: High-resolution $\theta/2\theta$ x-ray diffraction (XRD) scans of the (0 0 2) reflections comparing thin films grown by conventional thermal annealing (CTA) and rapid thermal annealing (RTA). Figure S2: Rocking curves of the (0-0-2) reflections of $\text{La}_2\text{NiMnO}_6/\text{SrTiO}_3$ thin film, and (b) $\text{La}_2\text{NiMnO}_6/\text{LaAlO}_3$ thin film. Figure S3: Zero-field-cooled (ZFC) and field-cooled (FC) magnetization curves measured at fields of 100 Oe and 1 kOe for two $\text{La}_2\text{NiMnO}_6$ epitaxial thin film samples, grown by rapid thermal annealing (RTA). Figure S4: Zero-field-cooled (ZFC) and field-cooled (FC) magnetization curves measured at fields of 100 Oe and 1 kOe for two $\text{La}_2\text{NiMnO}_6$ epitaxial thin film samples, grown by conventional thermal annealing (CTA).

Author Contributions: H.W. performed the experimental synthesis, characterization, and data analysis. C.F. contributed to characterization, data analysis and scientific discussions. B.M. and N.M. contributed to the study design, scientific discussions of the results and wrote the paper. All co-authors contributed to the manuscript. All authors have read and agreed to the published version of the manuscript.

Funding: This research was funded by the Spanish Ministry of Science, Innovation and Universities through Severo Ochoa (SEV-2015-04969) and Severo Ochoa FUNFUTURE (CEX2019-000917-S), SUMATE (RTI2018-095853-B-C21), and SPIN-CURIOX (RTI2018-099960-B-100) projects co-financed by the European Regional Development Fund. Hailin Wang acknowledges financial support from the China Scholarship Council (CSC). This work has been performed in the framework of the Ph.D. program in Materials Science of the Universitat Autònoma de Barcelona (UAB), through the CSC/UAB Joint Scholarship.

Acknowledgments: The authors thank B. Bozzo; and A. Crespi and F. J. Campos for their technical support during magnetic and X-ray diffraction measurements.

Conflicts of Interest: The authors declare no conflict of interest.

References

1. Cho, A.; Arthur, J. Molecular beam epitaxy. *Prog. Solid State Chem.* **1975**, *10*, 157–191, doi:10.1016/0079-6786(75)90005-9.
2. Schlom, D.G. Perspective: Oxide molecular-beam epitaxy rocks! *APL Mater.* **2015**, *3*, 062403, doi:10.1063/1.4919763.
3. Safi, I. Recent aspects concerning DC reactive magnetron sputtering of thin films: a review. *Surf. Coat. Technol.* **2000**, *127*, 203–218, doi:10.1016/s0257-8972(00)00566-1.
4. Galceran, R.; Frontera, C.; Balcells, L.; Cisneros-Fernández, J.; López-Mir, L.; Roqueta, J.; Santiso, J.; Bagués, N.; Bozzo, B.; Pomar, A.; et al. Engineering the microstructure and magnetism of $\text{La}_2\text{CoMnO}_6-\delta$ thin films by tailoring oxygen stoichiometry. *Appl. Phys. Lett.* **2014**, *105*, 242401, doi:10.1063/1.4904410.
5. Blank, D.H.; Koster, G.; Rijnders, A.J.; Van Setten, E.; Slycke, P.; Rogalla, H. Epitaxial growth of oxides with pulsed laser interval deposition. *J. Cryst. Growth* **2000**, *211*, 98–105, doi:10.1016/s0022-0248(99)00880-5.
6. Opel, M. Spintronic oxides grown by laser-MBE. *J. Phys. D Appl. Phys.* **2011**, *45*, 33001, doi:10.1088/0022-3727/45/3/033001.
7. Schwartz, R.W.; Schneller, T.; Waser, R. Chemical solution deposition of electronic oxide films. *Comptes Rendus Chim.* **2004**, *7*, 433–461, doi:10.1016/j.crci.2004.01.007.
8. Schneller, T.; Waser, R.; Kosec, M.; Payne, D. *Chemical Solution Deposition of Functional Oxide Thin Films*. Springer Science and Business Media LLC: Berlin, Germany, 2013; pp. 1–796.
9. Calzada, M.L. Sol-Gel Electroceramic Thin Films. In *The Sol-Gel Handbook*; Levy, D., Zayat, M., Eds.; Wiley: Hoboken, NY, USA, 2015; pp. 841–882.
10. Jia, Q.X.; McCleskey, T.M.; Burrell, A.K.; Lin, Y.; Collis, G.E.; Wang, H.; Li, A.D.Q.; Foltyn, S.R. Polymer-assisted deposition of metal-oxide films. *Nat. Mater.* **2004**, *3*, 529–532, doi:10.1038/nmat1163.

11. Bassiri-Gharb, N.; Bastani, Y.; Bernal, A. Chemical solution growth of ferroelectric oxide thin films and nanostructures. *Chem. Soc. Rev.* **2014**, *43*, 2125–2140, doi:10.1039/c3cs60250h.
12. Han, H.; Chen, Y.; Wang, Z. Effect of heating rates on the crystallization process of (111)-oriented lead zirconate titanate thin films prepared by the sol–gel method. *Ceram. Int.* **2015**, *41*, 15208–15216, doi:10.1016/j.ceramint.2015.08.098.
13. Queraltó, A.; De La Mata, M.; Arbiol, J.; Obradors, X.; Puig, T. Disentangling Epitaxial Growth Mechanisms of Solution Derived Functional Oxide Thin Films. *Adv. Mater. Interfaces* **2016**, *3*, 1600392, doi:10.1002/admi.201600392.
14. Schwartz, R.W. Chemical Solution Deposition of Perovskite Thin Films. *Chem. Mater.* **1997**, *9*, 2325–2340, doi:10.1021/cm970286f.
15. Gunawan, R.; Jung, M.; Seebauer, E.; Braatz, R. Optimal control of rapid thermal annealing in a semiconductor process. *J. Process. Control.* **2004**, *14*, 423–430, doi:10.1016/j.jprocont.2003.07.005.
16. Vasala, S.; Karppinen, M. A2B'B'O6 perovskites: A review. *Prog. Solid State Chem.* **2015**, *43*, 1–36, doi:10.1016/j.prosolidstchem.2014.08.001.
17. Anderson, M.; Greenwood, K.; Taylor, G.; Poeppelmeier, K. B-cation arrangements in double perovskites. *Prog. Solid State Chem.* **1993**, *22*, 197–233, doi:10.1016/0079-6786(93)90004-b.
18. Wang, H.; Gazquez, J.; Frontera, C.; Chisholm, M.F.; Pomar, A.; Martínez, B.; Mestres, N. Spontaneous cationic ordering in chemical-solution-grown La2CoMnO6 double perovskite thin films. *NPG Asia Mater.* **2019**, *11*, 44, doi:10.1038/s41427-019-0144-8.
19. Wang, H.; Frontera, C.; Herrero-Martín, J.; Pomar, A.; Roura-Grabulosa, P.; Martínez, B.; Mestres, N. Aqueous Chemical Solution Deposition of Functional Double Perovskite Epitaxial Thin Films. *Chem.-A Eur. J.* **2020**, *26*, 9338–9347, doi:10.1002/chem.202000129.
20. Kareev, M.; Prosandeev, S.; Liu, J.; Gan, C.; Kareev, A.; Freeland, J.W.; Xiao, M.; Chakhalian, J. Atomic control and characterization of surface defect states of TiO2 terminated SrTiO3 single crystals. *Appl. Phys. Lett.* **2008**, *93*, 061909, doi:10.1063/1.2971035.
21. Stamenov, P.; Coey, J. Sample size, position, and structure effects on magnetization measurements using second-order gradiometer pickup coils. *Rev. Sci. Instrum.* **2006**, *77*, 15106, doi:10.1063/1.2149190.
22. Carcano, G.; Ceriani, M.; Soglio, F. Spin Coating with High Viscosity Photoresist on Square Substrates—Applications in the Thin Film Hybrid Microwave Integrated Circuit Field. *Microelectron Int.* **1993**, *10*, 12–20, doi:10.1108/eb044507.
23. Kim, M.K.; Moon, J.Y.; Choi, H.Y.; Oh, S.H.; Lee, N.; Choi, Y.J. Investigation of the magnetic properties in double perovskite R2CoMnO6 single crystals (R = rare earth: La to Lu). *J. Phys. Condens Matter* **2015**, *27*, 426002, doi:10.1088/0953-8984/27/42/426002.
24. Guo, H.; Burgess, J.; Street, S.; Gupta, A.; Calvarese, T.G.; Subramanian, M.A. Growth of epitaxial thin films of the ordered double perovskite La2NiMnO6 on different substrates. *Appl. Phys. Lett.* **2006**, *89*, 022509, doi:10.1063/1.2221894.
25. Goodenough, J.B. An interpretation of the magnetic properties of the perovskite-type mixed crystals La1-xSrxCoO3-x. *J. Phys. Chem. Solids* **1958**, *6*, 287–297, doi:10.1016/0022-3697(58)90107-0.
26. Kanamori, J. Superexchange interaction and symmetry properties of electron orbitals. *J. Phys. Chem. Solids* **1959**, *10*, 87–98, doi:10.1016/0022-3697(59)90061-7.
27. Anderson, P.W. Antiferromagnetism. Theory of Superexchange Interaction. *Phys. Rev.* **1950**, *79*, 350–356, doi:10.1103/physrev.79.350.
28. Balcels, L.; Navarro, J.; Bibes, M.; Roig, A.; Martínez, B.; Fontcuberta, J. Cationic ordering control of magnetization in Sr2FeMoO6 double perovskite. *Appl. Phys. Lett.* **2001**, *78*, 781–783, doi:10.1063/1.1346624.
29. Truong, K.D.; Singh, M.K.; Jandl, S.; Fournier, P. Influence of Ni/Mn cation order on the spin-phonon coupling in multifunctional La2NiMnO6 epitaxial films by polarized Raman spectroscopy. *Phys. Rev. B* **2009**, *80*, 134424, doi:10.1103/physrevb.80.134424.
30. Singh, M.P.; Grygiel, C.; Sheets, W.C.; Boullay, P.; Hervieu, M.; Prellier, W.; Mercey, B.; Simon, C.; Raveau, B. Absence of long-range Ni/Mn ordering in ferromagnetic La2NiMnO6 thin films. *Appl. Phys. Lett.* **2007**, *91*, 012503, doi:10.1063/1.2753715.
31. Singh, M.; Charpentier, S.; Truong, K.D.; Fournier, P. Evidence of bidomain structure in double-perovskite La2CoMnO6 thin films. *Appl. Phys. Lett.* **2007**, *90*, 211915, doi:10.1063/1.2743387.

32. Galceran, R.; López-Mir, L.; Bozzo, B.; Cisneros-Fernández, J.; Santiso, J.; Balcells, L.; Frontera, C.; Martínez, B. Strain-induced perpendicular magnetic anisotropy in $\text{La}_2\text{CoMnO}_{6-\epsilon}$ thin films and its dependence on film thickness. *Phys. Rev. B* **2016**, *93*, 144417, doi:10.1103/physrevb.93.144417.
33. López-Mir, L.; Galceran, R.; Herrero-Martin, J.; Bozzo, B.; Cisneros-Fernández, J.; Miner, E.V.P.; Pomar, A.; Balcells, L.; Martínez, B.; Frontera, C. Magnetic anisotropy and valence states in $\text{La}_2\text{Co}_{1-x}\text{Mn}_{1+x}\text{O}_6$ ($x \approx 0.23$) thin films studied by x-ray absorption spectroscopy techniques. *Phys. Rev. B* **2017**, *95*, 224434, doi:10.1103/PhysRevB.95.224434.
34. Choudhury, D.; Mandal, P.; Mathieu, R.; Hazarika, A.; Rajan, S.; Sundaresan, A.; Waghmare, U.V.; Knut, R.; Karis, O.; Nordblad, P.; et al. Near-Room-Temperature Colossal Magnetodielectricity and Multiglass Properties in Partially Disordered $\text{La}_2\text{NiMnO}_6$. *Phys. Rev. Lett.* **2012**, *108*, 127201, doi:10.1103/physrevlett.108.127201.
35. Pal, S.; Govinda, S.; Goyal, M.; Mukherjee, S.; Pal, B.; Saha, R.; Sundaresan, A.; Jana, S.; Karis, O.; Freeland, J.W.; et al. Effect of anti-site disorder on magnetism in $\text{La}_2\text{NiMnO}_6$. *Phys. Rev. B* **2018**, *97*, 165137, doi:10.1103/physrevb.97.165137.
36. Nasir, M.; Kumar, S.; Patra, N.; Bhattacharya, D.; Jha, S.N.; Basaula, D.R.; Bhatt, S.; Khan, M.; Liu, S.-W.; Biring, S.; et al. Role of Antisite Disorder, Rare-Earth Size, and Superexchange Angle on Band Gap, Curie Temperature, and Magnetization of R_2NiMnO_6 Double Perovskites. *ACS Appl. Electron. Mater.* **2019**, *1*, 141–153, doi:10.1021/acsaelm.8b00062.
37. Dass, R.I.; Goodenough, J.B. Multiple magnetic phases of $\text{La}_2\text{CoMnO}_{6-\delta}$ ($0 < \delta < 0.05$). *Phys. Rev. B* **2003**, *67*, 014401. doi: 10.1103/PhysRevB.67.014401.
38. Guo, H.Z.; Gupta, A.; Zhang, J.; Varela, M.; Pennycook, S.J. Effect of oxygen concentration on the magnetic properties of $\text{La}_2\text{CoMnO}_6$ thin films. *Appl. Phys. Lett.* **2007**, *91*, 202509, doi:10.1063/1.2814919.
39. Shi, J.; Wang, C.; Xu, Z.; Shen, Q.; Zhang, L. Enhanced electrical and magnetic properties of post-annealed plasma-activated-sintered $\text{La}_2\text{CoMnO}_6$ ceramics. *Ceram. Int.* **2019**, *45*, 20855–20859, doi:10.1016/j.ceramint.2019.07.073.
40. Spurgeon, S.R.; Du, Y.; Droubay, T.; Devaraj, A.; Sang, X.; Longo, P.; Yan, P.; Kotula, P.G.; Shutthanandan, V.; Bowden, M.E.; et al. Competing Pathways for Nucleation of the Double Perovskite Structure in the Epitaxial Synthesis of $\text{La}_2\text{MnNiO}_6$. *Chem. Mater.* **2016**, *28*, 3814–3822, doi:10.1021/acs.chemmater.6b00829.
41. Shannon, R.D. Revised effective ionic radii and systematic studies of interatomic distances in halides and chalcogenides. *Acta Crystallogr. Sect. A Cryst. Phys. Diffr. Theor. Gen. Crystallogr.* **1976**, *32*, 751–767, doi:10.1107/s0567739476001551.
42. Nasir, M.; Khan, M.; Kumar, S.; Bhatt, S.; Patra, N.; Bhattacharya, D.; Jha, S.N.; Biring, S.; Sen, S. The effect of high temperature annealing on the antisite defects in ferromagnetic $\text{La}_2\text{NiMnO}_6$ double perovskite. *J. Magn. Magn. Mater.* **2019**, *483*, 114–123, doi:10.1016/j.jmmm.2019.03.083.
43. Wu, S.-Q.; Cheng, S.; Lu, L.; Liu, M.; Jin, X.-W.; Cheng, S.; Mi, S. B-site ordering and strain-induced phase transition in double-perovskite $\text{La}_2\text{NiMnO}_6$ films. *Sci. Rep.* **2018**, *8*, 2516, doi:10.1038/s41598-018-20812-4.

Publisher's Note: MDPI stays neutral with regard to jurisdictional claims in published maps and institutional affiliations.



© 2020 by the authors. Licensee MDPI, Basel, Switzerland. This article is an open access article distributed under the terms and conditions of the Creative Commons Attribution (CC BY) license (<http://creativecommons.org/licenses/by/4.0/>).

Supporting Information

for Materials 2020, 13, 4966

Rapid Thermal Annealing of Double Perovskite Thin Films Formed by Polymer Assisted Deposition

Hailin Wang, Carlos Frontera, Benjamín Martínez* and Narcís Mestres*

Rapid Thermal Annealing of Double Perovskite Thin Films Formed by Polymer Assisted Deposition

Hailin Wang, Carlos Frontera, Benjamín Martínez* and Narcís Mestres*

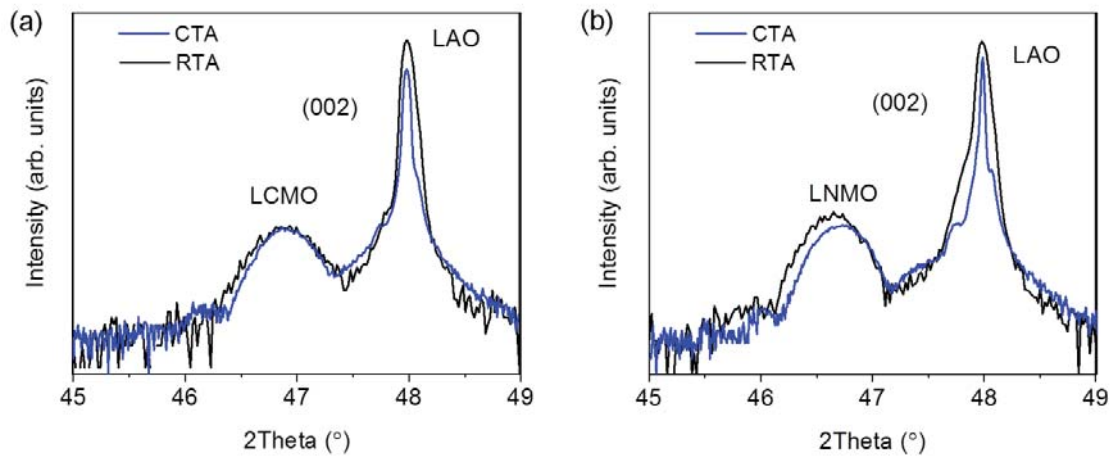


Figure S1. High-resolution $\theta/2\theta$ x-ray diffraction (XRD) scans of the (0 0 2) reflections comparing thin films grown by conventional thermal annealing (CTA) and rapid thermal annealing (RTA). (a) LCMO/LAO and (b) LNMO/LAO thin films. The slightly different strained state observed between the RTA and CTA LNMO/LAO thin films may be due to small differences on thickness or strain relaxation of the films.

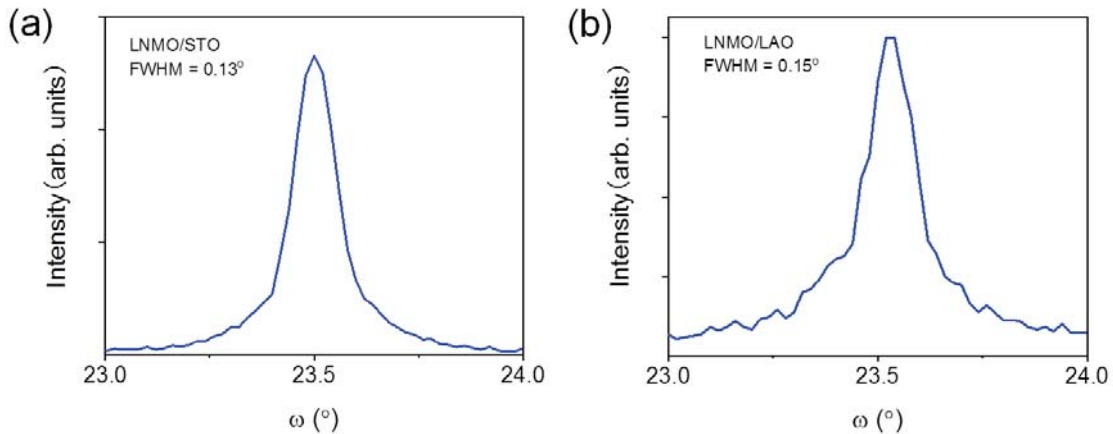


Figure S2. Rocking curves of the (0-0-2) reflections of (a) LNMO/STO thin film, and (b) LNMO/LAO thin film. The full width at half maximum (FWHM) values indicates the good crystallinity of the samples with some mosaicity.

Zero field cooled-field cooled (ZFC-FC) magnetization curves for different $\text{La}_2\text{NiMnO}_6$ (LNMO) epitaxial films prepared by rapid thermal annealing (RTA), measured at 100 Oe and 1 kOe are shown in Figure S3. For low fields (below coercive field H_c) irreversibility between ZFC and FC magnetization branches extends down to low temperatures. However, on increasing the applied field to 1 kOe, i.e. a field larger than H_c , the irreversibility is fully suppressed in samples prepared by conventional annealing process (see Figure S4), while it persists below about 40 K in the case of samples prepared by RTA (see Figure S3a).

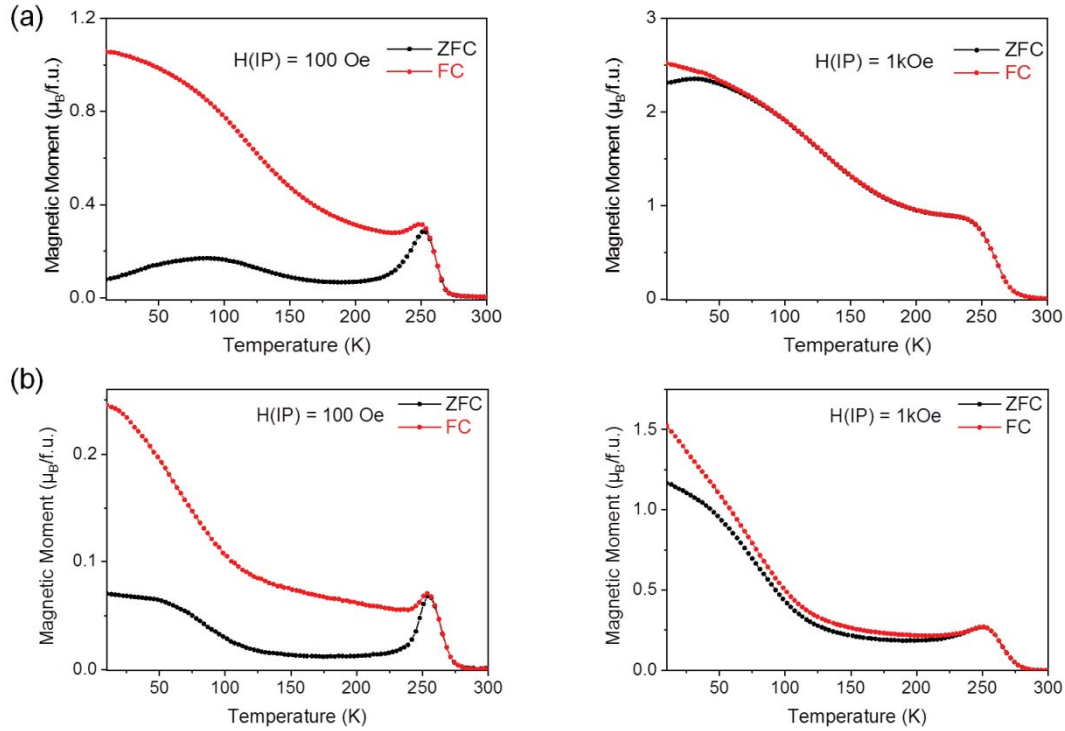


Figure S3. Zero-field-cooled (ZFC) and field-cooled (FC) magnetization curves measured at fields of 100 Oe and 1 kOe for LNMO epitaxial thin film samples grown by Rapid Thermal Annealing (RTA). (a) LNMO/STO film thermally treated in RTA conditions (20 °C/s heating ramp, dwell time 20 min at 900 °C); (b) LNMO/LAO epitaxial film thermally treated in RTA conditions (20 °C/s heating ramp, dwell time 10 min at 900 °C).

The existence of this low temperature irreversibility, for fields above H_c , in RTA samples is indicative of the existence of a higher magnetic disorder. This magnetic disorder should be attributable to the disorder generated by the simultaneous nucleation of grains in RTA samples and their interaction with anti site disorder (ASD). ASDs promote the appearance of $\text{Ni}^{2+}\text{-O-Ni}^{2+}$ and $\text{Mn}^{4+}\text{-O-Mn}^{4+}$ antiferromagnetic (AFM) interactions mimicking a spin glass-like behavior. Variations in the irreversibility between the ZFC and FC magnetization branches at low temperature should be somehow correlated with the amount of ASDs in the structure. In the case of LNMO/LAO with a higher degree of disorder irreversibility between ZFC and FC branches extends to higher temperatures (see Fig. S3b) even the global behavior is the same.

As pointed out by Choudhury *et al.* [1], the random crystallographic occupation sets the stage for mixed ferromagnetic (FM) and AFM interactions between the transition metal cations and in turn, leads to inhomogeneous magnetic behavior in $\text{La}_2\text{NiMnO}_6$. In a perfectly ordered double perovskite, the magnetic exchange is governed by the FM $\text{Ni}^{2+}\text{-O-Mn}^{4+}$ interaction. With the occurrence of site disorder, additional AFM $\text{Ni}^{2+}\text{-O-Ni}^{2+}$ and $\text{Mn}^{4+}\text{-O-Mn}^{4+}$ paths are introduced. The spin glass like behavior that appears at low temperatures has its origin in the multiple exchange paths that arise due to mixed interactions [1, 2]. The competition between the FM and AFM interactions is the origin of the magnetic frustration which results in a spin glass-like state.

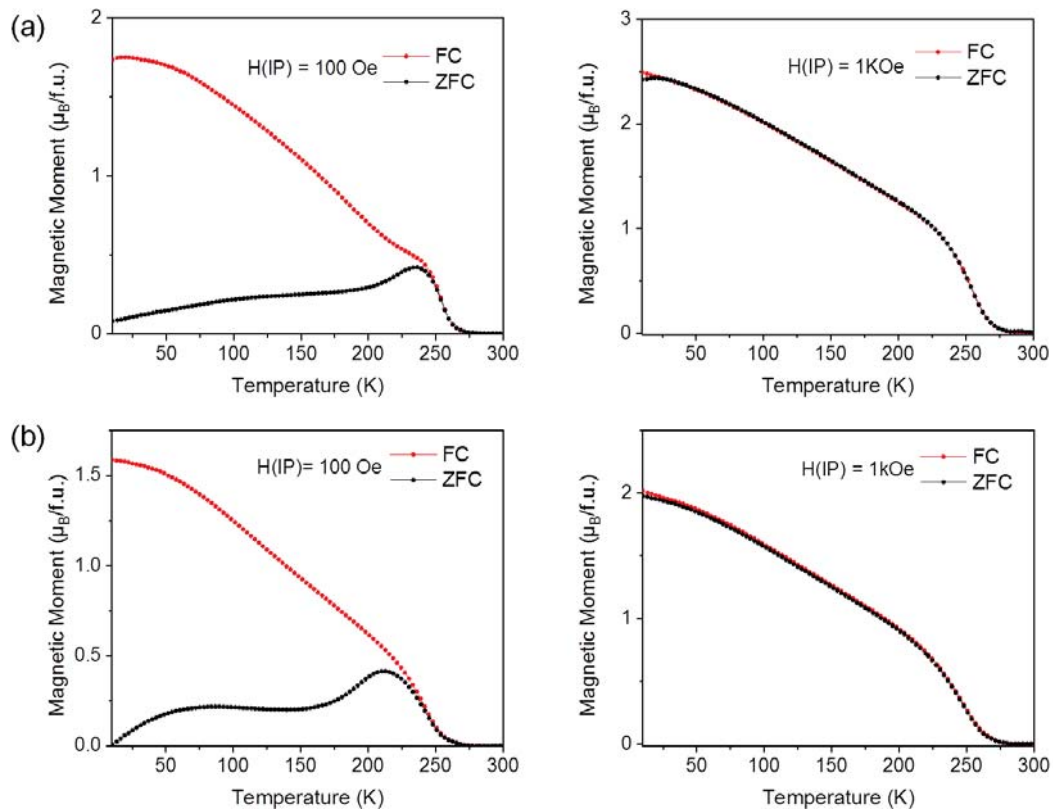


Figure S4. Zero-field-cooled (ZFC) and field-cooled (FC) magnetization curves measured at fields of 100 Oe and 1 kOe for LNMO epitaxial thin film samples grown by conventional thermal annealing (CTA). (a) LNMO/STO film thermally treated with 2 °C/min heating and cooling ramps, dwell time 30 min at 875°C under oxygen flow, 0.4 l/min; (b) LNMO/LAO epitaxial film thermally treated at the same conditions as previous sample.

References

1. Choudhury, D.; Mandal, P.; Mathieu, R.; Hazarika, A.; Rajan, S.; Sundaresan, A.; Waghmare, U. V.; Knut, R.; Karis, O.; Nordblad, P.; Sarma, D. D., Near-room-temperature colossal magnetodielectricity and multiglass properties in partially disordered $\text{La}_2\text{NiMnO}_6$. *Phys. Rev. Lett.* **2012**, *108*, 127201. doi: 10.1103/PhysRevLett.108.127201.
2. Devi Chandrasekhar, K.; Das, A.K.; Venimadhav, A., Spin glass behavior and extrinsic origin of magnetodielectric effect in non-multiferroic $\text{La}_2\text{NiMnO}_6$ nanoparticles. *J. Phys.: Condens. Matter* **2012**, *24*, 376003. doi:10.1088/0953-8984/24/37/376003.

4.4 Dynamic magnetic properties and spin pumping in $\text{La}_{0.92}\text{MnO}_3$ epitaxial thin films prepared by polymer assisted deposition

As already mentioned in the previous chapters, growth of thin films by chemical methods has been a hot topic in the recent years as they offer appealing advantages over vacuum techniques as stoichiometric versatility and low-cost scalability. Among them, Polymer-Assisted-Deposition (PAD) is particularly attractive as it relies in environmentally friendly water-based solutions. However, serious concerns have been raised on the control of their interfacial quality hampering their use in emergent applications relaying in flat sharp interfaces, for example, for spintronics.

In this work it is shown that $\text{La}_{0.92}\text{MnO}_3$ (LMO) epitaxial thin films grown by PAD are of high microstructural quality with low magnetic damping, thus suitable for spintronic applications.

The preparation of the precursor solutions and the spin-coating processes are similar to that followed in the previous works. The final aqueous precursor solutions with the desired La/Mn 0.92:1 final stoichiometry were prepared. After the polymeric layer was deposited, it was annealed in a horizontal tube furnace under an oxygen flow, at 950 °C for 30 min.

XRD patterns and reciprocal space maps reveal that the films grow epitaxial, cube-on-cube and fully strained with the SrTiO_3 substrate. AFM topography studies show flat surfaces with RMS surface roughness values of ~ 0.2 nm. The observation of arrays of alternating dark and clear fringes in the scanning electron microscopy (SEM) images suggests the formation of ordered rhombohedral twin domains. These two features in AFM and SEM images demonstrate the high structural quality of the grown films.

The M - T curves and M - H loops reveal that the LMO films are ferromagnetic with $T_C \sim 290$ K, and $M_S \sim 330$ emu/cm³. The transport properties exhibited a well defined metal-to-insulator transition with $T_{MI} = 280$ K, and $\rho_{10K} = 6 \times 10^{-4}$ Ω cm.

Ferromagnetic resonance measurements in LMO/Pt bilayers give clear indications of the aperture of a new angular momentum dissipation channel that would be indicative of injection of pure spin currents into the Pt layer by spin pumping. This transfer of

spin angular momentum through the interface between the ferromagnetic layer (LMO) and Pt layer is evidenced by an increase of magnetic damping. These results are of strong interest since they demonstrate that PAD technique allows obtaining complex oxide thin films of high microstructural quality suitable for spintronic applications. We also present a deep study of the temperature dependence of the magnetodynamic properties of LMO thin films prepared by PAD showing that microstructural strain release from rhombohedral bulk phase results in an in-plane four-fold anisotropy with [110] as easy axis.

Our results suggest that LMO films grown by PAD may be used as efficient spin source systems in heterostructures for spintronic devices.

**Dynamic magnetic properties and spin pumping in polymer-assisted-
deposited $\text{La}_{0.92}\text{MnO}_3$ thin films**

Hailin Wang, Alberto Pomar, * Sergi Martín-Rio, Carlos Frontera, Narcís Mestres and Benjamín Martínez

Instituto de Ciencia de Materiales de Barcelona, ICMAB-CSIC,

Campus de la UAB, 08193 Bellaterra, Spain.

E-mail: apomar@icmab.es

Cite this: *J. Mater. Chem. C*, 2019,
7, 12633

Dynamic magnetic properties and spin pumping in polymer-assisted-deposited $\text{La}_{0.92}\text{MnO}_3$ thin films

Hailin Wang,^{id} Alberto Pomar,^{id}* Sergi Martín-Rio,^{id} Carlos Frontera,^{id}
Narcis Mestres^{id} and Benjamín Martínez^{id}

Complex oxide thin films grown by using chemical methods are of strong interest because of their low-cost, environment friendly fabrication and easy scalability. However, their introduction in spintronic applications or magnetic devices is still scarce mainly because of concerns regarding their interfacial quality. Here, we report on the preparation by polymer-assisted-deposition (PAD) of epitaxial $\text{La}_{0.92}\text{MnO}_3$ (LMO) thin films. We demonstrate that ferromagnetic conducting LMO thin films with smooth surfaces (rms ~ 0.2 nm) can be prepared by PAD. By means of temperature-dependent broadband ferromagnetic resonance (FMR), we show that the LMO film exhibits a four-fold in-plane anisotropy, with [110] being the easy in-plane axis, compatible with strain release from the rhombohedral bulk phase. It has also been found that the isotropic Gilbert damping, α , determined from the broadening of the FMR linewidth, does not show a relevant extrinsic contribution and it exhibits an intraband-like temperature dependence, *i.e.* it increases as temperature decreases. By capping LMO thin films with a 10 nm thick Pt layer deposited *ex situ*, damping is substantially enhanced, from a value at 150 K of $\alpha_{\text{LMO}} \sim 1 \times 10^{-2}$ for the bare LMO film to $\alpha_{\text{LMO+Pt}} \sim 2.5 \times 10^{-2}$ for the Pt capped film. This strong increase of magnetic damping is indicative of the transfer of spin momentum from LMO to the Pt layer by spin pumping. Our results demonstrate that LMO films grown by PAD may be used as efficient spin source systems in heterostructures for spintronic devices.

Received 23rd July 2019,
Accepted 16th September 2019

DOI: 10.1039/c9tc04008k

rsc.li/materials-c

1 Introduction

The utilization of transition metal oxides in spintronic applications relies on the availability of high-quality thin films that may be helpful in the ever-increasing demands of miniaturization and reduced power consumption. Among the different promising technologies, devices based on the spin transfer torque effect are very appealing due to the possibility of manipulating spin configurations in an efficient way with low power consumption.¹ Thus, a noticeable effort has been devoted to studying the magnetization switching processes, crucial to spin torque phenomena and, in particular, to understanding and controlling magnetic damping.^{2,3} In general, low magnetic damping constants may be achieved in transition metal oxide films, either in insulating materials as yttrium iron garnet⁴ or in half-metallic compounds as $\text{La}_{2/3}\text{Sr}_{1/3}\text{MnO}_3$.⁵ In the last case, the main drawback arises from the important extrinsic contribution to damping associated with the scattering of conduction electrons by the two magnon mechanism.⁶ This extrinsic damping is enhanced by the presence of surface/interface roughness or magnetic inhomogeneity originating from the defect landscape of the film. Nevertheless, a tough tuning of the growth conditions

allows obtaining intrinsic damping values in the order of 10^{-3} for films grown by using physical methods (pulsed laser deposition, sputtering or molecular beam epitaxy).² These low Gilbert damping values open the possibility to use half-metallic manganite-based oxides to generate pure spin currents by, for example, spin pumping into a non magnetic metal. Although few investigations have been made, there are already several promising results proving this approach.^{7–10}

The strong activity in the field has boosted a fast improvement in the quality of grown thin films. Although high-vacuum methods, such as molecular beam epitaxy,¹¹ RF sputtering¹² and pulsed laser deposition,^{13–15} offer unquestionable advantages for the growth of metal oxide thin films like high crystal quality, precise control of composition and thickness at atomic-scale even for several unit cell thick films, more affordable alternatives are desirable. Generally speaking, chemical deposition techniques offer the ability to grow over large areas at low cost and the versatility to easily tune stoichiometry in complex oxides makes chemical deposition techniques very appealing. In particular, polymer assisted deposition (PAD) has appeared as a competitive route for environment friendly approaches as it is based on the deposition of cationic aqueous solutions.¹⁶ It is also worth noting that since the aqueous PAD precursor solutions are largely stable, they enable setting a metal library easily to be mixed afterwards to obtain finely compositionally controlled complex oxides.

Instituto de Ciencia de Materiales de Barcelona, ICMA-B-CSIC, Campus de la UAB,
08193 Bellaterra, Spain. E-mail: apomar@icmab.es; Tel: +34 935801853



Moreover, although larger processing times may appear as a drawback, the slow growth conditions of PAD close to thermodynamic equilibrium conditions are adequate for the epitaxial growth of ternary and complex oxides as has already been demonstrated for a large variety of oxide films.^{17,18} Since the energy balance involved during the growth process is quite delicate, chemical growth methods may lead to a defect landscape different from that generated by using vacuum techniques, resulting in the modification of the physical properties of the films, as for example, magnetic anisotropy.¹⁹ In spite of their importance, the dynamic magnetic properties of chemically grown films remain an open and unexplored topic.

The main aim of this work is to study the magnetic anisotropy and damping of oxide thin films grown by PAD and to demonstrate that they are suitable for spintronic applications. For this, we have selected the ferromagnetic-metallic $\text{La}_{0.92}\text{MnO}_3$. LaMnO_3 , the parent compound of the colossal magnetoresistance family of manganite perovskites, has recently regained new attention as an oxide catalyst for fuel cells and metal–air batteries,²⁰ and as an electrode material for supercapacitors,²¹ as well as due to its unexpected ferromagnetic behavior in thin films.^{22–24} Although bulk stoichiometric LaMnO_3 is a Mott insulator and an A-type antiferromagnet (AF), in thin film form, its properties may be tuned into a ferromagnetic (FM) state due to the structural strain induced by the substrate^{25,26} or by introducing ion vacancies (both in La and Mn sites) in the material.^{27–29} However, LaMnO_3 is a complex system where it is very difficult to disentangle the effects of strain, oxygenation and cation vacancies on the magnetic state. On one hand, theoretical studies indicated that the FM behavior in LaMnO_3 thin films originates from the strain-induced orbital ordering²⁶ and this mechanism was invoked to explain the tuning between AF and FM states in stoichiometric LaMnO_3 thin films prepared under different growth oxygen pressures.²⁵ On the other hand, the dependence of magnetic properties on film thickness is still puzzling as, while an increase of saturation magnetization and transition temperature with increasing thickness was reported for films grown on SrTiO_3 ,³⁰ the opposite seems to occur for films grown on LaAlO_3 substrates.³¹ It is worth noting that, in the case of stoichiometric samples, the material exhibits an insulating character in both the AF and the FM states.²⁵ However, in the presence of cationic vacancies, to preserve charge neutrality, a mixed Mn^{3+} and Mn^{4+} valence state appears. This mixed valence state promotes the appearance of double exchange interaction *via* oxygen atoms driving the system into a ferromagnetic and metallic state.²⁸ As an example, 8% of La site vacancies in LaMnO_3 creates 24% of holes at the Mn sites leading to a robust ferromagnetic ordering. This is the amount of holes present in $\text{La}_{0.76}\text{Ca}_{0.24}\text{MnO}_3$, for example, although the smaller cationic disorder in $\text{La}_{0.92}\text{MnO}_3$ makes its electronic conductivity much larger, and its Curie temperature increases up to values close to $T_c = 300$ K making it interesting for spintronic applications. In this work, we have studied, by broadband ferromagnetic resonance, the magnetodynamic properties of ferromagnetic $\text{La}_{0.92}\text{MnO}_3$ thin films prepared by PAD. The interest of this research is twofold. First, from a materials point of view, it is crucial to investigate if the continuous progress in the quality of PAD films may overcome the challenging difficulties

of roughness and homogeneity control even for properties highly dependent on defect structure as magnetic damping. Second, from a physics point of view, an attempt is made to clarify the mechanisms controlling the magnetodynamic behavior, which will be fundamental for future prospects.

2 Thin film growth and characterization

The $\text{La}_{0.92}\text{MnO}_3$ (LMO) thin films studied in this work were grown by polymer-assisted-deposition (PAD) on (001)- SrTiO_3 (STO) single-crystal substrates. Individual solutions of the different metal ions were prepared by dissolving the corresponding La and Mn nitrates in water with ethylenediaminetetraacetic acid (EDTA, 1:1 molar ratio) and polyethylenimine (PEI), Sigma Aldrich, Ref 408727, with an average molecular weight of 25 000 (1:1 mass ratio to EDTA). Each individual solution was filtrated using Amicon filtration units (10 kDa), and retained portions were analyzed by Inductively Coupled Plasma (ICP) spectroscopy (Optima 4300 DV™ ICP-OES PerkinElmer). The solutions were mixed according to the desired La:Mn 0.92:1 final stoichiometry ratio and spin coated on top of $5 \times 5 \text{ mm}^2$ (001)- SrTiO_3 (STO) substrates purchased from Crystec GmbH, Germany. The as-received substrates were chemically etched and thermally treated to make them TiO_2 -terminated with atomically flat terraces.³² After the deposition of the polymeric layer, it was annealed in a horizontal tube furnace under oxygen flow at 950°C for 30 min. The results discussed in this paper correspond to the layers of LMO of 10 nm as determined by X-ray reflectometry. They were obtained using solutions with a total cation concentration of 139 mM and a rate of 5000 rpm for 90 seconds during spinning.

Systematic θ - 2θ X-ray measurements as shown in Fig. 1(a) demonstrate that LMO thin films are in a single phase with no signatures of reflections other than the standard pseudocubic (00 l) ones. High crystallinity and excellent out-of-plane orientation of the film were evidenced by the low values, less than 0.1° , of the full-width at half-maximum (FWHM) of the rocking curves around the (002) reflection peak (see the inset in Fig. 1(a)). In Fig. 1(b), we show the detail of the θ - 2θ scan around the (002) diffraction peak where the deconvolution of the substrate and film peaks is indicated by the corresponding lines. Fitting of the (00 l) peak positions leads to a pseudocubic out-of-plane parameter of $a_\perp \sim 3.87 \text{ \AA}$. The strain state of the LMO films was studied by using reciprocal space maps around $(-103)_{\text{STO}}$ reflections, as shown in Fig. 1(c). As thin film reflection is very close to the substrate one, in this case, to increase the signal-to-noise ratio, thicker films ($\sim 20 \text{ nm}$) were used. The in-plane lattice parameter of the LMO film, a_\parallel , matches that of the substrate one, *i.e.*, $a_\parallel = 3.905 \text{ \AA}$. With these a_\parallel and a_\perp values, a rough estimation of pseudocubic volume can be calculated leading to $V_{\text{pc}} = a_\parallel^2 a_\perp \sim 59.0 \text{ \AA}^3$. The above obtained values may be compared with the reported bulk ones. It is known that the crystal structure of LaMnO_3 perovskite strongly depends on oxygen content. In particular, for La-deficient $\text{La}_{0.92}\text{MnO}_x$ samples, a transition has been reported from the



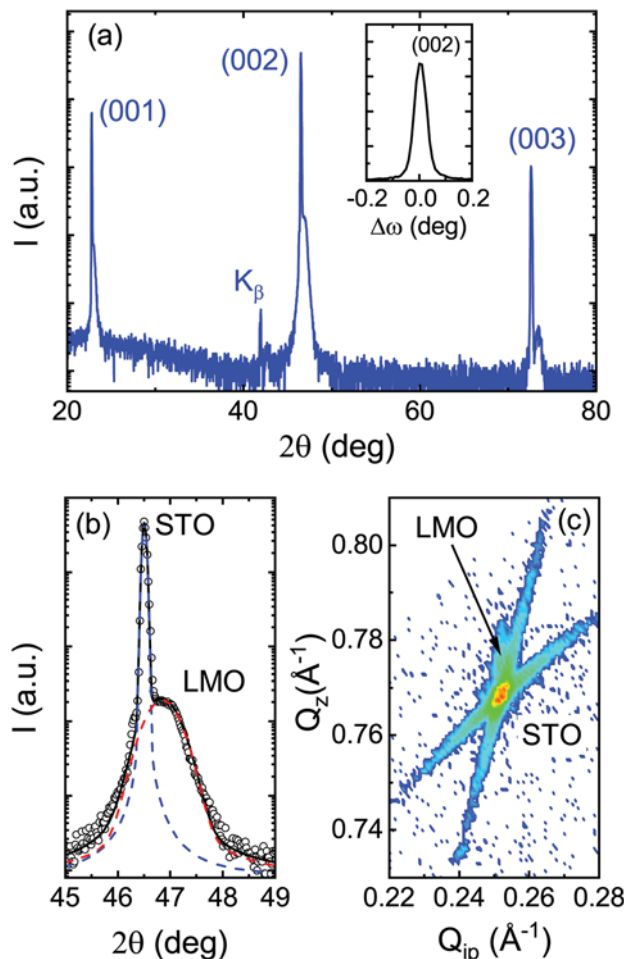


Fig. 1 (a) X-ray θ - 2θ scan of the $\text{La}_{0.92}\text{MnO}_3$ thin film on a SrTiO_3 substrate. For the LMO film, only (00 l) reflections were observed. The inset shows the rocking curve obtained around the (002) reflection of LMO exhibiting a FWHM = 0.06°. (b) Details of the θ - 2θ scan around the (002)_{STO} reflection showing the deconvolution between the STO substrate peak (blue lines) and the LMO peak (red lines). (c) Reciprocal space map of the (-103)_{STO} peak revealing in-plane compressive strain in the films. Pseudocubic notation is always used.

orthorhombic $Pnma$ structure for $x = 2.88$ to a rhombohedral $R\bar{3}c$ one for $x = 2.98$.³³ Concomitant to this structural evolution, unit cell volume is reduced from $V_{\text{ort}} = 61.0 \text{ \AA}^3$ for $Pnma$ to $V_{\text{rh}} = 58.9 \text{ \AA}^3$ for $R\bar{3}c$. Furthermore, rhombohedral lattice parameters $a_{\text{rh}} = 5.477 \text{ \AA}$ and $\alpha_{\text{rh}} = 60.614^\circ$ correspond to a pseudocubic matching distance of $a_{\text{pc}} = 1/2\sqrt{3} - 2\cos\alpha_{\text{rh}} \sim 3.89 \text{ \AA}$ leading to a +0.4% tensile mismatch by the STO substrate.³⁴ Thus, our experimental results suggest a strain accommodation mainly through elastic mechanisms from the rhombohedral phase.³⁵

Morphological characteristics of the LMO film surfaces were analyzed *via* Atomic Force Microscopy (AFM) in tapping mode. Under optimal growth conditions, films develop an atomically flat surface that mimics the terrace-step morphology of the surface of the underlying STO substrate, as shown in Fig. 2(a). Quantitative analysis of a $5 \mu\text{m} \times 5 \mu\text{m}$ image indicates a flat surface with rms $\sim 0.25 \text{ nm}$, *i.e.*, less than one unit cell. Further confirmation of the high quality of the surface

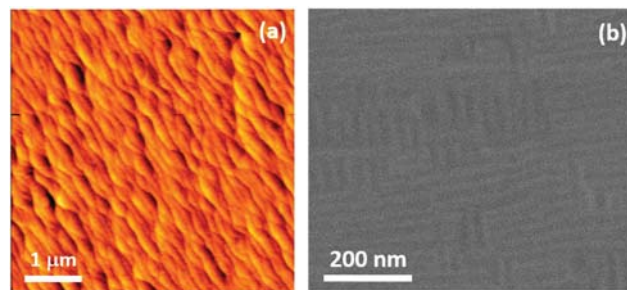


Fig. 2 (a) Topography of the surface of a LMO thin film obtained *via* atomic force microscopy in tapping mode. Terrace-step morphology inherited from the underlying STO substrate can be seen. Overall roughness rms $\sim 0.2 \text{ nm}$. (b) Scanning electron microscopy of a LMO thin film. The observation of arrays of alternating dark and clear fringes suggests the formation of ordered rhombohedral twin domains. These two features in (a) and (b) demonstrate the high quality of the surfaces of films prepared by using chemical methods.

morphology and microstructure of the films was obtained *via* scanning electron microscopy (SEM). Fig. 2(b) shows a typical SEM image of a 10 nm thick LMO film. In this image, taken at a small tilting angle of 2° , we may observe the occurrence of alternating parallel stripes with bright and dark contrast. Such stripes are almost aligned with the [100] edges of the substrate and they form domains of $\sim 25 \text{ nm}$ wide. As reported previously for Sr doped LMO films, they are typical of an ordered twin structure in rhombohedral films grown under tensile strain and they are the result of smooth strain accommodation during film growth.³⁶

Static magnetic properties were measured using a Quantum Design SQUID magnetometer with the external magnetic field applied parallel to the substrate plane. Field-cooled temperature dependence of magnetization, Fig. 3(a), as well as isothermal hysteresis loops, Fig. 3(b), were measured. Note that magnetic measurements have been corrected using the diamagnetic contribution of the STO substrate. LMO films are strongly ferromagnetic and no significant differences were observed as a function of thickness for samples in the range of 10–25 nm, as evidenced in Fig. 3(a). Hysteresis loops recorded between 10 K and 200 K shown in Fig. 3(b) reflect the reduction of the saturation and remnant magnetization expected from the temperature dependence of magnetization presented in Fig. 3(a). On the other hand, coercive fields are very small (less than 15 mT at 100 K) and very similar for all the studied samples irrespective of their thickness, which suggests that in the thickness range analysed (10–20 nm) the microstructure of the samples is very similar. As mentioned above, although stoichiometric LaMnO_3 is an antiferromagnetic insulator, the presence of La vacancies leads to a mixed valence state of the Mn cation (Mn^{3+} - Mn^{4+}) that promotes the strong ferromagnetic interaction mediated by the standard double exchange mechanism. The obtained values of saturation magnetization $M(5 \text{ K}) \sim 330 \text{ emu cm}^{-3}$ (corresponding to $\sim 2.1 \mu_{\text{B}} \text{ f.u.}^{-1}$) and transition temperature, $T_c \sim 290 \text{ K}$, are slightly lower than expected for $\text{La}_{0.92}\text{MnO}_3$ composition. Two main mechanisms may be invoked to explain the reduction of the saturation magnetization in thin films with respect to the bulk value. First, it is known that at



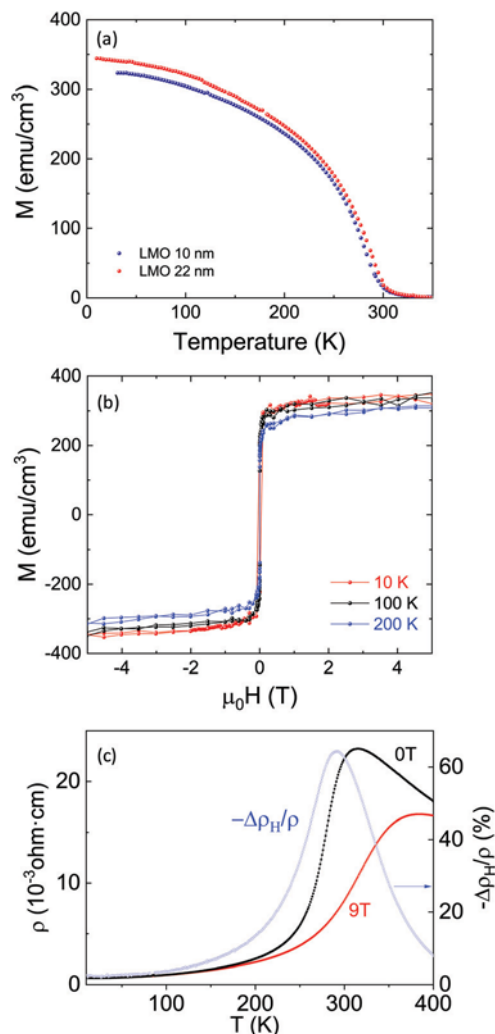


Fig. 3 (a) Temperature dependence of the magnetization measured at 5 kOe (field-cooled) for a 10 nm (blue symbols) and a 22 nm (red symbols) LMO film. (b) Hysteresis loops of a 10 nm LMO film measured at 10 K (red), 100 K (black) and 200 K (blue). (c) Temperature dependence of the electrical resistivity in the absence of an external magnetic field (0 T) (black curves) and with a magnetic field of 9 T (red curves). Magnetoresistance defined as $\Delta\rho_H/\rho = (\rho_H - \rho_0)/\rho_0$ is also shown (blue curves).

the interface with the substrate, a non magnetic dead layer may be formed due to the relaxation of biaxial stress during growth.³⁵ In this case, the measured magnetization values are affected by a wrong estimation of the real magnetic thickness. However, this dead layer tends to be of the order of a few unit cells and it cannot explain the strong deviation from the expected magnetization value in our films.³⁵ A second possibility is linked to the oxygen content of the film. In mixed valence manganites, where ferromagnetism is mediated by double-exchange interactions, saturation magnetization is controlled by the ratio $\text{Mn}^{3+}/\text{Mn}^{4+}$. A significant amount of oxygen vacancies implies a lower concentration of Mn^{4+} cations and thus a reduction of magnetization. This is the usual scenario in oxygen-deficient films. However, in LaMnO_3 , a reduction of magnetization was also observed in overoxidized bulk samples.²⁸ Here, growth under strong oxidizing conditions promotes the

creation of cation vacancies (as interstitial sites are not available for excess oxygen) and Mn^{4+} -rich clusters may be formed. These clusters enhance antiferromagnetic correlations between Mn^{4+} cations and thus, full ferromagnetism is not achieved. So, we cannot disregard either of these mechanisms to explain our results shown in Fig. 3(a). In the standard double exchange picture, a metal-insulator transition (MIT) takes place, concomitant to the magnetic transition. We have measured the transport properties of the films, *i.e.*, temperature dependence of their electrical resistivity and magnetoresistance, defined as $\Delta\rho_H/\rho = (\rho_H - \rho_0)/\rho_0$ by using a standard 4-probe van der Pauw configuration. The results are plotted in Fig. 3(c). Films exhibited a well defined metal-to-insulator transition with $T_{\text{MI}} = 280$ K defined as the inflexion point in the $\rho(T)$ curve. Residual resistance was found to be $\rho_{10\text{K}} = 6 \times 10^{-4} \Omega \text{ cm}$. This value is lower than that reported for La-deficient LMO films grown by using physical methods.²⁹ At an applied magnetic field of 9 T, the maximum value of magnetoresistance was found to be 60% at 280 K, *i.e.*, close to the transition temperature. As a summary, static magnetic and magnetotransport measurements confirmed that LMO films grown by the PAD route exhibit low disorder and strong ferromagnetic character driven by a double-exchange mechanism.

3 Magnetodynamic properties and discussion

The dynamic magnetic properties of LMO thin films as a function of temperature were studied by using a ferromagnetic resonance spectrometer (FMR) made of a broadband coplanar waveguide (NanOsc), inserted in a Physical Properties Measurements System (PPMS by Quantum Design). Measurements were performed at constant temperature using a sweeping external field at several fixed microwave frequencies (between 2 GHz and 17 GHz). Two main in-plane orientations were studied, either with the field applied along the main substrate edges, *i.e.*, $\mu_0 H \parallel [100]\text{STO}$, or at 45° of the edges, *i.e.*, $\mu_0 H \parallel [110]\text{STO}$. Fig. 4(a) shows typical FMR spectra obtained at 9 GHz and 100 K for both orientations. Note that, for a better comparison, measured signals (proportional to the first derivative of the microwave absorption intensity) have been renormalized to their respective maximum values. Each FMR spectrum may be fitted to the derivative of the sum of symmetric and antisymmetric Lorentzian components as previously suggested.³⁷ Solid lines in Fig. 4(a) correspond to the respective fitting curves. From these fittings, accurate values of the resonant field, H_{res} , and of the half-width at half-maximum linewidth, ΔH , are obtained. In transition metal oxide thin films, the presence of a small secondary resonant mode attributed to the presence of sample inhomogeneity is usually reported (secondary phase or regions with slightly different Curie temperature or magnetization that resonate at a different frequency/field).³⁸ In our case, in the whole studied temperature range, no signature of another resonant mode was observed.

The noticeable difference of the resonance field for both configurations just reflects a different saturation magnetization



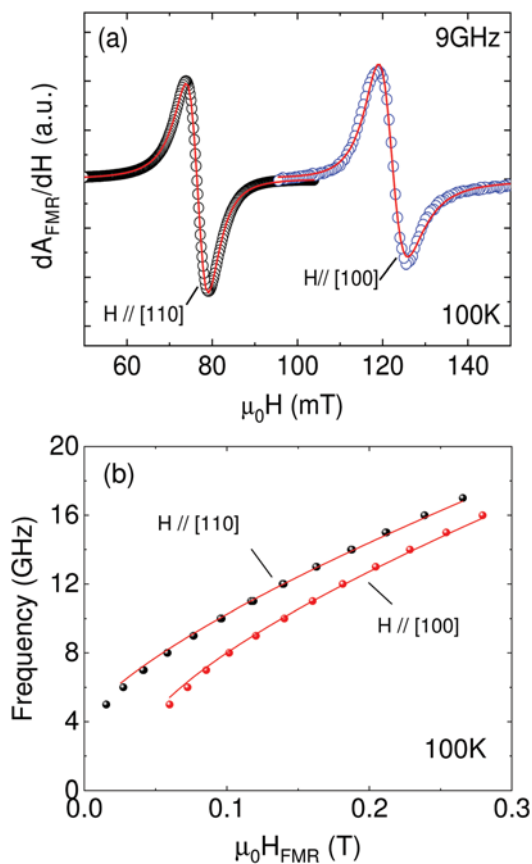


Fig. 4 (a) Ferromagnetic resonance spectra as a function of applied field for the two main in-plane orientations, *i.e.*, [110] and [100], taken at 100 K and 9 GHz. Solid lines represent the best fittings to the sum of symmetric and antisymmetric Lorentz line shapes as explained in the main text. (b) Frequency dependence of the resonant field at 100 K for the two main in-plane orientations. Solid lines correspond to the best simultaneous fit of both experimental data to eqn (2) and (3) in the main text.

in each direction, *i.e.*, in-plane magnetocrystalline anisotropy. In this case, [110] represents the in-plane easy axis (lower resonant field). Such in-plane anisotropy has been previously reported in other manganite based thin films³⁹ and it is believed to be a direct consequence of the highly epitaxial growth of materials with lower symmetry (orthorhombic/rhombohedral) onto cubic substrates as [110] is the in-plane projection of the [111] direction that, in manganite based perovskites, is the bulk easy axis.⁴⁰ It is worth noting that in the present case, no measurable differences in the FMR response between [100] and [010] directions have been observed. This is in agreement with previous results in thin films grown by chemical methods.¹⁹ The absence of any extra in-plane uniaxial anisotropy, which, on the contrary, is usually observed in thin films grown by physical methods,⁴¹ has been attributed to the different relaxation mechanisms involved during epitaxial growth using diverse techniques. This leads to different octahedral rotation patterns in the films to accommodate the stress and, as a consequence, to change orbital overlap and the magnetocrystalline anisotropy.

In the presence of in-plane anisotropy, the frequency dependence of the resonant field is no longer described by the simple

Kittel relationship and symmetry considerations need to be taken into account. For epitaxial thin films, a good approach is to consider a tetragonal symmetry, *i.e.*, by assuming [100] and [010] directions to be equivalent. In this case, the resonance condition may be written as⁴¹

$$f = \frac{\gamma}{2\pi} \mu_0 (H_R + H_{4ip} \cos 4\phi)^{1/2} \times \left[H_R + M_{\text{eff}} + \frac{1}{4} H_{4ip} (3 + \cos 4\phi) \right]^{1/2} \quad (1)$$

where γ is the gyromagnetic ratio, ϕ is the angle between the in-plane applied magnetic field and the [100] direction, and M_{eff} is defined as $4\pi M_{\text{eff}} = 4\pi M_S - 2K_{\perp}/M_S$ and includes the out-of-plane uniaxial anisotropy term K_{\perp} , whereas H_{4ip} is a four-fold in-plane anisotropy field, $H_{4ip} = +2K_{4ip}/M_S$.

For the main in-plane directions, eqn (1) easily simplifies and it may be written for $H \parallel [100]$, $\phi = 0^\circ$, as

$$f = \frac{\gamma}{2\pi} \mu_0 (H_R + H_{4ip})^{1/2} (H_R + M_{\text{eff}} + H_{4ip})^{1/2} \quad (2)$$

and, for $H \parallel [110]$, $\phi = 45^\circ$ as

$$f = \frac{\gamma}{2\pi} \mu_0 (H_R - H_{4ip})^{1/2} \left(H_R + M_{\text{eff}} + \frac{1}{2} H_{4ip} \right)^{1/2} \quad (3)$$

We have found that our experimental results may be nicely fitted by eqn (2) and (3). Fig. 4(b) shows an example for data taken at $T = 100$ K with solid lines being the best data fits according to the above equations.

Although eqn (2) and (3) are overparametrized, simultaneous and self-consistent fitting for both orientations allows obtaining reliable values of H_{4ip} . Its relation with temperature is plotted in Fig. 5(a). In this plot, error bars arise by averaging the data from several samples and taking into account the uncertainty in the fitting. First, we may see that H_{4ip} is negative, reflecting that indeed [110] is the in-plane easy axis. Secondly, it monotonously decreases when approaching the transition temperature. At 10 K, H_{4ip} is of the order of -100 mT. By using M_S values obtained from static SQUID measurements, this H_{4ip} value leads to an anisotropic constant of $K_{4ip}(10 \text{ K}) = -1.8 \times 10^4 \text{ erg cm}^{-3}$, which is similar to the reported values for manganite-based thin films.^{19,39,42,43} Anisotropic fields are expected to decay with temperature faster than saturation magnetization. In general, a power law dependence of the type $K(T)/K(T_0) = [M_S(T)/M_S(T_0)]^l$ is expected, where $K(T_0)$ and $M_S(T_0)$ are, respectively, the anisotropic field and magnetization at low temperature while l depends on the order of the anisotropy constant.⁴¹ The inset in Fig. 5(a) shows the experimental dependence of $K_{4ip}(T)/K_{4ip}(T_0)$ as a function of $M_S(T)/M_S(T_0)$ with $T_0 = 10$ K. Experimental data are properly described by a power-law behavior that can be fitted by an exponent $l = 6$ (solid line).

On the other hand, γ and M_{eff} are closely interdependent during the fitting process and a wide interval of values leads to equally good fittings. Nevertheless, best fits have been obtained for $\gamma/2\pi = g\mu_B/h \sim 29.5 \text{ GHz T}^{-1}$ implying that the gyromagnetic factor, $g \sim 2.1$, is slightly higher than the spin-only value of 2 usually observed in manganites and it seems to suggest a small contribution from orbital angular momentum. With the



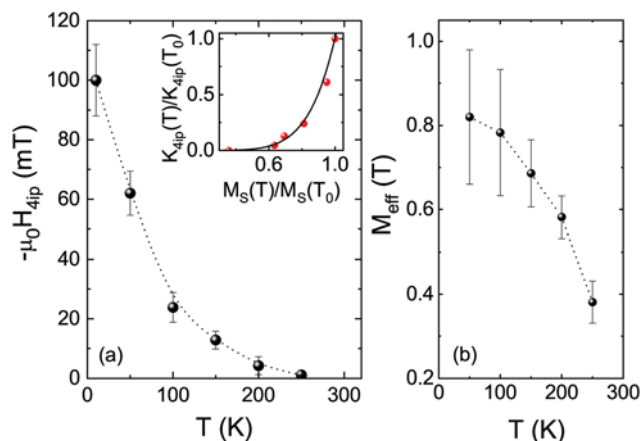


Fig. 5 (a) Temperature dependence of the fourfold in-plane anisotropy field, H_{4ip} , extracted from fits as shown in Fig. 4. The inset shows the power-law dependence of the normalized in-plane anisotropy constant $K_{4ip}(T)/K_{4ip}(T_0)$ as a function of normalized magnetization $M_S(T)/M_S(T_0)$. (b) Temperature dependence of M_{eff} . Error bars correspond to the uncertainty in the fit procedure and average over different samples. Dotted lines are guides for the eyes.

Table 1 Dynamic magnetic properties obtained from FMR and SQUID measurements

Parameter	LMO/STO
Gyromagnetic ratio, $\gamma/2\pi$	29.5 GHz T^{-1}
Gilbert damping, α at 150 K	1×10^{-2}
Inhomogeneous line-width, ΔH_0 at 150 K	$< 1 \text{ mT}$
In-plane anisotropic constant, K_{4ip} at 10 K	$-1.8 \times 10^4 \text{ erg cm}^{-3}$
In-plane anisotropy field, H_{4ip} at 10 K	-100 mT
Spin-mixing conductance, $g_{\uparrow\downarrow}$ at 150 K	$\sim 2 \times 10^{14} \text{ cm}^{-2}$

above assumptions, the temperature dependence of M_{eff} was obtained and it is plotted in Fig. 5(b) where error bars reflect uncertainty in the fitting parameters. By using the M_S values obtained from SQUID measurements, it easily follows that only negative values of K_{\perp} are able to fit the experimental data. As mentioned above, K_{\perp} includes not only any uniaxial magnetocrystalline anisotropy but also shape anisotropy and both are indistinguishable. A summary of the main magnetic parameters extracted from static and dynamic magnetic measurements is presented in Table 1.

The broadening of the resonance line, characterized by the linewidth ΔH , is a direct measure of the magnetic damping of the system. Damping is a key parameter for spintronic applications since it is closely related to the magnetization switching speed. Ideally, only intrinsic mechanisms contribute to the magnetic damping and, in such cases, the broadening of the ferromagnetic resonance linewidth may be described by a linear dependence on the frequency:⁴¹

$$\Delta H = \Delta H_0 + \frac{4\pi}{\gamma} \alpha f \quad (4)$$

In this expression, ΔH_0 represents an inhomogeneous broadening and α is the intrinsic Gilbert damping. Fig. 6 shows the dependence of ΔH as a function of frequency obtained at

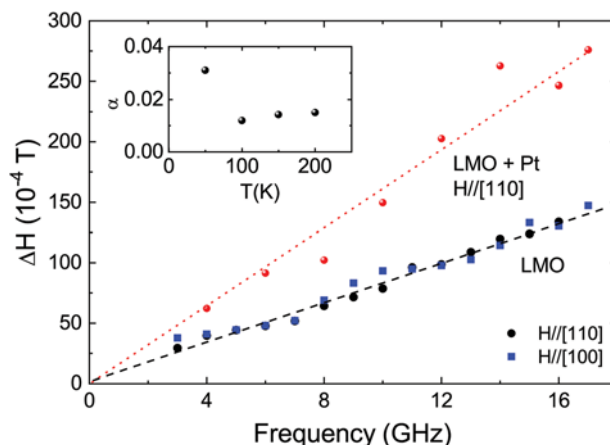


Fig. 6 Linewidth of ferromagnetic resonance of a LMO thin film as a function of frequency for two in-plane orientations taken at 150 K (blue squares and black dots). Linear behaviour corresponding to pure Gilbert damping may be observed and it is represented by the dotted line. The enhancement of damping after deposition of Pt as a cap layer is also presented (red points) and it may be associated with spin pumping through the FM/NM interface. Inset: Measured temperature dependence of Gilbert damping for the same LMO film.

150 K for the two in-plane directions, $H_{\parallel}[100]$ and $H_{\parallel}[110]$. Noticeably, linewidth broadening is independent of in-plane anisotropy and it is clear that the same straight line can nicely fit both curves. Two crucial results emerge from this result. First, ΔH_0 , which accounts for extrinsic broadening arising from small magnetic inhomogeneities in the sample, is very small ($\Delta H_0 \sim 1 \text{ mT}$), confirming overall the high quality of thin films prepared by PAD. Secondly, the absence of anisotropy in ΔH and its linear frequency dependence exclude the presence of any noticeable two-magnon scattering contribution to damping, that is known to be a limiting factor when obtaining low-damping ferromagnetic conducting materials.⁶ Furthermore, two-magnon scattering is usually activated by rough interfaces and surfaces and thus, their absence is in agreement with the smooth surface topography shown in Fig. 2. We may now soundly associate the slope of linear fits in Fig. 6 to the intrinsic Gilbert damping and by using eqn (4), we have obtained $\alpha_{LMO} \sim 1 \times 10^{-2}$ at $T = 150 \text{ K}$. This value is comparable with Gilbert damping values reported in the literature for other complex oxide thin films with similar thicknesses grown by using physical methods^{7,39,44} but there is still some room for improvement.⁵ In particular, improving the critical temperature of LMO thin films, either by optimizing oxygen stoichiometry or cation deficiency, may lead to enhanced damping parameters at room temperature. The inset in Fig. 6 shows the temperature evolution of the Gilbert coefficient. In general, Gilbert damping is related to the spin-orbit coupling linking the precessing magnetic moment to the lattice. The annihilation of magnons generates scattering of electron-hole pairs. Depending on if this occurs at the same band (intra-band) or not (inter-band), damping decreases with increasing temperature (conductivity-like, intra-band) or increases with temperature (resistivity-like, inter-band).^{2,5} Our results suggest that there is a large range of temperatures where damping is essentially



constant ($100 \text{ K} < T < 200 \text{ K}$) and it increases rapidly at low temperature ($T < 50 \text{ K}$), following a conductivity-like temperature dependence, usually associated with intraband behaviour. It is worth noting that our experimental finding is in agreement with the scenario suggested for manganites, where damping is governed by the so-called breathing Fermi surface model (intraband).⁵

The low damping parameter obtained in these PAD-grown LMO thin films opens the possibility to use them as a spin current source, through a spin pumping mechanism. In this phenomenon, a pure spin current is generated in a resonant ferromagnetic (FM) system and pumped into an adjacent non-magnetic (NM) conductor. When the conductor itself exhibits efficient spin-orbit coupling, as in the case of Pt, the spin-pumping mechanism will enhance the intrinsic Gilbert damping of the FM due to the extra dissipation channel of angular momentum because of spin pumping.⁴⁵ However, the diffusion of the spin-current towards the non-magnetic layer strongly depends on the so-called effective spin-mixing conductance $g_{\uparrow\downarrow}$ that measures the transparency of the FM/NM interface to spin current and their ability to relax within the non-magnetic layer. In this case, the Gilbert damping may be written as^{2,46}

$$\alpha_{\text{LMO+Pt}} = \alpha_{\text{LMO}} + \frac{g\mu_{\text{B}}}{4\pi M t_{\text{LMO}}} g_{\uparrow\downarrow} \quad (5)$$

where t_{LMO} is the thickness of the spin source film, *i.e.*, the LMO thin film, and μ_{B} is the Bohr magneton. The increase in Gilbert damping $\Delta\alpha = \alpha_{\text{LMO+Pt}} - \alpha_{\text{LMO}}$ has already been demonstrated for different FM/NM combinations, including alloys or oxides (as YIG⁴⁷ or LSMO¹⁰) as a spin source, grown by using vacuum techniques, such as sputtering or laser-ablation. However, it is believed to be extremely sensitive to the interface quality.² Thus, it is important to demonstrate that *ex situ* thin films grown by using chemical methods are suitable for spin generation. Red data points in Fig. 6 correspond to the FMR linewidth at 150 K along an easy axis of the same LMO thin film but after being capped with a 10 nm thick Pt film. In spite of higher noise in the curve, the increase in the damping is evident, and Gilbert damping is increased up to $\alpha_{\text{LMO+Pt}} \sim 2.5 \times 10^{-2}$. A rough estimation of the mixing conductance may be obtained from eqn (5). By using the values determined above, we have obtained $g_{\uparrow\downarrow}(150 \text{ K}) \sim 2 \times 10^{14} \text{ cm}^{-2}$, comparable to that reported for other oxide films,⁹ suggesting that interface transparency to spin transport is not inhibited by chemical growth methods.

4 Conclusions

We have demonstrated that $\text{La}_{0.92}\text{MnO}_3$ epitaxial thin films grown by polymer-assisted-deposition exhibit low roughness surfaces and magnetic properties fulfilling the requirements to be used as spin source active layers in heterostructures aimed for spintronic devices. Static magnetic and transport measurements show that LMO films are conducting and ferromagnetic, as expected from a double exchange scenario. On the other hand, dynamic magnetic properties were studied *via* broadband ferromagnetic resonance spectroscopy and we demonstrated

the presence of an in-plane four-fold magnetic anisotropy with [110] as an easy in-plane axis. In conjunction with microstructural analysis, this magnetic anisotropy resulted from the strained epitaxial growth of a LMO rhombohedral phase into the underlying cubic SrTiO_3 substrate. Magnetic damping exhibits mainly intrinsic Gilbert damping without appreciable contributions from extrinsic mechanisms. In the presence of a 10 nm Pt capping, we have observed a clear enhancement of magnetic damping that may be indicative of effective spin injection into the Pt layer by spin pumping from the LMO film. The effective mixing conductance estimated from the measurements reveals an interface between *ex situ* chemically grown LMO and Pt with reasonable transparency to spin transport to be suitable for applications in spintronic devices.

Conflicts of interest

There are no conflicts to declare.

Acknowledgements

We acknowledge financial support from the Spanish Ministry of Science, Innovation and Universities through Severo Ochoa (SEV-2015-04969), HETEROCOS (MAT2015-71664-R), SUMATE (RTI2018-095853-B-C21) and SPINCURIOX (RTI2018-099960-B-I00) projects cofinanced by the European Regional Development Fund. This project has received funding from the European Union through the Horizon 2020 research and innovation programme under the Marie Skłodowska-Curie grant agreement No 645658 (DAFNEOX Project) and through the FEDER Program. Hailin Wang acknowledges financial support from the China Scholarship Council (CSC). This work has been performed in the framework of the PhD programme in Materials Science of the Universitat Autònoma de Barcelona, through the China Scholarships Council (CSC)/Universitat Autònoma de Barcelona (UAB) Joint Scholarship. Authors thank Dr B. Bozzo and F. J. Campos for their technical support during magnetic and X-ray diffraction measurements. We acknowledge support of the publication fee by the CSIC Open Access Publication Support Initiative through its Unit of Information Resources for Research (URICI).

Notes and references

- 1 N. Locatelli, V. Cros and J. Grollier, *Nat. Mater.*, 2014, **13**, 11–20.
- 2 S. Azzawi, A. T. Hindmarch and D. Atkinson, *J. Phys. D: Appl. Phys.*, 2017, **50**, 473001.
- 3 A. Hoffmann and S. D. Bader, *Phys. Rev. Appl.*, 2015, **4**, 1–18.
- 4 L. Soumah, N. Beaulieu, L. Qassym, C. Carrétero, E. Jacquet, R. Lebourgeois, J. Ben Youssef, P. Bortolotti, V. Cros and A. Anane, *Nat. Commun.*, 2018, **9**, 3355.
- 5 Q. Qin, S. He, W. Song, P. Yang, Q. Wu, Y. P. Feng and J. Chen, *Appl. Phys. Lett.*, 2017, **110**, 112401.
- 6 M. A. Schoen, D. Thonig, M. L. Schneider, T. J. Silva, H. T. Nembach, O. Eriksson, O. Karis and J. M. Shaw, *Nat. Phys.*, 2016, **12**, 839–842.



- 7 G. Y. Luo, C. R. Chang and J. G. Lin, *J. Appl. Phys.*, 2014, **115**, 17C508.
- 8 G. Y. Luo, M. Belmeguenai, Y. Roussigné, C. R. Chang, J. G. Lin and S. M. Chérif, *AIP Adv.*, 2015, **5**, 097148.
- 9 H. K. Lee, I. Barsukov, A. G. Swartz, B. Kim, L. Yang, H. Y. Hwang and I. N. Krivorotov, *AIP Adv.*, 2016, **6**, 055212.
- 10 S. Emori, U. S. Alaán, M. T. Gray, V. Sluka, Y. Chen, A. D. Kent and Y. Suzuki, *Phys. Rev. B*, 2016, **94**, 224423.
- 11 D. G. Schlom, *APL Mater.*, 2015, **3**, 1–6.
- 12 I. Safi, *Surf. Coat. Technol.*, 2000, **127**, 203–218.
- 13 M. Opel, *J. Phys. D: Appl. Phys.*, 2012, **45**, 033001.
- 14 M. A. A. Mamun, A. Haque, A. Pelton, B. Paul and K. Ghosh, *IEEE Trans. Magn.*, 2018, **54**, 1–8.
- 15 A. Haque, A. R. Mahbub, M. Abdullah-Al Mamun, M. Reaz and K. Ghosh, *Appl. Phys. A: Mater. Sci. Process.*, 2019, **125**, 1–9.
- 16 Q. X. Jia, T. M. McCleskey, A. K. Burrell, Y. Lin, G. E. Collis, H. Wang, A. D. Li and S. R. Foltyn, *Nat. Mater.*, 2004, **3**, 529–532.
- 17 J. M. Vila-Funqueiriño, B. Rivas-Murias, J. Rubio-Zuazo, A. Carretero-Genevriér, M. Lazzari and F. Rivadulla, *J. Mater. Chem. C*, 2018, **6**, 3834–3844.
- 18 H. Wang, J. Gazquez, C. Frontera, M. F. Chisholm, A. Pomar, B. Martínez and N. Mestres, *NPG Asia Mater.*, 2019, **11**, 41.
- 19 J. M. Vila-Funqueiriño, C. T. Bui, B. Rivas-Murias, E. Winkler, J. Milano, J. Santiso and F. Rivadulla, *J. Phys. D: Appl. Phys.*, 2016, **49**, 315001.
- 20 J. Suntivich, H. A. Gasteiger, N. Yabuuchi, H. Nakanishi, J. B. Goodenough and Y. Shao-Horn, *Nat. Chem.*, 2011, **3**, 546–550.
- 21 J. T. Mefford, W. G. Hardin, S. Dai, K. P. Johnston and K. J. Stevenson, *Nat. Mater.*, 2014, **13**, 726–732.
- 22 J. Garcia-Barriocanal, J. C. Cezar, F. Y. Bruno, P. Thakur, N. B. Brookes, C. Ufeld, A. Rivera-Calzada, S. R. Giblin, J. W. Taylor, J. A. Duffy, S. B. Dugdale, T. Nakamura, K. Kodama, C. Leon, S. Okamoto and J. Santamaria, *Nat. Commun.*, 2010, **1**, 82.
- 23 M. Gibert, P. Zubko, R. Scherwitzl, J. Íñiguez and J. M. Triscone, *Nat. Mater.*, 2012, **11**, 195–198.
- 24 X. R. Wang, C. J. Li, W. M. Lü, T. R. Paudel, D. P. Leusink, M. Hoek, N. Poccia, A. Vailionis, T. Venkatesan, J. M. Coey, E. Y. Tsymbal, Ariando and H. Hilgenkamp, *Science*, 2015, **349**, 716–719.
- 25 J. Roqueta, A. Pomar, L. Balcells, C. Frontera, S. Valencia, R. Abrudan, B. Bozzo, Z. Konstantinović, J. Santiso and B. Martínez, *Cryst. Growth Des.*, 2015, **15**, 5332–5337.
- 26 Y. S. Hou, H. J. Xiang and X. G. Gong, *Phys. Rev. B: Condens. Matter Mater. Phys.*, 2014, **89**, 64415.
- 27 A. Gupta, T. R. McGuire, P. R. Duncombe, M. Rupp, J. Z. Sun, W. J. Gallagher and G. Xiao, *Appl. Phys. Lett.*, 1995, **67**, 3494.
- 28 J. Töpfer and J. B. Goodenough, *J. Solid State Chem.*, 1997, **130**, 117–128.
- 29 I. Marozau, P. T. Das, M. Döbeli, J. G. Storey, M. A. Uribe-Laverde, S. Das, C. Wang, M. Rössle and C. Bernhard, *Phys. Rev. B: Condens. Matter Mater. Phys.*, 2014, **89**, 174422.
- 30 Y. K. Liu, H. F. Wong, K. K. Lam, C. L. Mak and C. W. Leung, *J. Magn. Magn. Mater.*, 2019, **481**, 85–92.
- 31 A. M. Zhang, S. L. Cheng, J. G. Lin and X. S. Wu, *J. Appl. Phys.*, 2015, **117**, 1–5.
- 32 A. Biswas, C.-H. Yang, R. Ramesh and Y. H. Jeong, *Prog. Surf. Sci.*, 2017, **92**, 117–141.
- 33 N. Sakai, H. Fjellvag and B. Lebech, *Acta Chem. Scand.*, 1997, **51**, 904–909.
- 34 D. Fuchs, L. Dieterle, E. Arac, R. Eder, P. Adelman, V. Eyert, T. Kopp, R. Schneider, D. Gerthsen and H. V. Löhneysen, *Phys. Rev. B: Condens. Matter Mater. Phys.*, 2009, **79**, 1–9.
- 35 F. Sandiumenge, J. Santiso, L. Balcells, Z. Konstantinovic, J. Roqueta, A. Pomar, J. P. Espinós and B. Martínez, *Phys. Rev. Lett.*, 2013, **110**, 107206.
- 36 J. Santiso, J. Roqueta, N. Bagués, C. Frontera, Z. Konstantinovic, Q. Lu, B. Yildiz, B. Martínez, A. Pomar, L. Balcells and F. Sandiumenge, *ACS Appl. Mater. Interfaces*, 2016, **8**, 16823–16832.
- 37 M. Haidar, M. Ranjbar, M. Balinsky, R. K. Dumas, S. Khartsev and J. Åkerman, *J. Appl. Phys.*, 2015, **117**, 17D119.
- 38 S. Mercone, M. Belmeguenai, S. Malo, F. Ott, F. Cayrel, M. Golosovsky, B. Leridon, C. Adamo and P. Monod, *J. Phys. D: Appl. Phys.*, 2017, **50**, 045001.
- 39 Å. Monsen, J. E. Boschker, F. Macià, J. W. Wells, P. Nordblad, A. D. Kent, R. Mathieu, T. Tybell and E. Wahlström, *J. Magn. Magn. Mater.*, 2014, **369**, 197–204.
- 40 M. Konoto, T. Kohashi, K. Koike, T. Arima, Y. Kaneko, Y. Tomioka and Y. Tokura, *Appl. Phys. Lett.*, 2004, **84**, 2361–2363.
- 41 M. Farle, *Rep. Prog. Phys.*, 1998, **61**, 755–826.
- 42 M. Belmeguenai, F. Zighem, T. Chauveau, D. Faurie, Y. Roussigné, S. M. Chérif, P. Moch, K. Westerholt and P. Monod, *J. Appl. Phys.*, 2010, **108**, 063926.
- 43 F. Mompean, Z. Sefrioui, N. Reyren, T. Feher, M. Varela, C. Leon, J. Santamaria, M. Cabero, K. Nagy, F. Gallego, A. Sander and M. Rio, *APL Mater.*, 2017, **5**, 096104.
- 44 M. A. A. Mamun, A. Haque, A. Pelton, B. Paul and K. Ghosh, *J. Magn. Magn. Mater.*, 2019, **478**, 132–139.
- 45 Y. Tserkovnyak, A. Brataas and G. E. W. Bauer, *Phys. Rev. Lett.*, 2002, **88**, 117601.
- 46 Y. Liu, Z. Yuan, R. Wesselink, A. A. Starikov and P. J. Kelly, *Phys. Rev. Lett.*, 2014, **113**, 207202.
- 47 Y. Sun, H. Chang, M. Kabatek, Y.-Y. Song, Z. Wang, M. Jantz, W. Schneider, M. Wu, E. Montoya, B. Kardasz, B. Heinrich, S. G. E. te Velthuis, H. Schultheiss and A. Hoffmann, *Phys. Rev. Lett.*, 2013, **111**, 106601.



Chapter 5

General discussion

5. General discussion of the results

The aim of this Thesis is to setup and tune the PAD methodology for growing epitaxial functional oxide perovskite thin films of low surface roughness, high crystallinity, and optimal electric and magnetic properties, and investigate the possibility of applications.

Growth condition optimization

The optimization process for the growth conditions was carefully conducted for each system. The relationship between the growth parameters and the properties was studied, and then the ideal growth conditions were determined.

The thickness is easily controlled by the speed of spin-coating and the concentration of the precursor solution. The PAD method showed high reproducibility. Typical thicknesses are from 5~30 nm.

A very relevant process is the thermal treatment.

TGA/DSC was used to trace the thermal behavior of the precursor solution from room temperature to 600 °C. The results show that the organic species begin to decompose at 220 °C, and finish at around 550 °C.

The crystallization process at relatively higher temperature is more complicated. The conventional annealing process was studied firstly. The heating and cooling ramp, the final temperature, dwell, and the oxygen flow are very important parameters related to the surface roughness, crystallinity, electric and magnetic properties.

The results of growth conditions of LCMO films indicate that high enough temperatures (900 °C), longer annealing time and higher oxygen flow are favorable for the degree of crystallinity, the microstructural film's quality, and the magnetic properties; however, if these values are too high, the formation of segregations on the surface of the films occurs. Taking every aspect into consideration, we determined the ideal growth conditions (growth temperature of 900 °C, annealing time of ~1 h, heating and cooling ramps are 3 °C/min, and oxygen flow 0.3 l/min).

The optimized growth conditions for LNMO films are similar to those of LCMO films, although high ordering here is more difficult to attain due to the closer atomic radii of Ni^{2+} and Mn^{4+} .

The ideal growth conditions for LMO films are as follows, growth temperature ranges from 950°C to 990°C, annealing time of ~1 h, heating and cooling ramps are 2 ~ 4 °C/min, and oxygen flow 0.1 ~ 0.2 l/min.

B-site ordering in LCMO and LNMO prepared by conventional annealing process

Both LCMO and LNMO films were prepared by conventional annealing process. The magnetic properties of the LCMO films ($M_s \approx 6 \mu_B/\text{f.u.}$ and $T_C \approx 230 \text{ K}$) were close to the theoretical values, indicating almost full Co/Mn ordering. Then STEM in combination with EELS maps was used to prove the existence of full Co/Mn ordering. The sudden drop of the remnant magnetization at $H=0$ in the $M-H$ loops can be explained by the existence of APBs. In the case of LNMO films, T_C is around 270 K. However, M_s values are around $4 \mu_B/\text{f.u.}$, corresponding to around 10% ASD concentration. The sudden drop of the remnant magnetization at $H=0$ was not observed in the $M-H$ loop, indicating the absence of APBs. The X-ray absorption spectroscopy was used to measure the oxidation state of Ni, and Mn, they are +2 and +4, respectively. It proves that the reduction of the M_s comes from ASD, instead of different magnetic phases.

B-site ordering in LCMO and LNMO prepared by RTA process

The effect of fast heating rates was also investigated. The LCMO and LNMO films were also prepared by RTA with a heating ramp of 20 °C/s, and then compared with the counterpart samples prepared by conventional annealing process. The $M-T$ curves of the as-grown LCMO/STO samples show some kind of magnetic disorder. The sudden drop of the remnant magnetization at $H=0$ and the relatively high M_s value indicate the magnetic disorder is mainly associated with APBs. After post annealing at high temperature in oxygen flow, the APBs were completely suppressed. LCMO/LAO shows similar results. The as-grown LNMO/STO and LNMO/LAO show larger magnetic disorder, compared to the samples grown by conventional annealing process. The $M-$

T curves exhibit a non-monotonic behavior with a local minimum, and the M_S values are below $3.7 \mu_B/\text{f.u.}$. After a post-growth treatment in oxygen flow, the M_S increase to around $4.3 \mu_B/\text{f.u.}$, the $M-T$ curves show a slower decay rate of the magnetization and an increase of T_C . All these facts seem to indicate that the heating ramp rate has only minor influence on the B-B' site cationic ordering that is mainly controlled by charge difference and steric effects. The disordering in LCMO films is mainly caused by the APBs, and they can be suppressed by a post-grow annealing under oxygen flow. The main cause of disordering in LNMO films is ASD, high ASD density precludes the formation of APB, and ASD cannot be suppressed by a post growth annealing.

Dynamic magnetic properties and spin pumping in $\text{La}_{0.92}\text{MnO}_3$ thin films

The LMO films show low surface roughness, and high crystallinity. The T_C is around 290 K, and the T_{MI} is 280 K. At an applied magnetic field of 9 T, the magnetoresistance is 60% at 280 K. The dynamic magnetic properties were studied by using a ferromagnetic resonance spectrometer (FMR). The [110] axis is found to be the easy in-plane axis. The inhomogeneous line-width, ΔH_0 , is very small (~ 1 mT) at 150 K, confirming overall the high quality of thin films and the smooth surface topography. The intrinsic Gilbert damping is $\alpha_{LMO} \sim 1 \times 10^{-2}$ at 150 K, it opens the possibility to use the LMO films as a spin current source, through a spin pumping mechanism. A 10 nm thick Pt layer was deposited on top of LMO film by using sputtering. The Gilbert damping increases up to $\alpha_{LMO+Pt} \sim 2.5 \times 10^{-2}$. This increase of the magnetic damping is indicative of effective spin injection into the Pt layer by spin pumping from the LMO film. Our results demonstrate that LMO films grown by PAD may be used as efficient spin source systems in heterostructures for spintronic devices.

Chapter 6

Conclusions

6. Conclusions

This thesis focus on the preparation of complex oxide thin films by using a methodology based on aqueous chemical solutions made of metal salts and water-soluble polymers as film precursors known as polymer assisted deposition (PAD).

Chemical solution deposition (CSD) has many advantages over vacuum techniques, such as low cost scalability, the ability of coating on irregular surfaces, and stoichiometric versatility. PAD is a very attractive CSD method, since it is based on using aqueous solutions of environmentally friendly metal salts and commercially available polymers.

It was the first time that we faced the challenges of the PAD methodology at ICMAB-CSIC, so the basics of the thin film growth process had to be set up from the very beginning. The preparation of the precursor solutions, spin-coating, and thermal treatments are the key steps for the film growth. Following thin film growth, surface roughness, crystallinity and electric and magnetic properties were characterized.

The conclusions can be summarized as follows:

In the solution preparation process, PEI, EDTA and the salts were added to water in sequence. After they were dissolved completely, they were filtered with membranes (cut-off molecular weight of 10 kDa) to remove non-coordinated species and undesired anions. The pH value has a very important impact on the stability of the solutions. In the preparation process, the cations have specific pH ranges to reach high retention. But finally their pH values were adjusted to close 6 to avoid precipitation during the mixing. Six precursor solutions with different cations were prepared, namely La^{3+} , Sr^{2+} , Ni^{2+} , Co^{2+} , Mn^{2+} and Ru^{3+} . The concentrations of the cations were measured with ICP-AES. Most of the concentration values range from 100 mmol/l to 200 mmol/l. Typical viscosity values were in the range $\eta \approx 3\text{-}4$ MPa-s.

Individual solutions were mixed according to the stoichiometric ratio of the cations of a given composition. In this thesis, nine different poly-cationic solutions were prepared; they are $\text{La}_{0.92}\text{MnO}_3$, $\text{La}_2\text{CoMnO}_6$, $\text{La}_2\text{NiMnO}_6$, LaNiO_3 , $\text{La}_{0.7}\text{Sr}_{0.3}\text{MnO}_3$, $\text{La}_{0.5}\text{Sr}_{0.5}\text{CoO}_3$, LaCoO_3 , SrCoO_3 and SrRuO_3 .

Different films with thickness from 5 - 30 nm were prepared. The thickness is mainly controlled by the speed of spin-coating, and the concentration of the solutions. Speed above 4000 rpm is necessary for the uniformity of the thickness of the films.

The thermal behavior of the precursor solution was traced by TGA/DSC, the organic species decompose from 220 °C to around 550 °C. Crystallization takes place at temperatures above 600 °C. The surfaces roughness, crystallinity, magnetic and electronic properties are more related with the crystallization, the dwell time, the heating ramp, and the O₂ flow rate.

High-quality epitaxial LCMO, LNMO and LMO films have been prepared with a single one-step growth process using the PAD technique on top of STO and LAO (001)-oriented substrates. All the films are epitaxial and show low roughness surfaces, high crystallinity, and good magnetic properties.

The LCMO and LNMO samples prepared by conventional annealing process display high B-site cationic ordering. The magnetic properties of the LCMO films ($M_S \approx 6 \mu_B/\text{f.u.}$ and $T_C \approx 230 \text{ K}$) are indicative of almost full Co/Mn ordering. In the case of LNMO films, T_C is around 270 K. However, M_S values are around $4 \mu_B/\text{f.u.}$, indicating around 10% ASD. The existence of full Co/Mn cationic ordering is supported by STEM measurements; EELS maps indicate the ordered occupancy of B–B' sites by Co/Mn cations. By using X-ray absorption spectroscopy, we have verified that the oxidation state of Ni is +2, and that of Mn is +4, irrespective of the structural strain and the amount of ASD of the samples. We conclude that the reduction of magnetic moment in the LNMO samples is linked to the introduction of Ni²⁺-O²⁻-Ni²⁺ and Mn⁴⁺-O²⁻-Mn⁴⁺ superexchange AFM interactions at anti-sites reducing the M_S .

The magnetic properties of samples prepared by RTA are similar to the counterpart samples prepared by conventional annealing process. The annealing process seems to have only minor influence on the B-B' site cationic ordering that is mainly controlled by charge difference and steric effects, however, the microstructure of the samples seems to be different. In the case of the LCMO system samples prepared by RTA present almost full B-B' site cationic ordering, M - H loops exhibit the sudden drop of the remnant magnetization at $H=0$, indicative of the existence of APBs. In the case of

the LNMO system full B-B' site cationic ordering is hard to obtain since the ionic radii difference between Ni^{2+} and Mn^{4+} is too small. However, the values of M_S obtained both in LNMO/STO and LNMO/LAO, around $4.3 \mu_B/\text{f.u.}$, after a post-RTA thermal treatment corresponding to an ASD concentration below 10% are among the best reported in the literature. APBs in RTA grown LCMO samples are easily suppressed by a post-annealing treatment. ASD in RTA grown LNMO samples cannot be suppressed by a post growth annealing.

Static magnetic and transport measurements show that LMO films are metallic and ferromagnetic below $T_C \approx 300$ K. Dynamic magnetic properties show the presence of an in-plane four-fold magnetic anisotropy with [110] as an easy in-plane axis. Magnetic damping exhibits mainly intrinsic Gilbert damping without appreciable contributions from extrinsic mechanisms. In the presence of a 10 nm Pt capping, we have observed a clear enhancement of magnetic damping that may be indicative of effective spin injection into the Pt layer by spin pumping from the LMO film. The effective mixing conductance estimated from the measurements reveals an interface between ex situ chemically grown LMO and Pt with reasonable transparency to spin transport to be suitable for applications in spintronic devices.

We have proved that that the PAD technique allows obtaining epitaxial complex oxide thin films of high microstructural quality and low surface and interfacial roughness suitable for spintronics applications.

Chapter 7

Future perspectives

7. Future perspectives

The know-how gained during this PhD thesis work opens up a whole world in the field of PAD growth of functional oxide thin films and heterostructures. To mention a few interesting possibilities to be further investigated:

Integration of functional oxides on semiconductors

Coupling oxides with semiconductors can presage new and unexpected functionalities that exist in neither of the individual materials. As oxides and semiconductors exhibit properties that are complementary to one another, epitaxial heterostructures comprised of the two are promising to deliver rich functionalities. A serious challenge issue is to match the dissimilar (structurally, thermally, and in general chemically reactive) oxides and semiconductors in hybrid structures. Silicon is the most fundamental technological material for electronics. Thus, a successful coupling of functional oxides with silicon has an enormous potential for new applications in electronics. Therefore it is interesting to initiate the research on the integration of functional ferroelectric (BaTiO_3 , $\text{Hf}_{1-x}\text{Zr}_x\text{O}_2$) and ferromagnetic ($\text{La}_{0.7}\text{Sr}_{0.3}\text{MnO}_3$, $\text{La}_{0.92}\text{MnO}_3$...) oxides on Silicon using the PAD growth method. As a first approach it will be easier to use STO or YSZ buffer layers deposited on Silicon by physical methods (MBE or PLD).

Oxide Bilayers

Multiferroic materials possess at least two ferroic orders, like ferroelasticity, ferroelectricity, and ferro- or ferrimagnetism. Among the multiferroics, materials that show a coupling between the order phenomena are of special interest. In particular, the magnetoelectric (ME) coupling has attracted high interest for its potential applications in e.g. sensors or multistate data memories. Multiphase multiferroic systems are particularly attractive, since they often show strong ME-effects and the order temperatures of the different components can be tailored independently. The best examined multiferroic oxide systems are combinations of ferrimagnetic ferrite spinels like CoFe_2O_4 or NiFe_2O_4 and ferroelectric perovskites like barium titanate BaTiO_3 or lead zirconate titanate $\text{PbZr}_x\text{Ti}_{1-x}\text{O}_3$. The nowadays most common way to fabricate $\text{CoFe}_2\text{O}_4/\text{BaTiO}_3$ and $\text{NiFe}_2\text{O}_4/\text{BaTiO}_3$ thin films is pulsed laser deposition

(PLD), which generally results in epitaxial films with smooth surfaces on the atomic scale. The PAD approach is highly attractive because the technical requirements are low and a large variety of chemical compositions can be tested within short times. PAD grown bilayer films consisting of MFe_2O_4 ($M=Co, Ni$) and $BaTiO_3$ deposited on platinum coated silicon wafers are appealing to investigate the simultaneous presence of ferroelectric and ferrimagnetic properties of the bilayer samples as well as their magnetoelectric coupling.

PAD grown nanocomposites

In close connection with the previous paragraph, nanocomposite materials are artificial materials displaying enhanced functional properties or the combination of properties of different oxides. In this context, it is relevant the preparation from chemical solutions of nanocomposite oxide layers with better functional properties. Composite materials will be prepared from the incorporation into the PAD precursor solution of previously grown oxide nanoparticles (“ex-situ” approach) forming a colloidal solution. The preparation of multiferroic nanocomposites is foreseen. The aspects to be addressed will be the stability of the nanoparticles in the precursor solutions considering the specificities of the polymer based PAD solutions, the use of appropriate binders and solvents, the growth conditions (temperature, heating ramps, gas atmosphere, etc.) to obtain nanocomposites with a homogeneous distribution of nanoparticles, and the characterization of the structural and functional properties of the synthesized layers.

Ferromagnetic insulating tunnel barriers

The development of spintronic devices requires the generation and control of highly spin-polarized currents or pure spin currents. A way of obtaining a highly spin polarized current is by using the spin filtering effect through ferromagnetic-insulator-ferromagnetic tunnel barriers. It has been shown that the same effect can be obtained simply by using a ferromagnetic insulating barrier. A single ferromagnetic insulating barrier with strong magnetocrystalline anisotropy is sufficient for realizing sensor and memory functionalities in a tunneling device based on tunneling anisotropic magnetoresistance. However, ferromagnetic insulators (FMI) are very scarce; among

the few FMI the double perovskite $\text{La}_2\text{NiMnO}_6$ is very attractive due to its high Curie temperature, $T_C \approx 260\text{K}$, and magnetodielectric properties. The requirements needed for an ideal tunnel barrier are high crystalline epitaxial quality, thickness below 4 nm and very smooth surface. We think that these requirements can be reached for $\text{La}_2\text{NiMnO}_6$ grown on Nb-doped STO substrates by the PAD approach after proper tuning of the solution rheological properties, the spin coating conditions and the thermal treatment.

PAD solutions for inkjet printing

The devices fabricated by vapor deposition or chemical solution deposition always need stencils, and masks or subsequent separating, removing or etching processes to make patterns. Inkjet printing not only can overcome these problems, but also has more advantages like accurate deposition of minute quantity of materials, the resolution in sub-micrometer range for patterning, and the ability to produce meter-scale homogeneous films. Inkjet printing is attractive for various applications such as high temperature superconducting tape, electric devices, thin film transistor, and solar cells.

The key challenge of inkjet printing is the ink preparation, the requirements for the ink include stability, proper viscosity ($1\sim 25\text{ MPa}\cdot\text{s}$) and surface tension range ($20\sim 50\text{ mN}\cdot\text{m}^{-1}$), and it should be chemically compatible with the printer system. The precursor solution of PAD method can be stable for months, even for years. The viscosity is in the range of the requirements. The chemicals in the solution will not react with the printer system. As a result, PAD precursor solutions are promising to be used in inkjet-printing technology.

Appendix

Ferromagnetic resonance

The dynamic magnetic properties of thin films were studied by using a ferromagnetic resonance spectrometer (FMR) made of a broadband coplanar waveguide (CPW) (NanOsc), inserted in a Physical Properties Measurements System (PPMS by Quantum Design). This experimental setup allows for a complete characterization of the dynamic magnetic properties as function of the external applied field and temperature in the frequency range between 2 and 18 GHz.

Ferromagnetic resonance (FMR) is a very powerful experimental technique for the study of dynamical magnetic properties of materials. In our analysis, we will assume two basic simplifications: a) We will use the macrospin model, so that spatial variations of M are neglected and therefore, the magnetization is uniform over the sample. b) Internal effects such as exchange, anisotropy, and demagnetization are considered by a net effective internal field H_i , so that the total field is $H_{eff} = H_{ext} + H_i$.

When a ferromagnetic sample with a magnetization M is placed in an external magnetic field, H_{ext} , the magnetization will precess towards H_{ext} to minimize the energy. Thus, a torque appears to drive a continuous precession of the magnetic moments around the effective field H_{eff} . In the absence of losses, the equation of motion is given by: ¹

$$\frac{dM}{dt} = -\gamma M \times H \quad \text{Eq. A 1}$$

where $\gamma = g\mu_B/\hbar$ is the gyromagnetic ratio of the electron with the Landé factor $g \approx -2$. In absence of internal fields, the magnetization will precess around H_{ext} with the Larmor frequency $\omega_L = \gamma H_{ext} = 28 \text{ GHz T}^{-1}$. Eventually, M will reach equilibrium when it is parallel to H_{ext} . To induce the precession of the magnetization during an FMR experiment, an RF magnetic field, h_{rf} , is applied transverse to H_{eff} . The h_{rf} is applied by an electromagnetic signal that is transmitted through the CPW. When the frequency, f , of the transverse field is at the resonance condition, M will precess around H_{eff} in a

precessional cone. The equation that describes the magnetization's precession is the Landau-Lifshitz-Gilbert (LLG) equation:¹

$$\frac{dM}{dt} = -\gamma M \times \left(H_{eff} - \frac{\alpha}{\gamma M_S} \frac{dM}{dt} \right) = -\gamma M \times H_{eff} + \frac{\alpha}{M_S} M \frac{dM}{dt} \quad \text{Eq. A 2}$$

where α is the dimensionless Gilbert damping constant, of order 10^{-2} in ferromagnetic thin films. H_{eff} is the total effective magnetic field which is a sum of static applied magnetic field (H_{ext}) and internal magnetic field (H_{in}). The dynamics of the magnetization's precession involves two torques (Figure A 1): the first pulls M towards H (damping torque, blue) and the second points orthogonally to M and H (the precessional torque, green). The damping torque moves the local magnetization vector toward the local effective field direction. The Gilbert damping parameter, α , is a dimensionless scaling term for the damping vector. This phenomenological term is related to the magnetization relaxation rate, which is of high interest for technological applications.²

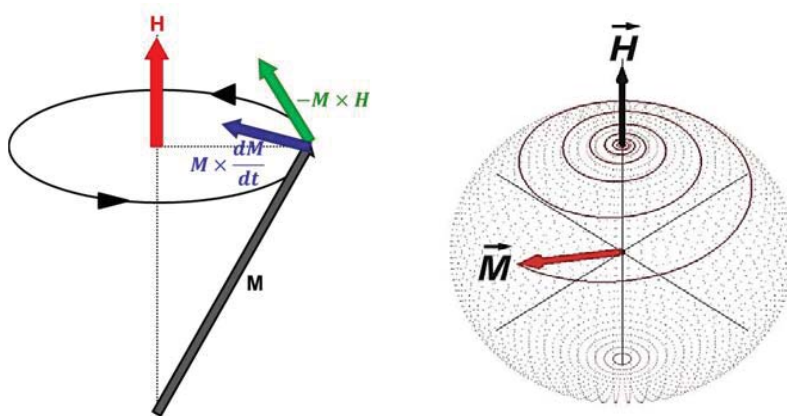


Figure A 1. (a) Torque components exerted on the magnetization M by rotational field H (b) Motion of M for constant H .¹

Experimental setup of FMR

A sketch of the experimental setup used in this thesis is shown in Figure A 2 together with a picture of the PPMS insert where the Helmholtz coils for field modulation, the sample holder with the CPW and RF coax cables are clearly appreciated.

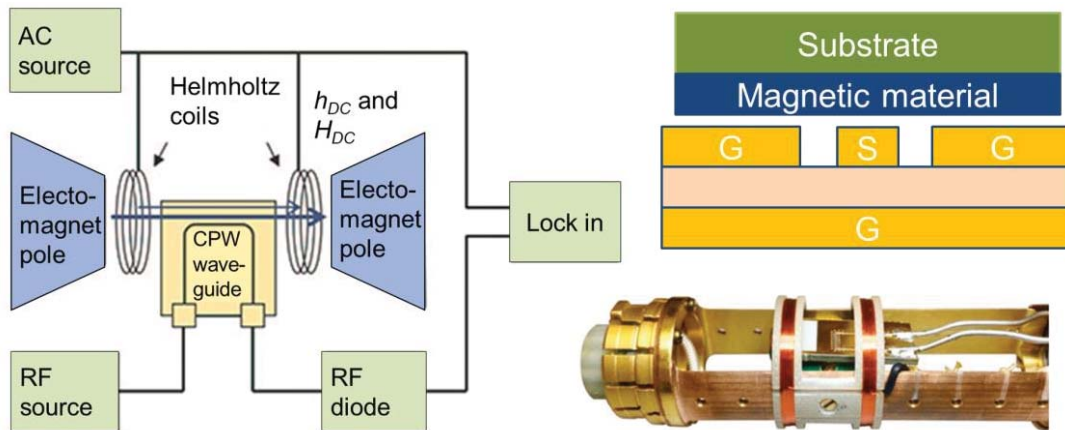


Figure A 2. (a) Schematic broadband FMR measurement setup highlighting the critical components. (b) Cross section view of the CPW (yellow) with a sample on top. (c) Head of the PPMS insert where Helmholtz coils for field modulation, the sample holder with the CPW and RF coax cables are clearly appreciated.

To measure a single FMR spectrum, the RF field is held at a fixed frequency while H_{DC} magnetic field is swept from a high magnetic field down past the resonance condition. As H_{DC} is swept through the resonance condition, the magnetization will begin to resonantly precess and will therefore absorb energy from the CPW. This decrease in transmitted RF energy when sweeping through the resonance field is converted to a DC voltage by a broadband RF diode. In order to improve the signal-to-noise ratio (SNR), a lock-in detection technique is often employed, which requires modulating the signal at a known frequency. This modulation is provided by an additional set of Helmholtz coils powered by an AC source which in-turn produces a small (~ 1 Oe) modulation (H_{AC}) to the much larger H_{DC} . Therefore, with this modified measurement scheme one actually measures the derivative of the transmitted power (dP/dH_{DC}). An example of typical spectra is shown in Figure A 3.

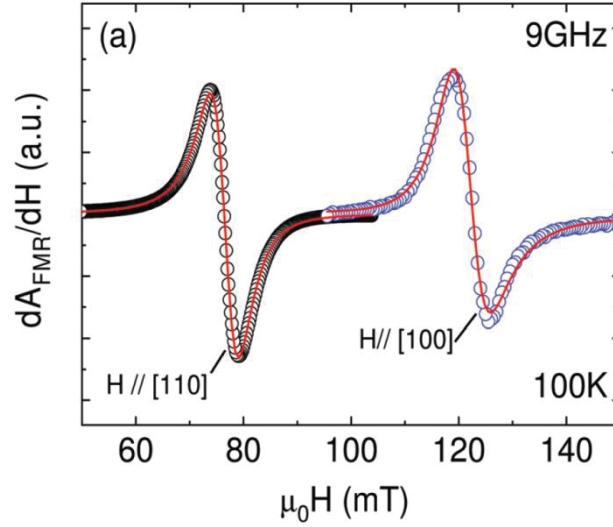


Figure A 3. Ferromagnetic resonance spectra as a function of applied field for the two main in-plane orientations, i.e., [110] and [100], taken at 100 K and 9 GHz in a La-deficient LMO film.

The single spectrum gives access to two important experimental parameters, the resonance field H_{res} and the spectrum linewidth, ΔH that are related to the magnetic properties of the sample. The H_{res} and ΔH are extracted by fitting the absorption signal to the derivative of an asymmetrical Lorentzian. By analyzing the frequency dependence of H_{res} and ΔH the dynamical parameters of interest, namely the gyromagnetic ratio (γ), the effective magnetization (M_{eff}), the Gilbert damping parameter (α), and the inhomogeneous broadening (ΔH_0) can be extracted. The resonant field, H_{res} , and the resonance frequency, f_{res} , are related through the Kittel equation:³

$$f_{res} = \frac{\gamma}{2\pi} \sqrt{H_{res}(H_{res} + 4\pi M_{eff})} \quad \text{Eq. A 3}$$

By fitting experimental data according to the previous formula γ and M_{eff} can be determined. Then, with the obtained value of γ by the fit of ΔH vs. f , values of α and ΔH_0 can be determined:⁴

$$\Delta H = \frac{2\alpha}{\gamma} f + \Delta H_0 \quad \text{Eq. A 4}$$

References

- [1] Sharma, M.; Pathak, S.; Sharm, M. FMR Measurements of Magnetic Nanostructures. In Ferromagnetic Resonance - Theory and Applications; 2013; Chapter Chapter 4, pp 93-95.
- [2] Tserkovnyak, Y.; Brataas, A.; Bauer, G. E. W. Enhanced Gilbert Damping in Thin Ferromagnetic Films. Phys. Rev. Lett. 2002, 88 (11), 117601.
- [3] Kittel, C. On the Theory of Ferromagnetic Resonance Absorption. Phys. Rev. 1948, 73 (2), 155-161.
- [4] Farle, M. Ferromagnetic resonance of ultrathin metallic layers. Reports on Progress in Physics 1998, 61 (7), 755-826.